Structure of copper halide melts, rare earth chalcogenide glasses and glassy germania at high pressure

Drewitt, James

Award date:
2009

Awarding institution:
University of Bath

Structure of copper halide melts, rare earth chalcogenide glasses and glassy germania at high pressure

James William Eric Drewitt

A thesis submitted for the degree of Doctor of Philosophy

University of Bath

Department of Physics

June 2009

Abstract

The structure of molten CuCl, CuI and $(CuCl)_x(CuI)_{1-x}$ $(0 \leq x \leq 1)$ mixtures was investigated at the total structure level by using neutron diffraction. The results are compared with those obtained for CuCl and CuI from other experiments, theory and computer simulation. It is found that existing models of CuCl and CuI must first be improved before a realistic attempt can be made to account for the structure of their mixtures.

The structure and thermal properties of $(R_2X_3)_{0.07}(Ga_2X_3)_{0.33}(GeX_2)_{0.60}$ glasses, where R denotes a rare earth element and X denotes a chalcogenide element S or Se, were studied using a combination isomorphic substitution in neutron and x-ray diffraction, ^{71}Ga magic angle spinning (MAS) nuclear magnetic resonance (NMR) and differential scanning calorimetry (DSC) methods. The results show that Ge and Ga are four-fold coordinated by the chalcogen element in these glasses. Difference function methods were applied to the diffraction results and for the large rare earth ions provided an R-S coordination number of 8.1(2) and nearest neighbour R-S bond distance of 3.03(3) Å in the sulphide glass and an R-Se coordination number of 8.0(2) and R-Se bond distance of 3.05(3) Å in the selenide glass. For the small rare earth ions in the selenide glass a smaller R-Se coordination number of 5.0(2) and R-Se bond distance of 2.93(3) Å were obtained.

In situ high pressure neutron diffraction experiments were performed on GeO_2 glass using the Paris-Edinburgh press on the D4C diffractometer at the Institut Laue-Langevin (ILL), France. An analysis procedure was developed to account for the gasket and background scattering at each pressure point

and improved neutron shielding led to the extraction of high quality total structure factors at pressures up to 8 GPa. Experiments were also performed using the PEARL instrument at the pulsed neutron source ISIS, UK, where improvements were made to the incident neutron beam collimation, pressure cell shielding and experimental methods to obtain the correctly normalised total structure factors for GeO_2 glass at pressures up to 14(1) GPa. The results show that Ge is four-fold coordinated by oxygen from ambient pressure to 5 GPa. A gradual increase in the Ge-O coordination number is then observed, reaching 4.9(1) at 9.0(5) GPa and 5.5(1) at 14(1) GPa, which is accompanied by an increase in the Ge-O bond length from 1.73(2) to 1.81(2) Å. With pressure increasing from ambient, there is a smooth increase in the position and decrease in height of the first sharp diffraction peak which is associated with the intermediate range order. The overall results are therefore consistent with two densification mechanisms, one associated with a collapse of the network structure and the other with an increase in the local coordination number and Ge-O bond length.

Acknowledgements

I would like to thank the many people at the University of Bath who I have worked with during my PhD for their friendship and expertise. In particular, I thank Prof. Phil Salmon for his excellent supervision and immense dedication to the physics of disordered materials. I also thank my colleagues in the liquid and amorphous materials (LAM) research group Dr. Anita Zeidler, Prae Chirawatkul and Dean Whittaker for their friendship and helpful discussions. A big thank you goes to Harry Bone (LAM group technician) for all his help in the lab and I acknowledge the invaluable help from Phil Jones (Chemistry glass blower), Wendy Lambson (Physics technician), Rev. Barry Chapman (Physics XRD technician), Eddie Lambson (Physics workshop), Paul Reddish (Physics workshop), Bob Draper (Physics workshop), Paul Frith (Mechanical Engineering workshop) and Adrian Hooper (Physics IT support).

I thank the staff at the central facilities that I have visited for their invaluable work and advice during the experimental beamtime, often at very late hours. In particular I thank the instrument scientists Dr. Chris Benmore (GLAD, IPNS and 11-ID-C, APS) who performed the 11-ID-C experiments, Dr. Matt Tucker (PEARL, ISIS), Dr. Henry Fischer (D4C, ILL), Dr. Alex Hannon (GEM, ISIS), Prof. Alan Soper (SANDALS, ISIS) and Dr. Veijo Honkimäki (ID15B, ESRF). I also thank the technical support staff Duncan Francis (ISIS), Jean-Luc Laborier (ILL) and Joan Swienie (IPNS) for their help in setting up the experiments. Furthermore, I thank Dr. Stefan Klotz (Paris) for sharing his expertise on the Paris-Edinburgh press and Dr. Malcolm Guthrie (Edinburgh) and Dr. Craig Bull (Edinburgh) for their help with the

PEARL experiments. I also thank Dr. Mei Qiang (APS) for helping with the 11-ID-C experiments.

I acknowledge the helpful discussions and contributions from colleagues at other institutions including Dr. Adrian Barnes (Bristol) who performed the ID11 experiment at the ESRF, Dr. Lawrie Skinner (Bristol), Dr. Martin Wilding (Aberystwyth), Dr. Rudi Winter (Aberystwyth), Prof. Mark Smith (Warwick), Dr. Luke O'Dell (Warwick) who performed the ^{71}Ga MAS NMR experiment, Dr. Donna Carroll (Warwick), Dr. Takeshi Usuki (Yamagata) and Dr. Mark Wilson (Oxford). I thank Dr. Shin'ichi Takeda and Dr. Yukinobu Kawakita from Kyushu university, Japan, for their work during the SANDALS experiment on molten copper halides.

I thank the Engineering and Physical Sciences Research Council (EPSRC) and the department of Physics for financial support and acknowledge use of the EPSRC Chemical Database Service.

Last but by no means least, I thank my family and friends for their love, support and encouragement. I would particularly like to thank my wonderful wife Amy and daughter Zoe for everything but especially for coping with living with me while I wrote this thesis.

This thesis is dedicated to
Harry Drewitt (1916-2006)
Chris Rippin (1982-2007)

Contents

1. Introduction

Knowledge of the atomic structure of liquids and glasses is a necessary prerequisite for understanding the physical and chemical properties of these materials which are of fundamental scientific and technological interest. This extensive field of research and the experimental techniques employed are reviewed in a number of textbooks and articles [1–5].

Many biological and chemical processes rely on the liquid state and such processes ultimately form the basis for the existence of life on earth. Liquids are also widely used in modern technology, for example liquid state electrolytes, coolants and fuel are all required to run a modern car. Glasses are typically formed by quenching a liquid sufficiently rapidly through its glass transition temperature such that the atomic configuration is unable to equilibrate into a regular crystalline lattice [1, 2]. The structure of a glass is therefore characteristic of the atomic arrangement of the supercooled liquid that has frozen into the solid state. Glasses may be formed naturally, for example obsidian is made by volcanic activity and was used by stone age cultures to make tools [6, 7]. It is also reputed that a large proportion of interstellar and planetary ice exists in the glassy state [8–10]. The production of man-made glass is a millennia old industry [11] with widespread modern use from glass windows, bottles, optical lenses and mirrors all the way through to optical fibres and amplifiers vital for optoelectronics and communications technology.

A complete understanding of the principles that give rise to the thermal and physical properties of glassy materials is a challenging problem in the field of condensed matter physics. This was expressed by Philip Anderson in

Science in 1995 who wrote,

> "The deepest and most interesting unsolved problem in solid state theory is probably the theory of the nature of glass and the glass transition."[12]

Recent interest and debate has focussed on the study of polyamorphism, i.e. abrupt and reversible phase transitions in liquids and glasses [13–15]. One of the key issues is whether the nature of the transition is first order or continuous. Recent high profile examples in the polyamorphism debate include the high pressure amorphous phases of water ice [16–19], the pressure transformations in chalcogenide glass [20], the synthesis of a high pressure amorphous phase of carbon dioxide [21], liquid phosphorus at high pressure and temperature [22], and yttria aluminate at high temperature [23]. As well as providing insight into the processes that occur at high pressure and high temperature conditions deep inside planetary interiors the study of polyamorphism may lead to the development of new materials with novel properties.

1.1 Structural probes

The bulk structure of liquids and glasses can be probed using a number of experimental techniques including, but not limited to, diffraction by neutrons and high energy x-rays, nuclear magnetic resonance (NMR) spectroscopy, together with extended x-ray absorption fine structure (EXAFS) and vibrational spectroscopy (e.g. Raman scattering and infra-red absorption) methods.

The work in this thesis reports, predominantly, on the results obtained from neutron and high energy x-ray diffraction experiments. In contrast to crystalline materials, the structure of liquids or amorphous solids cannot be described in terms of a periodically repeating unit cell and hence they are inherently difficult to characterise on the atomic scale due to a lack of long range structural order, although basic chemical bonding constraints can lead to a high degree of ordering on short or intermediate range length scales. Diffraction experiments provide information on the atomic structure of a system in

the form of the total pair distribution function $G(r)$ which provides a measure of the probability of finding two atoms a distance r apart. However, for a system comprising n different atomic species $G(r)$ comprises of a weighted sum of $n(n+1)/2$ overlapping correlations which makes it difficult to unambiguously interpret the experimental data. If diffraction experiments can be performed sufficiently accurately then methods including isotopic substitution in neutron diffraction, anomalous x-ray scattering or isomorphic substitution in both neutron and x-ray diffraction can be employed to extract the partial pair distribution functions of the system. Alternatively, the partial pair distribution functions may be derived by computer simulations, e.g. using the reverse Monte Carlo (RMC) method in which experimental data is used to constrain a three dimensional model of the system. The need for high accuracy and absolute normalisation of the measured intensities makes diffraction measurements on liquids and glasses particularly challenging requiring specialised instrumentation and data analysis techniques that involve a variety of delicate corrections and careful interpretation.

1.2 Thesis outline

The work in this thesis reports on the results of neutron and high energy x-ray diffraction experiments made on a variety of liquid and glassy systems and is organised as follows.

In chapter 2 the essential theory for neutron and x-ray diffraction by liquids and amorphous solids is provided. A general overview of advanced neutron and synchrotron x-ray sources, the diffraction instrumentation employed and the data correction procedures required are then detailed in chapter 3.

In chapter 4 neutron diffraction measurements on molten CuCl, CuI and $(\mathrm{CuCl})_x(\mathrm{CuI})_{1-x}$ $(0 \leq x \leq 1)$ mixtures are reported and the results are discussed by reference to the information that is available on the structure of CuCl and CuI from experiment, theory and computer simulation.

In chapter 5 the results obtained from a combination of neutron diffraction,

high energy x-ray diffraction and ^{71}Ga magic angle spinning (MAS) NMR experiments are reported for $(R_2S_3)_{0.07}(Ga_2S_3)_{0.33}(GeS_2)_{0.60}$ glass, where R denotes the large rare earth elements La, Ce or a 50:50 mixture of the two. The method of isomorphic substitution in neutron diffraction is used in chapter 6 to study the structure of $(R_2Se_3)_{0.07}(Ga_2Se_3)_{0.33}(GeSe_2)_{0.60}$ glass, where $R =$ La or Ce, and in chapter 7 the same glass composition, but with the smaller rare earth elements $R =$ Y and Ho, is studied by using method of isomorphic substitution in x-ray diffraction.

The development of *in situ* high pressure neutron diffraction methods using the Paris-Edinburgh press on the D4C diffractometer at the Institut Laue-Langevin (ILL), France, is the subject of chapter 8. High quality diffraction results for GeO_2, an archetypal network glass former, are reported at pressures up to 8.0(5) GPa. Developments in the experimental method and data analysis strategy for high pressure experiments on the PEARL instrument at the pulsed neutron source (ISIS), UK, are discussed in chapter 9. Sintered diamond anvils were used in the Paris-Edinburgh press to obtain *in situ* neutron diffraction results for GeO_2 glass at pressures up to 14(1) GPa.

Finally, an overall summary of the results and conclusions presented in each chapter of this thesis is provided in chapter 10 together with suggestions for further work.

2. Diffraction by liquids and amorphous solids

This chapter provides an introduction to the essential theory for neutron and x-ray diffraction by liquids and amorphous solids. The formalism employed follows that used in the recent review by Fischer *et al.* [4]. More fundamental descriptions of the scattering processes involved for liquids and glasses can be found in references [24–26] for neutrons and [27–29] for x-rays. A detailed description is given in chapter 3 of the instrumentation used, the diffraction experiments undertaken and the data treatment required to obtain the functions derived in this chapter.

2.1 Differential scattering cross section

Consider the scattering geometry for a diffraction experiment shown in figure 2.1. A collimated beam of incident quanta (neutrons or x-rays) with flux Φ is scattered by a system of scattering centres at the origin of coordinates. All quanta scattered in the direction of $\boldsymbol{R}$ are counted, regardless of their final energy, by a detector of area $\mathrm{d}S$ situated at a distance $|\boldsymbol{R}|$ from the scattering system and subtending a small solid angle $\mathrm{d}\Omega = \mathrm{d}S/R^2$. The differential scattering cross-section is defined by

$$\frac{\mathrm{d}\sigma}{\mathrm{d}\Omega} = \frac{\text{Number of quanta scattered into solid angle } \mathrm{d}\Omega \text{ per second}}{\Phi \mathrm{d}\Omega}. \quad (2.1)$$

For each scattering event, the scattering vector $\boldsymbol{Q}$ is calculated from the

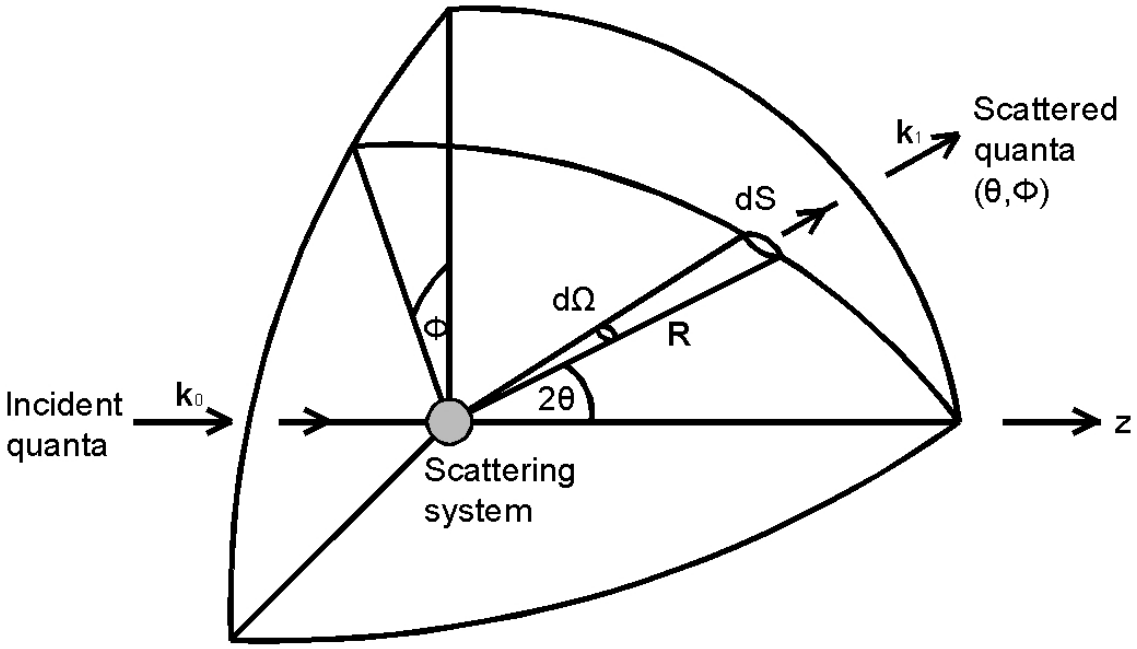

Figure 2.1: The geometry of a diffraction experiment where the position of the scattering system is at the origin of coordinates and the z-axis adopts the direction of the incident wave vector $\boldsymbol{k}_0$.

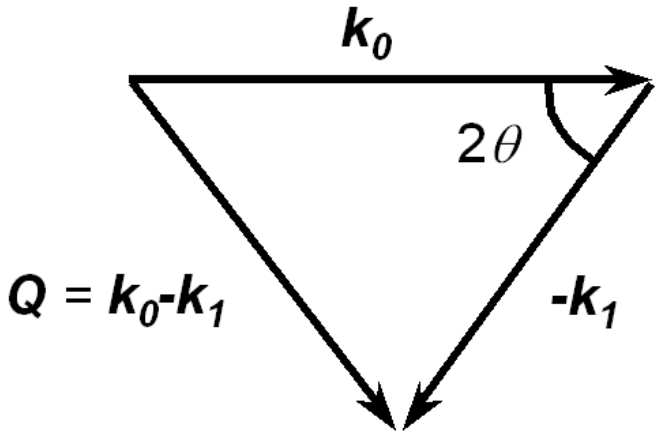

Figure 2.2: The scattering triangle relating the wave vectors $\boldsymbol{k}_0$ and $\boldsymbol{k}_1$ and the scattering vector $\boldsymbol{Q}$ to the scattering angle 2θ.

relation $\boldsymbol{Q} = \boldsymbol{k}_0 - \boldsymbol{k}_1$, where $\boldsymbol{k}_0$ and $\boldsymbol{k}_1$ are the wave vectors of the incident and scattered radiation, respectively. The magnitudes are given by $k_0 = \frac{2\pi}{\lambda_0}$ and $k_1 = \frac{2\pi}{\lambda_1}$ where λ_0 and λ_1 denote the wavelengths of the incident and scattered radiation, respectively. If one assumes that the incident energy of the radiation is much larger than the excitation energies in the sample, then the change in momentum of the quanta following a scattering event is negligible and hence $k_1 \approx k_0$. In this scenario, known as the static approximation, $\frac{\mathrm{d}\sigma}{\mathrm{d}\Omega}$ is dependant upon the elastic scattering vector Q. By applying the cosine rule to the scattering triangle shown in figure 2.2,

$$Q^2 = k_0^2 + k_1^2 - 2k_0k_1\cos(2\theta) \tag{2.2}$$

and since $k_1 \approx k_0$ it follows that the elastic scattering vector is given by

$$Q = \frac{4\pi}{\lambda}\sin(\theta). \tag{2.3}$$

2.2 Neutron diffraction

The neutron interacts with the target nucleus via the strong interaction. The neutron scattering length b, which gives a measure of the scattering power of each nucleus, varies erratically between the elements or even isotopes of the same element, as plotted in figure 2.3. For example, there is a large scattering length contrast between hydrogen and deuterium where $b(^1\mathrm{H}) = -3.7406(11)$ fm and $b(^2\mathrm{H}) = 6.671(4)$ fm [30]. In neutron diffraction, the differential scattering cross section for an isotropic system of N scattering centres is given by

$$\frac{\mathrm{d}\sigma}{\mathrm{d}\Omega}(Q) = \left\langle \sum_{i=1}^{N}\sum_{j=1}^{N} \overline{b_i b_j^*} e^{iQ\cdot\boldsymbol{r}_{ij}} \right\rangle, \tag{2.4}$$

where $\boldsymbol{r}_{ij} = \boldsymbol{r}_i - \boldsymbol{r}_j$ gives the relative position of scattering centres i and j, b_i is the bound neutron scattering length of atom i and b_i^* is its complex conjugate. The brackets $\langle\ \rangle$ denote a thermal average of the atomic positions. The averaging denoted by the horizontal bar takes into account the distribution

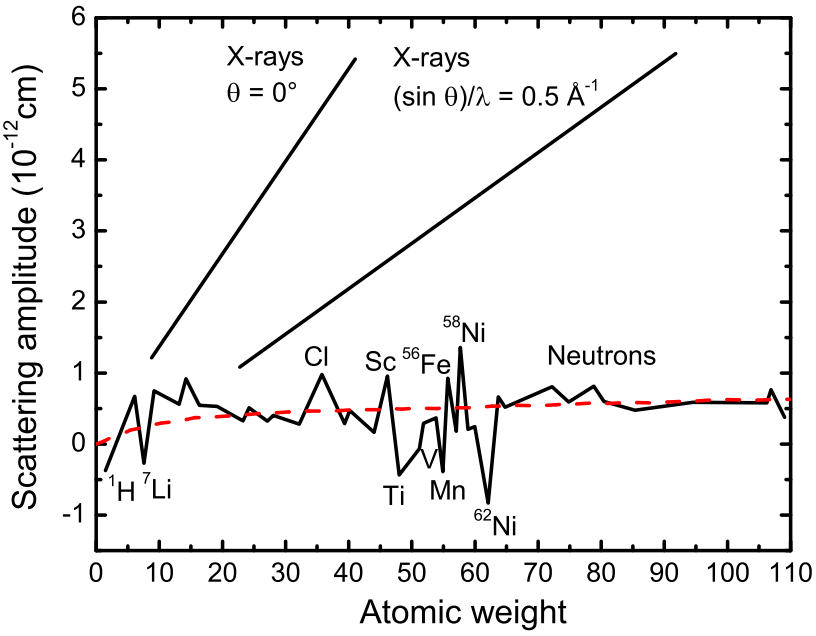

Figure 2.3: The coherent scattering length for x-rays, $r_e f$, (where $r_e = 2.818$ fm is the classical electron radius and f is the x-ray form factor at a fixed scattering angle 2θ) and for neutrons, b, as a function of the atomic weight [25]. Note the dependence of the scattering length on $Q \propto \sin\theta/\lambda$ for x-rays but not for neutrons. The dashed red curve indicates the potential scattering contribution for neutrons.

of b_i values over the scattering centre positions, where the scattering length for a site depends on the particular isotope occupying that site and on the relative orientation of the isotope and neutron spin.

For a system comprising n different atomic species, the differential scattering cross section is given by

$$\frac{1}{N}\left[\frac{\mathrm{d}\sigma}{\mathrm{d}\Omega}(Q)\right] = F(Q) + \sum_{\alpha=1}^{n} c_\alpha (b^2_{\mathrm{coh},\alpha} + b^2_{\mathrm{inc},\alpha})(1 + P_\alpha(Q)). \qquad (2.5)$$

Equation 2.5 is composed of two separate terms. The distinct term, given by the total structure factor $F(Q)$, represents the diffraction pattern obtained

from the interference of waves scattered from different atomic sites and hence contains the useful structural information. The remaining self term describes the isotropic diffraction from individual atomic sites, where c_α denotes the atomic fraction of each chemical species α in the system, $b_{\mathrm{coh},\alpha}$ is the coherent scattering length of chemical species α and $b_{\mathrm{inc},\alpha}$ is the incoherent scattering length of chemical species α and has contributions from both spin and isotope incoherence. In neutron diffraction, the static approximation does not entirely hold, particularly for light atoms. An inelasticity correction is therefore required to account for recoil effects, where the Placzek [31] correction denoted $P_\alpha(Q)$ is commonly employed.

Using the Faber-Ziman formalism [32], the total structure factor $F(Q)$ for a system of n chemical species is composed of a weighted sum of a set of $n(n+1)/2$ partial structure factors $S_{\alpha\beta}(Q)$ which represent the pair correlations between atomic species α and β, as given by

$$F(Q) = \sum_{\alpha=1}^{n}\sum_{\beta=1}^{n} c_\alpha c_\beta b_\alpha b_\beta [S_{\alpha\beta}(Q) - 1]. \tag{2.6}$$

The corresponding real space information is given by the total pair distribution function $G(r)$ which is obtained by the Fourier transform relation

$$\begin{aligned} G(r) &= \frac{1}{2\pi^2 r n_0}\int_0^\infty QF(Q)\sin(Qr)\mathrm{d}Q \\ &= \sum_{\alpha=1}^{n}\sum_{\beta=1}^{n} c_\alpha c_\beta b_\alpha b_\beta [g_{\alpha\beta}(r) - 1] \end{aligned} \tag{2.7}$$

where n_0 is the atomic number density of the system. The partial pair distribution function $g_{\alpha\beta}(r)$ determines the probability of an atom of type β being situated at a distance r from an atom of type α situated at the origin of coordinates and tends to unity at high r values. The $S_{\alpha\beta}(Q)$ and $g_{\alpha\beta}(r)$ partial pair correlation functions are related by the Fourier transform pair

$$S_{\alpha\beta}(Q) - 1 = \frac{4\pi n_0}{Q}\int_0^\infty r[g_{\alpha\beta}(r) - 1]\sin(Qr)\mathrm{d}r, \tag{2.8}$$

$$g_{\alpha\beta}(r) - 1 = \frac{1}{2\pi^2 r n_0} \int_0^\infty Q[S_{\alpha\beta}(Q) - 1]\sin(Qr)\mathrm{d}Q. \tag{2.9}$$

In practice, the finite maximum scattering vector $Q_{\max}$ accessible in a diffraction experiment leads to peak broadening and un-physical 'truncation ripples' in real space after Fourier transformation. This effect can be reduced by applying a damping function prior to Fourier transformation, for example the Lorch [33] modification function or a cosine window function. Oscillations present below the minimum atomic radius in $G(r)$ are un-physical and result, for example, from statistical noise in the reciprocal space data. The un-physical low-r features should oscillate about the calculated theoretical $G(0)$ limit of the system which is given by

$$G(0) = -\sum_{\alpha=1}^{n}\sum_{\beta=1}^{n} c_\alpha c_\beta b_\alpha b_\beta. \tag{2.10}$$

In reciprocal space, the sum-rule relation

$$\int_0^\infty F(Q)Q^2 dQ = 2\pi^2 n_0 G(0), \tag{2.11}$$

derived by Enderby *et al.* [34] should also be satisfied. This relation is obtained from equation 2.7 by considering the limit as $r \to 0$.

The peaks in the real space functions give average distances between pairs of atoms in amorphous materials. They also give the partial coordination number $\bar{n}_\alpha^\beta$, i.e. the average number of β atoms in a spherical coordination shell of radius $r_1 \leq r \leq r_2$ centered on an atom of type α. This is obtained by integrating over the real space peak of interest in a $g_{\alpha\beta}(r)$ partial pair distribution function, where

$$\bar{n}_\alpha^\beta = 4\pi n_0 c_\beta \int_{r_1}^{r_2} g_{\alpha\beta}(r) r^2 dr. \tag{2.12}$$

2.2.1 Magnetic Differential Scattering Cross Section

The neutron has a finite magnetic dipole moment, $\gamma_n = -1.913\ \mu_N$, where the nuclear magneton $\mu_N = 5.051 \cdot 10^{-27}$ J T^{-1}. Hence, neutrons interact with unpaired electrons in magnetic atoms. In magnetic materials, the total neutron scattering cross section therefore contains contributions from both nuclear and magnetic interactions, i.e.

$$\left[\frac{\mathrm{d}\sigma}{\mathrm{d}\Omega}(Q)\right]_{\text{total}} = \left[\frac{\mathrm{d}\sigma}{\mathrm{d}\Omega}(Q)\right]_{\text{nuclear}} + \left[\frac{\mathrm{d}\sigma}{\mathrm{d}\Omega}(Q)\right]_{\text{magnetic}}. \tag{2.13}$$

If in a diffraction experiment only the total nuclear scattering is desired, the magnetic contribution must be corrected for. In the case of paramagnetic ions, the magnetic scattering can be quantified using the free ion approximation [35, 36] such that

$$\left[\frac{\mathrm{d}\sigma}{\mathrm{d}\Omega}(Q)\right]_{\text{magnetic}} = c_{\mathrm{p}}(\gamma_n r_e)^2 \frac{1}{6} J(J+1) g_J^2 \mathscr{F}^2(Q), \tag{2.14}$$

where c_{p} is the atomic fraction of the paramagnetic ion in the sample, J is the total angular momentum quantum number, g_J is the Landé splitting factor [37], r_e is the classical radius of an electron and $(\gamma_n r_e)^2 = 0.2906$ barn. The magnetic form factor $\mathscr{F}(Q)$ is obtained from the expression

$$\begin{aligned}\mathscr{F}^2(Q) \;=\; & \langle j_0(Q)\rangle^2 + C_{02}\langle j_0(Q)\rangle\langle j_2(Q)\rangle + C_{22}\langle j_2(Q)\rangle^2 + C_{24}\langle j_2(Q)\rangle\langle j_4(Q)\rangle \\ & + C_{44}\langle j_4(Q)\rangle^2 + C_{46}\langle j_4(Q)\rangle\langle j_6(Q)\rangle + C_{66}\langle j_6(Q)\rangle^2,\end{aligned}$$

where the radial integrals $\langle j_i(Q)\rangle$ ($i = 0, 2, 4$ and 6) are given by [38] and the coefficients C_{ij} ($i = 0, 2, 4$ or 6 and $j = 2, 4$ or 6) are given by [35]. The magnetic form factor is similar to the atomic form factor in x-ray scattering (see § 2.3). However, since only the unpaired valence electrons of the ion contribute to the magnetic scattering of neutrons, the magnetic form factor decays more rapidly with increasing Q from the $\mathscr{F}(0) = 1$ limit than the atomic form factor.

2.2.2 Isotopic substitution in neutron diffraction

As plotted in figure 2.3, the neutron scattering length b is independent of the atomic number and depends on the particular nucleus and the spin state of the nucleus-neutron interaction [24]. Isotopes of a particular element therefore have different scattering lengths. This enables use of the method of isotopic substitution in neutron diffraction where contrasting diffraction patterns can be taken for different samples that are identical except for the isotopic composition of one or more of the elements [34]. This changes the weighting factors for the partial structure factors $S_{\alpha\beta}(Q)$ in equation 2.6 and allows for their separation by combining different diffraction patterns. Since a sample of n chemical species has $m = n(n+1)/2$ independent partial structure factors, the diffraction patterns of m samples of differing isotopic composition are required for a complete determination of the $S_{\alpha\beta}(Q)$ functions using difference function methods.

2.2.3 Isomorphic substitution in neutron diffraction

A scattering length contrast between samples of identical composition can also be obtained by using the method of isomorphic substitution in neutron diffraction where chemical isomorphs are substituted in place of different isotopes of the same chemical species. The substituted species must be carefully selected such that their chemical nature and atomic radii are as identical as possible. As described in chapter 5, adjacent rare earth ions such as La^{3+} and Ce^{3+} are ideal isomorphs and glass compositions containing substituted rare earth ions can be considered to be structurally identical. Specific correlations involving the rare earth ions and/or matrix species can therefore be extracted by using appropriate difference function methods as detailed in § 2.4.

2.3 X-ray diffraction

The formalism for x-ray diffraction is essentially the same as in the neutron diffraction case. However, x-rays scatter from spatially extended electron density distributions (i.e. orbitals and bonds) and the scattering length is therefore dependent on the scattering vector Q. The scattering length, or form factor, also has a strong dependance on the energy E_0 of the incident x-ray photons. The scattering length b in x-ray diffraction is therefore given by

$$b(Q, E_0) = r_e f(Q, E_0) = r_e \left[Z f_{\text{falloff}}(Q) + f'(E_0) + \mathrm{i} f''(E_0) \right], \tag{2.15}$$

where $r_e = 2.818$ fm is the classical radius of an electron, $f(Q, E_0)$ is the atomic form factor, Z is the atomic number, $f_{\text{falloff}}(Q)$ is the atomic form factor's modulation varying from 1 (at $Q = 0$) to 0 (at $Q = \infty$) and $f'(E_0)$ and $f''(E_0)$ denote the real and imaginary parts of the anomalous term, respectively. The anomalous terms vary in the vicinity of an absorption edge. This variance is exploited in anomalous x-ray diffraction by changing the incident x-ray energy close to an absorption edge to alter the weighting factors of the partial pair correlation functions in the diffraction patterns taken for a single sample.

The incident x-ray energies used for diffraction are sufficiently high (on the order of keV) that the static approximation is valid for x-ray diffraction. The Placzek [31] inelasticity correction applied in the case of neutron diffraction is therefore not required. However, additional inelastic scattering and re-emission processes, including Compton scattering, fluorescence and resonant-Raman scattering, do contribute to the total scattering and must be sufficiently corrected for to obtain the Rayleigh-Thomson (Ray-T) differential scattering cross-section pertinent to diffraction. At energies far enough from an absorption edge these processes, with the exception of Compton scattering, are negligible. The anomalous terms of the form factor, and hence their energy dependance, are also negligible at energies far from an absorption edge. The x-ray differential scattering cross section for a sample of N atoms and n chemical species α at an incident x-ray energy far from an absorption edge is

therefore defined by

$$\begin{aligned}\frac{1}{N}\left[\frac{\mathrm{d}\sigma}{\mathrm{d}\Omega}(Q)\right]^{X}_{\mathrm{Ray-T}} &= \left[\frac{\mathrm{d}\sigma}{\mathrm{d}\Omega}(Q)\right]^{X}_{\mathrm{Total}} - \left[\frac{\mathrm{d}\sigma}{\mathrm{d}\Omega}(Q)\right]^{X}_{\mathrm{Compton}}, \\ &= F_X(Q) + \sum_{\alpha=1}^{n} c_\alpha f_\alpha(Q)^2, \end{aligned} \tag{2.16}$$

where c_α is the atomic fraction and $f_\alpha(Q)$ is the atomic form factor for chemical species α, respectively. As for equation 2.5 the distinct term is given by the total x-ray structure factor $F_X(Q)$, where

$$F_X(Q) = \sum_{\alpha=1}^{n}\sum_{\beta=1}^{n} c_\alpha c_\beta f_\alpha(Q) f_\beta(Q)[S_{\alpha\beta}(Q) - 1]. \tag{2.17}$$

The remaining self term describes the isotropic diffraction from individual sites. The total scattering intensity is conventionally denoted by the normalised total x-ray structure factor $S_X(Q)$ which oscillates about unity at high-Q and is given by

$$S_X(Q) = \frac{F_X(Q)}{\left(\sum_{\alpha=1}^{n} c_\alpha f_\alpha(Q)\right)^2} + 1. \tag{2.18}$$

2.3.1 Isomorphic substitution in x-ray diffraction

As x-rays scatter from electron distributions their scattering power increases with atomic number Z. X-rays are therefore not very sensitive to light atoms and there is negligible contrast between adjacent elements. The Z-dependence can, however, be exploited to obtain a large contrast in the atomic form factor and hence change the weighting of the partial structure factors, in the diffraction patterns measured for samples of identical composition but containing different isomorphic elements. As described in chapter 7, the rare earth elements Y($Z = 39$) and Ho($Z = 67$) are ideal isomorphs which form glasses that are structurally identical. However, due to the large difference in their atomic number, the rare earth sites exhibit a large contrast in x-ray scattering power.

The same difference function methods can be applied as in neutron diffraction (see § 2.4) but the Q-dependance of the form factors must be considered when Fourier transforming into real space. The anomalous terms of the form factor must also be considered at energies close to an absorption edge. The isomorphic substitution method therefore has an advantage over the anomalous x-ray diffraction (AXD) method as the form factor contrast is typically much higher than in AXD and the incident x-ray energy is not limited to a specific energy around an absorption edge and hence high energy x-rays can be used to reduce attenuation effects and to give a large maximum scattering vector $Q_{\max}$ for good resolution in real space.

2.4 Difference function methods for multi-component glasses

As given in equation 2.6, the total structure factor $F(Q)$ for a system of n chemical species is composed of a weighted sum of a set of $m = n(n+1)/2$ partial structure factors $S_{\alpha\beta}(Q)$ such that

$$F(Q) = \sum_{\alpha=1}^{n} \sum_{\beta=1}^{n} c_\alpha c_\beta b_\alpha b_\beta [S_{\alpha\beta}(Q) - 1], \tag{2.19}$$

where c_α and b_α denote the atomic fraction and scattering length of chemical species α, respectively. The complete set of $S_{\alpha\beta}(Q)$ can therefore be obtained by measuring the diffraction patterns for m samples of differing isotopic or isomorphic composition. For a binary system only three samples are required to extract the full set of partial structure factors using difference function methods. However, many glassy materials of technological and scientific interest are complex systems involving many atomic species and it becomes unfeasible to be able to extract the full set of $S_{\alpha\beta}(Q)$. Nevertheless, if diffraction patterns are taken for a number of samples of differing isotopic or isomorphic composition, then difference function methods can be used to identify specific correlations

of interest. The following difference function methods are more pertinent to multi-component systems measured using neutron diffraction. However, they may also be applied to x-ray diffraction, although complications arise from the Q-dependence of the x-ray form factors, as dealt with in chapter 7.

2.4.1 First order difference functions

Consider that the $F(Q)$ functions have been measured for three separate samples of a four component rare earth glass system that are identical in every respect except for the neutron scattering length of the rare earth species. Let the matrix species be denoted by α, β and γ (e.g. Ge, Ga and S) and let R, R' or R'' represent rare earth isotopes or isomorphs with neutron scattering lengths $b_R > b_{R'} > b_{R''}$. The corresponding total structure factors, denoted by ${}^{R}F(Q)$, ${}^{R'}F(Q)$, and ${}^{R''}F(Q)$, are given by

$$\begin{aligned} {}^{R}F(Q) &= c_\alpha^2 b_\alpha^2 \left[S_{\alpha\alpha}(Q) - 1\right] + c_\beta^2 b_\beta^2 \left[S_{\beta\beta}(Q) - 1\right] \\ &+ c_\gamma^2 b_\gamma^2 \left[S_{\gamma\gamma}(Q) - 1\right] + c_R^2 b_R^2 \left[S_{RR}(Q) - 1\right] \\ &+ 2c_\alpha c_\beta b_\alpha b_\beta \left[S_{\alpha\beta}(Q) - 1\right] + 2c_\alpha c_\gamma b_\alpha b_\gamma \left[S_{\alpha\gamma}(Q) - 1\right] \\ &+ 2c_\alpha c_R b_\alpha b_R \left[S_{R\alpha}(Q) - 1\right] + 2c_\beta c_\gamma b_\beta b_\gamma \left[S_{\beta\gamma}(Q) - 1\right] \\ &+ 2c_\beta c_R b_\beta b_R \left[S_{R\beta}(Q) - 1\right] + 2c_\gamma c_R b_\gamma b_R \left[S_{R\gamma}(Q) - 1\right], \end{aligned} \tag{2.20}$$

$$\begin{aligned} {}^{R'}F(Q) &= c_\alpha^2 b_\alpha^2 \left[S_{\alpha\alpha}(Q) - 1\right] + c_\beta^2 b_\beta^2 \left[S_{\beta\beta}(Q) - 1\right] \\ &+ c_\gamma^2 b_\gamma^2 \left[S_{\gamma\gamma}(Q) - 1\right] + c_R^2 b_{R'}^2 \left[S_{RR}(Q) - 1\right] \\ &+ 2c_\alpha c_\beta b_\alpha b_\beta \left[S_{\alpha\beta}(Q) - 1\right] + 2c_\alpha c_\gamma b_\alpha b_\gamma \left[S_{\alpha\gamma}(Q) - 1\right] \\ &+ 2c_\alpha c_R b_\alpha b_{R'} \left[S_{R\alpha}(Q) - 1\right] + 2c_\beta c_\gamma b_\beta b_\gamma \left[S_{\beta\gamma}(Q) - 1\right] \\ &+ 2c_\beta c_R b_\beta b_{R'} \left[S_{R\beta}(Q) - 1\right] + 2c_\gamma c_R b_\gamma b_{R'} \left[S_{R\gamma}(Q) - 1\right], \end{aligned} \tag{2.21}$$

$$
\begin{aligned}
{}^{R''}F(Q) &= c_\alpha^2 b_\alpha^2 \left[S_{\alpha\alpha}(Q)-1\right] + c_\beta^2 b_\beta^2 \left[S_{\beta\beta}(Q)-1\right] \\
&+ c_\gamma^2 b_\gamma^2 \left[S_{\gamma\gamma}(Q)-1\right] + c_R^2 b_{R''}^2 \left[S_{RR}(Q)-1\right] \\
&+ 2c_\alpha c_\beta b_\alpha b_\beta \left[S_{\alpha\beta}(Q)-1\right] + 2c_\alpha c_\gamma b_\alpha b_\gamma \left[S_{\alpha\gamma}(Q)-1\right] \\
&+ 2c_\alpha c_R b_\alpha b_{R''} \left[S_{R\alpha}(Q)-1\right] + 2c_\beta c_\gamma b_\beta b_\gamma \left[S_{\beta\gamma}(Q)-1\right] \\
&+ 2c_\beta c_R b_\beta b_{R''} \left[S_{R\beta}(Q)-1\right] + 2c_\gamma c_R b_\gamma b_{R''} \left[S_{R\gamma}(Q)-1\right].
\end{aligned} \tag{2.22}
$$

The matrix correlations are equally weighted in all samples. However, the correlations involving the rare earth species are weighted differently in each sample. Hence, the correlations involving only matrix species can be eliminated by subtracting two total structure factors leaving only those correlations involving rare earth ions. The first order difference functions thus obtained, denoted by $\Delta F_R^{(i)}(Q)$ $(i = 1, 2, 3)$, are given by

$$
\begin{aligned}
\Delta F_R^{(1)}(Q) &= {}^{R}F(Q) - {}^{R''}F(Q) \\
&= c_R^2 \left(b_R^2 - b_{R''}^2\right) \left[S_{RR}(Q)-1\right] + 2c_\alpha c_R b_\alpha \left(b_R - b_{R''}\right) \left[S_{R\alpha}(Q)-1\right] \\
&+ 2c_\beta c_R b_\beta \left(b_R - b_{R''}\right) \left[S_{R\beta}(Q)-1\right] + 2c_\gamma c_R b_\gamma \left(b_R - b_{R''}\right) \left[S_{R\gamma}(Q)-1\right],
\end{aligned} \tag{2.23}
$$

$$
\begin{aligned}
\Delta F_R^{(2)}(Q) &= {}^{R}F(Q) - {}^{R'}F(Q) \\
&= c_R^2 \left(b_R^2 - b_{R'}^2\right) \left[S_{RR}(Q)-1\right] + 2c_\alpha c_R b_\alpha \left(b_R - b_{R'}\right) \left[S_{R\alpha}(Q)-1\right] \\
&+ 2c_\beta c_R b_\beta \left(b_R - b_{R'}\right) \left[S_{R\beta}(Q)-1\right] + 2c_\gamma c_R b_\gamma \left(b_R - b_{R'}\right) \left[S_{R\gamma}(Q)-1\right],
\end{aligned} \tag{2.24}
$$

$$
\begin{aligned}
\Delta F_R^{(3)}(Q) &= {}^{R'}F(Q) - {}^{R''}F(Q) \\
&= c_R^2 \left(b_{R'}^2 - b_{R''}^2\right) \left[S_{RR}(Q)-1\right] + 2c_\alpha c_R b_\alpha \left(b_{R'} - b_{R''}\right) \left[S_{R\alpha}(Q)-1\right] \\
&+ 2c_\beta c_R b_\beta \left(b_{R'} - b_{R''}\right) \left[S_{R\beta}(Q)-1\right] + 2c_\gamma c_R b_\gamma \left(b_{R'} - b_{R''}\right) \left[S_{R\gamma}(Q)-1\right].
\end{aligned} \tag{2.25}
$$

2.4.2 Total minus weighted difference function

Since the components in the $F(Q)$ functions involving only matrix species are identical, they can be grouped into the matrix-matrix difference functions

given by

$$\begin{aligned}\Delta^{(1)}_{\mu\mu}(Q) &\equiv \Delta^{(2)}_{\mu\mu}(Q) \equiv \Delta^{(3)}_{\mu\mu}(Q) \\ &= c^2_\alpha b^2_\alpha \left[S_{\alpha\alpha}(Q) - 1\right] + c^2_\beta b^2_\beta \left[S_{\beta\beta}(Q) - 1\right] \\ &+ c^2_\gamma b^2_\gamma \left[S_{\gamma\gamma}(Q) - 1\right] + 2c_\alpha c_\beta b_\alpha b_\beta \left[S_{\alpha\beta}(Q) - 1\right] \\ &+ +2c_\alpha c_\gamma b_\alpha b_\gamma \left[S_{\alpha\gamma}(Q) - 1\right] + 2c_\beta c_\gamma b_\beta b_\gamma \left[S_{\beta\gamma}(Q) - 1\right].\end{aligned} \tag{2.26}$$

The components in the first order difference functions involving only those correlations between the rare earth species and matrix atoms can also be grouped into the rare earth-matrix difference functions given by

$$\begin{aligned}\Delta^{(1)}_{R\mu}(Q) &= 2c_\alpha c_R b_\alpha \left(b_R - b_{R''}\right) \left[S_{R\alpha}(Q) - 1\right] \\ &+ 2c_\beta c_R b_\beta \left(b_R - b_{R''}\right) \left[S_{R\beta}(Q) - 1\right] \\ &+ 2c_\gamma c_R b_\gamma \left(b_R - b_{R''}\right) \left[S_{R\gamma}(Q) - 1\right],\end{aligned} \tag{2.27}$$

$$\begin{aligned}\Delta^{(2)}_{R\mu}(Q) &= 2c_\alpha c_R b_\alpha \left(b_R - b_{R'}\right) \left[S_{R\alpha}(Q) - 1\right] \\ &+ 2c_\beta c_R b_\beta \left(b_R - b_{R'}\right) \left[S_{R\beta}(Q) - 1\right] \\ &+ 2c_\gamma c_R b_\gamma \left(b_R - b_{R'}\right) \left[S_{R\gamma}(Q) - 1\right],\end{aligned} \tag{2.28}$$

$$\begin{aligned}\Delta^{(3)}_{R\mu}(Q) &= 2c_\alpha c_R b_\alpha \left(b_{R'} - b_{R''}\right) \left[S_{R\alpha}(Q) - 1\right] \\ &+ 2c_\beta c_R b_\beta \left(b_{R'} - b_{R''}\right) \left[S_{R\beta}(Q) - 1\right] \\ &+ 2c_\gamma c_R b_\gamma \left(b_{R'} - b_{R''}\right) \left[S_{R\gamma}(Q) - 1\right].\end{aligned} \tag{2.29}$$

The first order difference functions given in equations 2.23 to 2.25 may therefore be re-written in terms of the rare earth-matrix difference functions such that

$$\Delta F^{(1)}_R(Q) = \Delta^{(1)}_{R\mu}(Q) + c^2_R \left(b^2_R - b^2_{R''}\right) \left[S_{RR}(Q) - 1\right], \tag{2.30}$$

$$\Delta F_R^{(2)}(Q) = \Delta_{R\mu}^{(2)}(Q) + c_R^2 \left(b_R^2 - b_{R'}^2\right) \left[S_{RR}(Q) - 1\right], \tag{2.31}$$

$$\Delta F_R^{(3)}(Q) = \Delta_{R\mu}^{(3)}(Q) + c_R^2 \left(b_{R'}^2 - b_{R''}^2\right) \left[S_{RR}(Q) - 1\right]. \tag{2.32}$$

The total structure factors given in equations 2.20 to 2.22 may then be written in terms of the matrix-matrix and rare earth-matrix difference functions such that

$${}^{R}F(Q) = \Delta_{\mu\mu}^{(1)}(Q) + \frac{b_R}{b_R - b_{R''}} \Delta_{R\mu}^{(1)}(Q) + c_R^2 b_R^2 \left[S_{RR}(Q) - 1\right], \tag{2.33}$$

$${}^{R'}F(Q) = \Delta_{\mu\mu}^{(2)}(Q) + \frac{b_R}{b_R - b_{R'}} \Delta_{R\mu}^{(2)}(Q) + c_R^2 b_{R'}^2 \left[S_{RR}(Q) - 1\right], \tag{2.34}$$

$${}^{R''}F(Q) = \Delta_{\mu\mu}^{(3)}(Q) + \frac{b_{R'}}{b_{R'} - b_{R''}} \Delta_{R\mu}^{(3)}(Q) + c_R^2 b_{R''}^2 \left[S_{RR}(Q) - 1\right]. \tag{2.35}$$

The rare earth-matrix correlations are therefore eliminated by subtracting a weighted first order difference function from a total structure factor to leave only the matrix-matrix and rare earth-rare earth correlations. The so called "total minus weighted difference functions" are thus determined by

$$\begin{aligned} \Delta F^{(1)}(Q) &= {}^{R}F(Q) - \frac{b_R}{b_R - b_{R''}} \Delta F_R^{(1)}(Q) \\ &= \Delta_{\mu\mu}^{(1)}(Q) - c_R^2 b_R b_{R''} \left[S_{RR}(Q) - 1\right], \end{aligned} \tag{2.36}$$

$$\begin{aligned} \Delta F^{(2)}(Q) &= {}^{R}F(Q) - \frac{b_R}{b_R - b_{R'}} \Delta F_R^{(2)}(Q) \\ &= \Delta_{\mu\mu}^{(2)}(Q) - c_R^2 b_R b_{R'} \left[S_{RR}(Q) - 1\right], \end{aligned} \tag{2.37}$$

$$\begin{aligned}\Delta F^{(3)}(Q) &= {}^{R'}F(Q) - \frac{b_{R'}}{b_{R'} - b_{R''}}\Delta F_R^{(3)}(Q) \\ &= \Delta_{\mu\mu}^{(3)}(Q) - c_R^2 b_{R'} b_{R''}\left[S_{RR}(Q) - 1\right].\end{aligned} \tag{2.38}$$

The total minus weighted difference functions may also be expressed in terms of the total structure factors only, as given by

$$\Delta F^{(1)}(Q) = \frac{b_R\ {}^{R''}F(Q) - b_{R''}\ {}^{R}F(Q)}{b_R - b_{R''}}, \tag{2.39}$$

$$\Delta F^{(2)}(Q) = \frac{b_R\ {}^{R'}F(Q) - b_{R'}\ {}^{R}F(Q)}{b_R - b_{R'}}, \tag{2.40}$$

$$\Delta F^{(3)}(Q) = \frac{b_{R'}\ {}^{R''}F(Q) - b_{R''}\ {}^{R'}F(Q)}{b_{R'} - b_{R''}}. \tag{2.41}$$

The total minus weighted difference functions are particularly useful if only two structure factors are measured.

2.4.3 Second order difference functions

If three total structure factors are measured, the method of differences may be extended to obtain the second order or double difference function which represents the rare earth-rare earth partial structure factor $S_{RR}(Q)$. Using the first order difference functions we find

$$S_{RR}(Q) = \frac{(b_R - b_{R'})\Delta F_R^{(1)}(Q) - (b_R - b_{R''})\Delta F_R^{(2)}(Q)}{c_R^2[(b_R^2 - b_{R''}^2)(b_R - b_{R'}) - (b_R^2 - b_{R'}^2)(b_R - b_{R''})]} - 1. \tag{2.42}$$

Expressing in terms of the total structure factors ${}^{R}F(Q)$, ${}^{R'}F(Q)$ and ${}^{R''}F(Q)$

$$S_{RR}(Q) = \frac{\left[(1-\gamma)^R F(Q)\right] -^{R'} F(Q) + \gamma^{R''}F(Q)}{c_R^2\gamma(1-\gamma)a^2} - 1, \tag{2.43}$$

where the weighting factors $\gamma = \frac{b_R - b_{R'}}{b_R - b_{R''}}$ and $a = b_R - b_{R''}$.

With the extraction of $S_{RR}(Q)$ from the $F(Q)$ functions, it is possible to determine the matrix-matrix difference functions from equations 2.36 to 2.38 by using

$$\Delta^{(1)}_{\mu\mu}(Q) = \Delta F^{(1)}(Q) + c_R^2 b_R b_{R''} \left[S_{RR}(Q) - 1\right], \tag{2.44}$$

$$\Delta^{(2)}_{\mu\mu}(Q) = \Delta F^{(2)}(Q) + c_R^2 b_R b_{R'} \left[S_{RR}(Q) - 1\right], \tag{2.45}$$

$$\Delta^{(3)}_{\mu\mu}(Q) = \Delta F^{(3)}(Q) + c_R^2 b_{R'} b_{R''} \left[S_{RR}(Q) - 1\right]. \tag{2.46}$$

Similarly, the rare earth-matrix difference functions can be determined from equations 2.30 to 2.32 by using

$$\Delta^{(1)}_{R\mu}(Q) = \Delta F^{(1)}_R(Q) - c_R^2 \left(b_R^2 - b_{R''}^2\right) \left[S_{RR}(Q) - 1\right] \tag{2.47}$$

$$\Delta^{(2)}_{R\mu}(Q) = \Delta F^{(2)}_R(Q) - c_R^2 \left(b_R^2 - b_{R'}^2\right) \left[S_{RR}(Q) - 1\right] \tag{2.48}$$

$$\Delta^{(3)}_{R\mu}(Q) = \Delta F^{(3)}_R(Q) - c_R^2 \left(b_{R'}^2 - b_{R''}^2\right) \left[S_{RR}(Q) - 1\right]. \tag{2.49}$$

3. Diffraction instrumentation and data treatment

Neutrons and x-rays are valuable tools for the investigation of condensed matter. Neutrons and high energy x-rays have wavelengths comparable to atomic spacings, enabling the use of diffraction methods, discussed in chapter 2, to obtain information on atomic structure. As a neutral subatomic particle, the neutron has a large penetration depth and typically interacts only with atomic nuclei. However, due to its non-zero magnetic moment, the neutron does scatter from unpaired electrons in magnetic ions via a dipole-dipole interaction. High frequency photons, or x-rays, interact with the electronic distributions of atoms. High energy x-rays are required to overcome the relatively short penetration depth of x-rays in matter. Complementary information can be obtained by combining the two diffraction methods as the scattering sensitivity of neutrons is different to that of x-rays.

3.1 Neutron sources

Thermal neutrons, with wavelengths of the order of atomic spacings, are typically used in diffraction experiments. The wavelength λ_n of a neutron is given by the de Broglie equation

$$\lambda_n = \frac{h}{m_n v_n}, \tag{3.1}$$

where $m_n = 1.675 \cdot 10^{-27}$ kg is the neutron mass, $h = 6.626 \cdot 10^{-34}$ J s is the Planck constant and v_n is the neutron velocity (for thermal neutrons the

standard velocity $v_n = 2.20$ km s^{-1}). The energy E_n of a neutron is given by its kinetic energy

$$E_n = \frac{1}{2} m_n v_n^2 \tag{3.2}$$

which, expressed in terms of the neutron wavelength, is given by

$$E_n = \frac{h^2}{2 m_n \lambda_n^2}. \tag{3.3}$$

If the neutron energy is in units of meV and the wavelength is in units of Å then

$$E_n \,(\text{meV}) = \frac{81.81}{\left[\lambda_n \,(\text{Å})\right]^2}. \tag{3.4}$$

The high energy neutrons produced by most neutron sources are slowed to thermal energies by using a suitable moderator material. The neutrons lose energy by scattering with the nuclei in the moderator and emerge with a Maxwell Boltzmann distribution of velocities, where the peak velocity is dependent on the temperature of the moderator.

3.1.1 Fission neutron sources

Research nuclear reactors, for example the Institut Laue-Langevin (ILL) in Grenoble, France, produce neutrons n and energy E as a bi-product of the nuclear fission of ^{235}U, where a typical reaction is given by

$$n + {}^{235}\text{U} \rightarrow {}^{141}\text{Ba} + {}^{92}\text{K} + 3n + E. \tag{3.5}$$

The neutrons are transported from the source to the various instruments via a moderator using neutron guides, often by total internal reflection along nickel plated tubes, and collimated using neutron absorbers.

A typical layout for a diffraction experiment at a reactor source is shown in figure 3.1. The moderator produces a steady flux of incident neutrons covering a wide range of wavelengths. It is therefore necessary to use a single crystal monochromator to produce a neutron beam with a single neutron

wavelength λ_n. As derived in chapter 2, the scattering vector $\boldsymbol{Q}$ for neutrons scattered by a sample is given by $\boldsymbol{Q} = \boldsymbol{k}_0 - \boldsymbol{k}_1$ where, for elastic scattering, $|\boldsymbol{k}_0| = |\boldsymbol{k}_1| = 2\pi/\lambda_n$ such that

$$Q = \frac{4\pi}{\lambda_n}\sin(\theta). \tag{3.6}$$

Thus, a neutron diffractometer at a steady state neutron source measures the differential scattering cross section of a sample as a function of Q by scanning the detectors through various scattering angles 2θ.

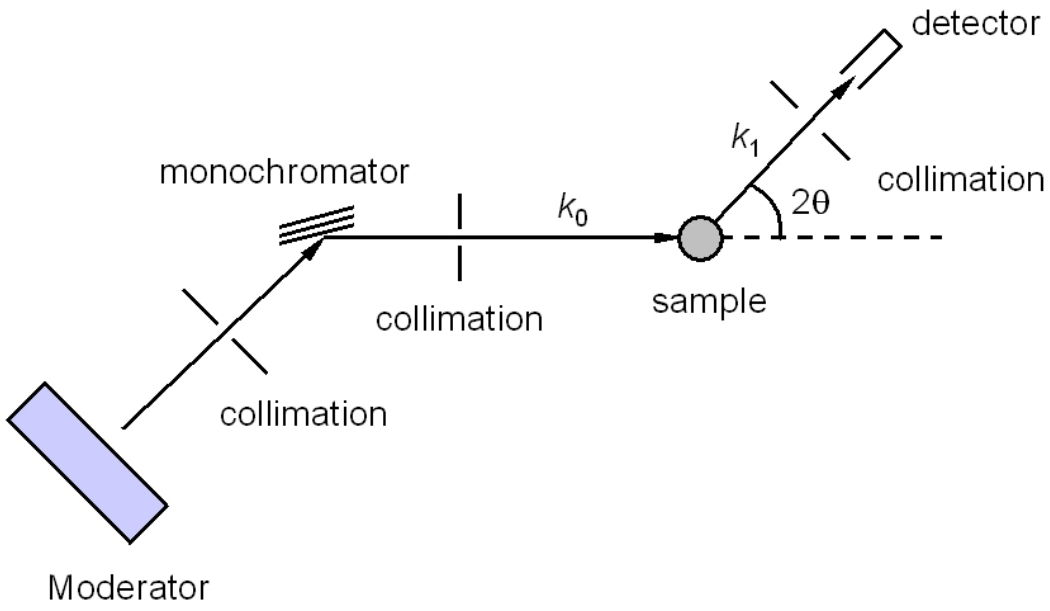

Figure 3.1: Schematic of a typical diffraction experiment at a reactor neutron source with neutrons of incident wave vector k_0 and scattered wave vector k_1.

3.1.2 Spallation neutron sources

High intensity neutrons may also be produced by the spallation process, for example at the ISIS pulsed neutron facility, Didcot UK. At ISIS an ion source produces H^- ions which are accelerated to high energy using a linear accelerator and injected into a synchrotron. The H^- beam is stripped of its electrons by

a 0.3 μm thick aluminium oxide stripping foil. The resulting protons are accumulated in the synchrotron and accelerated, making $\approx 10,000$ orbits of the synchrotron, before being kicked into the proton beamline, firing 4 μC of protons in 100 ns long pulses at a tungsten target with a repetition rate of 50 Hz. The resulting spallation interaction between the proton and target nucleus produces neutrons. Muons are also produced at ISIS employing a secondary carbon target. The muon target uses $2-3$ % of the proton beam which has a mean current of 200 μA.

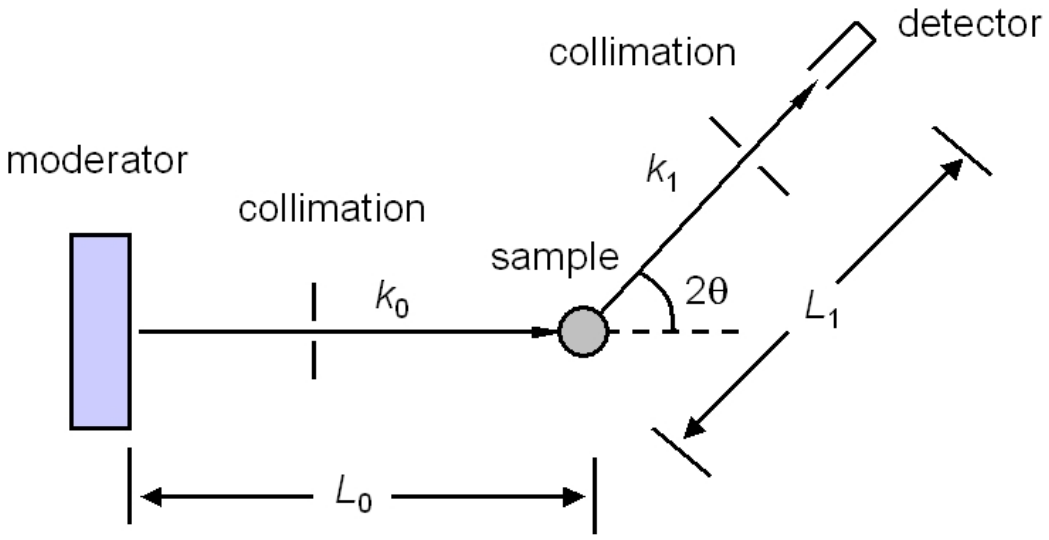

Figure 3.2: Schematic of a typical diffraction experiment at a spallation neutron source with neutrons of incident wave vector k_0 and scattered wave vector k_1, where the neutron wavelength is calculated from the time of flight over the distances L_0 and L_1.

The neutrons are moderated to thermal wavelengths and transported via neutron guides to the instrument beamlines. The time of flight technique, illustrated in figure 3.2, is used to determine the wavelength of the scattered neutrons for each pulse. If the time of flight t from the moderator to the detector is known, then the wavelength is calculated by using the relation

$$\lambda_n = \frac{ht}{m_n\left(L_0 + L_1\right)}, \tag{3.7}$$

where m_n is the neutron mass, L_0 is the incident path length and L_1 is the scattered path length. Thus, a neutron diffractometer at a spallation neutron source measures the differential scattering cross section of a sample as a function of Q by keeping the detectors at fixed scattering angles 2θ and varying the incident neutron wavelength λ_n.

3.2 Neutron diffraction instrumentation

3.2.1 D4C

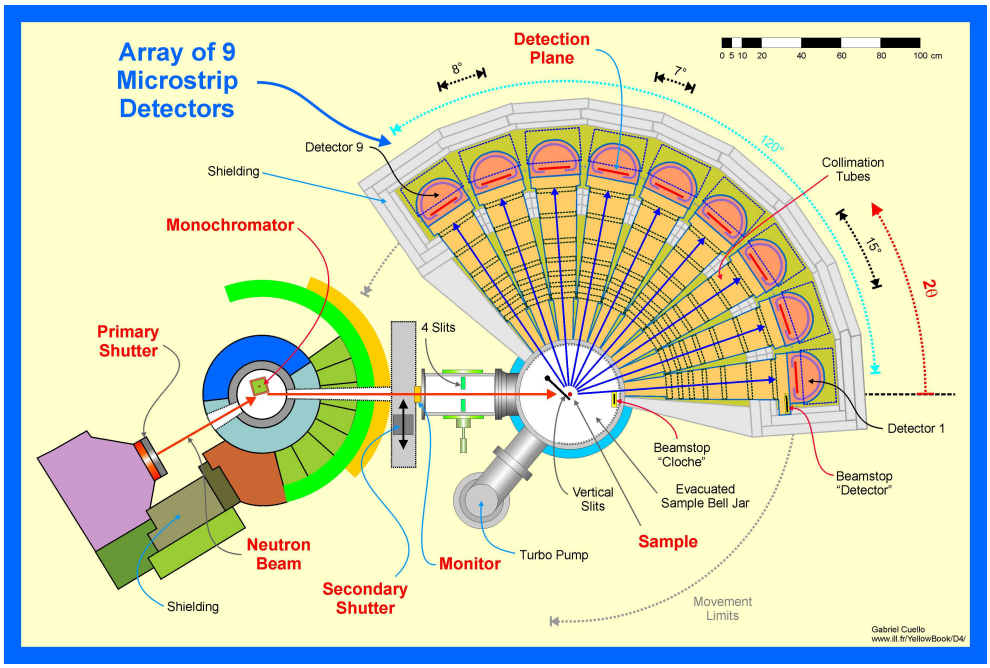

Figure 3.3: The D4C diffractometer layout [39].

The D4C instrument at the ILL (see figure 3.3) is a high precision diffractometer optimised for structural investigations of disordered materials [39]. The beamline employs high flux neutrons moderated to short wavelengths using a graphite moderator at 2400 K [40]. Incident neutrons can be monochromated to a wavelength of 0.35 Å, 0.5 Å or 0.7 Å using the (331), (220) or

(200) lateral faces of Cu monocrystals. The incident neutron flux is monitored by a low efficiency counter and the beam is collimated by a 4-slit diaphragm arrangement producing a trapezoidal neutron beam incident at the sample position which is situated within an evacuated belljar. The diffractometer consists of 9 microstrip ^{3}He gas detectors in the configuration shown in figure 3.3 providing a very high counting rate stability. The diffractometer accesses a scattering angle $1.5\ ^\circ \leq 2\theta \leq 137\ ^\circ$ and the entire detector ensemble rotates to cover the $7\ ^\circ$ gaps between detectors. The accessible Q-range for the three wavelengths are thus $0.5 \leq Q\ (\text{Å}^{-1}) \leq 33$ at 0.35 Å, $0.3 \leq Q\ (\text{Å}^{-1}) \leq 23$ at 0.5 Å and $0.2 \leq Q\ (\text{Å}^{-1}) \leq 17$ at 0.7 Å. The D4C instrument accommodates both low and high temperature sample environments and the first high pressure experiments made by installing a Paris-Edinburgh press on D4C are the subject of chapter 8.

3.2.2 SANDALS

The Small Angle Neutron Diffractometer for Amorphous and Liquid Samples (SANDALS) at the ISIS facility, illustrated in figure 3.4, enables measurement of the structure factors for disordered materials over a wide scattering vector range of $0.1 \leq Q\ (\text{Å}^{-1}) \leq 50$ [41]. The instrument was designed to minimise inelasticity corrections through small angle detection of high energy neutrons [4]. Neutrons are moderated by a liquid methane moderator at 110 K and have an incident flight path $L_0 = 11$ m. A boron carbide collimator defines a circular beam of neutrons of maximum diameter 32 mm at the sample position. At the time the SANDALS experiments described in chapter 4 were performed there were 1180 ^{6}Li ZnS detectors installed, arranged in 18 detector groups, as listed in table 3.1, providing continuous angular coverage from $3.8\ ^\circ$ to $39\ ^\circ$ with a final flight path range of $0.75 \leq L_1\ (\text{m}) \leq 4.0$. In 2005 the instrument was upgraded to improve detector stability.

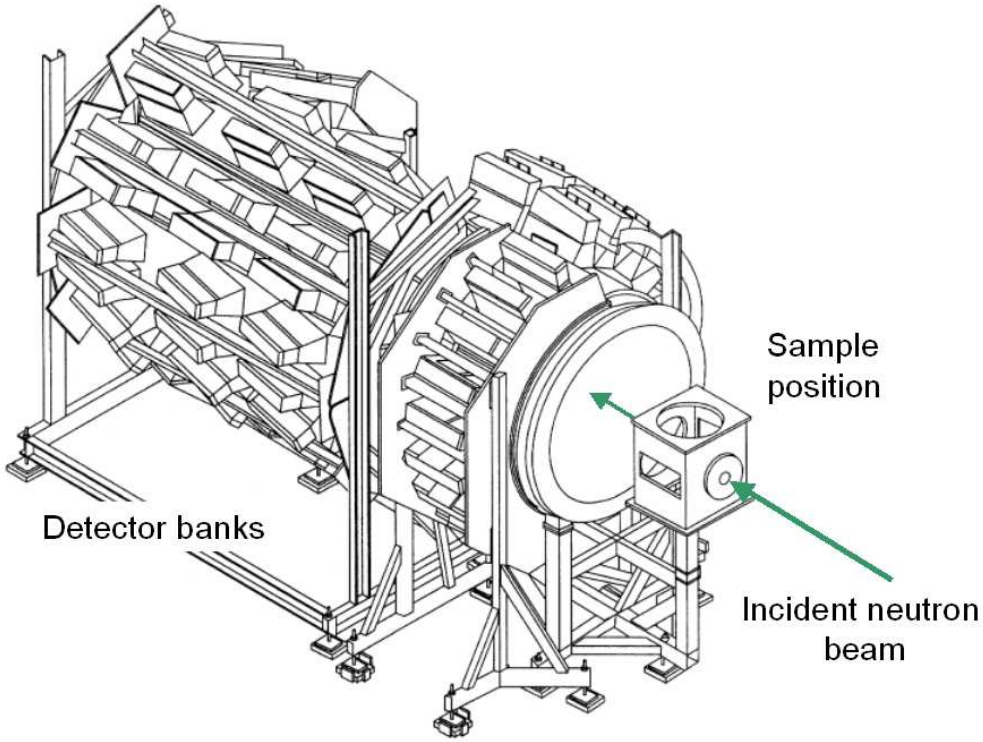

Figure 3.4: The SANDALS diffractometer [41].

Table 3.1: SANDALS detector groups

Group	Scattering Angle 2θ (°)	Group	Scattering Angle 2θ (°)
1	20.1	10	3.8
2	18.1	11	31.2
3	16.2	12	27.8
4	14.6	13	24.4
5	13.1	14	21.7
6	11.8	15	36.5
7	9.5	16	33.6
8	7.0	17	31.2
9	5.0	18	29.5

3.2.3 GEM

The GEM diffractometer at the ISIS facility, illustrated in figure 3.5, contains 7270 ^{6}Li ZnS detector elements in 8 detector banks giving a wide range of accessible scattering vectors of $0.15 \leq Q\ (\text{Å}^{-1}) \leq 50$, which leads to the good resolution in real space that is ideal for studying amorphous materials. Neutrons are moderated by a liquid methane moderator at a temperature of 110 K and have an incident flight path $L_0 = 17$ m. The dimensions of the incident neutron beam are accurately defined by boron carbide collimators and the neutrons have a range of final flight paths to the extensive detector array of $1.077 \leq L_1\ (\text{m}) \leq 2.767$.

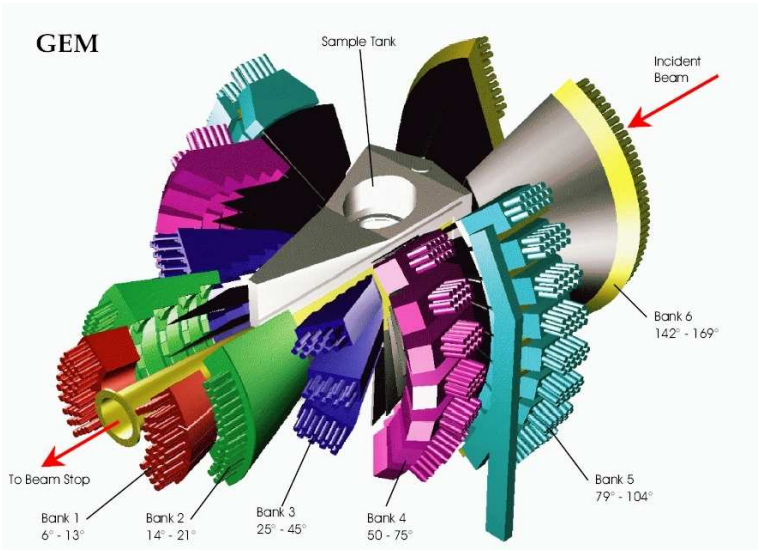

Figure 3.5: The General Materials (GEM) Diffractometer at ISIS [42].

3.2.4 GLAD

The Glass, Liquid and Amorphous Materials Diffractometer (GLAD) at the now decommissioned Intense Pulsed Neutron Source (IPNS) at the Argonne National Laboratory (ANL), Illinois, USA, was a time of flight diffractometer optimised to measure the total structure factor of amorphous materials over

a wide scattering vector Q range. Special emphasis was placed on the use of short-wavelength neutrons scattered at low scattering angles to reduce the corrections for absorption and inelasticity effects. Neutrons were moderated by a 28 K solid methane moderator and had an incident flight path of 10.5 m. A total of 235 ^{3}He linear position sensitive detectors spanning a nearly continuous range of $-47\ ^\circ \leq 2\theta \leq 125\ ^\circ$ (grouped into 7 detector banks and 19 detector groups) provided a wide scattering vector range of $0.2 \leq Q\ (\text{Å}^{-1}) \leq 45$ with a nominal final flight path $L_1 = 1.5$ m. The instrument layout and angular range of each detector bank is shown figure 3.6. In addition to a 9 sample room temperature sample changer (RTSC) the GLAD instrument accommodated several other sample environments including a cryostat and high pressure cell.

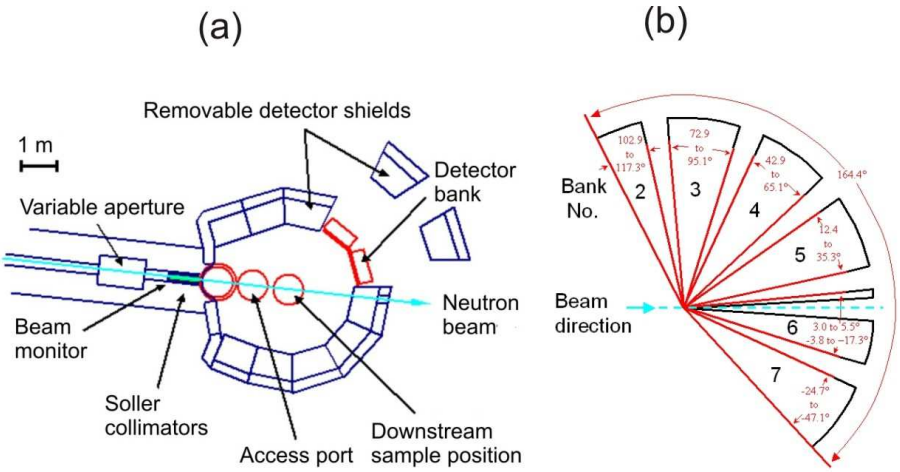

Figure 3.6: The GLAD diffractometer layout [43]. (a) Top view of the GLAD instrument. (b) Angular ranges of the detector banks.

3.2.5 PEARL

The PEARL high pressure (HiPr) instrument at the ISIS facility, illustrated in figure 3.7, is a medium resolution high-flux diffractometer optimised for data collection using the Paris-Edinburgh pressure cell, described in § 3.3, in

transverse (through anvil) scattering geometry. The main detector bank, consisting of nine detector modules each with 120 ^{6}Li ZnS scintillator detector elements, covers $83 \leq 2\theta^\circ \leq 97$ and provides a scattering vector range of $1.55 \leq Q$ (Å^{-1}) ≤ 19.6. The instrument gives good resolution in d-space and hence it is used extensively for crystallography. However, the restricted low-Q accessibility introduces limitations for studying amorphous materials. Additional detectors are available, covering $20 \leq 2\theta^\circ \leq 60$ and $100 \leq 2\theta^\circ \leq 160$ and should therefore allow access to a much wider scattering vector range. However, when mounting the Paris-Edinburgh cell in transverse geometry, these additional detector banks are shielded by the press assembly. Neutrons are moderated by a liquid methane moderator at a temperature of 110 K and have an incident flight path of $L_0 = 12.6$ m. The final flight path $L_1 = 0.6$ m to all detectors.

Figure 3.7: The PEARL high pressure (HiPr) diffractometer at ISIS [44].

3.3 The Paris-Edinburgh press

To study the behaviour of materials at extreme pressure, as experienced in planetary interiors, x-ray and spectroscopy methods are typically employed using single crystal diamond anvil cells (DACs) at pressures up to ≈ 400 GPa [46–48]. In contrast, neutron diffraction methods have been restricted to much lower pressures. This is, in part, due to the relatively low flux of neutron sources; the sample volume of a DAC is typically too small for neutron diffraction experiments which require a much larger sample volume by comparison with x-ray diffraction. However, with the recent development of a novel high pressure cell, the Paris-Edinburgh press, *in situ* neutron diffraction experiments can be performed at pressures up to 30 GPa [49, 50].

The different variants of the Paris-Edinburgh press are illustrated in figure 3.8. The V type press has four support pillars and the VX type has only two support pillars, helping to avoid unwanted scattering of the beam diffracted by the sample. The sample is encapsulated in a gasket made from a Ti-Zr null scattering alloy with a mean coherent neutron scattering length of zero and compressed between two opposed anvils. The standard Los Alamos type anvil assembly is illustrated in figure 3.9 (a). The die is formed by spark erosion of either tungsten carbide, cubic boron nitride or sintered diamond, with a hemispherical sample chamber and a toroidal groove for the Ti-Zr gasket. The toroidal groove provides (i) inward radial support for the gasket as it is compressed, (ii) separation of the central part of the anvil, which is under the most stress, from the edges thus allowing a more favourable pressure distribution and (iii) a reservoir for the gasket material to smooth out pressure variations that occur during phase transitions and heating [51]. The die is held in a tungsten carbide seat supported by a steel binding ring creating a radial compression of 1.0 GPa [49]. The anvils have a bevel angle of 7 ° giving a total accessible aperture of 14 °. Cubic boron nitride (BN) anvils with this geometry are capable of pressures up to 9 GPa. Sintered diamond anvils can achieve 15 GPa. Even higher pressures are capable by reducing the volume of the sample chamber and having two concentric grooves cut for

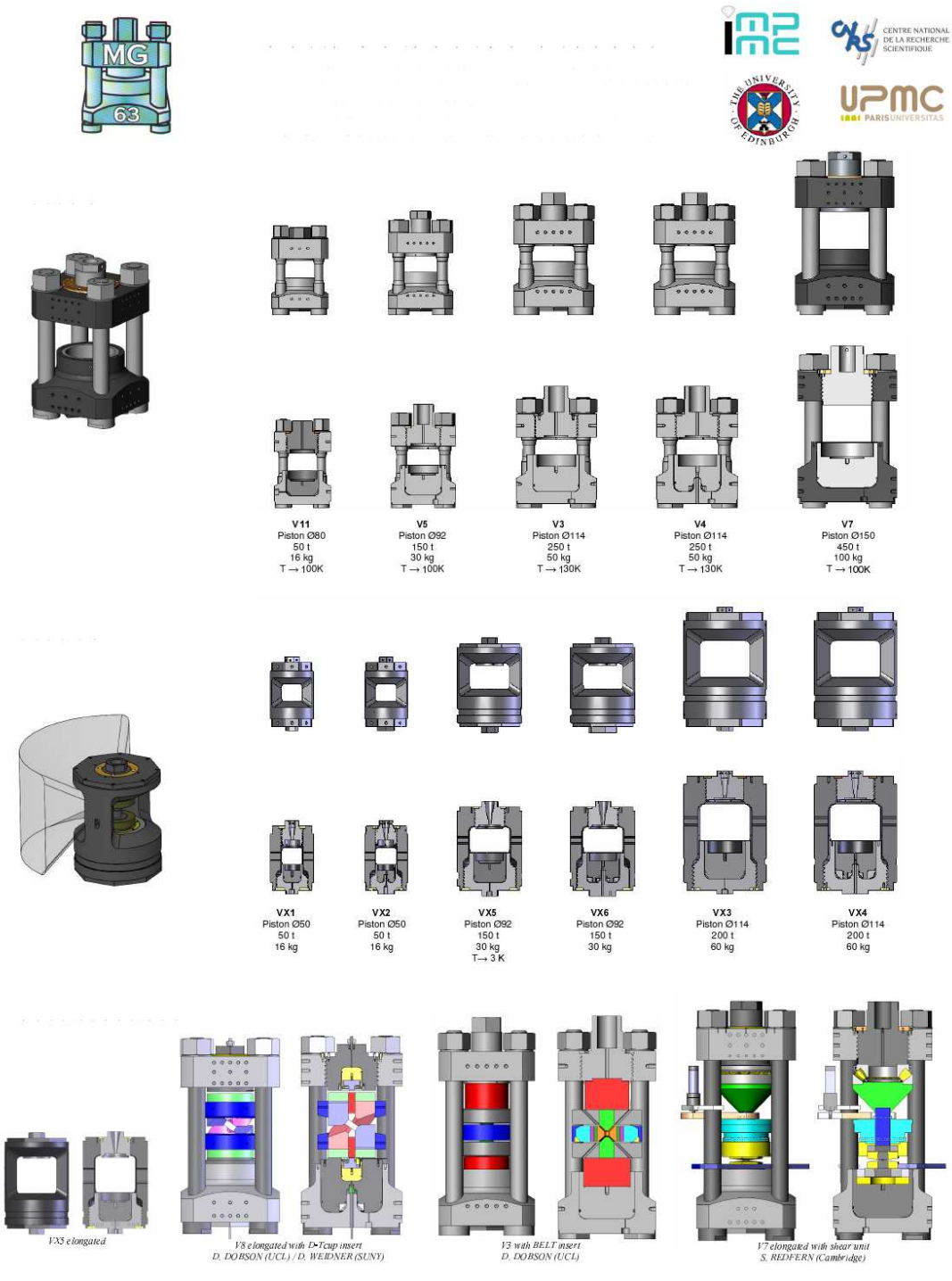

Figure 3.8: Paris-Edinburgh press variants [45].

(a) Single toroid anvil

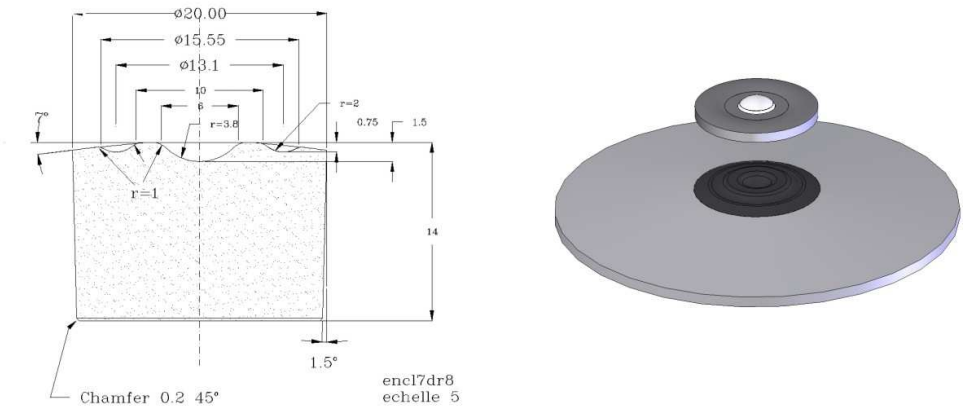

(b) Double toroid anvil

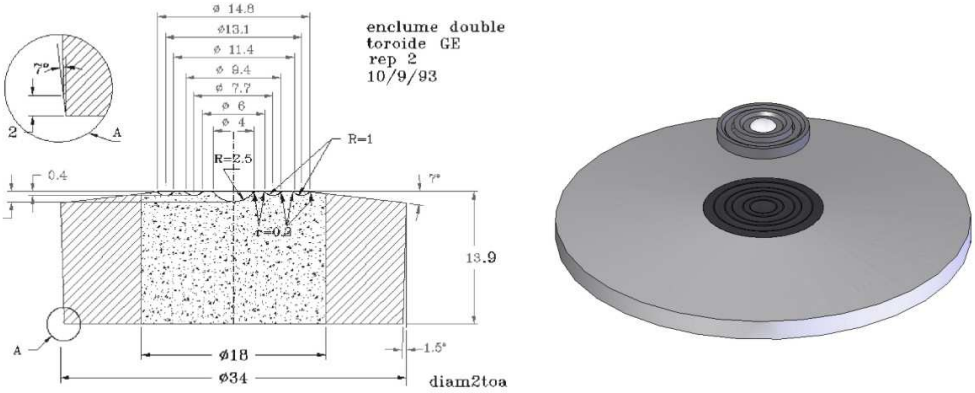

Figure 3.9: Single toroid and double toroid anvils. The 3D models were created following the drawings supplied by Klotz [45].

a double toroid gasket, as illustrated in figure 3.9 (b). Further development of the Paris-Edinburgh press and sintered diamond anvils should see neutron diffraction experiments at pressures much higher than 30 GPa becoming routine in the near future, bringing neutron diffraction into a pressure domain commonly obtained with DACs and providing complementary measurements to high pressure x-ray diffraction [19].

3.4 Synchrotron x-ray sources

In a third generation synchrotron radiation facility, for example the Advanced Photon Source (APS) at the Argonne National Laboratory (ANL), Illinois, USA illustrated in figure 3.10, electrons are accelerated using a linear accelerator (LINAC) and booster ring prior to injection into a main storage ring. Here powerful bending magnets and insertion devices force the high energy electrons to follow a curved trajectory and synchrotron radiation is emitted tangentially to this path. X-ray optics are used to produce intense focussed beams of high energy x-rays at the experimental beamlines where single x-ray wavelengths can be selected by using a monochromator.

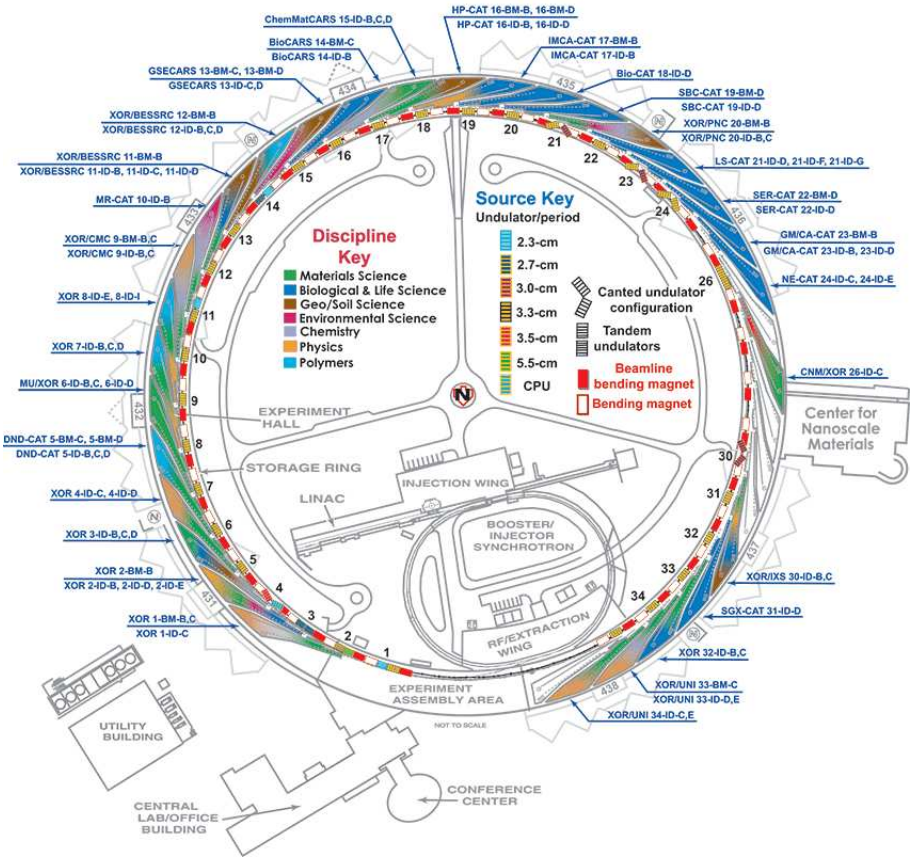

Figure 3.10: The Advanced Photon Source (APS) at the Argonne National Laboratory (ANL), Illinois, USA [52].

3.5 X-ray diffraction instrumentation

3.5.1 11-ID-C

The 11-ID-C beamline at the Basic Energy Sciences Synchrotron Radiation Center (BESSRC) at the APS provides a high flux high energy x-ray beam of photons with energy of 60, 98 or 115 keV with a large penetration depth in bulk samples. The diffractometer on this beamline enables access to a large maximum scattering vector $Q_{\max} \geq 45$ Å^{-1} giving the good resolution in real space that is required for studying amorphous materials. A typical experimental set-up using a Ge point detector at 11-ID-C is shown in figure 3.11, where only the sample and detector towers are needed to measure the total scattering from an amorphous sample.

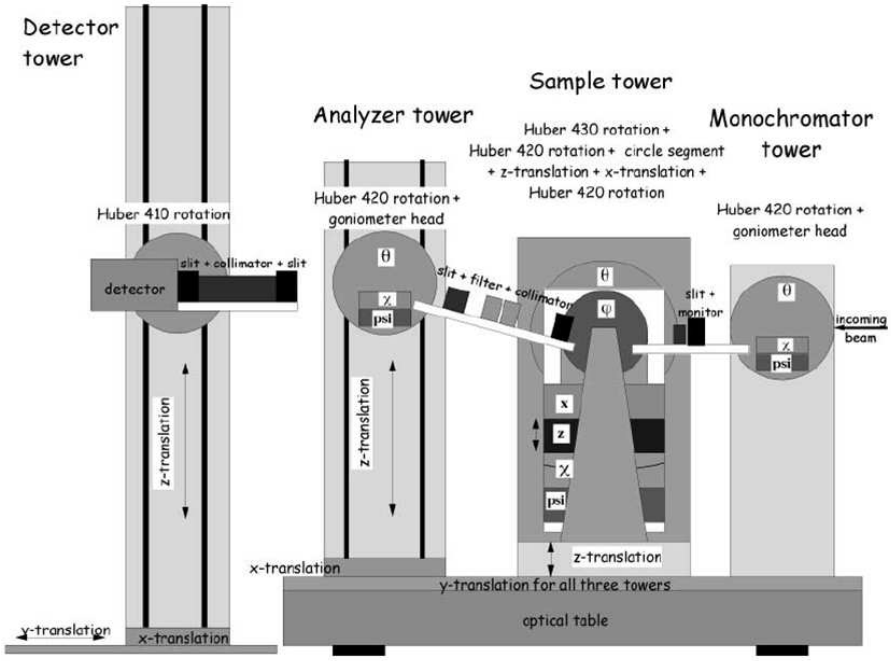

Figure 3.11: The experimental set up at the 11-ID-C beamline [53].

3.5.2 ID15B

The high energy x-ray beamline ID15B (see figure 3.12) at the European Synchrotron Radiation Facility (ESRF) in Grenoble, France, offers a high flux of highly collimated photons in the energy range 40 keV to 300 keV. The beamline uses a two-dimensional MAR345 image plate detector with 2300 x 2300 pixels each with a pixel size of 0.15 μm. A 2 mm aluminium filter is placed in front of the detector to avoid fluorescence from samples.

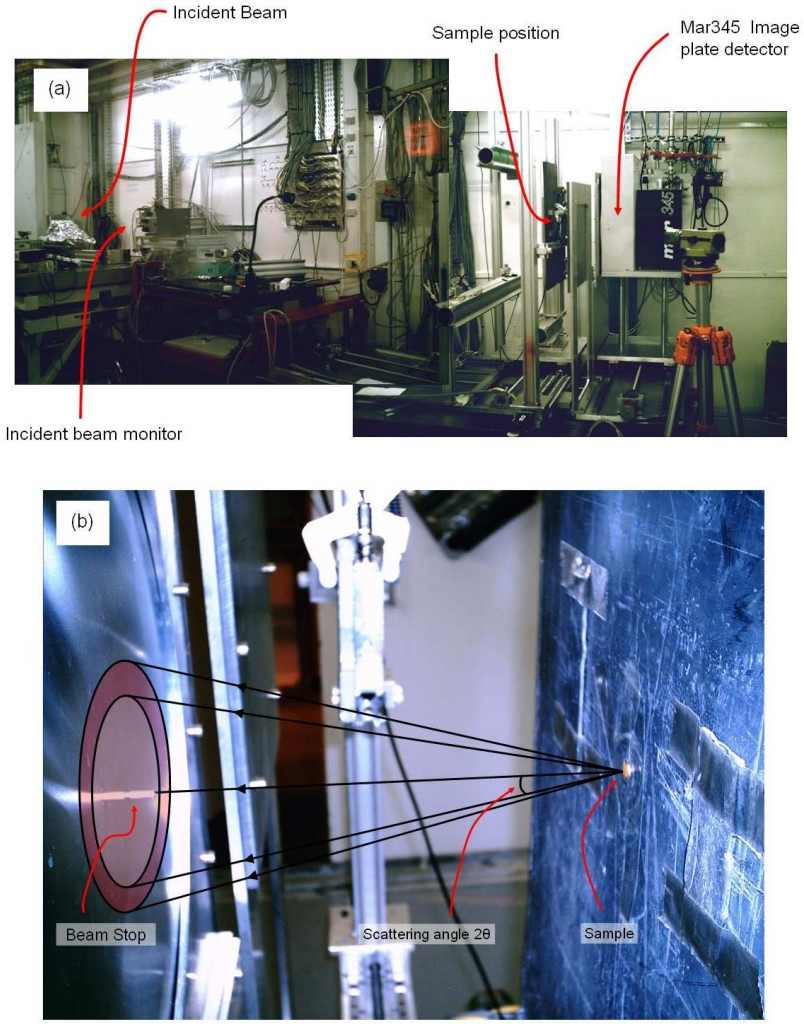

Figure 3.12: (a) The ID15B beamline (b) The sample geometry.

3.6 Neutron diffraction data treatment

The following data treatment and correction procedures are more pertinent for diffraction data that are obtained by using a single wavelength of incident neutrons. For time of flight data the corrections must be performed for each neutron wavelength at each scattering angle before merging the data from individual detectors. In the notation that follows, the subscripts S, C, V and H are used to denote the sample, container, vanadium and heater, respectively. The superscripts E and B denote the experimental intensities not corrected for background scattering and the background intensities, respectively.

3.6.1 Sample environment, container and background

To extract the differential scattering cross section $\frac{\mathrm{d}\sigma}{\mathrm{d}\Omega}(Q)$ from the scattered intensity obtained in a neutron diffraction experiment on an amorphous sample it is necessary to first normalise the measured intensities to the incident neutron monitor count and then correct for the scattered intensity arising from the sample container, the sample environment (e.g. furnace, cryostat) and the intrinsic instrument background (arising from neutrons and electronic noise). Therefore, separate diffraction patterns need to be measured for the sample in its container in the sample environment, the empty container in the sample environment, the empty sample environment and the empty instrument. In the data analysis procedure an account must be made of the beam attenuation (from absorption and scattering) and multiple scattering events originating from the sample environment, sample container and the sample itself. The sample container is typically made from a thin walled can of mainly incoherent scattering material such as vanadium or null scattering Ti-Zr alloy.

3.6.2 Attenuation, multiple scattering and Placzek corrections

Consider first a single component sample with cylindrical geometry and no container or heater. In a real experiment, absorption or scattering events will lead to an attenuation of the overall sample scattered intensity. An attenuation factor is therefore applied to the measured diffraction intensity, as calculated using the method of Paalman and Pings [54] for a sample with cylindrical geometry. The attenuation coefficient is dependent on the scattering angle and is denoted by $A_{i,j}(\theta)$ to represent neutrons that are scattered in medium i and attenuated in medium j. The neutrons may also undergo multiple scattering events prior to detection which must be corrected for and if the energy exchange between a neutron and target nucleus is not small by comparison to the incident neutron energy then a deviation from the static approximation necessitates the application of the Placzek [31] (inelasticity) correction. The background corrected intensity for the sample is given by

$$\begin{aligned} I'_S(\theta) &= I^E_S(\theta) - I^B_S(\theta) \\ &= A_{S,S}(\theta) I_S(\theta) + a(\theta) M_S(\theta), \end{aligned} \tag{3.8}$$

where $a(\theta)$ is the diffractometer calibration factor and $M_S(\theta)$ denotes the multiple scattering cross section defined by Soper and Egelstaff [55]. The single scattered intensity for the sample $I_S(\theta)$ is given by

$$\begin{aligned} I_S(\theta) &= a(\theta) N_S \left[\frac{\mathrm{d}\sigma}{\mathrm{d}\Omega}(\theta) \right]_S \\ &= a(\theta) N_S \left\{ b^2_{\mathrm{coh}} [S(Q) - 1] + (b^2_{\mathrm{coh}} + b^2_{\mathrm{inc}})(1 + P_S(\theta)) \right\}, \end{aligned} \tag{3.9}$$

where N_S is the number of sample scattering centres in the beam, $S(Q)$ is the structure factor for the sample, b_{coh} and b_{inc} are the coherent and incoherent scattering lengths of the sample, respectively, and $P_S(\theta)$ is the Placzek [31] correction factor for the sample. The multiple scattering cross section for the

sample, $M_S(\theta)$, is given by

$$M_S(\theta) = N_S A_{S,S}(\theta)\frac{\sigma_S}{4\pi}\Delta_S(\theta)(1 + P_S(\theta)), \tag{3.10}$$

where $\Delta_S(\theta)$ is the ratio of multiple to single scattering and $\sigma_S = 4\pi(b^2_{\text{coh}}+b^2_{\text{inc}})$ is the total scattering cross section for the sample.

3.6.3 Vanadium normalisation

The diffracted intensity for a sample can be normalised to an absolute cross-section by comparison with the measured intensity of a calibrant of known scattering cross-section. Vanadium is an ideal standard as it behaves as an isotropic elastic scatterer of thermal neutrons [56] and its coherent scattering length $b_{V,\text{coh}} = -0.03824(12)$ fm [30] is very small such that the scattering is mostly incoherent. The diffraction pattern for a solid piece of vanadium of comparable dimensions to the sample is thus typically used to normalise neutron diffraction data. Equation 3.8 gives the background corrected intensity for a vanadium rod, normalised to the monitor counts, as

$$\begin{aligned} I'_V(\theta) &= I^E_V(\theta) - I^B_V(\theta) \\ &= A_{V,V}(\theta)I_V(\theta) + a(\theta)M_V(\theta). \end{aligned} \tag{3.11}$$

The single scattered intensity for the vanadium $I_V(\theta)$ is given by

$$\begin{aligned} I_V(\theta) &= a(\theta)N_V\left[\frac{\mathrm{d}\sigma}{\mathrm{d}\Omega}(\theta)\right]_V \\ &= a(\theta)N_V\left\{\frac{\sigma_V}{4\pi}(1 + P_V(\theta))\right\}, \end{aligned} \tag{3.12}$$

where $\sigma_V = 4\pi b^2_{\text{inc}}$ is the vanadium total scattering cross section. The multiple scattering cross section $M_V(\theta)$ is given by

$$M_V(\theta) = N_V A_{V,V}(\theta)\frac{\sigma_V}{4\pi}\Delta_V(\theta)(1 + P_V(\theta)). \tag{3.13}$$

so that

$$\begin{aligned} I'_V(\theta) &= a(\theta)\left[A_{V,V}(\theta)N_V\frac{\sigma_V}{4\pi}(1+P_V(\theta)+N_V A_{V,V}(\theta)\frac{\sigma_V}{4\pi}\Delta_V(\theta)(1+P_V(\theta))\right] \\ &= a(\theta)A_{V,V}(\theta)N_V\frac{\sigma_V}{4\pi}(1+\Delta_V(\theta))(1+P_V(\theta)). \end{aligned} \tag{3.14}$$

By rearranging equation 3.14, the normalisation factor $a(\theta)$ is given by

$$a(\theta) = \frac{I'_V(\theta)4\pi}{A_{V,V}(\theta)N_V\sigma_V(1+\Delta_V(\theta))(1+P_V(\theta))}. \tag{3.15}$$

In practice, the vanadium diffraction pattern does contain some coherent scattering contributions giving rise to the appearance of small Bragg peaks which must be removed by smoothing routines.

3.6.4 Corrections for a sample in a container in a heater

In general diffraction patterns are taken for a sample which is placed within a container in a specific sample environment such as a heater or a cryostat. The background corrected intensities, normalised to the monitor counts, for the sample in a container in a heater $I'_{SCH}(\theta)$, the empty container in the heater $I'_{CH}(\theta)$ and the empty heater $I'_H(\theta)$ are given by

$$\begin{aligned} I'_{SCH}(\theta) &= I^E_{SCH}(\theta) - I^B_{SCH}(\theta) \\ &= A_{S,SCH}(\theta)I_S(\theta) + A_{C,SCH}(\theta)I_C(\theta) + A_{H,SCH}(\theta)I_H(\theta) + a(\theta)M_{SCH}(\theta), \end{aligned} \tag{3.16}$$

$$\begin{aligned} I'_{CH}(\theta) &= I^E_{CH}(\theta) - I^B_{CH}(\theta) \\ &= A_{C,CH}(\theta)I_C(\theta) + A_{H,CH}(\theta)I_H(\theta) + a(\theta)M_{CH}(\theta), \end{aligned} \tag{3.17}$$

$$\begin{aligned} I'_H(\theta) &= I^E_H(\theta) - I^B_H(\theta) \\ &= A_{H,H}(\theta)I_H(\theta) + a(\theta)M_H(\theta), \end{aligned} \tag{3.18}$$

where $M_{SCH}(\theta)$, $M_{CH}(\theta)$ and $M_H(\theta)$ denote the multiple scattering cross-sections. Re-arranging for the single scattered intensities $I_S(\theta)$, $I_C(\theta)$ and $I_H(\theta)$ we find

$$I_S(\theta) = \frac{1}{A_{S,SCH}(\theta)} \left[I'_{SCH}(\theta) - a(\theta) M_{SCH}(\theta) - A_{C,SCH}(\theta) I_C(\theta) - A_{H,SCH}(\theta) I_H(\theta) \right], \tag{3.19}$$

$$I_C(\theta) = \frac{1}{A_{C,CH}(\theta)} \left[I'_{CH}(\theta) - a(\theta) M_{CH}(\theta) - A_{H,CH}(\theta) I_H \right], \tag{3.20}$$

$$I_H(\theta) = \frac{1}{A_{H,H}(\theta)} \left[I'_H(\theta) - a(\theta) M_H(\theta) \right]. \tag{3.21}$$

As in equation 3.9 the single scattered intensity for the sample is given by

$$I_S(\theta) = a(\theta) N_S \left[\frac{\mathrm{d}\sigma}{\mathrm{d}\Omega}(\theta) \right]_S. \tag{3.22}$$

By substituting equations 3.21 and 3.20 into equation 3.19 and rearranging we find

$$\begin{aligned} \left[\frac{\mathrm{d}\sigma}{\mathrm{d}\Omega}(\theta) \right]_S = \frac{1}{Q_1(\theta)} \Bigg[& \left(\frac{I'_{SCH}(\theta)}{a(\theta)} - M_{SCH}(\theta) \right) \\ & - Q_2(\theta) \left(\frac{I'_{CH}(\theta)}{a(\theta)} - M_{CH}(\theta) \right) \\ & - Q_3(\theta) \left(\frac{I'_H(\theta)}{a(\theta)} - M_H(\theta) \right) \Bigg], \end{aligned} \tag{3.23}$$

where

$$Q_1(\theta) = N_S A_{S,SCH}(\theta), \tag{3.24}$$

$$Q_2(\theta) = \frac{A_{C,SCH}(\theta)}{A_{C,CH}(\theta)}, \tag{3.25}$$

$$Q_3(\theta) = \frac{1}{A_{H,H}(\theta)} \left[A_{H,SCH}(\theta) - A_{C,SCH}(\theta) \frac{A_{H,CH}(\theta)}{A_{C,CH}(\theta)} \right]. \tag{3.26}$$

In the absence of a heater $Q_3(\theta) = 0$ and the subscript H can be omitted so that equation 3.23 reduces to

$$\left[\frac{\mathrm{d}\sigma}{\mathrm{d}\Omega}(\theta)\right]_S = \frac{1}{Q_1(\theta)}\left[\left(\frac{I'_{SC}(\theta)}{a(\theta)} - M_{SC}(\theta)\right) - Q_2(\theta)\left(\frac{I'_C(\theta)}{a(\theta)} - M_C(\theta)\right)\right]. \tag{3.27}$$

For a multi-component system the differential scattering cross-section for the sample is given by equation 2.5 and the total structure factor $F(Q)$ is therefore extracted by using

$$F(Q) = \left[\frac{\mathrm{d}\sigma}{\mathrm{d}\Omega}(\theta)\right]_S - \sum_{\alpha=1}^{n} c_\alpha(b^2_{\mathrm{coh},\alpha} + b^2_{\mathrm{inc},\alpha})(1 + P_\alpha(Q)). \tag{3.28}$$

3.7 X-ray diffraction data treatment

As in neutron diffraction, to extract the differential scattering cross section $\frac{\mathrm{d}\sigma}{\mathrm{d}\Omega}(Q)$ from the scattered intensity obtained in an x-ray diffraction experiment on an amorphous sample it is necessary to first normalise the measured intensities to the incident x-ray monitor count and then subtract contributions to the diffracted intensity arising from the sample container, the sample environment and the intrinsic instrument background. The attenuation corrections due to absorption are typically large for x-rays, although the absorption cross section is reduced by using a high energy incident x-ray beam. The sample containers used in the present work were made from kapton 77-80 thin films which are highly transparent to x-rays.

Consider x-ray diffraction measurements made using a slab sample geometry, as illustrated in figure 3.13. The incident beam intensity I_0 is attenuated by the sample giving a scattered beam intensity

$$I_1(\theta) = A_{S,S}(\theta)I_0. \tag{3.29}$$

In slab geometry, the self-shielding attenuation factor is calculated, using the

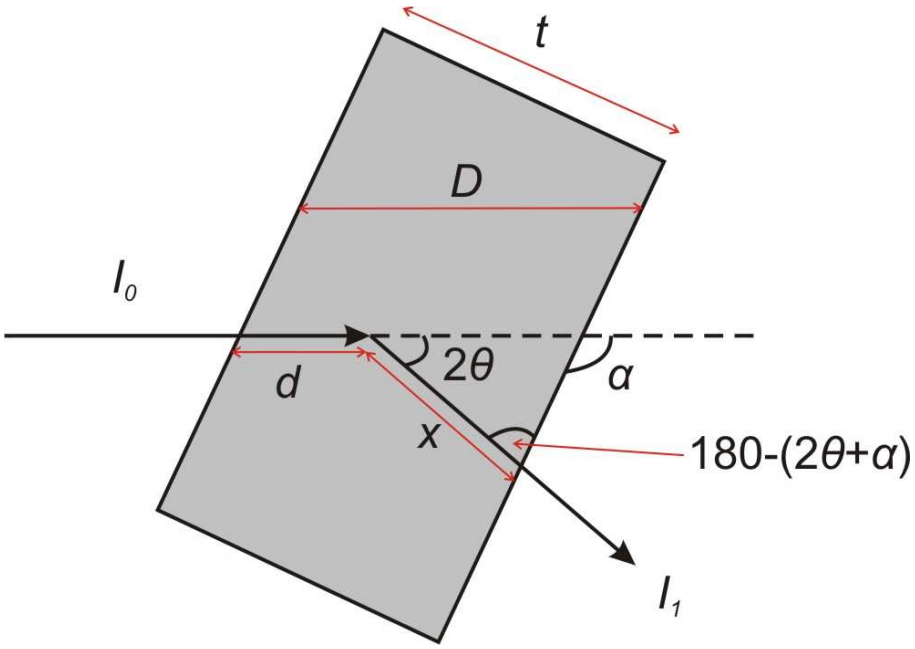

Figure 3.13: Slab sample geometry where I_0 and I_1 are the intensities of the incident and scattered beam, respectively, d, x, D and t are distances, 2θ is the scattering angle and α is the angle between the outward face of the sample and the incident beam.

method derived by Carlile [57], from

$$A_{S,S}(2\theta) = \exp\left(-\mu L \frac{\sin(\alpha)}{\sin(2\theta+\alpha)}\right) \cdot \left[\frac{\exp\left(\left\{(\mu\frac{\sin(\alpha)}{\sin(2\theta+\alpha)} - \mu\right\} L\right) - 1}{\left\{\mu\frac{\sin(\alpha)}{sin(2\theta+\alpha)} - \mu\right\} L}\right], \tag{3.30}$$

where μ denotes the attenuation coefficient, the distances d, x, D, t and angle α are defined in figure 3.13 and 2θ denotes the scattering angle. The background corrected intensity for the sample is given by

$$\begin{aligned} I'_S(\theta) &= I^E_S(\theta) - I^B_S(\theta) \\ &= A_{S,S}(\theta) I_S(\theta), \end{aligned} \tag{3.31}$$

where the single scattered intensity for the sample is related to the total x-ray

scattering cross section by

$$I_S(\theta) = aN_S \left[\frac{\mathrm{d}\sigma}{\mathrm{d}\Omega}(Q)\right]^X_{\text{Total}} \tag{3.32}$$

and a is the diffractometer calibration factor which is assumed to be independent of θ.

The background scattering is typically largest at small scattering angles and the attenuation of the background by the sample at low angles must be taken into account. The regions that contribute to the background scattering are shown in figure 3.14. If in the absence of a sample and container we assume a vacuum for region δ, such that there is no scattering from this region, then the background intensity is given by

$$I^B_S(\theta) = I_\alpha(\theta) + I_\beta(\theta) + I_\gamma(\theta). \tag{3.33}$$

If a highly absorbing sample, such as lead (Pb), is placed in the sample position, then the contribution to the background scattering from region β is eliminated and the measured background intensity

$$I^E_{Pb}(\theta) = I_\alpha(\theta) + I_\gamma(\theta). \tag{3.34}$$

The intensity arising from region β with no sample in the beam can therefore be determined by

$$I_\beta(\theta) = I^B_S(\theta) - I^E_{Pb}(\theta). \tag{3.35}$$

In the presence of a sample in region δ, the background contribution from region β is attenuated such that

$$I^E_S(\theta) = I_\alpha(\theta) + I_\gamma(\theta) + A_{S,S}(\theta)I_\beta(\theta) + I'_S(\theta). \tag{3.36}$$

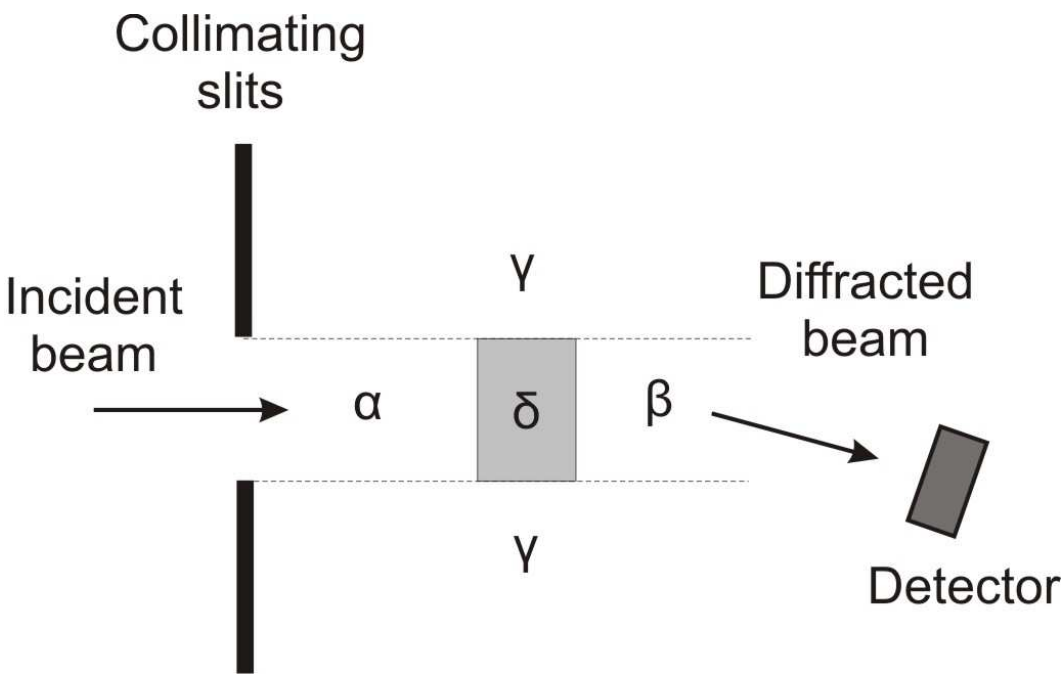

Figure 3.14: The regions α, β, γ that contribute to background scattering in the presence of a sample in region δ.

The background corrected intensity at low angles is therefore obtained from

$$\begin{aligned} I'_S(\theta) &= I^E_S(\theta) - \{I_\alpha(\theta) + I_\gamma(\theta) + A_{S,S}(\theta) I_\beta(\theta)\} \\ &= I^E_S(\theta) - \left\{I^E_{Pb}(\theta) + A_{S,S}(\theta)\left[I^B_S(\theta) - I^E_{Pb}(\theta)\right]\right\}. \end{aligned} \tag{3.37}$$

A similar correction can be made for neutron diffraction experiments with a fixed incident wavelength where a suitable neutron absorber such as cadmium (Cd) is used in place of Pb.

There is no equivalent to vanadium, as used in neutron diffraction, for normalizing x-ray diffraction intensities. Instead the constant a in equation 3.32 is used to scale $I'_S(\theta)$ until it agrees with the sum of the Compton scattering cross section and self scattering contributions at high Q values to obtain the

total x-ray differential scattering cross section (see equation 2.16) where

$$\left[\frac{\mathrm{d}\sigma}{\mathrm{d}\Omega}(Q)\right]^{X}_{\mathrm{Total}} = \frac{I'_S(\theta)}{aN_S A_{S,S}(\theta)} = \left[\frac{\mathrm{d}\sigma}{\mathrm{d}\Omega}(Q)\right]^{X}_{\mathrm{Compton}} + \left[\frac{\mathrm{d}\sigma}{\mathrm{d}\Omega}(Q)\right]^{X}_{\mathrm{Ray-T}}$$
$$= \left[\frac{\mathrm{d}\sigma}{\mathrm{d}\Omega}(Q)\right]^{X}_{\mathrm{Compton}} + \sum_{\alpha=1}^{n} c_\alpha f_\alpha(Q)^2 + F_X(Q) \qquad (3.38)$$

and $F_X(Q) \rightarrow 0$ at high Q values. The total x-ray structure factor is then obtained from

$$F_X(Q) = \left[\frac{\mathrm{d}\sigma}{\mathrm{d}\Omega}(Q)\right]^{X}_{\mathrm{Total}} - \left[\frac{\mathrm{d}\sigma}{\mathrm{d}\Omega}(Q)\right]^{X}_{\mathrm{Compton}} - \sum_{\alpha=1}^{n} c_\alpha f_\alpha(Q)^2. \qquad (3.39)$$

4. A neutron diffraction study of molten copper halides

The work presented in this chapter is also reported in Ref. [58].

4.1 Introduction

The copper halides CuX (X = Cl, Br, I) exhibit superionic conductivity at elevated temperatures or pressures in which Cu^+ cations move through a network of voids formed by an anion sub-lattice [59] leading to an exceptionally high (liquid-like) ionic conductivity whilst in the solid state [59–63]. The key structural transformations of the CuX system are summarised in table 4.1 where they are compared to AgI, a typical superionic compound. In particular, at 673 K CuI undergoes a transition into the superionic α-phase which is accompanied by an increase in the self diffusion coefficient of Cu^+ from the order of 10^{-6} cm^2s^{-1} in the β-phase to a liquid-like value of $3.5{\cdot}10^{-5}$ cm^2s^{-1} in the α-phase [64]. The ionic conductivity of the superionic α-phase and the molten phase is comparable at ≈ 1 Ω^{-1} cm^{-1} [62, 65]. In comparison, CuCl undergoes a transition into the β-phase at 681 K from which the system melts at 703 K. Despite the relatively high ionic conductivity value of ≈ 0.1 Ω^{-1} cm^{-1} [65] and a liquid-like Cu^+ self diffusion coefficient [66], the β-phase of CuCl is not generally considered to be a true superionic phase since the cations are reported to have only a limited occupation of the interstitial voids formed by the anion sublattice [63, 67]. However, the application of a moderate pressure

Table 4.1: Summary of the phase transitions observed at temperature, T, in the CuX system compared to AgI. The superionic phases are denoted by *, where † denotes a phase obtainable only at elevated pressures.

Compound	Phase	Structure	T(K)	Reference
CuCl	γ	zinc-blende	< 681	[67]
	β	wurtzite	$681 \rightarrow 703$	[67]
	melt		< 703	[68]
	III*	AgI type bcc	$\gtrsim$ 700 †	[67]
CuBr	γ	zinc-blende fcc	$<$ 664	[67]
	β	wurtzite	$664 \rightarrow 744$	[69]
	α^*	AgI type bcc	$744 \rightarrow 765$	[69]
	melt		$<$ 765	[68]
CuI	γ	zinc-blende	$<$ 642	[63]
	β	hexagonal	$642 \rightarrow 680$	[63]
	α^*	fcc	$680 \rightarrow 878$	[63]
	melt		$<$ 878	[68]
	VII*	bcc	$\gtrsim$ 920 †	[63]
AgI	γ	zinc-blende	$<$ 420	[70]
	β	wurtzite	$<$ 420	[70]
	α^*	bcc	$420 \rightarrow 831$	[70]
	melt		$<$ 831	[68]
	III*	rocksalt	$\gtrsim$ ambient †	[63]

$\gtrsim$ 0.2 GPa at a temperature $\gtrsim$ 700 K leads to the III-phase of CuCl which has a structure analogous to the ambient pressure superionic structures of α-AgI and α-CuBr [67]. This promotion of superionic behaviour at elevated pressure is counter-intuitive, since more densely packed anion sublattices will be formed reducing the free-space available for the mobile cations. Nevertheless CuI has also been shown to adopt a bcc superionic VII-phase at a moderate pressure $\gtrsim$ 2 GPa at a temperature $\gtrsim$ 920 K in addition to its ambient pressure superionic α-phase and AgI can be transformed at ambient temperature into a rocksalt superionic III-phase by the application of a pressure $\gtrsim$ 0.5 GPa [63].

The superionic properties of CuX systems make them ideal candidates for use in solid state battery technology, particularly if the superionic-phase is sta-

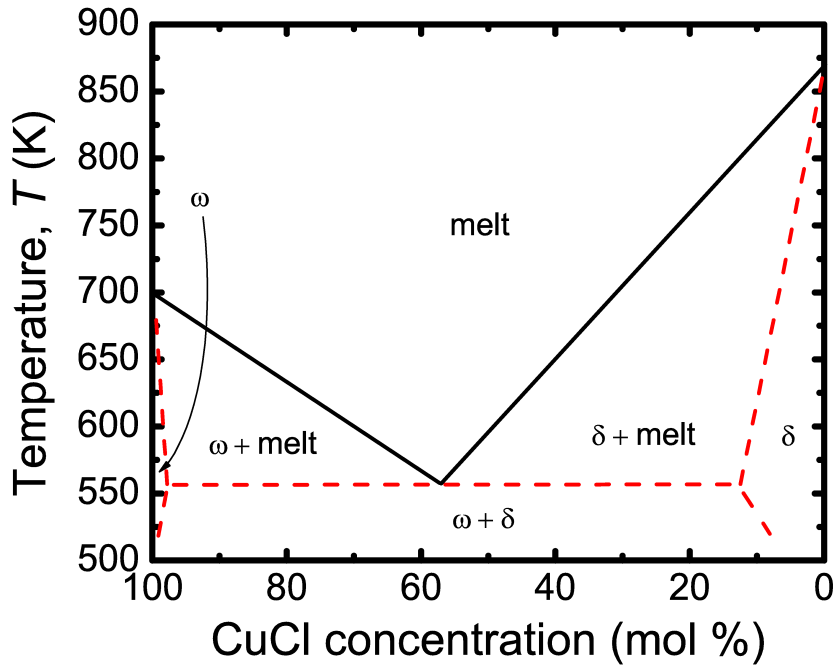

Figure 4.1: The phase diagram for the CuCl-CuI system [71]. The onset of crystallisation for the CuCl-CuI mixtures is given by the solid (black) line. The eutectic point occurs at 58 mol % CuCl. The solubility of CuCl is relatively high in CuI and forms a mixed crystalline δ-phase containing up to 12 mol % CuCl. In contrast, the solubility limit of CuI in CuCl is lower forming a mixed crystalline ω-phase containing only a few mol % CuI. A mixture of the ω and δ crystalline phases exists below the eutectic, as marked by the horizontal dashed (red) line.

bilised at ambient temperature. This can be achieved via the introduction of the copper halides into network glasses to produce fast-ion conducting glasses such as CuI-$CuPO_3$ and CuI-PbI_2-As_2Se_3 [72–77]. It is therefore important to understand the structure of the copper halides, particularly in the superionic and molten phases, in order to provide insight into their basic physico-chemical properties and to provide sufficient criteria and constraints for developing realistic models of this system and other related materials.

The purpose of this investigation is to make a systematic study of the structure of molten $(CuCl)_x(CuI)_{1-x}$ $(0 \leq x \leq 1)$ mixtures using neutron

diffraction. The phase diagram for the CuCl-CuI system is plotted in figure 4.1 where the minimum in the liquidus curve (or eutectic point) lies at the composition $x = 0.58$ and temperature $T = 557$ K. In the solid-phase, CuI is relatively insoluble in CuCl but does form mixed crystals containing up to 12 mol % CuCl. The structure and properties of molten CuCl [78–97] and CuI [85–105] have been extensively studied by experiment, theory and computer simulations providing an important reference point on which to base a study of their mixtures. In particular, the full set of partial structure factors for molten CuCl were measured by Page and Mika [78] in one of the first applications of the method of isotopic substitution in neutron diffraction using the Curran and Badger I instruments at the DIDO reactor (Harwell, UK) [78]. This work was subsequently improved upon by Eisenberg *et al.* [106] in 1982, at the ILL reactor (Grenoble, France) using the D4 instrument, following a redetermination of the coherent neutron scattering length of the chlorine isotopes [107], which had a discrepancy of $\sim 18\%$ for ^{37}Cl. The Reverse Monte Carlo (RMC) method has also been used to deduce the partial structure factors of molten CuI from the diffraction patterns obtained from anomalous x-ray scattering [99] or neutron and x-ray diffraction [103, 104]. Prior to this study, very limited measurements had been performed on the structure and properties of molten copper halide mixtures. However, some properties including the magnetic susceptibility, ultrasonic velocity, sound attenuation and density measurements had been made on the copper halides and their mixtures [96, 108, 109]. The magnetic susceptibility for the CuCl-CuBr melts displays a deviation from the linear dependence on composition observed for the CuBr-CuI and CuCl-CuI melts [108]. The structure of CuCl-CuBr melts has also been studied by neutron diffraction [110].

4.2 Theory

As derived in § 2.2, the coherent scattered intensity obtained by a neutron diffraction experiment on $(\mathrm{CuCl})_x(\mathrm{CuI})_{1-x}$ melts can be represented by the

total structure factor $F(Q)$, defined as

$$F(Q) = \sum_{\alpha=1}^{n}\sum_{\beta=1}^{n} c_\alpha c_\beta b_\alpha b_\beta [S_{\alpha\beta}(Q) - 1], \tag{4.1}$$

where $n = 3$ is the total number of chemical species α or β, c_α and b_α represent the atomic fraction and coherent neutron scattering length of chemical species α, respectively, $S_{\alpha\beta}(Q)$ is a Faber-Ziman partial structure factor and Q is the scattering vector. For the natural isotopic abundance, the coherent neutron scattering lengths are $b(\mathrm{Cl}) = 9.5770(8)$ fm, $b(\mathrm{Cu}) = 7.718(4)$ fm and $b(\mathrm{I}) = 5.28(2)$ fm [30] and the weighting factors for the $S_{\alpha\beta}(Q)$ partial structure factors are listed in table 4.2. The corresponding real space information is given by the total pair distribution function $G(r)$ which is obtained by the Fourier transform

$$\begin{aligned} G(r) &= \frac{1}{2\pi^2 r n_0}\int_0^\infty QF(Q)\sin(Qr)\mathrm{d}Q \\ &= \sum_{\alpha=1}^{n}\sum_{\beta=1}^{n} c_\alpha c_\beta b_\alpha b_\beta [g_{\alpha\beta}(r) - 1] \end{aligned} \tag{4.2}$$

where n_0 denotes the atomic number density, $g_{\alpha\beta}(r)$ is a partial pair distribution function and r is a distance in real space.

Table 4.2: Weighting factors (in barn) for the $S_{\alpha\beta}(Q)$ partial structure factors in the $F(Q)$ functions of the $(\mathrm{CuCl})_x(\mathrm{CuI})_{1-x}$ samples.

x	$S_{\mathrm{CuCu}}(Q)$	$S_{\mathrm{CuCl}}(Q)$	$S_{\mathrm{CuI}}(Q)$	$S_{\mathrm{ClCl}}(Q)$	$S_{\mathrm{II}}(Q)$
1	0.1489(2)	0.3696(2)	–	0.22930(4)	–
0.801	0.1489(2)	0.29603(3)	0.0405(2)	0.14712(2)	0.00276(2)
0.576	0.1489(2)	0.2129(1)	0.0864(3)	0.07608(1)	0.01253(9)
0.294	0.1489(2)	0.10866(6)	0.1439(5)	0.019820(3)	0.0347(3)
0	0.1489(2)	–	0.2037(8)	–	0.0697(5)

4.3 Experimental procedure

The experimental work was conducted in August 2000 by Salmon, Takeda and Kawakita [58] following the procedure outlined below. The data analysis and interpretation was performed by the author.

4.3.1 Sample preparation

The $(CuCl)_x(CuI)_{1-x}$ ($x = 1, 0.801, 0.576, 0.294, 0$) samples were prepared by weighing CuCl (Aldrich, 99.995+ %) and CuI (Aldrich, 99.999 %) in the correct proportions in a dry nitrogen filled glove box to prevent contamination of the sample by atmospheric impurities. The samples were loaded into matched silica ampoules of 7 mm inner diameter and 1 mm wall thickness and sealed under vacuum. Prior to preparation, the ampoules had been cleaned using chromic acid and distilled water and thoroughly dried. The samples used in the experiment are shown in figure 4.2.

4.3.2 The SANDALS neutron diffraction experiment

Neutron diffraction experiments were performed on the $(CuCl)_x(CuI)_{1-x}$ samples using the SANDALS instrument with a maximum scattering vector $Q_{\max} = 49.9$ Å^{-1}. The samples were heated to above their melting temperatures using the Leicester furnace. Diffraction patterns were taken for the samples in their silica containers in the furnace, an empty silica container in the furnace at several high temperatures, the empty furnace, the empty instrument, and a vanadium rod of diameter 8.35 mm for normalisation purposes. After eliminating non-functioning or noisy detectors, the GUDRUN analysis program [111] was used to process the data detector-by-detector, correcting for attenuation, background, multiple scattering and inelasticity effects and normalising to the vanadium standard. The results were then merged to produce the total structure factor $F(Q)$. The neutron wavelength range used in the data analysis was limited to $0.075 \leq \lambda\ (\text{Å}) \leq 4.95$, thus limiting the neutron energy to

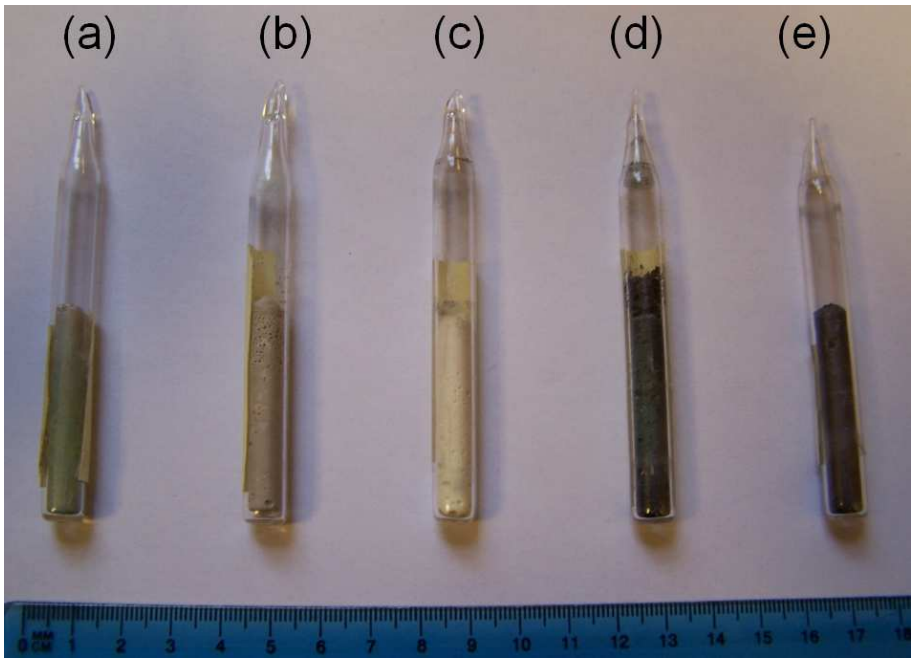

Figure 4.2: The $(CuCl)_x(CuI)_{1-x}$ samples sealed in silica ampoules and photographed after the diffraction measurements. The samples are (a) CuCl (b) $(CuCl)_{0.801}(CuI)_{0.199}$ (c) $(CuCl)_{0.576}(CuI)_{0.424}$ (d) $(CuCl)_{0.294}(CuI)_{0.706}$ and (e) CuI.

$14.544 \leq E_n$ (eV) ≤ 3.339 (see equation 3.3) in order to avoid the neutron resonances of iodine at 20 eV and 31 eV [112].

Self consistency checks were performed on the data sets ensuring that (i) each measured $F(Q)$ obeys the correct sum-rule given in table 4.3, (ii) the low-r features in $G(r)$ oscillate about the theoretical $G(0)$ limit given in table 4.3 and (iii) the Fourier backtransform of $G(r)$ after the low-r features are set to the theoretical $G(0)$ limit are in good overall agreement with the original $F(Q)$ [113].

The temperature and number density of the molten samples investigated are given in table 4.3. The number density for the CuCl-CuI mixtures at temperature T (in °C) was determined from the measured molar volume V_{M}

of CuCl and CuI [114]:

$$V_M(\mathrm{CuCl})(\mathrm{cm}^3\ \mathrm{mol}^{-1}) = 24.34\left(1 + 2.10 \cdot 10^{-4}T + 3.4 \cdot 10^{-8}T^2\right), \quad (4.3)$$

$$V_M(\mathrm{CuI})(\mathrm{cm}^3\ \mathrm{mol}^{-1}) = 34.71\left(1 + 3.83 \cdot 10^{-4}T - 5.12 \cdot 10^{-8}T^2\right), \quad (4.4)$$

and by the application of Vegard's law which assumes a linear relationship between the molar volume of the alloy $(\mathrm{CuCl})_x(\mathrm{CuI})_{1-x}$ and the concentrations x and $(1-x)$ of the constituents such that

$$V_M((\mathrm{CuCl})_{\mathrm{x}}(\mathrm{CuI})_{1-\mathrm{x}}) = xV_M(\mathrm{CuCl}) + (1-x)V_M(\mathrm{CuI}). \quad (4.5)$$

It is noted that there does exist, for CuCl-CuBr melts, a discrepancy between the measured molar volume and the value calculated from Vegard's law, but this is small at $\lesssim$ 3 % [109].

Table 4.3: Experimental parameters for the $(\mathrm{CuCl})_x(\mathrm{CuI})_{1-x}$ melts studied using neutron diffraction. The temperature T is given together with the atomic number density n_0, theoretical $G(0)$ limits and sum rule value for each sample.

x	T(K)	n_0 (Å^{-3})	$G(0)$ (barn)	Sum rule (barn Å^{-3})
1	733(3)	0.0448(5)	-0.7478(4)	-0.661(7)
0.801	693(3)	0.0411(3)	-0.6757(5)	-0.548(4)
0.576	613(3)	0.0381(3)	-0.5985(7)	-0.450(4)
0.576	873(3)	0.0357(3)	-0.5985(7)	-0.422(4)
0.294	773(3)	0.0342(3)	-0.5085(10)	-0.343(3)
0	933(3)	0.0282(3)	-0.4224(10)	-0.235(3)

4.4 Results

The measured total structure factors $F(Q)$ for the $(\mathrm{CuCl})_x(\mathrm{CuI})_{1-x}$ melts are plotted in figure 4.3. The $F(Q)$ functions for molten CuCl and CuI are in good overall agreement with the previous neutron diffraction results also plotted in figures 4.3 (a) and (f) [103, 106]. Oscillations are visible in the $F(Q)$ functions

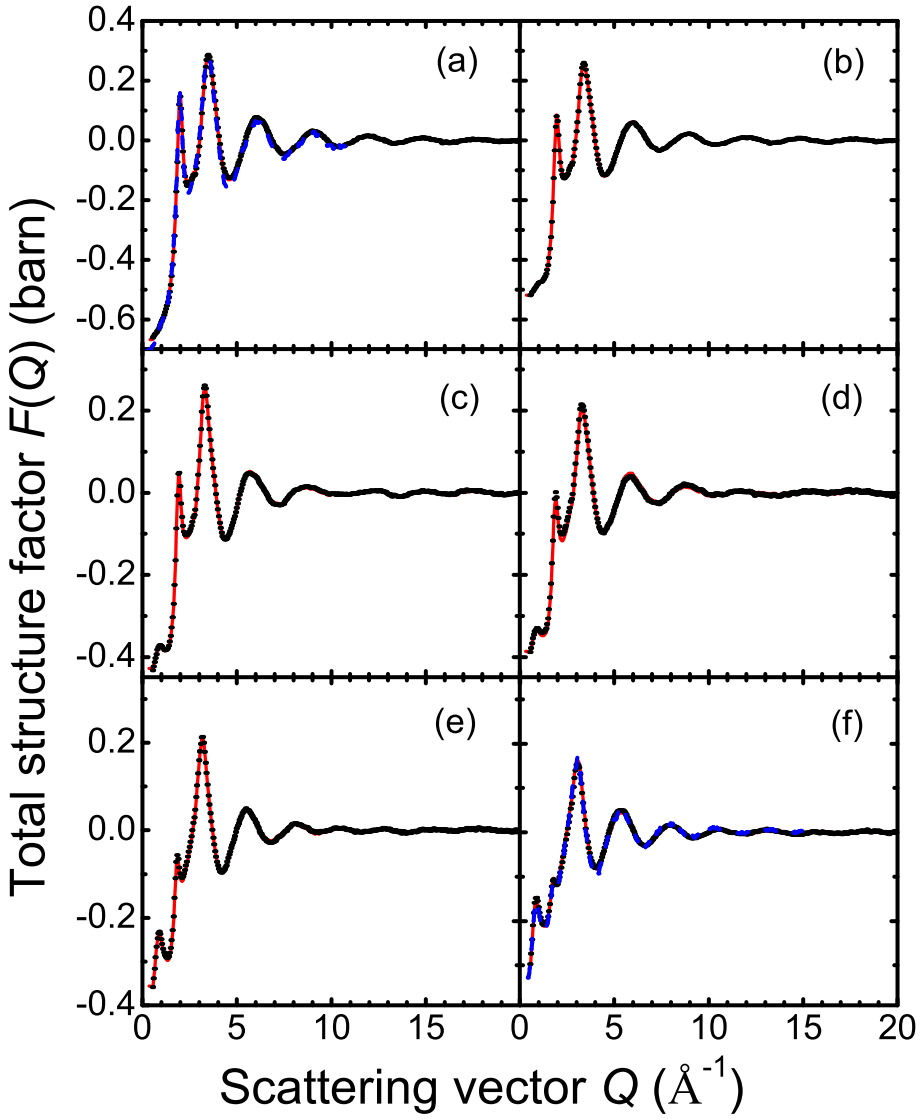

Figure 4.3: The measured total structure factors $F(Q)$ for (a) CuCl at 733 K, (b) $(CuCl)_{0.801}(CuI)_{0.199}$ at 693 K, (c) $(CuCl)_{0.576}(CuI)_{0.424}$ at 613 K, (d) $(CuCl)_{0.576}(CuI)_{0.424}$ at 873 K, (e) $(CuCl)_{0.294}(CuI)_{0.706}$ at 773 K and (f) CuI at 933 K. The bars represent the statistical errors and the solid (red) curves are the Fourier back-transform of the corresponding $G(r)$ functions given in figure 4.4 after the un-physical low-r oscillations are set to their theoretical $G(0)$ limit. The dashed (blue) curve shows the $F(Q)$ function measured for (a) CuCl at 773 K by Eisenberg *et al.* [106] or (f) CuI at 923 K by Takeda *et al.* [103]

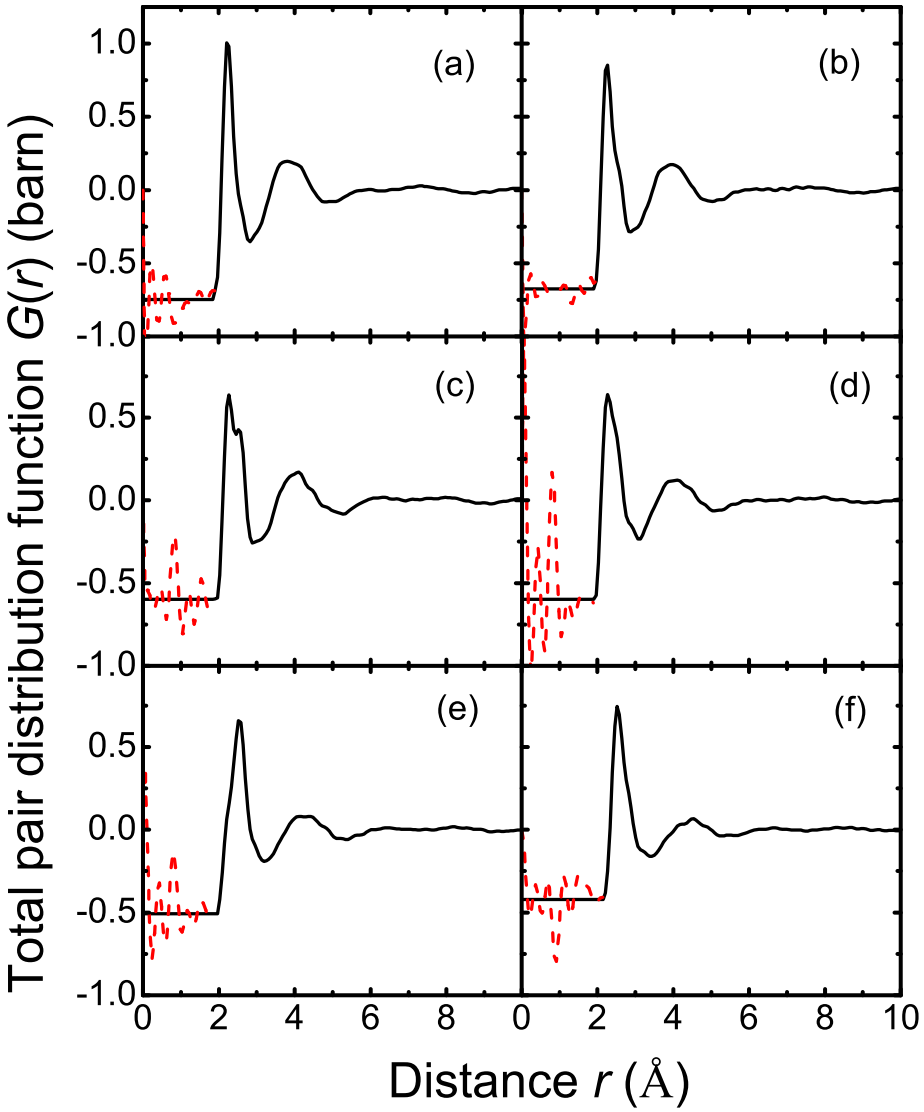

Figure 4.4: The total pair distribution functions $G(r)$ for (a) CuCl at 733 K, (b) $(CuCl)_{0.801}(CuI)_{0.199}$ at 693 K, (c) $(CuCl)_{0.576}(CuI)_{0.424}$ at 613 K, (d) $(CuCl)_{0.576}(CuI)_{0.424}$ at 873 K, (e) $(CuCl)_{0.294}(CuI)_{0.706}$ at 773 K and (f) CuI at 933 K as obtained by Fourier transforming the corresponding $F(Q)$ functions shown in figure 4.3 after making a Harwell spline fit [115] to the data and truncating at $Q_{\max} = 20$ Å^{-1} (a-c) or applying a cosine window function between ≈ 18 and 20 Å^{-1} (d-f). The dashed (red) curves indicate the extent of the un-physical low-r oscillations.

Table 4.4: The leading peak positions in the measured $F(Q)$ and $G(r)$ functions for $(CuCl)_x(CuI)_{1-x}$ melts at temperature T. For CuCl ($x = 1$) there is no FSDP in $F(Q)$ at ≈ 1 Å^{-1}. For CuCl and CuI ($x = 0$) the first physical peak in $G(r)$ is asymmetric but the shoulders at 2.57(2) and 2.84(2) Å, respectively, are not listed.

		$F(Q)$			$G(r)$		
x	T (K)	q_1 (Å^{-1})	q_2 (Å^{-1})	q_3 (Å^{-1})	r_1 (Å)	r_2 (Å)	r_3 (Å)
1	733	-	2.00(2)	3.49(2)	2.23(2)	–	3.80(3)
0.801	693	1.07(2)	1.96(2)	3.39(2)	2.25(2)	2.57(2)	3.95(2)
0.576	613	0.94(2)	1.93(2)	3.30(2)	2.27(2)	2.57(2)	4.09(3)
0.576	873	0.92(2)	1.90(2)	3.27(2)	2.28(2)	2.58(2)	4.10(3)
0.294	773	0.90(2)	1.86(2)	3.18(2)	2.25(2)	2.54(2)	4.14(3)
0	933	0.88(2)	1.79(2)	3.04(2)	–	2.53(2)	4.52(3)

out to 20 Å^{-1}. This is an improvement on the $F(Q)$ obtained previously for molten CuCl by Eisenberg *et al.* [106], measured using a neutron wavelength of 0.696 Å and $Q_{\max} = 17$ Å^{-1}, where structural features were lost beyond ≈ 11.25 Å^{-1} due to poor statistical precision. The total pair-distribution functions $G(r)$ are plotted in figure 4.4 and were obtained by Fourier transforming the corresponding $F(Q)$ after making a Harwell spline fit [115] to the data and applying either a straight forward truncation at 20 Å^{-1} ($x = 1, 0.801, 0.576$ at 613 K) or by applying a smooth cosine window function between ≈ 18 and 20 Å^{-1} ($x = 0, 0.294, 0.576$ at 873 K). The positions of the leading peaks in reciprocal and real space are listed in table 4.4.

The measured $F(Q)$ for molten CuCl exhibits a sharp principal peak at 2.00(2) Å^{-1} which undergoes a progressive reduction in intensity with the exchange of halide ion from Cl^- to I^-. With the exception of CuCl, all of the $F(Q)$ functions exhibit a first sharp diffraction peak (FSDP) at ≈ 1Å^{-1}, indicative of ordering on an intermediate length scale [116], which increases in intensity whilst tending to a lower Q value with increasing I^- concentration. The measured $F(Q)$ for molten CuI exhibits a principal peak at 1.79(2) Å^{-1} and an FSDP at 0.88(2) Å^{-1}. The features in the measured $F(Q)$ functions for the CuCl-CuI mixtures are qualitatively reproduced in figure 4.5 by su-

perposing the $F(Q)$ for pure CuCl at 733 K and CuI at 933 K weighted by the corresponding concentrations x and $(1-x)$ such that the reconstructed total structure factor ${}^{\text{rec}}F(Q) = x^{\text{CuCl}}F(Q) + (1-x)^{\text{CuI}}F(Q)$. A comparison of the partial structure factors $S_{\alpha\beta}(Q)$ for CuCl and CuI, plotted in figures 4.7 and 4.11 respectively, suggests that the FSDP in CuI results from the Cu-Cu correlations.

The measured $G(r)$ functions do not show any distinct structure beyond the second coordination shell. The first peak in $G(r)$ at 2.23(2) Å for molten CuCl arises from the nearest neighbour Cu-Cl correlations, as evident from the partial pair distribution functions $g_{\alpha\beta}(r)$ plotted in figure 4.8. Similarly, the first peak in $G(r)$ at 2.53(2) Å for molten CuI arises from the nearest neighbour Cu-I correlations, as evident from the $g_{\alpha\beta}(r)$ functions plotted in figure 4.12. It is also clear from the $g_{\text{CuCu}}(r)$ partial pair distribution functions that the Cu-Cu correlations penetrate into the first coordination shell accounting for the asymmetry observed on the first peak in $G(r)$ for CuCl and CuI. In the measured $G(r)$ functions for the molten CuCl-CuI mixtures, a shoulder appears on the nearest neighbour peak. This shoulder at ≈ 2.5 Å results from the introduction of nearest neighbour Cu-I correlations and increases in intensity as the halide ion is exchanged from Cl^- to I^-. The $x = 0.576$ mixture was measured at two different temperatures and the nearest neighbour Cu-Cl and Cu-I correlations are resolved in the $G(r)$ function at 613 K, as shown in figure 4.4 (c). However, as shown in figure 4.4 (d), the resolution of the two peaks is lost after increasing the temperature to 873 K. The nearest neighbour peak in $G(r)$ shifts to larger r and reduces in intensity with increasing I^- concentration, consistent with an increase in the mean anion radius and a reduction in the mean anion coherent scattering length. The observed features in the measured $G(r)$ functions for the CuCl-CuI mixtures are also qualitatively reproduced by superposing the $G(r)$ functions of the pure CuCl and CuI components, as shown in figure 4.6.

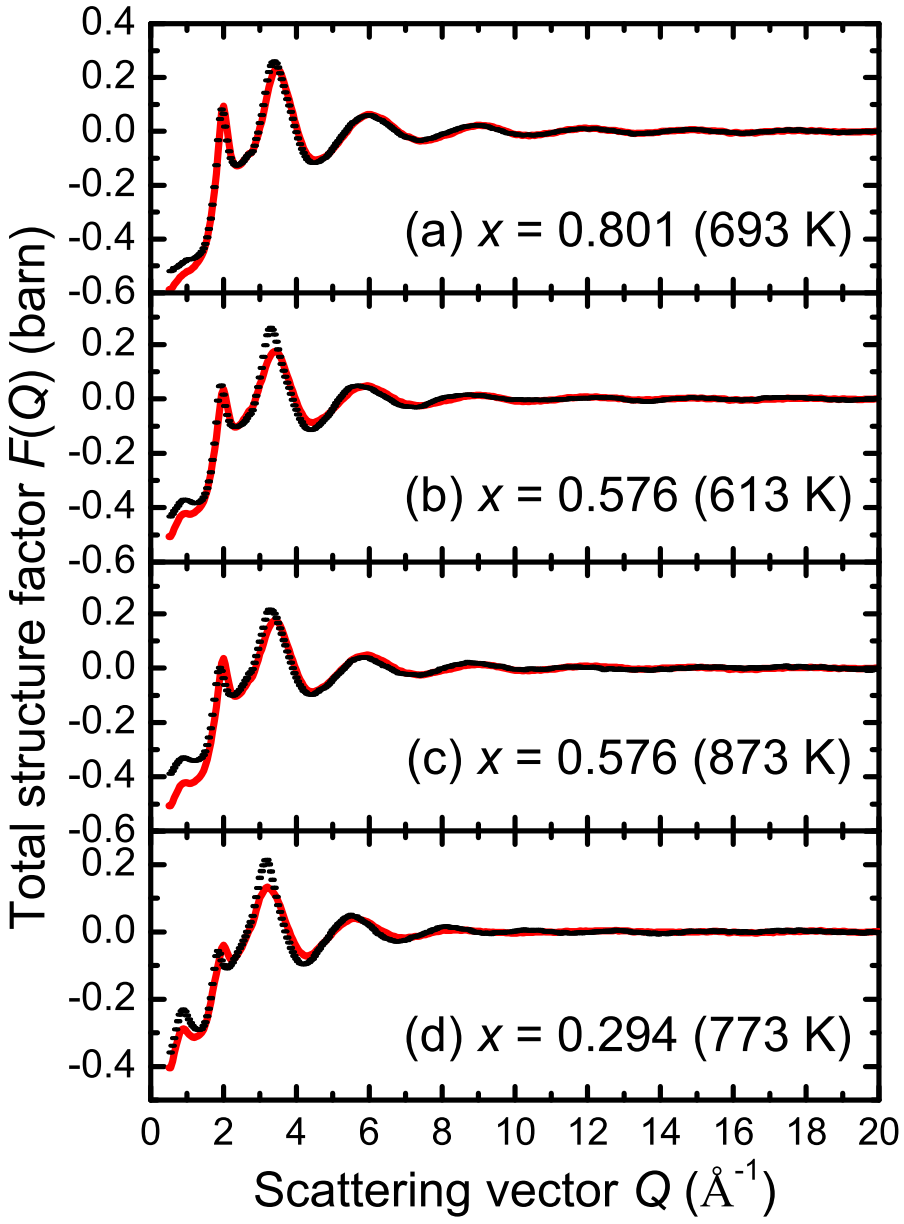

Figure 4.5: The total structure factors $F(Q)$ for the $(CuCl)_x(CuI)_{1-x}$ melts given in figure 4.3 (error bars), where (a) $x = 0.801$ at 693 K, (b) $x = 0.576$ at 613 K, (c) $x = 0.576$ at 873 K, and (d) $x = 0.294$ at 773 K, compared to their reconstruction ${}^{\mathrm{rec}}F(Q)$ (solid red curves) from the measured ${}^{\mathrm{CuCl}}F(Q)$ for CuCl at 733 K and ${}^{\mathrm{CuI}}F(Q)$ for CuI at 933 K, where ${}^{\mathrm{rec}}F(Q) = x\,{}^{\mathrm{CuCl}}F(Q) + (1-x)\,{}^{\mathrm{CuI}}F(Q)$.

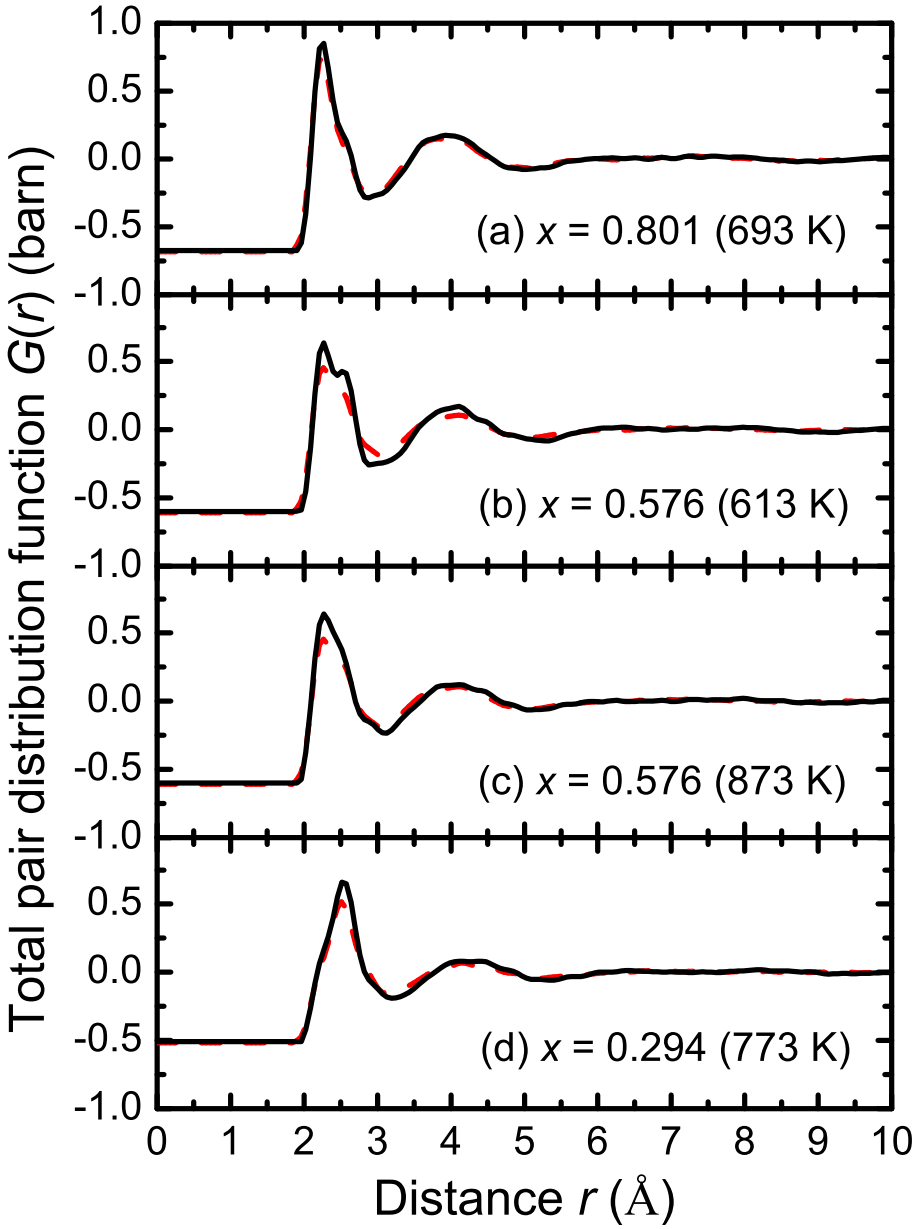

Figure 4.6: The total pair distribution functions $G(r)$ for the $(CuCl)_x(CuI)_{1-x}$ mixtures given in figure 4.4 (solid black curves), where (a) $x = 0.801$ at 693 K, (b) $x = 0.576$ at 613 K, (c) $x = 0.576$ at 873 K, and (d) $x = 0.294$ at 773 K, compared to their reconstruction ${}^{\text{rec}}G(r)$ (dashed red curves) from the measured ${}^{\text{CuCl}}G(r)$ for CuCl at 733 K and ${}^{\text{CuI}}G(r)$ for CuI at 933 K, where ${}^{\text{rec}}G(r) = x{}^{\text{CuCl}}G(r) + (1-x){}^{\text{CuI}}G(r)$.

4.5 Discussion

4.5.1 The structure of molten CuCl

The partial pair distribution functions $g_{\alpha\beta}(r)$ for molten CuCl at 773 K from Eisenberg *et al.* [106] are plotted in figure 4.8. These functions were obtained by Fourier transforming the partial structure factors $S_{\alpha\beta}(Q)$, from Eisenberg *et al.* [106] plotted in figure 4.7, after they had been multiplied by a Bartlett modification function $M(Q) = 1 - (|Q|/Q_{\max})$ for $|Q| \leq Q_{\max}$, $M(Q) = 0$ for $|Q| > Q_{\max}$ with a low $Q_{\max}$ value of 9.73 Å^{-1} chosen to coincide with a node of the $S_{\alpha\beta}(Q)$ functions [106]. The $g_{\alpha\beta}(r)$ functions obtained by McGreevy and Pusztai [117] are also plotted, where the RMC method was used to deduce these functions from the $F(Q)$ obtained by Eisenberg *et al.* [106]. Although the measured $F(Q)$ for CuCl at 733 K is in good overall agreement with the $F(Q)$ obtained from Eisenberg *et al.* [106] (see figure 4.9 (a)), it is clear, by comparison of the measured $G(r)$ for CuCl at 733 K and the $G(r)$ functions derived by applying equation 4.2 to the Eisenberg *et al.* [106] and McGreevy and Pusztai [117] $g_{\alpha\beta}(r)$ functions, that the application of the Bartlett modification function leads to a relative broadening in the nearest neighbour peak (see figure 4.10 (a)). However, despite the discrepancies between the Eisenberg *et al.* [106] and McGreevy and Pusztai [117] $g_{\alpha\beta}(r)$ functions, both results show that molten CuCl is characterised by a relatively featureless $g_{\text{CuCu}}(r)$ function that penetrates deeply into the first peak arising from the nearest neighbour Cu-Cl correlations. In the β-phase of CuCl the Cu^+ ions are highly mobile and occupy tetrahedral holes in an hcp sublattice of chloride ions [67]. In the liquid, the Cu-Cl coordination number $\bar{n}_{\text{Cu}}^{\text{Cl}} = 3.0(7) - 3.4$ [83, 106] with a large degree of first shell penetration by Cu-Cu correlations (see figure 4.8).

It was evident from the early work of Page and Mika [78] that the structure of liquid CuCl was not typical of other molten salts, for example the structure of NaCl subsequently measured by Edwards *et al.* [118] and revised by Biggin and Enderby [119], for which the anion-anion and cation-cation partial structure factors are similar. The structure does, however, resemble that of molten

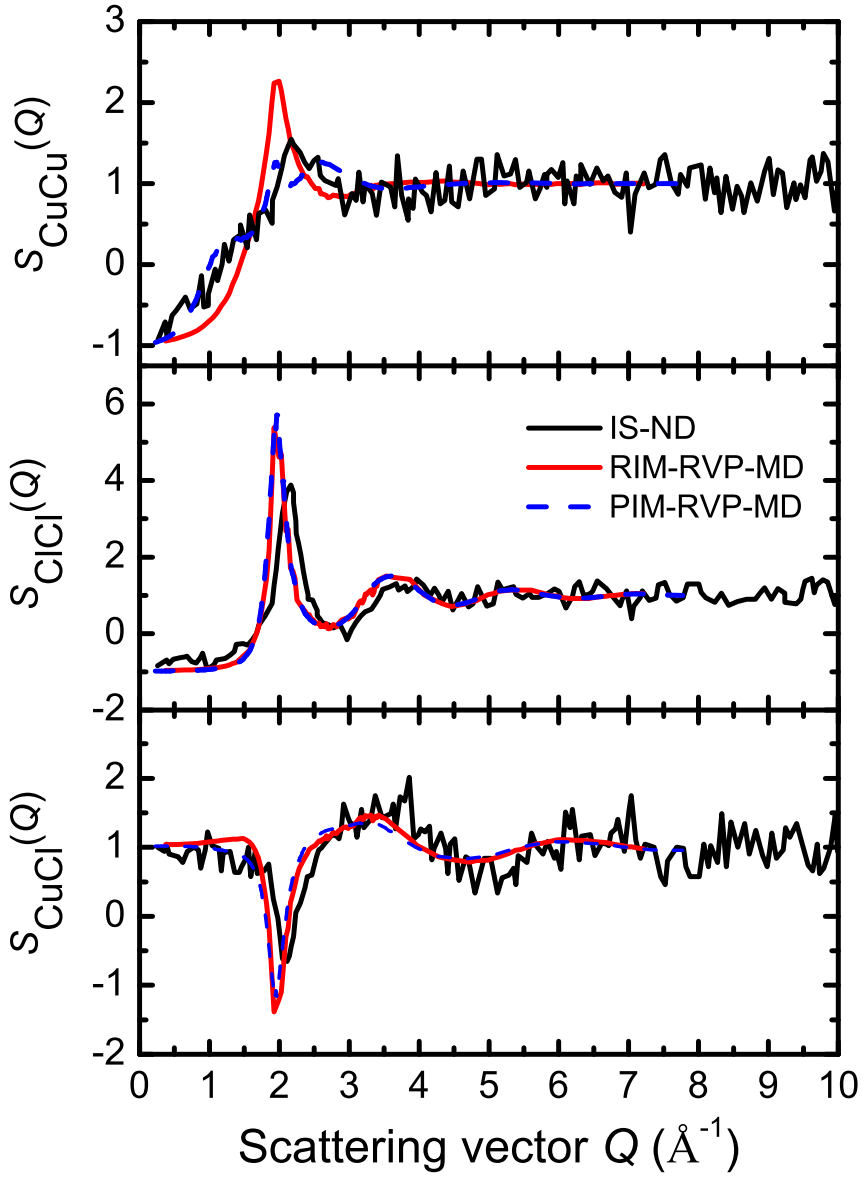

Figure 4.7: The partial structure factors $S_{\alpha\beta}(Q)$ for molten CuCl obtained from isotopic substitution in neutron diffraction (IS-ND) by Eisenberg *et al.* [106] (solid black curves) and from Molecular Dynamics simulations with Rahman-Vashishta-Parrinello effective pair potentials (RVP-MD) by Trullàs [91] using rigid ion model (RIM-RVP-MD) (solid red curves) and polarisable ion model (PIM-RVP-MD) (dashed blue curves) potentials.

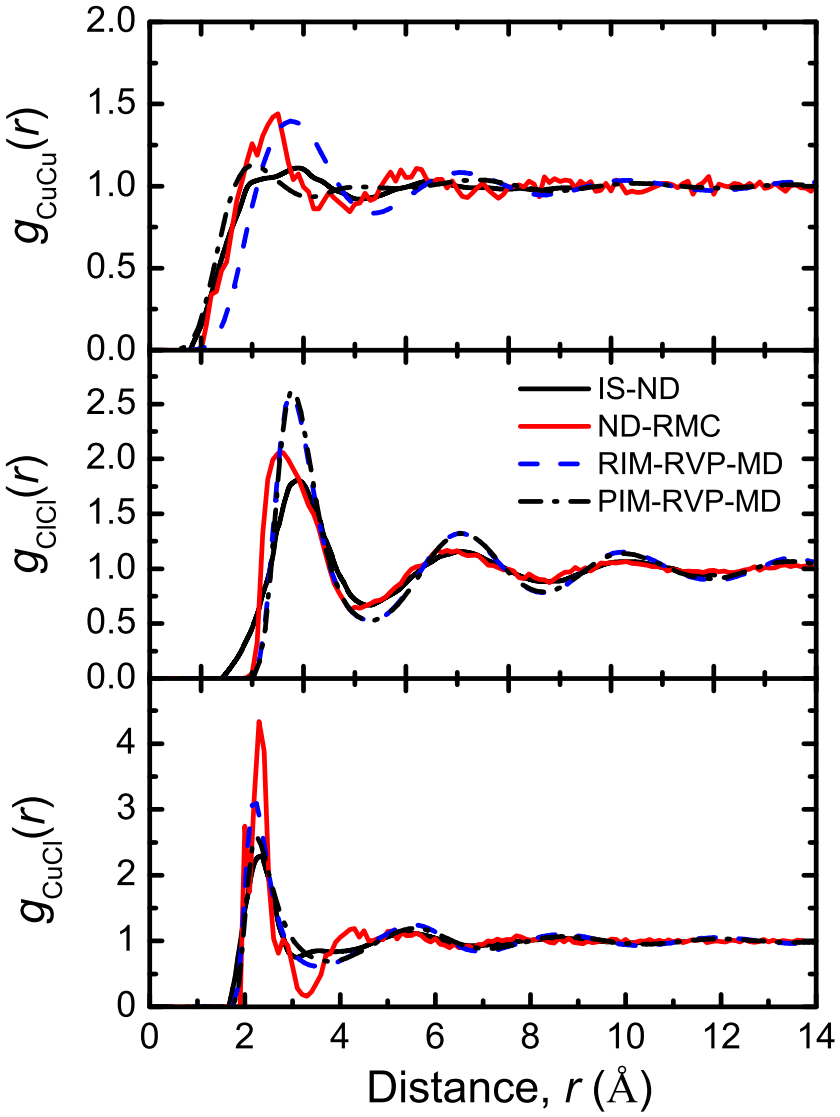

Figure 4.8: The partial pair distribution functions $g_{\alpha\beta}(r)$ for molten CuCl obtained from isotopic substitution in neutron diffraction (IS-ND) by Eisenberg *et al.* [106] (solid black curves), from a Reverse Monte Carlo fit to the neutron diffraction $F(Q)$ [106] (ND-RMC) by McGreevy and Pusztai [117] (solid red curve) and from Molecular Dynamics simulations with Rahman-Vashishta-Parrinello effective pair potentials (RVP-MD) by Trullàs [91] using rigid ion model (RIM-RVP-MD) (dashed blue curve) and polarisable ion model (PIM-RVP-MD) (chained black curve) potentials.

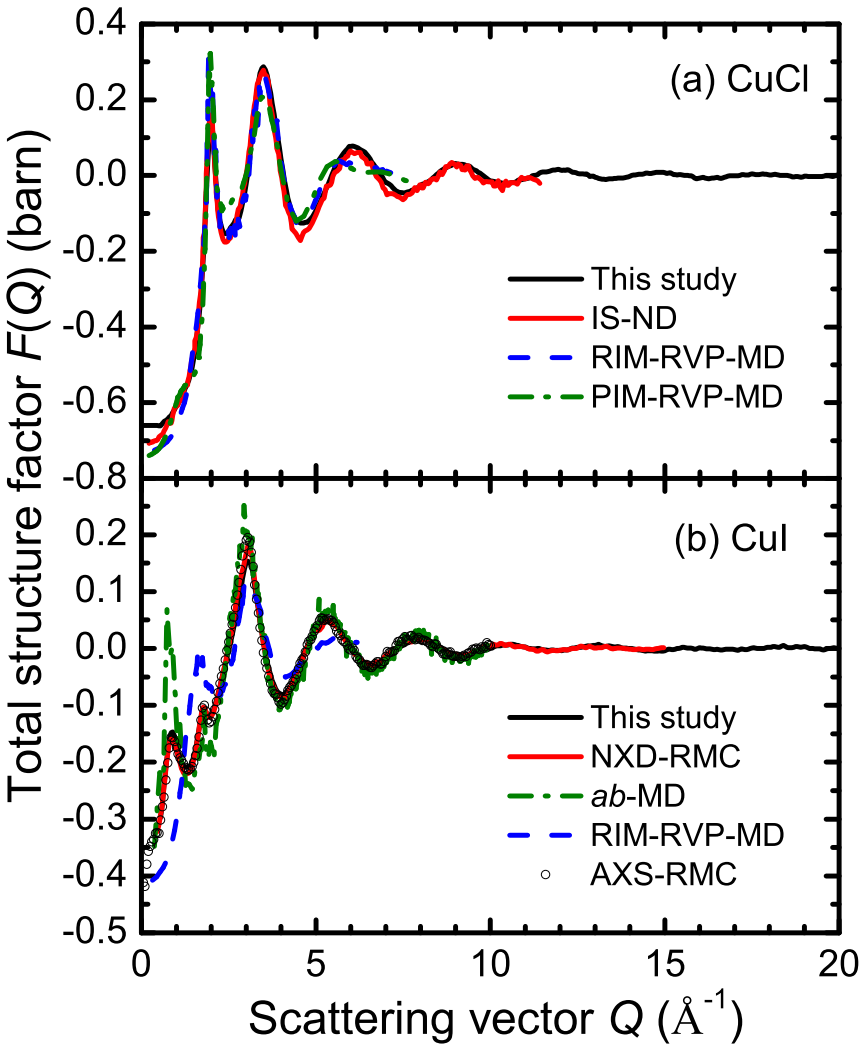

Figure 4.9: The weighted sum of the $S_{\alpha\beta}(Q)$ functions, using equation 4.1, obtained for (a) CuCl (see figure 4.7) and (b) CuI (see figure 4.11), using isotopic substitution in neutron diffraction (IS-ND) [106], Molecular Dynamics simulations with Rahman-Vashishta-Parrinello effective pair potentials (RVP-MD) using rigid ion model (RIM-RVP-MD) or polarisable ion model (PIM-RVP-MD) potentials [91], neutron and x-ray diffraction with RMC (NXD-RMC) [103], *ab initio* Molecular Dynamics (*ab*-MD) [101] or anomalous x-ray scattering with RMC (AXS-RMC) [99]. The corresponding total structure factors $F(Q)$ measured in the present study for CuCl and CuI are plotted for comparison (black curves).

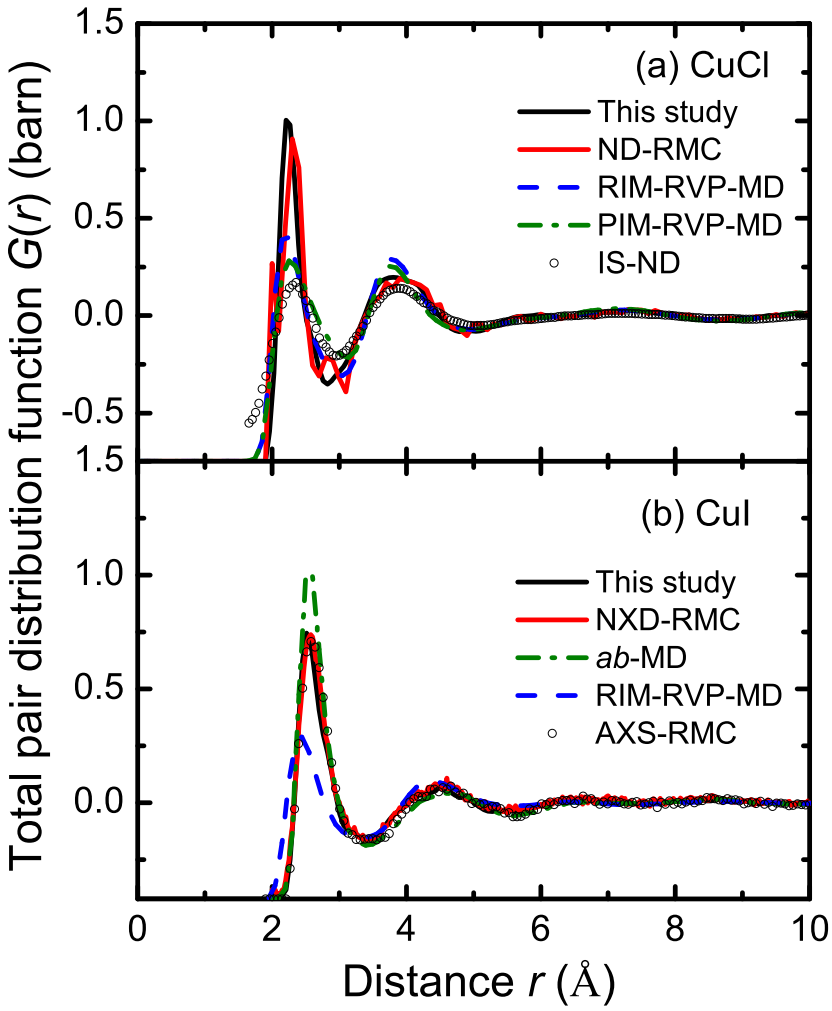

Figure 4.10: The weighted sum of the $g_{\alpha\beta}(r)$ functions, using equation 4.2, obtained for (a) CuCl (see figure 4.8) and (b) CuI as (see figure 4.12), using isotopic substitution in neutron diffraction (IS-ND) [106], neutron diffraction with RMC [117], Molecular Dynamics simulations with Rahman-Vashishta-Parrinello effective pair potentials (RVP-MD) using rigid ion model (RIM-RVP-MD) or polarisable ion model (PIM-RVP-MD) potentials [91], neutron and x-ray diffraction with RMC (NXD-RMC) [103], *ab initio* Molecular Dynamics (*ab*-MD) [101] or anomalous x-ray scattering with RMC (AXS-RMC) [99]. The corresponding total pair distribution functions $G(r)$ measured in the present study for CuCl and CuI are plotted for comparison (black curves).

LiCl [117, 120] in which the Li^+ radius of 0.59 Å is comparable to the Cu^+ radius of 0.60 Å [121] (for 4-fold coordination). Page and Mika [78] could not explain the observed differences between the Cu-Cu and Cl-Cl partial structure factors by considering a purely ionic system and instead proposed a partially covalent bonding scheme whereby several Cl^- ions can associate with one Cu^+ ion in the form $(CuCl_n)^{[n-1]-}$ leading to an excess of Cu^+ ions. These excess ions effectively form a plasma, accounting for the lack of structure in the $g_{CuCu}(r)$ partial pair distribution function.

An entirely molecular interpretation of the structure of molten CuCl was proposed by Powles [79] in which the liquid comprises covalently bonded diatomic units of CuCl with dissociating Cu^+ ions. Similar work by Bhatia and Ratti [81] suggest the formation of $CuCl_2$ units. However, Gillan [80] criticised Powles approach for failing to consider the effect of orientational correlations between the molecules. Gillan showed that taking these correlations into account has a substantial effect on the Cu-Cl and Cu-Cu pair distribution functions. Moreover, this molecular model is inconsistent with the coordination number $\bar{n}_{Cu}^{Cl} = 3.0(7)$ subsequently measured by Eisenberg *et al.* [106]. It also conflicts with the measured physical properties of liquid CuCl, including the high ionic conductivity of the liquid ($\approx$ 1 Ω^{-1} cm^{-1}), and the relatively long nuclear magnetic resonance relaxation time [82, 83] which are indicative of an ionic system. Nevertheless, there are several properties of molten CuCl that point to only a partially ionic system including its molar volume, entropy change on fusion, viscosity and self-diffusion coefficient [78, 106]. A covalent bonding character is also suggested by the discrepancy between the sum of the ionic radii of Cu^+ at 0.6 Å and Cl^- at 1.81 Å and the measured nearest neighbour distance of 2.23(2) Å.

Ginoza *et al.* [84] suggest that the structural features observed in CuCl are typical of systems that melt from the superionic phase. In fact, the full set of partial structure factors for molten CuBr was determined by Allen and Howe [122] in 1992 using isotopic substitution in neutron diffraction and the results showed very similar structural features to CuCl, namely (i) featureless Cu-Cu

pair correlation functions in both Q- and r-space, (ii) considerable asymmetry between the Cu-Cu and Br-Br pair distribution functions and (iii) a large degree of first-shell penetration by the copper ions. In order to fully understand and successfully model the structure of molten CuCl and other CuX systems, it is suggested that proper attention should be given to the structure of the solid prior to melting [84]. For example, the mobility of the cations in the superionic phase of the copper halides is enhanced by the ability of the cations to form mixed ionic-covalent bonds at each intermediate position in their diffusion pathway [60, 61, 63]. If retained in the molten phase, this mechanism would explain the partial covalent nature observed in molten CuCl. The diffuse Cu-Cu partial structure factor, small entropy of fusion and comparable conductivity of molten CuCl in relation to the other molten alkali halides can also be understood if the molten structure retains a memory of the structure from the β-phase.

Many of the contemporary models for CuCl and other CuX systems [85–91, 123] use molecular dynamics simulations with Rahman-Vashishta-Parrinello [124, 125] effective pair potentials (RVP-MD). The $S_{\alpha\beta}(Q)$ and $g_{\alpha\beta}(r)$ functions for molten CuCl at 773 K obtained by Trullàs [91] using the standard rigid ion model RVP potentials (RIM-RVP-MD) and a polarisable ion model interaction scheme (PIM-RVP-MD) are plotted in figures 4.7 and 4.8. In PIM-RVP-MD, non-integer effective charges are used on the ions to mimic the effect of the 'covalent' interactions. The weighted sum of the RVP-MD $S_{\alpha\beta}(Q)$ and $g_{\alpha\beta}(r)$ functions, according to equations 4.1 and 4.2, are plotted in figures 4.9 (a) and 4.10 (a), respectively. The RVP-MD results are in good overall agreement with the $S_{\alpha\beta}(Q)$ functions obtained by Eisenberg *et al.* [106], (although the latter appear shifted to higher Q by $\approx$ 0.2 Å^{-1}). However, it appears that the PIM result is in better agreement with the $S_{\mathrm{CuCu}}(Q)$ partial from Eisenberg *et al.* [106] exhibiting less structure than the RIM result and suggesting that polarisation effects are an important consideration when modelling these systems.

4.5.2 The structure of molten CuI

The RMC method has been applied to the diffraction patterns of molten CuI, measured by Waseda *et al.* [99] using anomalous x-ray scattering at 940 K and by Takeda *et al.* [103] using a combination of neutron and x-ray diffraction at 923 K, where the resulting partial structure factors $S_{\alpha\beta}(Q)$ and corresponding partial pair distribution functions $g_{\alpha\beta}(r)$ are plotted in figures 4.11 and 4.12 respectively. The short range part of $g_{\mathrm{CuI}}(r)$ and $g_{\mathrm{CuCu}}(r)$ obtained by Trapananti *et al.* [100] using x-ray absorption spectroscopy at 903 K are also plotted. The weighted sum of the $S_{\alpha\beta}(Q)$ and $g_{\alpha\beta}(r)$ functions according to equations 4.1 and 4.2 are shown in figures 4.9 (b) and 4.10 (b), respectively. The results of the Waseda *et al.* [99] and Takeda *et al.* [103] accurately reproduce the measured $F(Q)$ and $G(r)$ functions for CuI measured at 933 K. CuI shows several of the structural characteristics found for molten CuCl (see figure 4.8) and CuBr [99, 122, 126, 127], namely a relatively featureless $g_{\mathrm{CuCu}}(r)$ function that penetrates deeply into the Cu-X nearest neighbour correlations. In the superionic α-phase of CuI the Cu^+ ions are highly mobile and occupy tetrahedral sites in an fcc iodine sublattice [128]. In the liquid the coordination number $\bar{n}^{\mathrm{I}}_{\mathrm{Cu}} \simeq 2.7$ [104]. The discrepancy between the nearest neighbour Cu-I distance of 2.53(2) Å and the sum of the ionic radii of Cu^+ at 0.6 Å and I^- at 2.20 Å [121] is larger for CuI than for CuCl. This is supported by the smaller ionicity f_i of 0.692 for CuI compared to 0.746 for CuCl, according to the Philips electronegativity scale [129]. It is argued that compounds with f_i greater than 0.785 do not exhibit superionic behaviour, since the cation is constrained near the anions due to strong Coulombic attraction, resulting in zero diffusion [130].

In figure 4.13 a comparison is made between the $g_{\alpha\beta}(r)$ functions from Chahid and McGreevy [131], obtained by applying the RMC method to neutron diffraction patterns for the superionic α-phase of CuI at 713 K, and from Takeda *et al.* [103] for the molten phase of CuI at 923 K. The measured $G(r)$ function for molten CuI at 933 K is also plotted in comparison to the $G(r)$ deduced from the weighted sum of the $g_{\alpha\beta}(r)$ functions of Chahid and Mc-

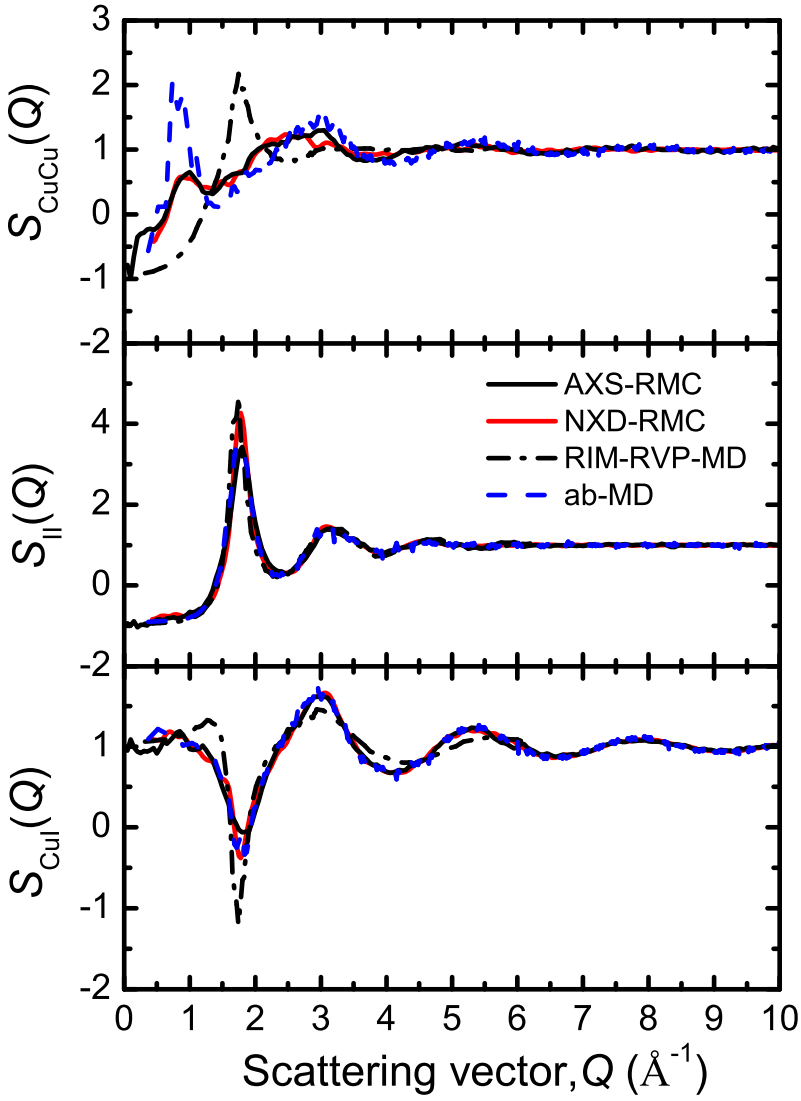

Figure 4.11: The partial structure factors $S_{\alpha\beta}(Q)$ for molten CuI obtained from anomalous x-ray scattering at 940 K with RMC (AXS-RMC) by Waseda *et al.* [99] (solid black curve), neutron and x-ray diffraction at 923 K with RMC (NXD-RMC) by Takeda *et al.* [103] (solid red curve), Rahman-Vashista-Parrinello Molecular Dynamics at 938 K using rigid ion model (RIM-RVP-MD) potentials by Trullàs [91] (chained black curve) and *ab initio* Molecular Dynamics (*ab*-MD) at 900 K by Shimojo *et al.* [101] (dashed blue curve).

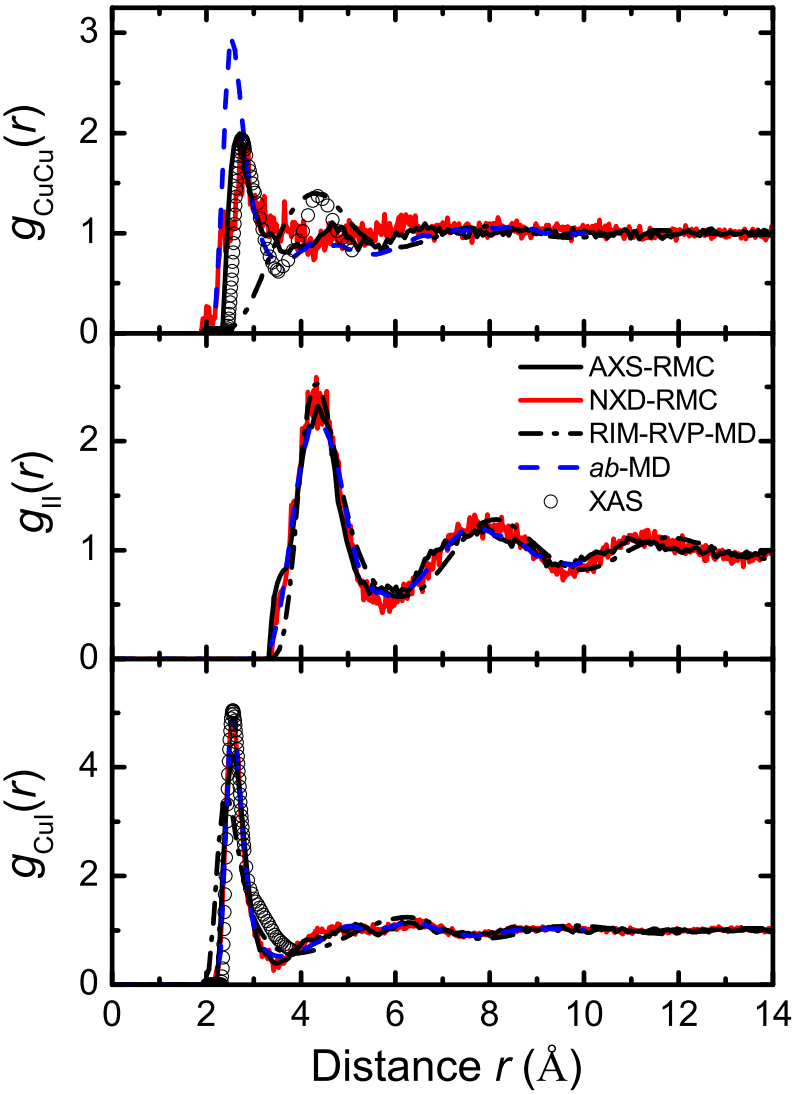

Figure 4.12: The partial pair distribution functions $g_{\alpha\beta}(r)$ for molten CuI obtained from anomalous x-ray scattering at 940 K with RMC (AXS-RMC) by Waseda *et al.* [99] (solid black curve), neutron and x-ray diffraction at 923 K with RMC (NXD-RMC) by Takeda *et al.* [103] (solid red curve), Rahman-Vashishta-Parrinello Molecular Dynamics at 938 K using rigid ion model (RIM-RVP-MD) potentials by Trullàs [91] (chained black curve), *ab initio* Molecular Dynamics (*ab*-MD) at 900 K by Shimojo *et al.* [101] (dashed blue curve) and x-ray absorption spectroscopy (XAS) at 903 K by Trapananti *et al.* [100] (black open circles).

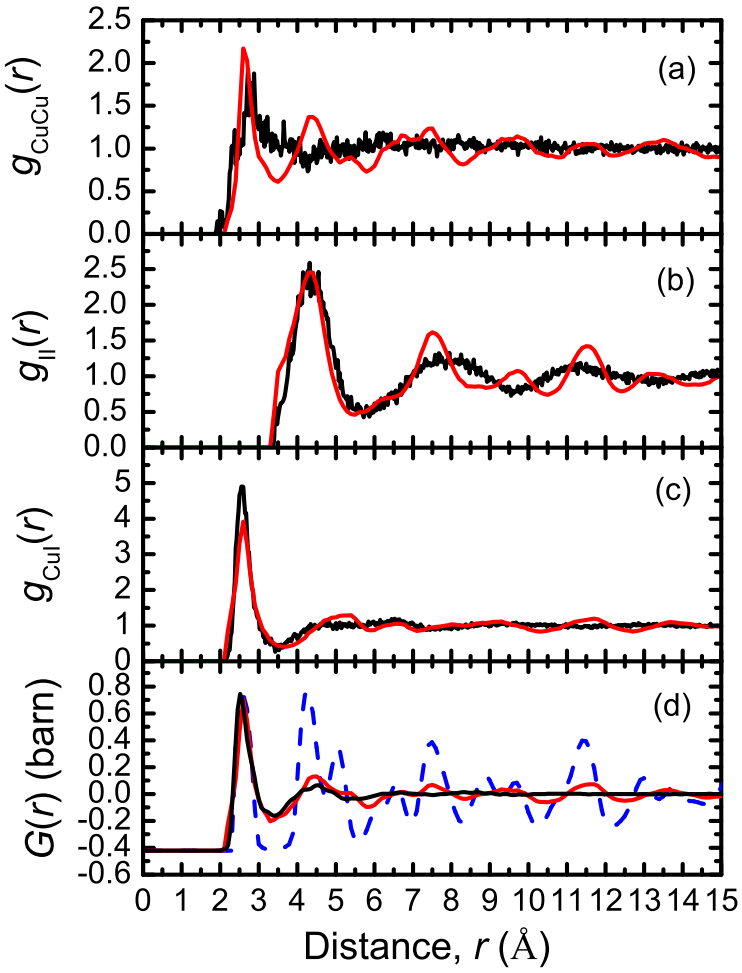

Figure 4.13: Comparison between the solid and molten structures of CuI. (a) - (c) The partial pair distribution functions $g_{\alpha\beta}(r)$ for the melt at 923 K (solid black curve), as obtained from an RMC analysis of neutron and x-ray diffraction data by Takeda *et al.* [103], compared to the superionic α-phase at 713 K (solid red curve), as obtained from an RMC analysis of neutron diffraction data by Chahid and McGreevy [131]. (d) The measured total pair distribution function $G(r)$ for the melt at 933 K from figure 4.4 (a) (solid black curve) compared to the weighted sum of the $g_{\alpha\beta}(r)$ partial pair distribution functions, using equation 4.2, for the superionic α-phase at 713 K (solid red curve) in (a) - (c) and the weighted sum of the $g_{\alpha\beta}(r)$ partial pair distribution functions, using equation 4.2, for the zinc-blende phase at 298 K (dashed blue curve) given by Chahid and McGreevy [131].

Greevy [131], using equation 4.2, for the crystalline zinc-blende phase of CuI at 298 K and the superionic α-phase of CuI at 713 K. A remarkable similarity is observed between the local structure of the liquid and solid superionic phase. This reflects the assertion made by Ginoza *et al.* [84] and the measured structure of other superionic systems and their melts, for example AgI [132], CuBr [122, 127], Ag_2Se [133] and Ag_2Te [134], suggesting that the structure of the melt does indeed retain a memory of the structure of the solid superionic phase i.e. liquid like correlations are present in the high temperature phases of these materials. In the present work, the diffuse Cu-Cu partial pair distribution function in the molten CuX system can be attributed to the high mobility of the Cu^+ ions through the interstitial sites of the X^- sublattice, as in the superionic solid-phase.

As for CuCl, RVP-MD simulations have also been performed on the solid and liquid phases of CuI using non integer ionic charges to take into account the partially covalent character of the bonding [85–87, 89–91, 123, 130, 135–139]. Recently, *ab initio* molecular dynamics (*ab*-MD) simulations have been employed to model the superionic and liquid phases of CuI [101, 105, 140]. The partial structure factors $S_{\alpha\beta}(Q)$ and partial pair distribution functions $g_{\alpha\beta}(r)$ for molten CuI, deduced by Trullàs [91] at 938 K using RIM-RVP-MD simulations and at 903 K using *ab*-MD simulations by Shimojo *et al.* [101], are plotted for comparison with the experimentally derived functions in figures 4.11 and 4.12. The results obtained from the RVP-MD simulations do not reproduce the measured structure of molten CuI or the superionic α-phase [100, 131, 136]. For example, they do not reproduce the measured FSDP at 0.88(2) Å^{-1} in the $F(Q)$ or $S_{\text{CuCu}}(Q)$ functions. Conversely, the *ab initio* calculations do predict the general features in these functions, however, the FSDP is too large and the $g_{\text{CuCu}}(r)$ partial pair distribution function is not precisely reproduced showing greater structure (see figures 4.9 (b) and 4.10 (b)). The authors attribute these discrepancies to (i) the cubic supercell (144 atoms: 72Cu + 72I) used being of insufficient size to accurately reproduce the collective motion of atoms, or (ii) an incorrect interatomic interaction resulting from the generalised gradient

approximation used in the density functional theory [105].

The *ab*-MD simulations of Shimojo and Aniya [140] for the superionic α-phase of CuI indicate a time evolution of the Cu-I bonding interactions as the Cu^+ ions diffuse through the I^- sublattice, as illustrated in figure 4.14. The *ab*-MD simulations for molten CuI by Shimojo *et al.* [101] show almost no covalent character for the I-I interactions but a partial covalent character for both the Cu-I and the Cu-Cu interactions [101, 105], which accounts for the anomalously short Cu-Cu distance. The inadequacy of an effective pair potential approach is therefore partly due to a failure to properly account for the covalent character of the bonding in CuI.

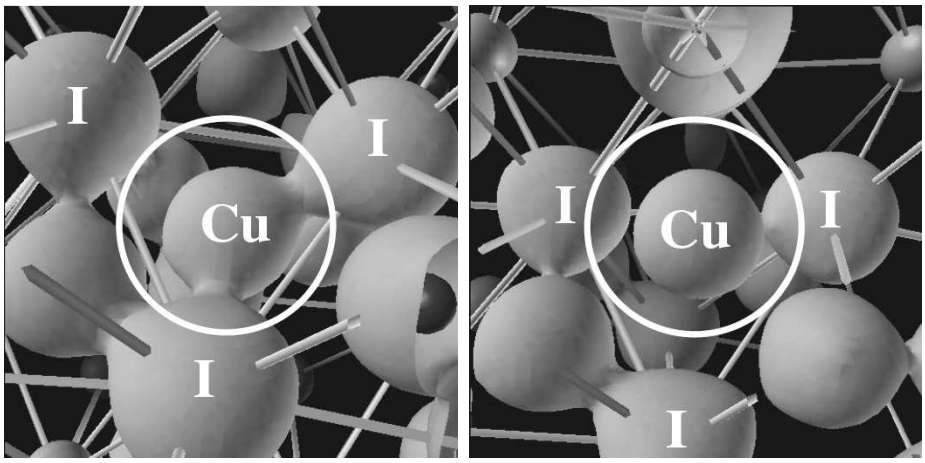

(a) (b)

Figure 4.14: The isosurface of electron density at 0.022 a.u. around the Cu^+ ion in α-CuI. The Cu^+ ions may occupy either (a) tetrahedral sites or (b) octahedral sites. Although the Cu^+ ions prefer to occupy the tetrahedral sites, they must pass through an octahedral site along their diffusion pathway between tetrahedral sites. [140].

4.5.3 The structure of molten CuCl-CuI mixtures

As shown in figures 4.5 and 4.6 the structure of the $(CuCl)_x(CuI)_{1-x}$ melts can be qualitatively reproduced by a superposition of either the $F(Q)$ or $G(r)$ functions of the pure components. However, despite this qualitative agreement, caution is needed in interpreting the mixtures in this way since no account is taken for the effects of mixing on the liquid structure and although the Cu-X partial structure factors have the correct weighting, the X-X correlations are given an incorrect weighting.

In order to successfully model the structure of molten CuCl-CuI mixtures it is first necessary to improve existing models for the pure components. As shown in the case of CuCl, one approach is to use the polarisable ion model where induced dipole polarisation effects are added to the rigid ion model RVP pair potentials. However, this approach may not take into account the covalent character of bonding in the CuI system, as indicated by the *ab*-MD simulation results of Shimojo *et al.* [101, 105, 140] which shows the co-existence of both ionic and covalent bonding in the crystalline α (figure 4.14) and molten phases of CuI. However, as figures 4.11 and 4.12 show, even the *ab*-MD results do not entirely reproduce the structure of CuI as obtained by experimental methods.

4.6 Conclusions

The structure of molten CuCl, CuI and $(CuCl)_x(CuI)_{1-x}$ $(0 \leq x \leq 1)$ mixtures was investigated at the total structure level by using neutron diffraction. The results for CuCl show that the $g_{\alpha\beta}(r)$ functions reported by Eisenberg *et al.* [106] are artificially broadened, consistent with the use by these authors of a modification function with a small $Q_{\max}$ value. The measured $G(r)$ function for CuI at 933 K shows structural features very similar to those found in the superionic α-phase. This characteristic is common to other compounds which melt from a superionic phase.

The results show that the RIM-RVP effective potentials do not reproduce the structure of molten CuI, although they do produce a better representation

of the structure in CuCl with improved agreement still if polarisation effects are included. In order to make a realistic attempt at accounting for the structure of the CuCl-CuI system, the existing models for CuCl and CuI must be improved. The results of *ab initio* molecular dynamics simulations for CuI do provide better agreement with the experimental results although this method still does not sufficiently reproduce the Cu-Cu correlations.

Further experimental measurements are required to obtain accurate partial structure factors for both molten CuI and the CuCl-CuI mixtures. This could be achieved by employing the method of isotopic substitution in neutron diffraction, to obtain the full set of partial structure factors in CuI and the Cu-Cu partial structure factor in the ternary CuCl-CuI system.

5. Structure of La/Ce-Ge-Ga-S glasses by the method of isomorphic substitution in neutron diffraction

5.1 Introduction

Glasses containing luminescent rare earth ions are frequently used in modern technology, particularly in optoelectronics as fibre amplifiers and solid-state lasers [141]. The development of novel glass hosts to increase the effectiveness and capability of optoelectronic systems is an area of current research that is receiving much attention (see Ref. [142] for a recent review). Specifically, chalcogenide glasses are promising hosts for rare earth ions and for use as infra-red transmitting and luminescent materials [143–145]. The experimental determination of the structure of rare earth chalcogenide glasses is therefore of significant technological and scientific interest and will assist, for example, the development of structural models that can aid the engineering of these materials with specific functional properties for use in optoelectronic devices. The main objectives of this investigation are to provide new insight into (i) the structural transformations that enhance rare earth solubility when Ga is incorporated into Ge-S/Se glasses, (ii) the effect on the glass structure of incorporating either small or large rare earth ions, and (iii) the effect on the

glass structure of exchanging the chalcogen from S to Se.

The general properties of rare earth ions and their incorporation into chalcogenide glasses are discussed below. The remainder of the chapter reports on an experimental study using neutron diffraction to investigate the structure of La/Ce-Ge-Ga-S glasses. Further experimental studies on La/Ce-Ge-Ga-Se glasses using neutron diffraction and Y/Ho-Ge-Ga-Se glasses using high energy x-ray diffraction are reported in chapters 6 and 7, respectively.

5.1.1 Rare earth isomorphism

Table 5.1: The electronic configurations for the lanthanoid elements [146].

	K	L		M			N				O				P			
Element	1	2		3			4				5				6			
	s	s	p	s	p	d	s	p	d	f	s	p	d	f	s	p	d	f
^{57}La	2	2	6	2	6	10	2	6	10	..	2	6	1	..	2	..	..	..
^{58}Ce	2	2	6	2	6	10	2	6	10	2*	2	6	..	..	2	..	..	..
^{59}Pr	2	2	6	2	6	10	2	6	10	3	2	6	..	..	2	..	..	..
^{60}Nd	2	2	6	2	6	10	2	6	10	4	2	6	..	..	2	..	..	..
^{61}Pm	2	2	6	2	6	10	2	6	10	5	2	6	..	..	2	..	..	..
^{62}Sm	2	2	6	2	6	10	2	6	10	6	2	6	..	..	2	..	..	..
^{63}Eu	2	2	6	2	6	10	2	6	10	7	2	6	..	..	2	..	..	..
^{64}Gd	2	2	6	2	6	10	2	6	10	7	2	6	1	..	2	..	..	..
^{65}Tb	2	2	6	2	6	10	2	6	10	9*	2	6	..	..	2	..	..	..
^{66}Dy	2	2	6	2	6	10	2	6	10	10	2	6	..	..	2	..	..	..
^{67}Ho	2	2	6	2	6	10	2	6	10	11	2	6	..	..	2	..	..	..
^{68}Er	2	2	6	2	6	10	2	6	10	12	2	6	..	..	2	..	..	..
^{69}Tm	2	2	6	2	6	10	2	6	10	13	2	6	..	..	2	..	..	..
^{70}Yb	2	2	6	2	6	10	2	6	10	14	2	6	..	..	2	..	..	..
^{71}Lu	2	2	6	2	6	10	2	6	10	14	2	6	1	..	2	..	..	..

The rare earth elements, namely scandium (^{21}Sc), yttrium (^{39}Y) and lanthanum (^{57}La) through to lutetium (^{71}Lu) have similar physical and chemical properties and adjacent ions can share a common structural chemistry [146]. These similarities can be quantified by comparison of the Pettifor chemical

parameters of each element which form a phenomenological scale used to characterise the structure of binary compounds with a given stoichiometry [147]. The properties of the rare earth elements result from the progressive addition of electrons into the 4f orbitals along the lanthanoid series (^{58}Ce to ^{71}Lu). Since (^{21}Sc), (^{39}Y) and (^{57}La) do not have any 4f electrons, they are excluded from the lanthanoid series but nevertheless exhibit many characteristics indistinguishable from the lanthanoids. The electronic configuration of a neutral lanthanum atom may be considered equivalent to a xenon core with three additional electrons in the higher energy 5d and 6s orbitals. As the nuclear charge increases along the lanthanoid series, electrons fill the 4f orbital (see table 5.1) and are drawn into the core xenon orbital structure by strong electromagnetic attraction. The deep lying 4f electron shell is thus sufficiently removed from the valency shell that adjacent rare earth elements often form isostructural compounds and may be considered to be isomorphic [148]. The lanthanoid series exhibits a steady decrease in atomic radius with increasing atomic number known as the lanthanoid contraction. The 4f electrons imperfectly shield one another from the nuclear charge such that the effective nuclear charge attracting each electron steadily increases through the lanthanoid series resulting in the atomic radius decrease from $r_{La} = 1.061$ Å to $r_{Lu} = 0.850$ Å [68]. Therefore, elements at the end of the lanthanoid series are often isomorphic with the much lighter rare earth elements ^{39}Y and ^{21}Sc.

5.1.2 Rare earth luminescence

Most of the tri-valent rare earth ions exhibit intra-4f shell luminescence leading to technological applications including the use of rare earth ions in phosphors, where the visible transitions of the rare earth ions are exploited in full colour displays [142]. The luminescence of rare earth ions in crystalline and glassy hosts is also exploited in solid state lasers with the notable application of Nd^{3+} in the powerful neodymium-doped yttrium aluminium garnet (Nd:YAG) solid state laser [141, 149]. The principal area of current rare earth luminescence research is in the field of optoelectronics where there is a demand for optical

sources and amplifiers operating at wavelengths compatible with fibre communications technology [142].

Rare earth luminescence may be limited by a number of factors. For example multiphonon relaxation can lead to a higher probability of non-radiative transitions if the phonon energy of the glass hosts are close to the energy gap ΔE between the upper and lower energy states of the rare earth ion [142]. Selection of novel glass hosts with low phonon energies, such as chalcogenide glasses (see § 5.1.3), can reduce the contribution of multiphonon relaxation.

The solubility of rare earth ions in a solid host is also an important limiting factor, where if the concentration of the active ion exceeds a critical concentration the emission efficiency tends to decrease [148]. This concentration quenching effect results from a non-uniform distribution of rare-earth ions in the glassy matrix as the rare earth ions tend to form precipitates. These may take the form of clusters of rare-earth ions or as compounds or alloys formed with other components of the host matrix which quench luminescence by e.g. increasing the number of non-radiative decay channels or by the formation of rare earth compounds that are not optically active [142]. The critical concentration of rare earth ions may vary between hosts from a few parts per million to several atomic per cent. Optical amplifier technology is limited by the rare earth solubility limit in common glassy hosts which can lead to several meters of fibre amplifiers being required for sufficient gain [142]. It is therefore desirable to find replacement glass hosts with not only low phonon energies but also high rare earth ion solubility limits.

5.1.3 Chalcogenide glasses

Chalcogenide glasses, containing one or more of the group VIa chalcogen elements (S, Se, Te), have a high degree of covalent bonding between the atoms. The term molecular solid is sometimes applied to chalcogenide glasses since paths of covalent bonds effectively connect every atom with every other atom in a macroscopic sample of the material [1]. The chalcogenides tend to satisfy the $z = 8 - n$ rule, where n is the number of s and p valence electrons

and z is the most characteristic covalent coordination number expected on the basis of the number of shared electrons required to attain a closed shell [1]. Chalcogenide glasses have a number of desirable optical and physical properties with various photonic applications including phase change materials for digital memory technology [150], thermal imaging [151] and infrared transmitting media [143–145]. Chalcogenide glasses are also ideal hosts for luminescent rare earth ions since their low phonon energies ($\approx$ 150 - 400 cm^{-1}), compared to oxide ($\approx$ 1100 cm^{-1}) and fluoride ($\approx$ 550 cm^{-1}) glasses, leads to a higher quantum efficiency of the radiative intra-4f shell transitions [145, 152–154]. Additionally, the high refractive index (> 2.1) of chalcogenide glasses leads to an increase in the absorption and emission cross sections which helps to improve emission efficiency [155, 156].

A promising candidate for the incorporation of luminescent rare earth ions R^{3+} is the Ga_2X_3-GeX_2 ($X = \mathrm{S}, \mathrm{Se}$) glass system. As well as offering the afore mentioned favourable characteristics, this system also exhibits an exceptionally high rare earth solubility [157–163]. Extensive investigations have been performed to characterise the physicochemical, optical and luminescent properties of R-Ge-Ga-S/Se glasses [153–189], proving them to be effective materials for use in integrated optoelectronic devices.

5.2 La/Ce-Ge-Ga-S glass

The aim of this experiment is to use the method of isomorphic substitution in neutron diffraction to measure the structure of a R-Ge-Ga-S glass, where R represents La, Ce, or a 50:50 mixture of the two (denoted 'Mix'). The rare earth ions La^{3+} and Ce^{3+} are suitable neutron isomorphs since they are adjacent to one another in the rare earth series, have comparable structural chemistry as indicated by their Pettifor chemical parameters (0.705 cf. 0.7025) [147], and the tri-valent cations have comparable radii (1.16 cf. 1.14 Å) [121]. However, the neutron scattering lengths are different, with $b_{\mathrm{La}} = 8.24(4)$ fm and $b_{\mathrm{Ce}} = 4.84(2)$ fm [30] and, therefore, the difference function methods described in § 2.4 can be employed.

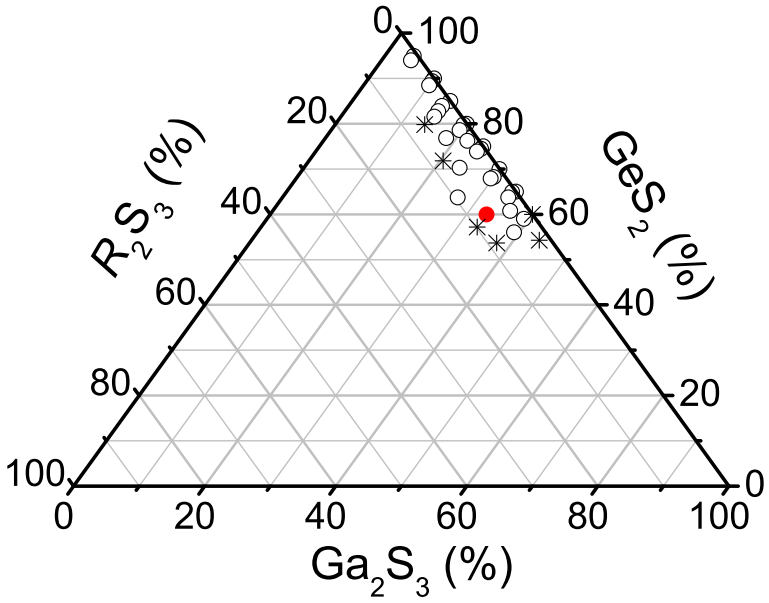

Figure 5.1: The glass forming region for the ternary system R_2S_3-GeS_2-Ga_2S_3, where R=Nd [160]. The open circles denote glass forming compositions, the stars denote partially crystalline compositions and the solid (red) circle denotes the glass composition synthesised for this study.

The glass forming region of the GeS_2-Ga_2S_3 system lies within the range $0 \geq n \geq 0.5$ when the liquid is quenched from 1000 °C in cold water, where $n = c_{Ga}/(c_{Ga} + c_{Ge})$ and c_{Ga} and c_{Ge} are the atomic fractions of Ga and Ge respectively [190]. This range can be extended to $n = 0.55$ by quenching the melt from 1100 °C [190]. The phase diagram for the Nd_2S_3-GeS_2-Ga_2S_3 system is plotted in figure 5.1 [160] where the glassy melts were quenched from 1100 °C. The glass forming region extends to ≈ 40 mol% Ga_2S_3 and up to ≈ 10 mol% Nd_2S_3. The glass composition $(R_2S_3)_{0.07}(Ga_2S_3)_{0.33}(GeS_2)_{0.60}$ was selected for investigation in this study since it lies well within the glass forming region of figure 5.1 and contains a relatively large fraction of rare earth ion $c_R = 3.68$ % which is required to obtain a measurable scattering intensity contrast between the different rare earth glasses.

5.3 Theory

As derived in § 2.2, the coherent scattered intensity obtained by a neutron diffraction experiment on a R-Ge-Ga-S glass is represented by the total structure factor $F(Q)$, defined as

$$F(Q) = \sum_{\alpha=1}^{n} \sum_{\beta=1}^{n} c_\alpha c_\beta b_\alpha b_\beta [S_{\alpha\beta}(Q) - 1], \tag{5.1}$$

where $n = 4$ is the total number of chemical species denoted by α or β, c_α represents the atomic fraction of chemical species α, $S_{\alpha\beta}(Q)$ is a Faber-Ziman partial structure factor and Q is the scattering vector. The natural isotopic abundance coherent neutron scattering lengths are $b_S = 2.84(1)$ fm, $b_{Ga} = 7.288(2)$ fm, $b_{Ge} = 8.185(20)$ fm, $b_{La} = 8.24(4)$ fm, $b_{Mix} = 6.54(4)$ fm and $b_{Ce} = 4.84(2)$ fm [30]. Expanding in terms of the partial structure factors $S_{\mu\mu'}(Q)$, that involve only the matrix species (Ge, Ga, S), and the partial structure factors $S_{R\mu}(Q)$ or $S_{RR}(Q)$, that involve the rare earth species R, we

can write $F(Q)$ as

$$\begin{aligned} F(Q) &= c_R^2 b_R^2 \left[S_{RR}(Q) - 1\right] + 2c_R c_{\mathrm{S}} b_R b_{\mathrm{S}} \left[S_{R\mathrm{S}}(Q) - 1\right] + 2c_R c_{\mathrm{Ge}} b_R b_{\mathrm{Ge}} \left[S_{R\mathrm{Ge}}(Q) - 1\right] \\ &+ 2c_R c_{\mathrm{Ga}} b_R b_{\mathrm{Ga}} \left[S_{R\mathrm{Ga}}(Q) - 1\right] + \sum_{\mu=1}^{m} \sum_{\mu'=1}^{m} c_\mu c_{\mu'} b_\mu b_{\mu'} \left[S_{\mu\mu'}(Q) - 1\right], \end{aligned}$$

where $m = 3$ is the total number of matrix species denoted by μ or μ'. If the $F(Q)$ functions are measured for samples containing the rare earth ions La^{3+}, Ce^{3+} or a 50:50 mixture of the two, where the neutron scattering lengths $b_{\mathrm{La}} > b_{\mathrm{Mix}} > b_{\mathrm{Ce}}$, then the difference function methods described in § 2.4 can be employed. The $S_{\mu\mu'}(Q)$ partial structure factors may be eliminated by subtracting two $F(Q)$ functions to give the first order difference functions

$$\begin{aligned} \Delta F_R^{(1)}(Q) &\equiv {}^{\mathrm{La}}F(Q) - {}^{\mathrm{Ce}}F(Q) \\ &= \Delta_{R\mu}^{(1)}(Q) + c_R^2 \left(b_{\mathrm{La}}^2 - b_{\mathrm{Ce}}^2\right) \left[S_{RR}(Q) - 1\right], \end{aligned} \tag{5.2}$$

$$\begin{aligned} \Delta F_R^{(2)}(Q) &\equiv {}^{\mathrm{La}}F(Q) - {}^{\mathrm{Mix}}F(Q) \\ &= \Delta_{R\mu}^{(2)}(Q) + c_R^2 \left(b_{\mathrm{La}}^2 - b_{\mathrm{Mix}}^2\right) \left[S_{RR}(Q) - 1\right], \end{aligned} \tag{5.3}$$

$$\begin{aligned} \Delta F_R^{(3)}(Q) &\equiv {}^{\mathrm{Mix}}F(Q) - {}^{\mathrm{Ce}}F(Q) \\ &= \Delta_{R\mu}^{(3)}(Q) + c_R^2 \left(b_{\mathrm{Mix}}^2 - b_{\mathrm{Ce}}^2\right) \left[S_{RR}(Q) - 1\right], \end{aligned} \tag{5.4}$$

where the matrix to rare earth difference functions are given by

$$\begin{aligned} \Delta_{R\mu}^{(1)}(Q) &= 2c_R c_{\mathrm{S}} b_{\mathrm{S}} \left(b_{\mathrm{La}} - b_{\mathrm{Ce}}\right) \left[S_{R\mathrm{S}}(Q) - 1\right] \\ &+ 2c_R c_{\mathrm{Ge}} b_{\mathrm{Ge}} \left(b_{\mathrm{La}} - b_{\mathrm{Ce}}\right) \left[S_{R\mathrm{Ge}}(Q) - 1\right] \\ &+ 2c_R c_{\mathrm{Ga}} b_{\mathrm{Ga}} \left(b_{\mathrm{La}} - b_{\mathrm{Ce}}\right) \left[S_{R\mathrm{Ga}}(Q) - 1\right], \end{aligned} \tag{5.5}$$

$$\begin{aligned}\Delta^{(2)}_{R\mu}(Q) &= 2c_Rc_Sb_S\left(b_{La}-b_{Mix}\right)\left[S_{RS}(Q)-1\right] \\ &+ 2c_Rc_{Ge}b_{Ge}\left(b_{La}-b_{Mix}\right)\left[S_{RGe}(Q)-1\right] \\ &+ 2c_Rc_{Ga}b_{Ga}\left(b_{La}-b_{Mix}\right)\left[S_{RGa}(Q)-1\right],\end{aligned} \tag{5.6}$$

$$\begin{aligned}\Delta^{(3)}_{R\mu}(Q) &= 2c_Rc_Sb_S\left(b_{Mix}-b_{Ce}\right)\left[S_{RS}(Q)-1\right] \\ &+ 2c_Rc_{Ge}b_{Ge}\left(b_{Mix}-b_{Ce}\right)\left[S_{RGe}(Q)-1\right] \\ &+ 2c_Rc_{Ga}b_{Ga}\left(b_{Mix}-b_{Ce}\right)\left[S_{RGa}(Q)-1\right].\end{aligned} \tag{5.7}$$

The $S_{R\mu}(Q)$ partial structure factors may be eliminated by subtracting a suitably weighted $\Delta F^{(i)}_R(Q)$ $(i=1,2,3)$ function from an $F(Q)$ function to yield the so called "total minus weighted difference functions" given by

$$\begin{aligned}\Delta F^{(1)}(Q) &\equiv {}^{La}F(Q)-\frac{b_{La}}{b_{La}-b_{Ce}}\Delta F^{(1)}_R(Q)\equiv\frac{b_{La}\,{}^{Ce}F(Q)-b_{Ce}\,{}^{La}F(Q)}{b_{La}-b_{Ce}} \\ &= \sum_{\mu=1}^{m}\sum_{\mu'=1}^{m}c_\mu c_{\mu'}b_\mu b_{\mu'}\left[S_{\mu\mu'}(Q)-1\right]-c_R^2b_{La}b_{Ce}\left[S_{RR}(Q)-1\right],\end{aligned} \tag{5.8}$$

$$\begin{aligned}\Delta F^{(2)}(Q) &\equiv {}^{La}F(Q)-\frac{b_{La}}{b_{La}-b_{Mix}}\Delta F^{(2)}_{La}(Q)\equiv\frac{b_{La}\,{}^{Mix}F(Q)-b_{Mix}\,{}^{La}F(Q)}{b_{La}-b_{Mix}} \\ &= \sum_{\mu=1}^{m}\sum_{\mu'=1}^{m}c_\mu c_{\mu'}b_\mu b_{\mu'}\left[S_{\mu\mu'}(Q)-1\right]-c_R^2b_{La}b_{Mix}\left[S_{RR}(Q)-1\right],\end{aligned} \tag{5.9}$$

$$\begin{aligned}\Delta F^{(3)}(Q) &\equiv {}^{Mix}F(Q)-\frac{b_{Mix}}{b_{Mix}-b_{Ce}}\Delta F^{(3)}_R(Q)\equiv\frac{b_{Mix}\,{}^{Ce}F(Q)-b_{Ce}\,{}^{Mix}F(Q)}{b_{Mix}-b_{Ce}} \\ &= \sum_{\mu=1}^{m}\sum_{\mu'=1}^{m}c_\mu c_{\mu'}b_\mu b_{\mu'}\left[S_{\mu\mu'}(Q)-1\right]-c_R^2b_{Mix}b_{Ce}\left[S_{RR}(Q)-1\right].\end{aligned} \tag{5.10}$$

The real space functions $G(r)$, $\Delta G^{(i)}_R(r)$ and $\Delta G^{(i)}(r)$ $(i=1,2,3)$ are obtained by Fourier transforming the corresponding reciprocal space functions using the

Table 5.2: Weighting factors (in millibarn) for the $g_{\alpha\beta}(r)$ partials in the $G(r)$, $\Delta G_R^{(i)}(r)$ and $\Delta G^{(i)}(r)$ functions, together with the limiting values at r=0 (in barn), for the $(R_2S_3)_{0.07}(Ga_2S_3)_{0.33}(GeS_2)_{0.60}$ glasses, where R = La, Ce or a 50:50 mixture of the two, as measured by neutron diffraction using the GEM instrument.

	$g_{\mathrm{RR}}(r)$	$g_{\mathrm{RS}}(r)$	$g_{\mathrm{RGe}}(r)$	$g_{\mathrm{RGa}}(r)$	$g_{\mathrm{GeGe}}(r)$	$g_{\mathrm{GeS}}(r)$	$g_{\mathrm{GeGa}}(r)$	$g_{\mathrm{GaGa}}(r)$	$g_{\mathrm{GaS}}(r)$	$g_{\mathrm{SS}}(r)$	$r=0$ limit
$^{\mathrm{La}}G(r)$	0.92(1)	10.94(6)	7.76(5)	7.76(6)	16.3(1)	45.9(2)	32.6(2)	16.3(2)	45.9(2)	32.4(1)	-0.2168(4)
$^{\mathrm{Mix}}G(r)$	0.582(8)	8.68(6)	6.16(5)	6.16(5)	16.3(1)	45.9(2)	32.6(2)	16.3(2)	45.9(2)	32.4(1)	-0.2110(4)
$^{\mathrm{Ce}}G(r)$	0.320(3)	6.43(3)	4.56(3)	4.56(3)	16.3(1)	45.9(2)	32.6(2)	16.3(2)	45.9(2)	32.4(1)	-0.2053(4)
$\Delta G_R^{(1)}(r)$	0.61(1)	4.51(7)	3.20(6)	3.21(7)	0.0(2)	0.0(3)	0.0(3)	0.00(2)	0.0(4)	0.0(1)	-0.0115(6)
$\Delta G_R^{(2)}(r)$	0.34(1)	2.26(9)	1.60(7)	1.60(8)	0.0(2)	0.0(3)	0.0(3)	0.00(2)	0.0(4)	0.0(1)	-0.0057(6)
$\Delta G_R^{(3)}(r)$	0.263(8)	2.26(7)	1.60(5)	1.60(6)	0.0(2)	0.0(3)	0.0(3)	0.00(2)	0.0(4)	0.0(1)	-0.0057(6)
$\Delta G^{(1)}(r)$	-0.54(3)	0.0(2)	0.0(1)	0.0(2)	16.3(4)	45.9(6)	32.6(7)	16.3(6)	45.9(9)	32.4(4)	-0.189(2)
$\Delta G^{(2)}(r)$	-0.73(6)	0.0(4)	0.0(3)	0.0(4)	16.3(8)	45.9(9)	32.6(9)	16.3(9)	45.9(9)	32.4(7)	-0.189(3)
$\Delta G^{(3)}(r)$	-0.43(3)	0.0(3)	0.0(2)	0.0(2)	16.3(6)	45.9(9)	32.6(9)	16.3(9)	45.9(9)	32.4(6)	-0.189(2)

relations

$$G(r) = \frac{1}{2\pi^2 r n_0}\int_0^\infty QF(Q)\sin(Qr)\mathrm{d}Q, \tag{5.11}$$

$$\Delta G_R^{(i)}(r) = \frac{1}{2\pi^2 r n_0}\int_0^\infty Q\Delta F_R^{(i)}(Q)\sin(Qr)\mathrm{d}Q, \tag{5.12}$$

$$\Delta G^{(i)}(r) = \frac{1}{2\pi^2 r n_0}\int_0^\infty Q\Delta F^{(i)}(Q)\sin(Qr)\mathrm{d}Q, \tag{5.13}$$

where n_0 is the atomic number density of the glass and r is a distance in real space. The relevant equations for $G(r)$, $\Delta G_R^{(i)}(r)$ and $\Delta G^{(i)}(r)$ are obtained by replacing each $S_{\alpha\beta}(Q)$ by the corresponding partial pair distribution function $g_{\alpha\beta}(r)$ in the equations given for $F(Q)$, $\Delta F_R^{(i)}(r)$ and $\Delta F^{(i)}(r)$, respectively. The theoretical low-r limit of these functions is given by the sum of the weighting factors of the partial pair distribution functions $g_{\alpha\beta}(r)$ given in table 5.2. As shown by equation 2.12, the coordination number $\bar{n}_\alpha^\beta$ is obtained by integrating over a relevant peak in real space.

If three total structure factors ${}^{\mathrm{La}}F(Q)$, ${}^{\mathrm{Mix}}F(Q)$ and ${}^{\mathrm{Ce}}F(Q)$ have been measured, it is possible to separate the rare earth partial correlation functions $S_{RR}(Q)$ and $g_{RR}(r)$ using the second order difference function method, as described in section § 2.4.3. However, if the rare earth ion concentration c_R is too small, as it proves to be in the present study, then the weighting given to the $S_{RR}(Q)$ partial in the $F(Q)$ function is also small and its extraction therefore becomes unfeasible.

In an x-ray diffraction experiment, the scattered intensity is conventionally denoted by the total x-ray structure factor $S_X(Q)$ which, within the independent atom approximation, is given by

$$\begin{aligned} S_X(Q) - 1 &= \frac{F_X(Q)}{\left[\sum_{\alpha=1}^{n} c_\alpha f_\alpha(Q)\right]^2} \\ &= \frac{1}{\left[\sum_{\alpha=1}^{n} c_\alpha f_\alpha(Q)\right]^2}\sum_{\alpha=1}^{n}\sum_{\beta=1}^{n} c_\alpha f_\alpha(Q) c_\beta f_\beta(Q)\left[S_{\alpha\beta}(Q) - 1\right], \end{aligned} \tag{5.14}$$

where $f_\alpha(Q)$ represents the Q dependent neutral atom form factor for atomic species α. There is very little contrast between the form factors $f_{\mathrm{La}}(Q)$ and $f_{\mathrm{Ce}}(Q)$ since the atomic numbers are $Z(\mathrm{La}) = 57$ and $Z(\mathrm{Ce}) = 58$. Therefore, the x-ray diffraction patterns measured for samples containing these elements should be more-or-less identical provided the atomic structures are the same. The total x-ray pair distribution function $G_X(r)$ is obtained by Fourier transforming the $S_X(Q)$ function. However, because the partial structure factors are weighted by Q-dependant form factors, the $g_{\alpha\beta}(r)$ correlations are convoluted by the Fourier transform of the form factors in real space. The coordination number $\bar{n}_\alpha^\beta$ cannot therefore be calculated by directly integrating over the relevant peaks in the real space functions. Instead, if there is a clearly defined peak in $G_X(r)$ that can be assigned to a particular $g_{\alpha\beta}(r)$, the $F_X(Q)$ function is divided by the weighting factor for the relevant $S_{\alpha\beta}(Q)$ function such that in the Fourier transform the r-dependent weighting factor is removed from the $g_{\alpha\beta}(r)$ function of interest [191].

5.4 Experimental procedure

5.4.1 Glass preparation

Very high purity starting materials and inert synthesis environments are required for the preparation of chalcogenide glasses, since chemical and physical impurities influence the rare earth solubility, glass forming ability and optical properties of the material [145, 167, 169]. The R-Ge-Ga-S glass samples were therefore prepared by weighing the high purity starting constituents Ge (Aldrich, $\geq$ 3 mm chips, 99.999 %), Ga (Aldrich, 99.9999 %), S (Alfa Aesar, pieces, Puratronic®, 99.9995 %), La_2S_3 (Alfa Aesar, powder 99.9 %) and Ce_2S_3 (Alfa Aesar, powder 99.9 %) in the correct proportions within a dry Argon filled glove box with levels of $H_2O \leq 6$ ppm and $O_2 \leq 30$ ppm. The Ge and S elements were powdered using a stainless steel and agate pestle and mortar, respectively, while the Ga, which has a melting point of 29.78 °C [68], was melted on a hotplate at $\approx$ 35 °C. The samples were loaded into silica am-

poules of 5 mm inner diameter and 1 mm wall thickness. Prior to preparation, the ampoules had been cleaned using concentrated HF(aq) (Fisher, 40 wt. %), distilled water and acetone (Aldrich, 99.999 %) before being dried at 110 °C and de-gassed under $\approx 5 \cdot 10^{-5}$ Torr vacuum at 750 °C for 2 hours. Cylindrical ampoules promote the formation of homogeneous glasses by ensuring uniform thermal conduction throughout the sample during the quenching process [192] and their small size was chosen to increase the quench rate. The ampoules containing ≈ 3 g of starting materials were removed from the glovebox, evacuated at $\approx 5 \cdot 10^{-5}$ Torr for ≥ 24 hours at room temperature and sealed under vacuum.

Due to the high temperature (up to 1100 °C [160, 190]) required for the synthesis of *R*-Ge-Ga-S glasses, the existing rocking tube furnaces in the Liquid and Amorphous Materials (LAM) research laboratory were re-designed to operate at a higher maximum power output whilst maintaining temperature homogeneity over the entire length of the ampoule of ≈ 180 mm. The furnace elements were constructed by winding nichrome wire of 0.91 mm diameter around an alumina tube of 450 mm length, 40 mm inner diameter and 50 mm outer diameter using a Myford lathe. Homogenous windings were made at a rate of 12 revolutions per inch (rpi) along the first 110 mm length of the tube, 10 rpi along the central 230 mm length and 12 rpi along the remaining 110 mm length of tube. An alumina cement consisting of alumina powder, water and sodium silicate solution was cast ≈ 5 mm thick over the heating elements which were subsequently dried in an oven at 110 °C for 24 hours. The purpose of the cement layer was to provide mechanical strength, thermal insulation, and to prevent the oxidation of the nichrome wire during operation. The new furnace elements were further thermally insulated by wrapping them in a Kao wool refractory blanket. The elements were incorporated into the existing rocking tube furnace assembly, as illustrated in figure 5.2, and the void between the elements and furnace cladding was filled with vermiculite granules. Electrical current was supplied to the heating elements via a Eurotherm temperature controller, where the temperature was monitored at the central section of the

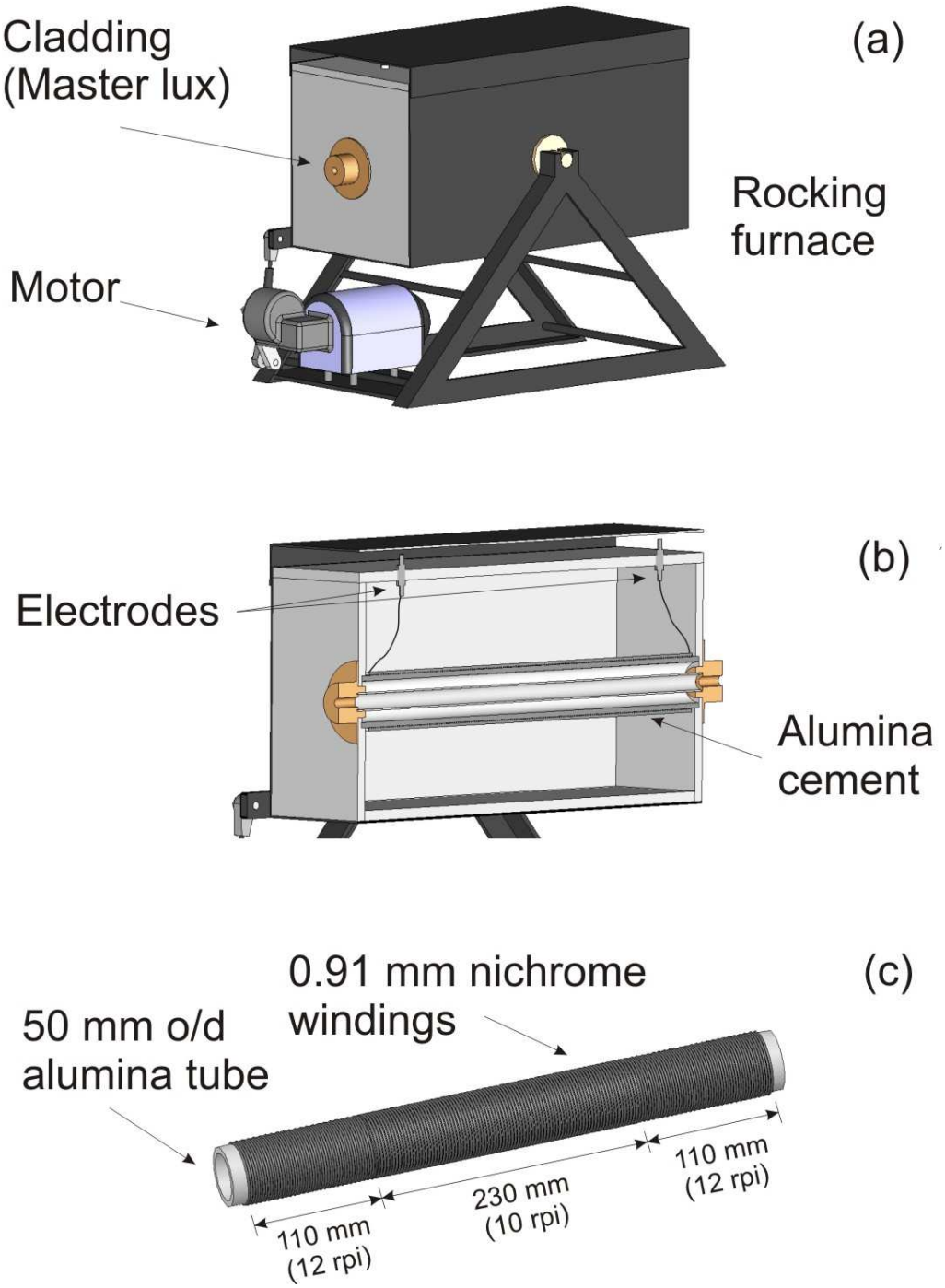

Figure 5.2: Rocking furnace schematic. (a) The rocking tube furnace assembly. (b) Furnace cross section. (c) The furnace windings. The windings were wrapped in a Kao wool refractory blanket and vermiculite granules were used to fill the void between the elements and furnace cladding.

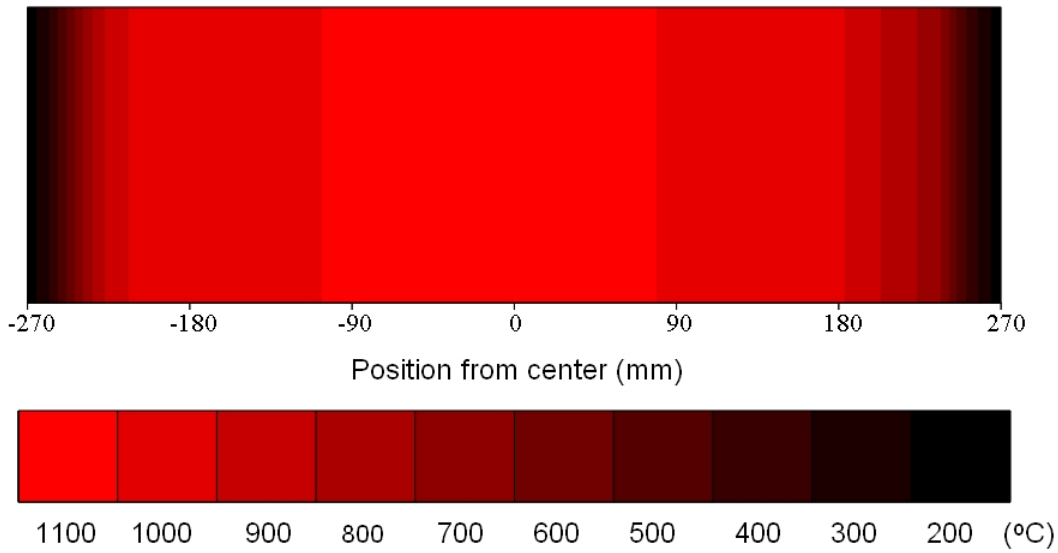

Figure 5.3: Temperature profile of the rocking furnace operating at 1100 °C.

furnace using a Pt/Rh thermocouple. The maximum operating power output P of the heating elements is calculated from

$$P = \frac{V^2}{L \cdot \Lambda} = \frac{240^2}{28 \cdot 2.22} = 927 \text{ W}, \tag{5.15}$$

where V is the maximum supply voltage from the Eurotherm temperature controller (where 240 V lies within the tolerance of the United Kingdom rms mains supply voltage), $\Lambda = 2.22\ \Omega\text{m}^{-1}$ is the resistance per meter of the nichrome wire used, and $L = 28$ m is the length of wire used. The original furnace windings had a total resistance $R = 74\ \Omega$, providing a maximum operating power

$$P = \frac{V^2}{R} = \frac{240^2}{74} = 778 \text{ W}. \tag{5.16}$$

Thus, the maximum operating power of the furnace was increased by 19 % by reducing the resistance of the furnace windings. The temperature profile of the improved furnace operating at 1100 °C is plotted in figure 5.3 and was determined by probing the temperature using a K-type thermocouple at 10 mm intervals along the length of the tube furnace.

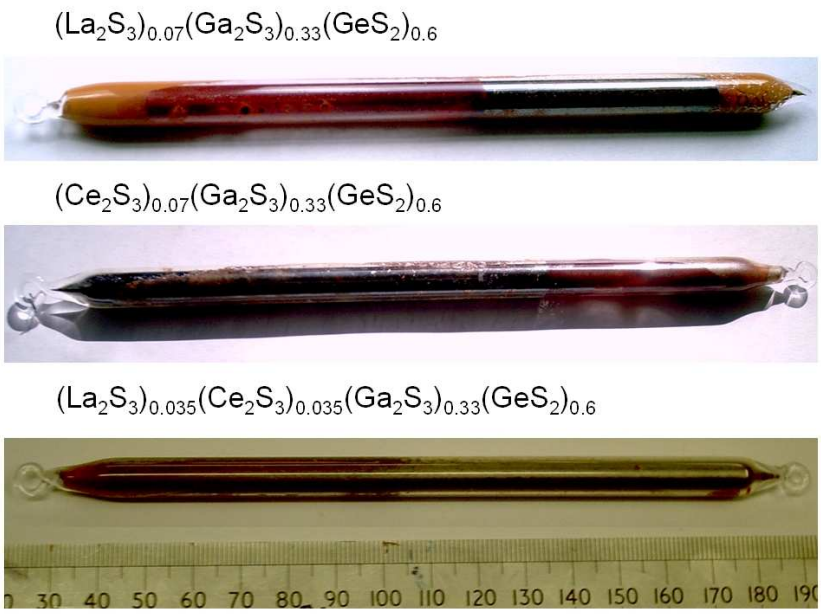

Figure 5.4: The as quenched *R*-Ge-Ga-S glasses contained within silica ampoules.

The sealed ampoules containing the powdered starting materials were fixed in position in the centre of the furnace using thin nichrome wire attached to hooks at each end of the ampoule. In order to ensure adequate mixing of the elements, the furnaces rocked continuously throughout the heating procedure at 5 rpm and at $\pm$ 45 ° relative to the horizontal axis. The samples were heated at a rate of 1 °C min^{-1} and held for 4 hours at 112 and 445 °C, corresponding to the melting and boiling points of S, and at 937 °C, corresponding to the melting temperature of Ge. These dwelling temperatures were important to prevent a sudden build up of vapour pressure, which in the case of sulphur is very high. Once the final synthesis temperature of 1100 °C had been reached and held for $\geq$ 24 hours, the furnace was rotated vertically and held for a further 12 hours before rapidly quenching the ampoule in ice water by cutting the wire that fixed it in place. Two 3 g batches of each glass, containing either La, Ce or a 50:50 mixture of the two, were prepared to fill the vanadium container used to hold the sample in the neutron diffraction experiment. Photographs of the as quenched glasses in their silica ampoules are shown in figure 5.4.

On breaking open the ampoules, the samples did not come away very cleanly from the silica surface and were scraped off the silica surface using tweezers. The mean atomic fractions of the glasses, as averaged over all the samples, are $c_R = 0.0369(1)$, $c_{\mathrm{Ge}} = 0.1559(4)$, $c_{\mathrm{Ga}} = 0.1752(9)$ and $c_{\mathrm{S}} = 0.632(1)$, forming the required molar composition of $(R_2\mathrm{S}_3)_{0.07}(\mathrm{Ga}_2S_3)_{0.33}(\mathrm{GeS}_2)_{0.60}$.

5.4.2 Sample characterisation

Table 5.3: Properties of the $(R_2\mathrm{S}_3)_{0.07}(\mathrm{Ga}_2\mathrm{S}_3)_{0.33}(\mathrm{GeS}_2)_{0.60}$ glasses, where R represents La, Ce or a 50:50 mixture of the two. The measured mass density ρ and number density n_0 are listed together with the glass transition temperature T_{g} and crystallisation temperatures $T_{\mathrm{c}}^{(1)}$ and $T_{\mathrm{c}}^{(2)}$ as measured by differential scanning calorimetry.

R	ρ (g cm^{-3})	n_0 (Å^{-3})	T_{g} (°C)	$T_{\mathrm{c}}^{(1)}$ (°C)	$T_{\mathrm{c}}^{(2)}$ (°C)
La	3.26(1)	0.0401(6)	430(2)	544.6(1)	574.8(1)
Mix	3.27(1)	0.0402(6)	444(5)	599.4(1)	–
Ce	3.24(1)	0.0399(6)	446(2)	580.2(1)	604.0(1)

The amorphous nature of the R-Ge-Ga-S glasses was confirmed by the absence of crystalline Bragg peaks in the diffraction patterns obtained using a Philips $\theta - 2\theta$ x-ray diffractometer with CuKα radiation of wavelength $\lambda_{K\alpha 1} = 1.54060$ Å and $\lambda_{K\alpha 2} = 1.54439$ Å. The density of each of the samples was measured at the ISIS facility using a Quantachrome helium gas pycnometer and is listed in table 5.3.

The glass transition temperature T_g, crystallisation temperature T_c and mass loss on heating of the glass samples were measured, after the neutron diffraction experiments had been performed, by differential scanning calorimetry (DSC) and thermal gravimetric analysis (TGA) using a TA Instruments SDT Q600 machine. The finely powdered samples of mass ≈ 25 mg were contained in alumina pans and heated over the temperature range 250 °C to 600 °C at a rate of 10.00 °C min^{-1}. The heat flow and sample mass were recorded every 0.5 s and are plotted in figure 5.5. Nitrogen gas (BOC, Oxygen free),

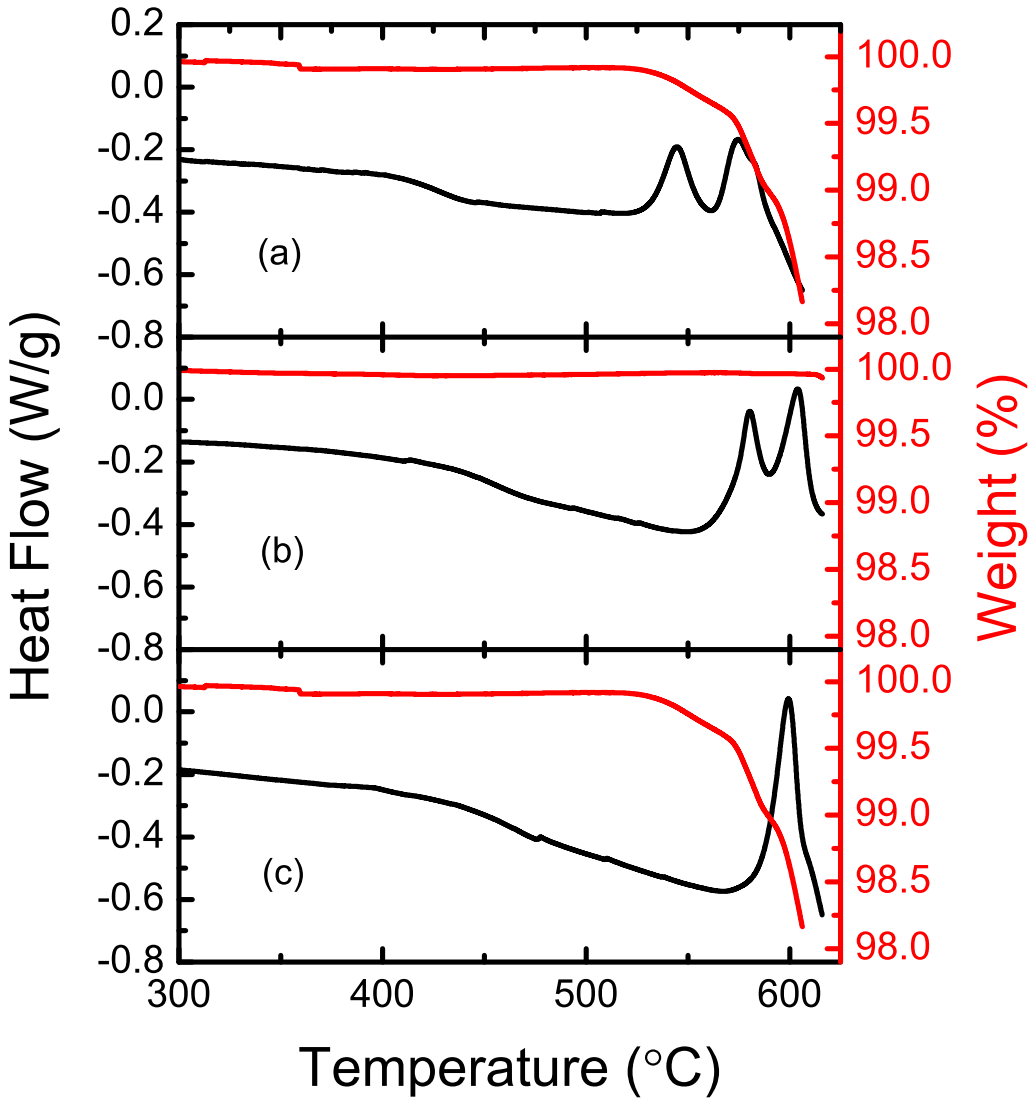

Figure 5.5: Differential Scanning Calorimetry (DSC) and thermal gravimetric analysis (TGA) measurements for the $(R_2S_3)_{0.07}(Ga_2S_3)_{0.33}(GeS_2)_{0.60}$ glasses where (a) R = La, (b) R = Mix (denoting a 50:50 mixture of La and Ce), and (c) R = Ce. The black curves show the total heat flow obtained from DSC and the red curves show the mass loss measured by TGA.

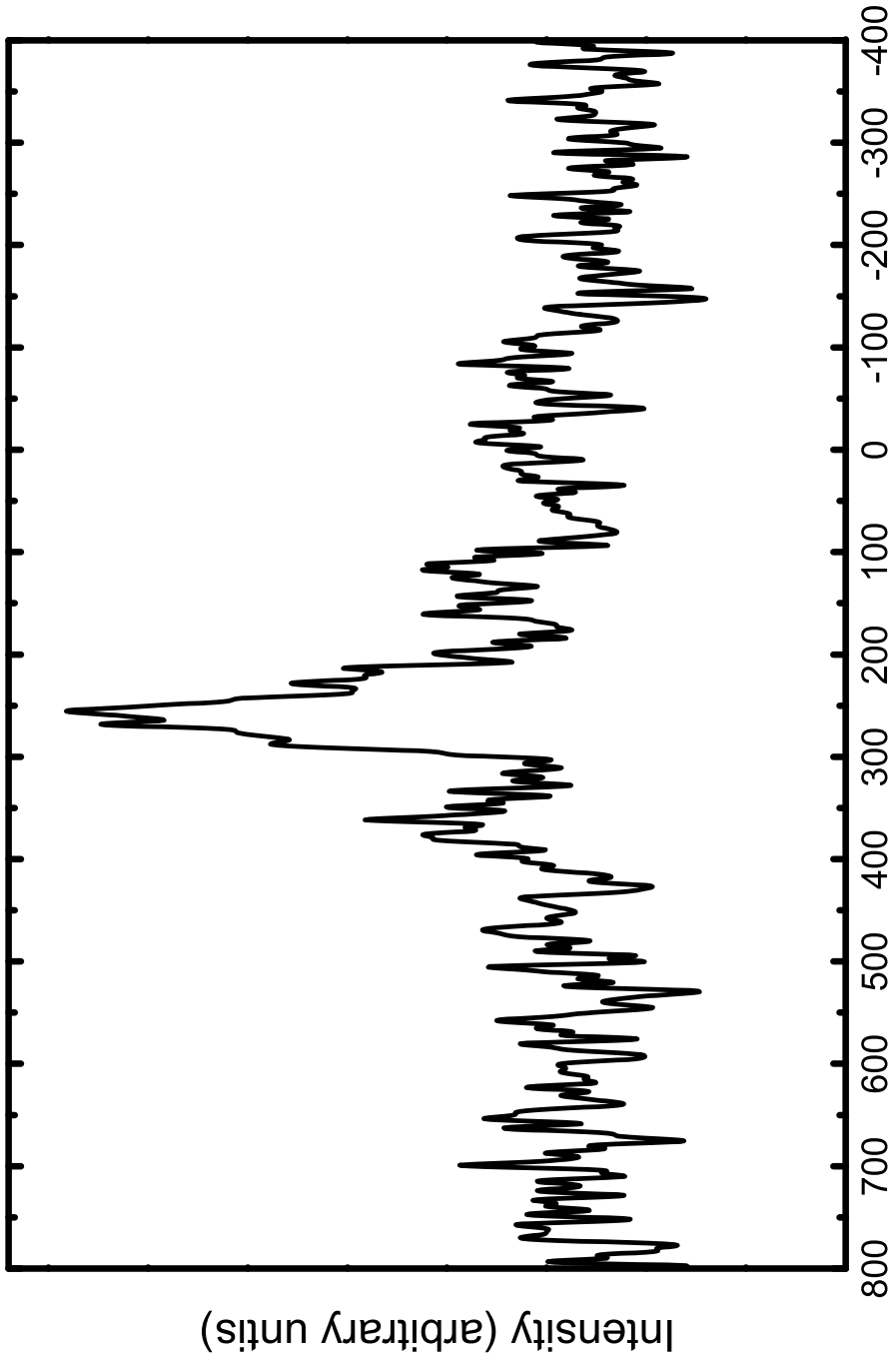

Figure 5.6: ^{71}Ga MAS NMR spectrum for the $(La_2S_3)_{0.07}(Ga_2S_3)_{0.33}(GeS_2)_{0.60}$ glass.

flowing at 100 ml min^{-1}, was used to purge the instrument of moisture and oxygen and to provide efficient heat transfer between the sample pans and the DSC cell contacts. The mid-point glass transition temperature T_g was obtained by drawing a tangent line to the data in the transition region of the heat flow to find the point of inflection. The crystallisation temperature T_c is given by the position of the exothermic peak following T_g. The values of T_g and T_c are listed in table 5.3. All of the samples give similar traces although the glasses containing La exhibit two crystallisation peaks. The experiments were terminated before melting of the sample occurred due to the volatile nature of molten sulphur compounds, exemplified by the observed sample mass loss in the vicinity of T_c.

5.4.3 The ^{71}Ga MAS NMR experiments

Gallium has two nuclei observable by Nuclear Magnetic Resonance (NMR), namely ^{69}Ga and ^{71}Ga, both with a nuclear spin of $I = 3/2$ and natural abundances of 60.4 % and 39.6 %, respectively. However, despite its higher natural abundance, ^{69}Ga spectra are more readily affected by second-order quadrupolar broadening, giving less sensitivity and less resolution than for ^{71}Ga NMR [193].

A ^{71}Ga Magic Angle Spinning (MAS) NMR experiment was performed on the $(La_2S_3)_{0.07}(Ga_2S_3)_{0.33}(GeS_2)_{0.60}$ glass by Dell and Smith [194] at the Department of Physics, University of Warwick, using a 600 MHz Bruker Avance spectrometer with an applied magnetic field $B_0 = 14.1$ T producing a Larmor frequency of 183 MHz. The sample was contained within a Zirconia rotor of diameter 3.2 mm and was spun at a frequency of 20 kHz about an axis orientated at the magic angle $\theta_M = 54.7°$ relative to the applied magnetic field B_0 in order to remove effects from e.g. chemical shift anisotropy [195]. A spin-echo sequence (1-τ-2 μs) was used with a recycle delay of 10 s and the time set to the reciprocal of the MAS frequency [196]. The resulting spectrum is plotted in figure 5.6, where the chemical shifts are referenced to $Ga(H_2O)_6^{3+}$ at 0 parts per million (ppm). The poor signal to noise (S/N) ratio is due to the

relatively short acquisition time of 2 hours. The main resonance observed at $\delta = 250(5)$ ppm is indicative of tetrahedral Ga sites, by comparison with the α and β phases of Ga_2O_3 [196].

5.4.4 The GEM neutron diffraction experiments

Neutron diffraction experiments were performed on the R-Ge-Ga-S glasses at the ISIS facility using the GEM instrument, described in § 3.2.3, with a maximum scattering vector $Q_{\max} = 49.5$ Å^{-1}. The samples were finely powdered using an agate pestle and mortar and held in a cylindrical vanadium container of 6.8 mm inner diameter and 0.1 mm wall thickness at ambient temperature (≈ 25 °C). Diffraction patterns were taken for the samples in the vanadium container, the empty vanadium container, the empty instrument and a cylindrical vanadium rod of diameter 8.36 mm. The intensities for each detector group were saved at regular intervals (every 500 μAhr^{-1}) and no deviation between each scan was observed outside statistical variation, verifying the diffractometer stability [197]. In order to attain good counting statistics, a total run time of ≈ 2750 μAhr per sample was made, which at an average ISIS beam current of 170 μA equates to ≈ 18 hours of neutron counting time per sample. After eliminating non-functioning or noisy detectors, the GUDRUN analysis program [111] was used to process the data detector-by-detector, correcting for attenuation, background, multiple scattering and inelasticity effects and normalising to the vanadium standard. The results were then merged and the data sets for the Ce and mixture samples were also corrected for the contribution from Ce^{3+} paramagnetic scattering [36] (see § 2.2.1).

The total structure factors ${}^{\mathrm{La}}F(Q)$, ${}^{\mathrm{Mix}}F(Q)$ and ${}^{\mathrm{Ce}}F(Q)$ of figure 5.7 were Fourier transformed to give the total pair distribution functions ${}^{\mathrm{La}}G(r)$, ${}^{\mathrm{Mix}}G(r)$ and ${}^{\mathrm{Ce}}G(r)$ shown in figure 5.8. It was suggested, from a peak at 1.60(1) Å in the $G(r)$ functions, that the samples were contaminated by a small quantity of SiO_2 glass from the silica ampoules. A scaled total structure factor for SiO_2 glass, denoted ${}^{\mathrm{Si}}F(Q)$, measured using the GEM instrument [198] was therefore subtracted from each measured $F(Q)$ function, as shown in figure 5.7,

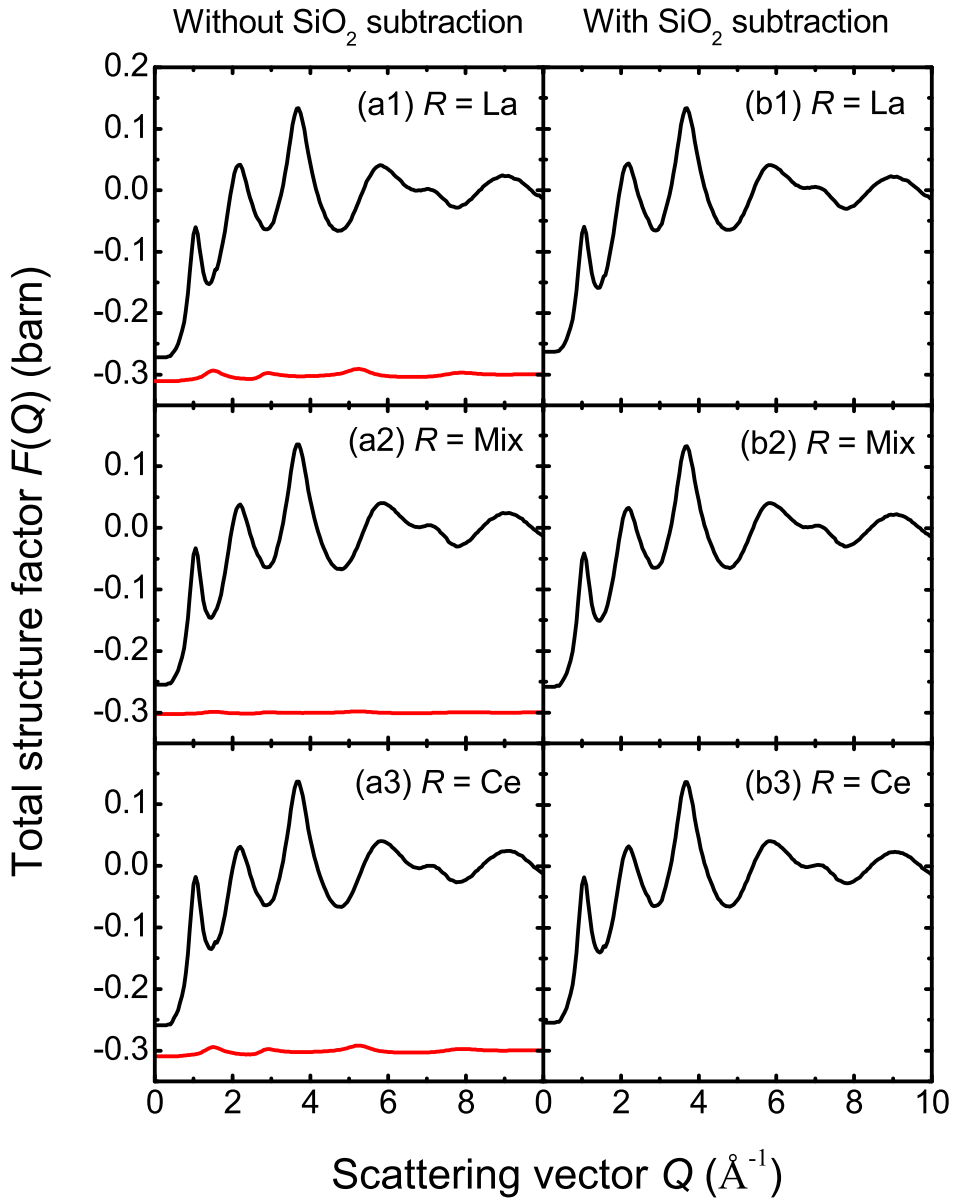

Figure 5.7: The total structure factors $F(Q)$ up to 10 Å^{-1} for the $(R_2S_3)_{0.07}(Ga_2S_3)_{0.33}(GeS_2)_{0.60}$ glasses as measured on the GEM instrument for (a1) R = La, (a2) R = Mix (denoting a 50:50 mixture of La and Ce), and (a3) R = Ce (black curves) plotted together with the corresponding scaled ${}^{Si}F(Q)$ for silica as given by equations 5.17 to 5.19 and displaced by -0.3 barn (red curves). The $F(Q)$ functions corrected for SiO_2 are given in (b1), (b2) and (b3).

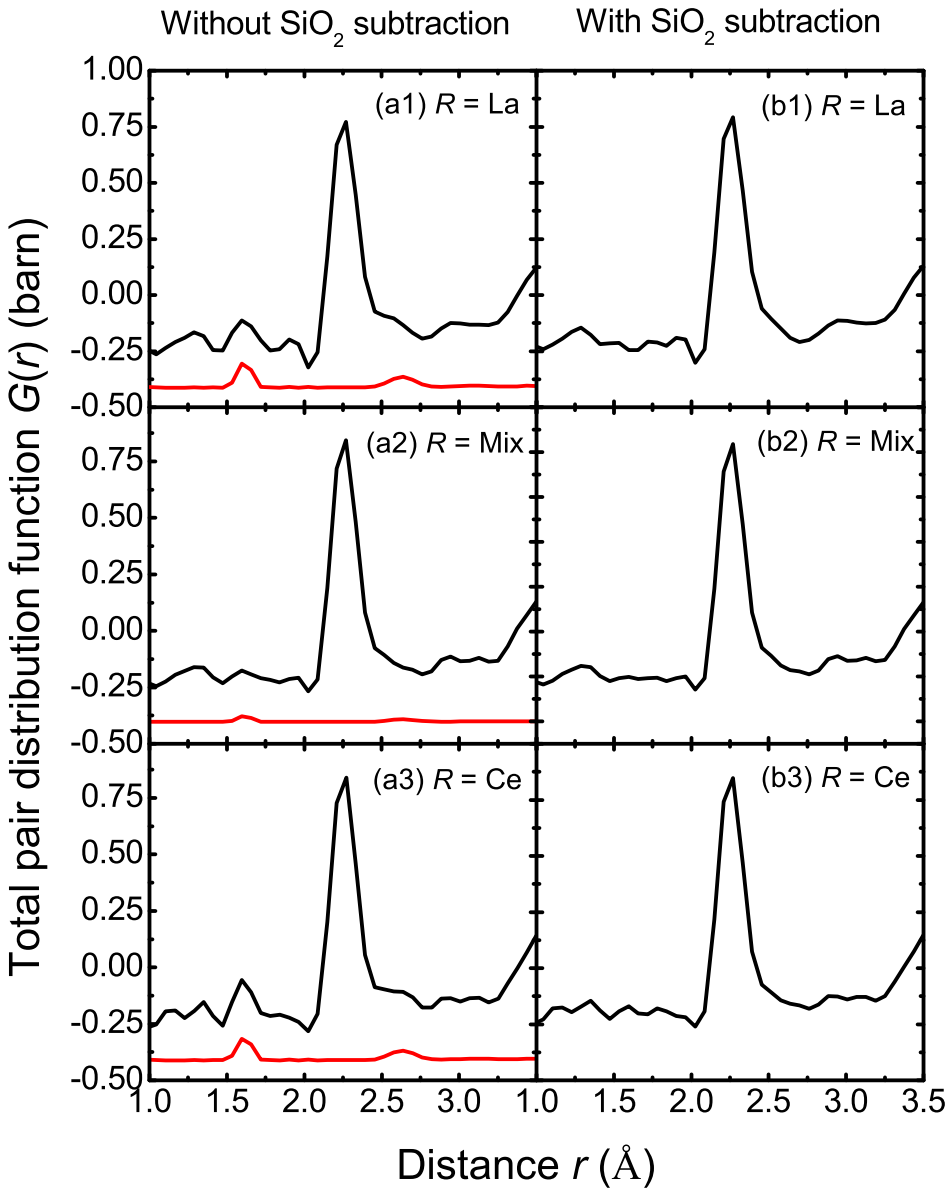

Figure 5.8: The total pair distribution functions $G(r)$ for the $(R_2S_3)_{0.07}(Ga_2S_3)_{0.33}(GeS_2)_{0.60}$ glasses obtained by Fourier transforming the corresponding $F(Q)$ functions given in figure 5.7 for (a1) R = La, (a2) R = Mix (denoting a 50:50 mixture of La and Ce), and (a3) R = Ce (black curves) plotted together with the corresponding $^{Si}G(r)$ for silica scaled according to equations 5.17 to 5.19) displaced by -0.4 barn (red curves). The $G(r)$ functions corrected for SiO_2 are given in (b1), (b2) and (b3).

such that

$$^{\mathrm{La}}F(Q) = {}^{\mathrm{La}}F(Q) - l \cdot {}^{\mathrm{Si}}F(Q), \quad (5.17)$$

$$^{\mathrm{Mix}}F(Q) = {}^{\mathrm{Mix}}F(Q) - m \cdot {}^{\mathrm{Si}}F(Q), \quad (5.18)$$

$$^{\mathrm{Ce}}F(Q) = {}^{\mathrm{Ce}}F(Q) - n \cdot {}^{\mathrm{Si}}F(Q), \quad (5.19)$$

where the scaling factors $l = 0.045$, $m = 0.01$ and $n = 0.04$ were chosen to eliminate the peak at 1.60(1) Å in the $G(r)$ functions (see figure 5.8). It is noted, however, that further NMR measurements on the La containing sample did not find any evidence of a ^{29}Si resonance [194]. Also, the $G_X(r)$ functions obtained from the subsequent x-ray diffraction measurements on the glasses, described below, did not find any evidence of the Si-O peak at 1.60 Å. Several factors may account for this discrepancy including the relatively low sensitivity of the ^{29}Si nucleus in NMR, the relatively small atomic number of Si leading to low sensitivity by x-rays and since smaller samples were required for the NMR and x-ray diffraction experiments only small fractions of the bulk samples used in the neutron diffraction experiments were measured. As shown in figure 5.8, the Si-O peak at 1.60(1) Å is clearly visible above the un-physical low-r oscillations in the measured $G(r)$ functions and the O-O peak at 2.64(1) Å contributes to a shoulder on the nearest neighbour peak. The correction for silica proved to be essential in order to (i) obtain reasonable agreement between the reciprocal space functions and the back transforms of the corresponding real space functions after the un-physical low-r oscillations had been set to their theoretical $G(0)$ limit, and (ii) obtain consistent values for the calculated coordination numbers.

Further self consistency checks were performed on the data sets to ensure that each corrected $F(Q)$ function obeys the sum-rule relation (see equation 2.11) and that the low-r features in the corresponding real space functions oscillate about their theoretical $r = 0$ limit as given in table 5.2 [113].

5.4.5 The ID15B x-ray diffraction experiments

In order to confirm the glass samples were isomorphic, high energy x-ray diffraction experiments were performed on the ID15B beamline at the ESRF, France, described in § 3.5.2. A MAR345 image plate detector was used, in the setup shown in figure 3.12, with a detector to sample distance $D = 303.552$ mm and an incident x-ray energy of 88.76 keV. The finely powdered samples were held in a washer and sealed each side with kapton 77-80 tape to give an approximate slab geometry with a sample thickness of 1.0 mm. Two dimensional diffraction patterns were taken at ambient temperature (≈ 25 °C) for the three samples in their container, the empty container, the empty instrument and a piece of Pb of thickness 10.2 mm covering the incident beam aperture. An example of a measured two dimensional x-ray diffraction pattern is plotted in figure 5.9. The FIT2D [199] analysis program was used to correct the data for geometrical effects, such as non-orthogonality of the detector relative to the incident beam, and polarisation of the incident beam before integrating over the two dimensional regions to produce a one dimensional diffraction pattern. The detector regions covered by the beam stop or bad pixels were masked off such that they did not influence the results of the integration.

Each data set was normalised to the incident beam intensity and, following the procedure detailed in § 3.7, corrected for background scattering and attenuation effects and scaled to fit the sum of the Compton scattering cross section (given in Ref. [200]) and self scattering $\sum_\alpha c_\alpha f_\alpha(Q)^2$ contributions at high Q values, where the neutral atom form factors $f_\alpha(Q)$ were taken from Ref. [201]. The fit is plotted in figure 5.10 and was performed over the region $4 \leq Q(\text{Å}^{-1}) \leq 15$. The Compton scattering contribution was subtracted to obtain the Rayleigh-Thomson differential scattering cross-section, from which the total x-ray structure factor $S_X(Q)$ was obtained.

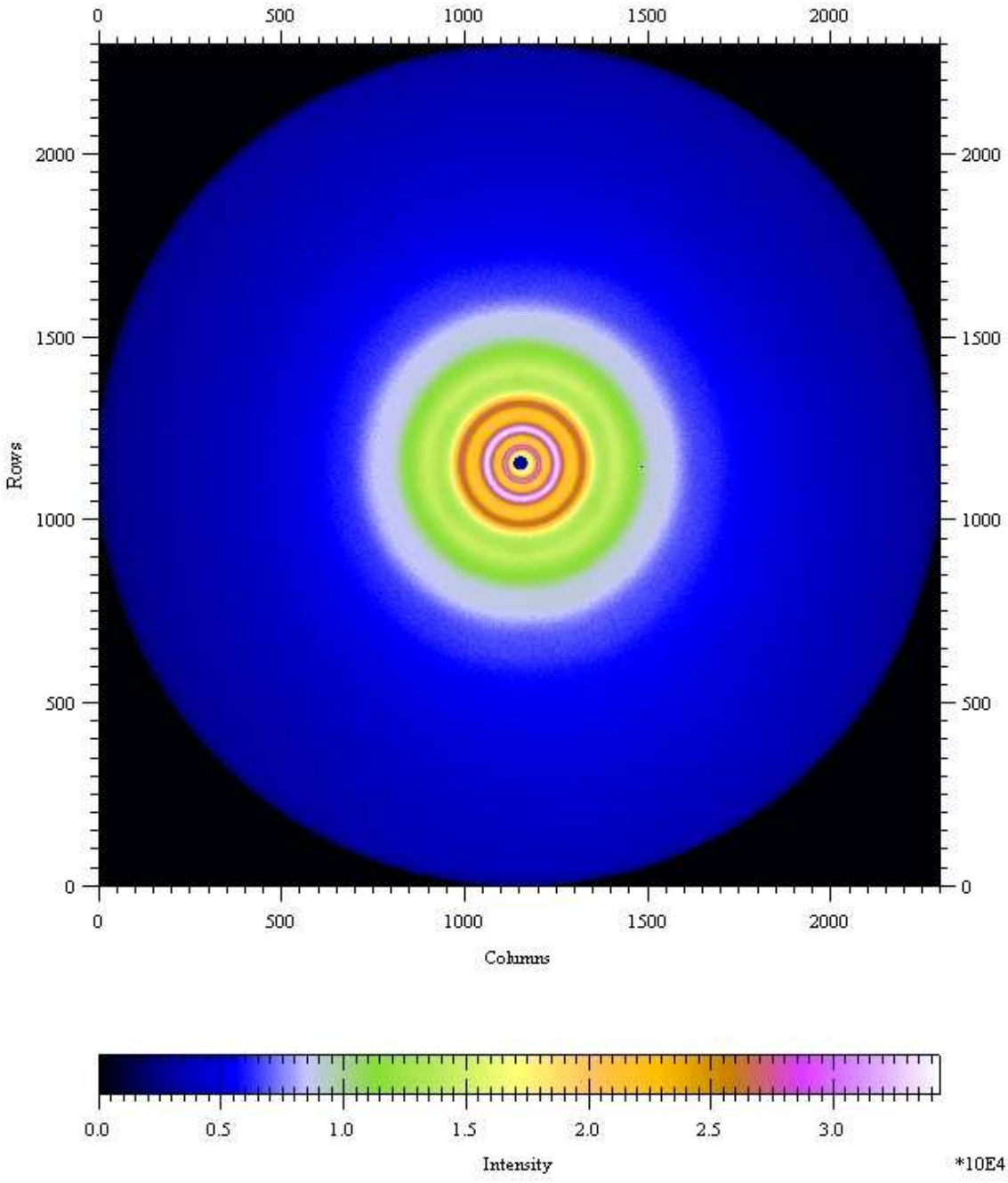

Figure 5.9: Two dimensional image plate x-ray diffraction pattern for the $(La_2S_3)_{0.035}(Ce_2S_3)_{0.035}(Ga_2S_3)_{0.33}(GeS_2)_{0.60}$ glass taken on the ID15B beamline at the ESRF, France, using a MAR345 image plate detector.

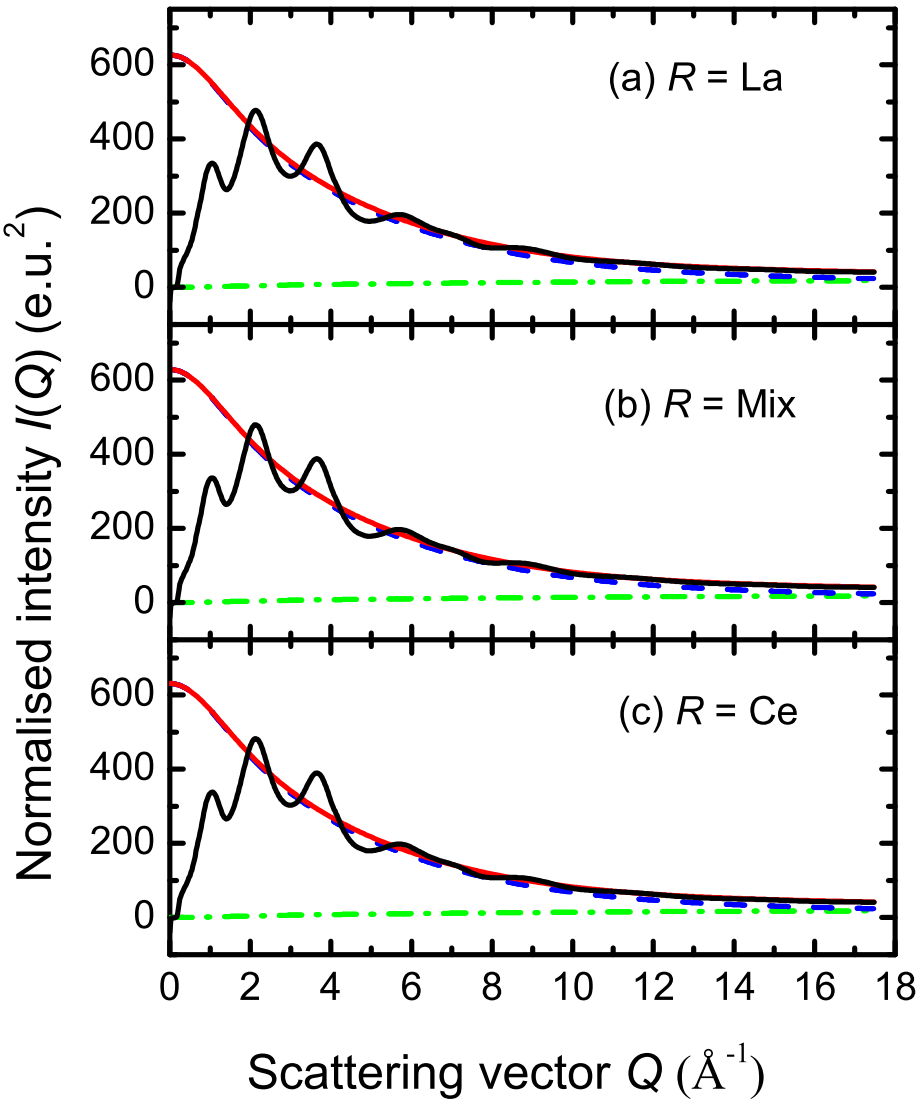

Figure 5.10: Contributions to the total x-ray scattered intensity for the $(R_2S_3)_{0.07}(Ga_2S_3)_{0.33}(GeS_2)_{0.60}$ glasses, where (a) R = La, (b) R = Mix, denoting a 50:50 mixture of La and Ce, and (c) R = Ce, as measured on the ID15B beamline at the ESRF. The dashed (blue) curves show the self scattering, the chained (green) curves show the Compton scattering, the solid (red) curves show the sum of the self scattering and Compton scattering and the solid (black) curves show the x-ray diffraction data that have been normalised by fitting to the sum of the self scattering and Compton scattering intensities.

5.5 Results

The total structure factors ${}^{\mathrm{La}}F(Q)$, ${}^{\mathrm{Mix}}F(Q)$ and ${}^{\mathrm{Ce}}F(Q)$ for the R-Ge-Ga-S glasses, as measured by neutron diffraction on the GEM instrument at ISIS, are plotted in figure 5.11. The total pair distribution functions ${}^{\mathrm{La}}G(r)$, ${}^{\mathrm{Mix}}G(r)$ and ${}^{\mathrm{Ce}}G(r)$ are plotted in figure 5.12 and were obtained by Fourier transforming the corresponding $F(Q)$ functions after making a Harwell spline fit [115] to the data and applying a cosine window function between 25 and 30 $\mathrm{\AA}^{-1}$. The positions of the leading peaks in the $F(Q)$, $G(r)$ and corresponding difference functions are listed in table 5.4 together with the coordination number $\bar{n}^{\mathrm{S}}_{\mathrm{Ge}}$ or $\bar{n}^{\mathrm{S}}_{\mathrm{R}}$ obtained from the real space functions as detailed below.

The $F(Q)$ functions exhibit a first sharp diffraction peak (FSDP), indicative of ordering on intermediate length scales [116], at $q_1 \simeq 1.05(2)$ $\mathrm{\AA}^{-1}$. There is a clear contrast in intensity between the $F(Q)$ functions, particularly in the vicinity of the FSDP which experiences an increase in height with the substitution of La by Ce. This is emphasised by the first order difference functions $\Delta F^{(i)}_R(Q)$ $(i = 1, 2, 3)$ plotted in figure 5.13 which exhibit a trough at $q_1 \simeq 1.05(2)$ Å that must therefore result from one or more of the $S_{RR}(Q)$ and $S_{R\mu}(Q)$ partial structure factors.

The first peak at $r_1 \simeq 2.25(2)$ Å in the $G(r)$ functions is attributed to a superposition of the nearest neighbour Ge-S and Ga-S correlations by comparison with the nearest neighbour distances $2.17 \leq r_{\mathrm{GeS}}$ (Å) ≤ 2.27 reported for crystalline GeS_2 [205–207] and $2.08 \leq r_{\mathrm{GaS}}$ (Å) ≤ 2.46 reported for crystalline Ga_2S_3 [208–210]. Assuming the number of homopolar bonds to be negligible, a coordination number of $\bar{n}^{\mathrm{S}}_{\mathrm{Ge}} = 3.9(1)$ was obtained from the first peak in the $G(r)$ functions by integrating over the range $2.02 \leq r$ (Å) ≤ 2.64 and subtracting the contribution to the peak area from the Ga-S correlations by taking $\bar{n}^{\mathrm{S}}_{\mathrm{Ga}} = 4$, as confirmed by the ^{71}Ga MAS NMR spectrum (see figure 5.6). However, a small shoulder is present on the first peak at $r \simeq 2.55$ Å. This shoulder cannot be safely attributed to Ge-S or Ga-S correlations since, in crystalline R-Ge-S [203, 211, 212] and R-Ga-S [204] materials, where R denotes a large rare earth element, these correlations exhibit distances that are comparable to

Table 5.4: Leading peak positions q_1, q_2 and q_3 for the reciprocal space functions for the $(R_2S_3)_{0.07}(Ga_2S_3)_{0.33}(GeS_2)_{0.60}$ glasses, where R denotes La, Ce, or a 50:50 mixture of the two, as measured by neutron diffraction on the GEM instrument at ISIS. The leading peak positions r_1, r_2, r_3 and r_4 for the corresponding real space functions are also given together with the coordination numbers $\bar{n}^{\mathrm{S}}_{\mathrm{Ge}}$ and $\bar{n}^{\mathrm{S}}_{R}$.

	q_1 (Å^{-1})	q_2 (Å^{-1})	q_3 (Å^{-1})	$\bar{n}^{\mathrm{S}}_{\mathrm{Ge}}$	$\bar{n}^{\mathrm{S}}_{R}$	r_1 (Å)	r_2 (Å)	r_3 (Å)	r_4 (Å)
$^{\mathrm{La}}F(Q)$	1.05(2)	2.18(2)	3.68(2)	3.9(1)	8.8(9)	2.25(2)	3.01(3)	3.63(5)	–
$^{\mathrm{Mix}}F(Q)$	1.07(2)	2.19(2)	3.68(2)	3.9(1)	11.8(9)	2.25(2)	2.97(3)	3.62(5)	–
$^{\mathrm{Ce}}F(Q)$	1.05(2)	2.19(2)	3.68(2)	3.9(1)	10.2(9)	2.24(2)	2.94(3)	3.60(5)	–
$\Delta F^{(1)}_R(Q)$	1.05(2)	1.95(2)	–	–	8.2(2)	–	3.05(3)	3.89(5)	4.69(5)
$\Delta F^{(2)}_R(Q)$	1.02(2)	1.92(2)	–	–	8.1(2)	–	3.16(3)	3.84(5)	4.56(5)
$\Delta F^{(3)}_R(Q)$	1.06(2)	1.97(2)	–	–	8.0(2)	–	3.07(3)	3.85(5)	4.70(5)
$\Delta F^{(1)}(Q)$	1.05(2)	2.22(2)	3.67(2)	4.0(1)	–	2.24(2)	–	3.59(5)	–
$\Delta F^{(2)}(Q)$	1.05(2)	2.23(2)	3.67(2)	4.1(1)	–	2.25(2)	–	3.61(5)	–
$\Delta F^{(3)}(Q)$	1.05(2)	2.21(2)	3.67(2)	4.1(1)	–	2.24(2)	–	3.57(5)	–
$^{\mathrm{La}}S_X(Q)$	1.08(2)	2.19(2)	3.71(2)	4.0(1)	8.5(2)	2.25(2)	3.03(3)	3.66(5)	–
$^{\mathrm{Mix}}S_X(Q)$	1.08(2)	2.19(2)	3.71(2)	4.1(1)	8.4(2)	2.25(2)	3.03(3)	3.66(5)	–
$^{\mathrm{Ce}}S_X(Q)$	1.08(2)	2.19(2)	3.71(2)	4.1(1)	8.4(2)	2.25(2)	3.03(3)	3.66(5)	–

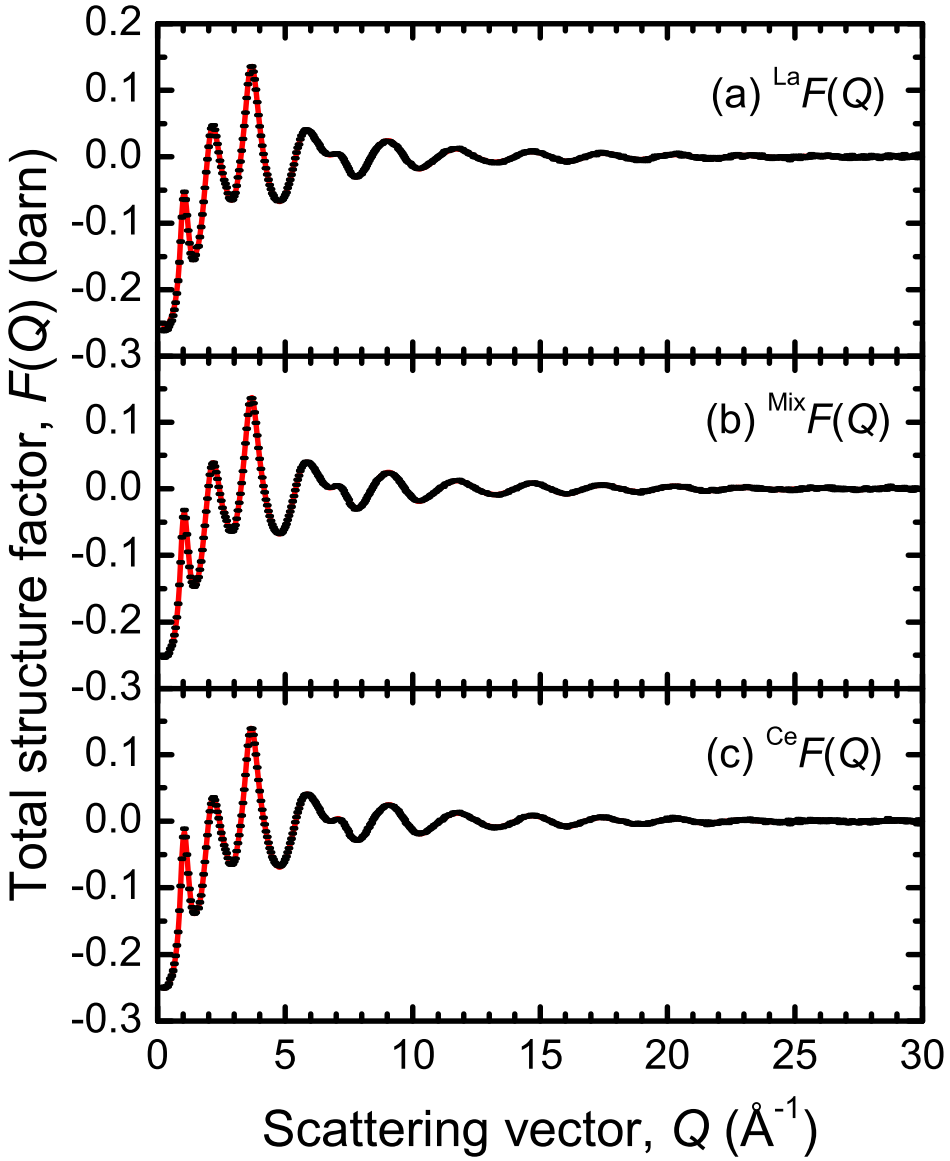

Figure 5.11: The total structure factors (a) $^{La}F(Q)$, (b) $^{Mix}F(Q)$, and (c) $^{Ce}F(Q)$ for the $(R_2S_3)_{0.07}(Ga_2S_3)_{0.33}(GeS_2)_{0.60}$ glasses as measured by neutron diffraction on the GEM instrument at ISIS. The bars represent the statistical errors and the solid (red) curves are the Fourier back-transforms of the corresponding $G(r)$ functions, plotted in figure 5.12, after the un-physical low-r oscillations are set to the theoretical $G(0)$ limits listed in table 5.2.

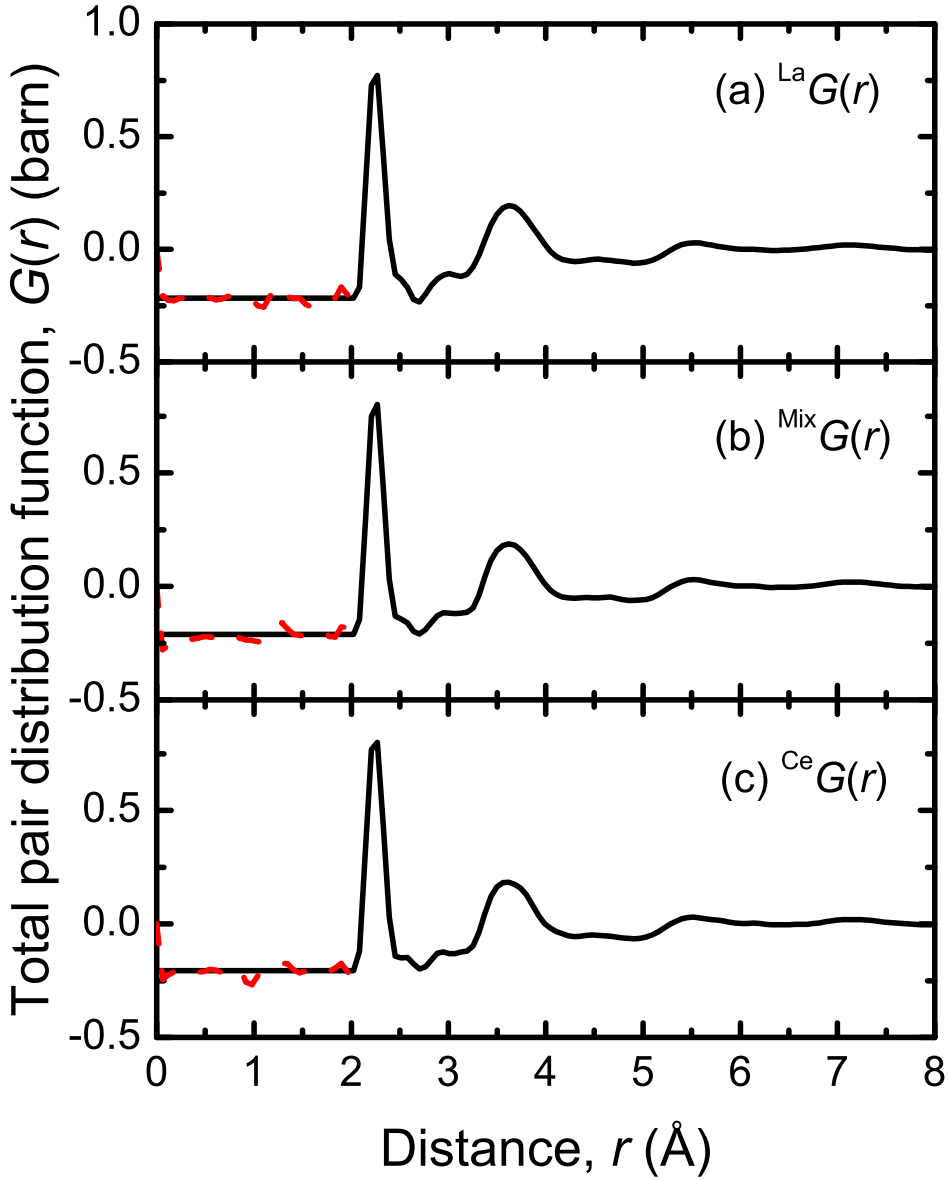

Figure 5.12: The total pair distribution functions (a) $^{\mathrm{La}}G(r)$, (b) $^{\mathrm{Mix}}G(r)$, and (c) $^{\mathrm{Ce}}G(r)$ for the $(R_2S_3)_{0.07}(Ga_2S_3)_{0.33}(GeS_2)_{0.60}$ glasses as obtained by Fourier transforming the corresponding $F(Q)$ functions in figure 5.11 after making a Harwell spline fit [115] to the data and applying a cosine window function between 25 and 30 Å^{-1}. The dashed (red) curves indicate the extent of the un-physical low-r oscillations.

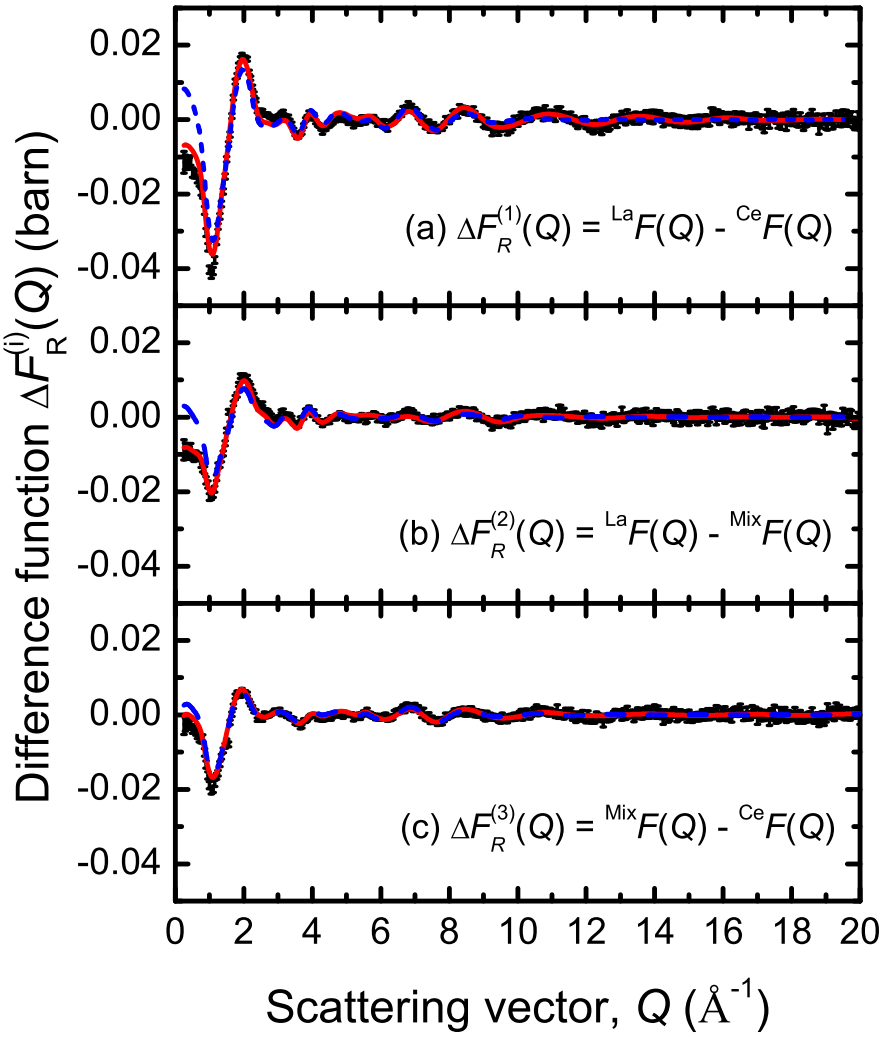

Figure 5.13: First order difference functions (a) $\Delta F_R^{(1)}(Q)$, (b) $\Delta F_R^{(2)}(Q)$, and (c) $\Delta F_R^{(3)}(Q)$, for the $(R_2S_3)_{0.07}(Ga_2S_3)_{0.33}(GeS_2)_{0.60}$ glasses. The bars represent the statistical errors. The solid (red) curves are the Fourier back-transforms of the corresponding $\Delta G_R^{(i)}(r)$ $(i = 1, 2, 3)$ functions, plotted in figure 5.15, after the un-physical low-r oscillations up to the onset of the nearest neighbour bond distance in the $G(r)$ functions ($r_{\rm cut} = 2.02$ Å) are set to the theoretical $\Delta G_R^{(i)}(0)$ limits listed in table 5.2. The dashed (blue) curves are the Fourier back-transforms of the corresponding $\Delta G_R^{(i)}(r)$ $(i = 1, 2, 3)$ functions after the un-physical low-r oscillations, up to the onset of the R-S peak ($r_{\rm cut} = 2.76$ Å), are set to the theoretical $\Delta G_R^{(i)}(0)$ limits.

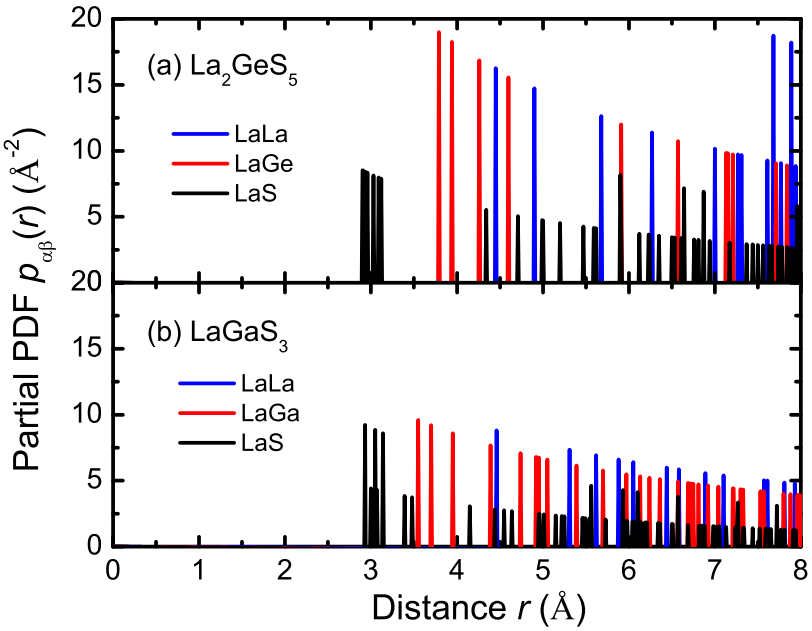

Figure 5.14: Partial pair distribution (PDF) functions $p_{\alpha\beta}(r)$ involving La calculated using the DISCUS program [202] from the unit cell parameters of (a) crystalline La_2GeS_5 [203] and (b) crystalline $LaGaS_3$ [204] for neutron radiation and neglecting the broadening effect of thermal motions.

those reported for GeS_2 [205–207] and Ga_2S_3 [208–210]. Instead, by comparison with the nearest neighbour Ga-Ga bond distances $2.44 \leq r_{\mathrm{GaGa}}$ (Å) ≤ 2.82 reported for liquid Ga [213–218] and $r_{\mathrm{GaGa}} = 2.48$ Å reported for crystalline Ga [219], the shoulder may indicate the existence of Ga-Ga homopolar bonds. Integrating the $G(r)$ functions over a shorter range of $2.02 \leq r$ (Å) ≤ 2.52 to exclude this shoulder results in a smaller coordination number $\bar{n}^{\mathrm{S}}_{\mathrm{Ge}} \simeq 3.6(1)$ suggesting that the Ga-Ga correlations do play a small but important role in the bonding of the basic structural units.

The second much smaller peak in the $G(r)$ functions at a mean distance $r_2 = 2.97(3)$ Å undergoes a progressive reduction in intensity from the glass containing La to the mixture to Ce, which is consistent with this peak arising from correlations involving the rare earth ion since $b_{\mathrm{La}} > b_{\mathrm{Mix}} > b_{\mathrm{Ce}}$. The peak

is attributed to the nearest neighbour R-S correlations by comparison with the partial atomic pair distribution (PDF) functions plotted in figure 5.14, as calculated from the unit cell parameters of the La_2GeS_5 [203] and $LaGaS_3$ [204] crystal structures using the DISCUS program [202]. The coordination number $\bar{n}_R^S$ was obtained from the R-S peak in the $G(r)$ functions by integrating over the range $2.76 \leq r$ (Å) ≤ 3.19. However, different values were obtained from each $G(r)$ (see table 5.4) which may indicate that other correlations involving matrix atoms also contribute to the peak.

The real space first order difference functions $\Delta G_R^{(i)}(r)$ $(i = 1, 2, 3)$ are plotted in figure 5.15 and were obtained by Fourier transforming the corresponding $\Delta F_R^{(i)}(Q)$ functions after making a Harwell spline fit [115] to the data and applying a cosine window function between 15 and 20 Å^{-1}. By comparison with the calculated PDF functions shown in figure 5.14, the first peak in the $\Delta G_R^{(i)}(r)$ functions at a mean distance $r_2 = 3.09(3)$ Å is attributed to the nearest neighbour R-S correlations alone, the second peak at a mean distance $r_3 = 3.86(5)$ Å is attributed to a superposition of R-Ge and R-Ga correlations and the third peak at a mean distance $r_4 = 4.65(5)$ Å is consistent with the nearest neighbour R-R distance. It is noted, however, that the Fourier backtransforms of the $\Delta G_R^{(i)}(r)$ functions after the low-r oscillations, up to the onset of the R-S peak at $r_{\text{cut}} = 2.76$ Å, are set to the theoretical $\Delta G_R^{(i)}(0)$ limits (listed in table 5.2) do not agree with the $\Delta F_R^{(i)}(Q)$ functions at low Q values (see figure 5.13). This suggests that the μ-μ' correlations, involving only the matrix atoms (μ, μ' = Ge, Ga, S), are not entirely eliminated in the first order difference functions. The Fourier backtransforms of the $\Delta G_R^{(i)}(r)$ functions after the low-r oscillations up to the onset of the nearest neighbour peak in the $G(r)$ functions at $r_{\text{cut}} = 2.02$ Å are set to the theoretical $\Delta G_R^{(i)}(0)$ limits are, however, in good overall agreement with the $\Delta F_R^{(i)}(Q)$ functions. Nevertheless, consistent values were obtained for the coordination number $\bar{n}_R^S$ from the R-S peak in the $\Delta G_R^{(i)}(r)$ functions (see table 5.4) by integrating over the range $2.76 \leq r$ (Å) ≤ 3.50 giving a mean value of $\bar{n}_R^S = 8.1(2)$.

The total minus weighted difference functions $\Delta F^{(i)}(Q)$ $(i = 1, 2, 3)$ are

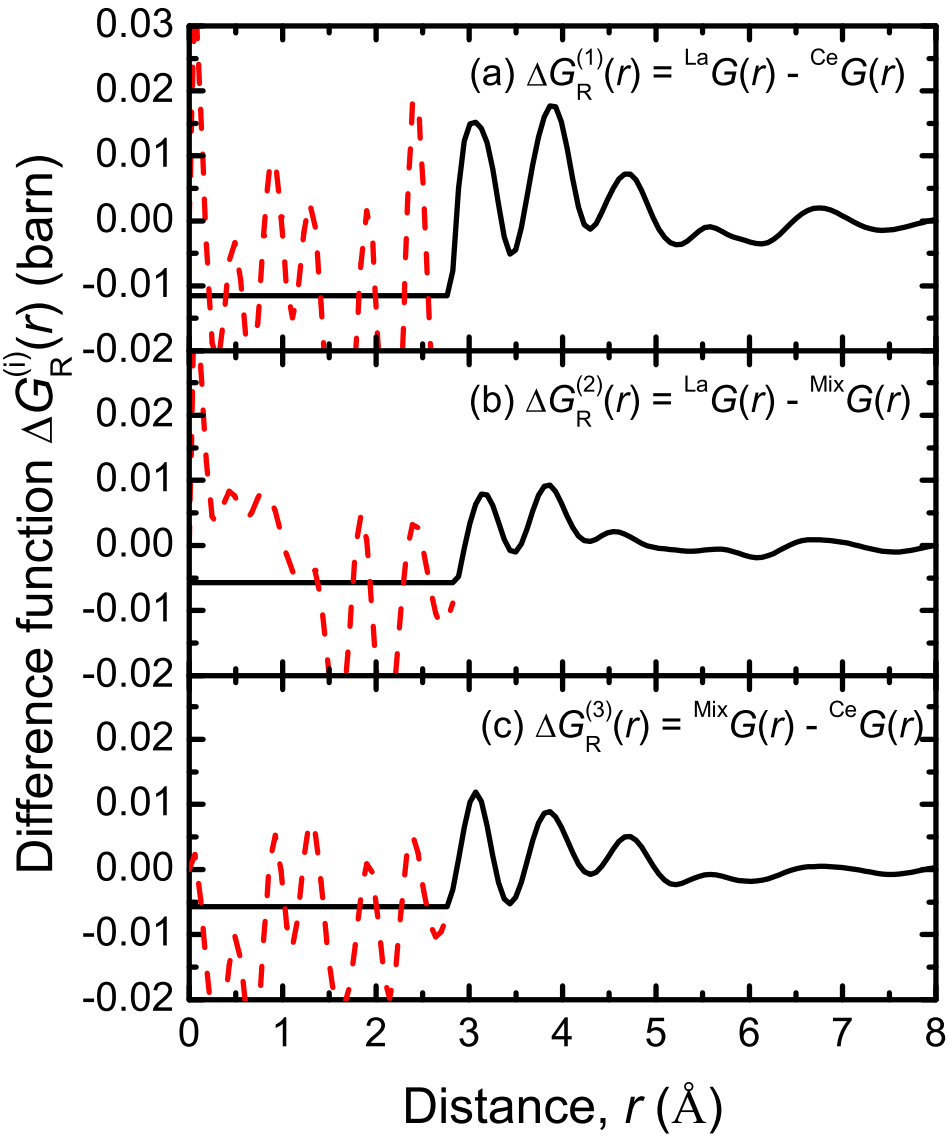

Figure 5.15: Real space first order difference functions (a) $\Delta G_R^{(1)}(r)$, (b) $\Delta G_R^{(2)}(r)$ and (c) $\Delta G_R^{(3)}(r)$, for the $(R_2S_3)_{0.07}(Ga_2S_3)_{0.33}(GeS_2)_{0.60}$ glasses, as obtained by Fourier transforming the corresponding $\Delta F_R^{(i)}(Q)$ (i=1,2,3) functions, plotted in figure 5.13, after making a Harwell spline fit [115] to the data and applying a cosine window function between 15 Å^{-1} and 20 Å^{-1}. The dashed curves indicate the extent of the un-physical low-r oscillations.

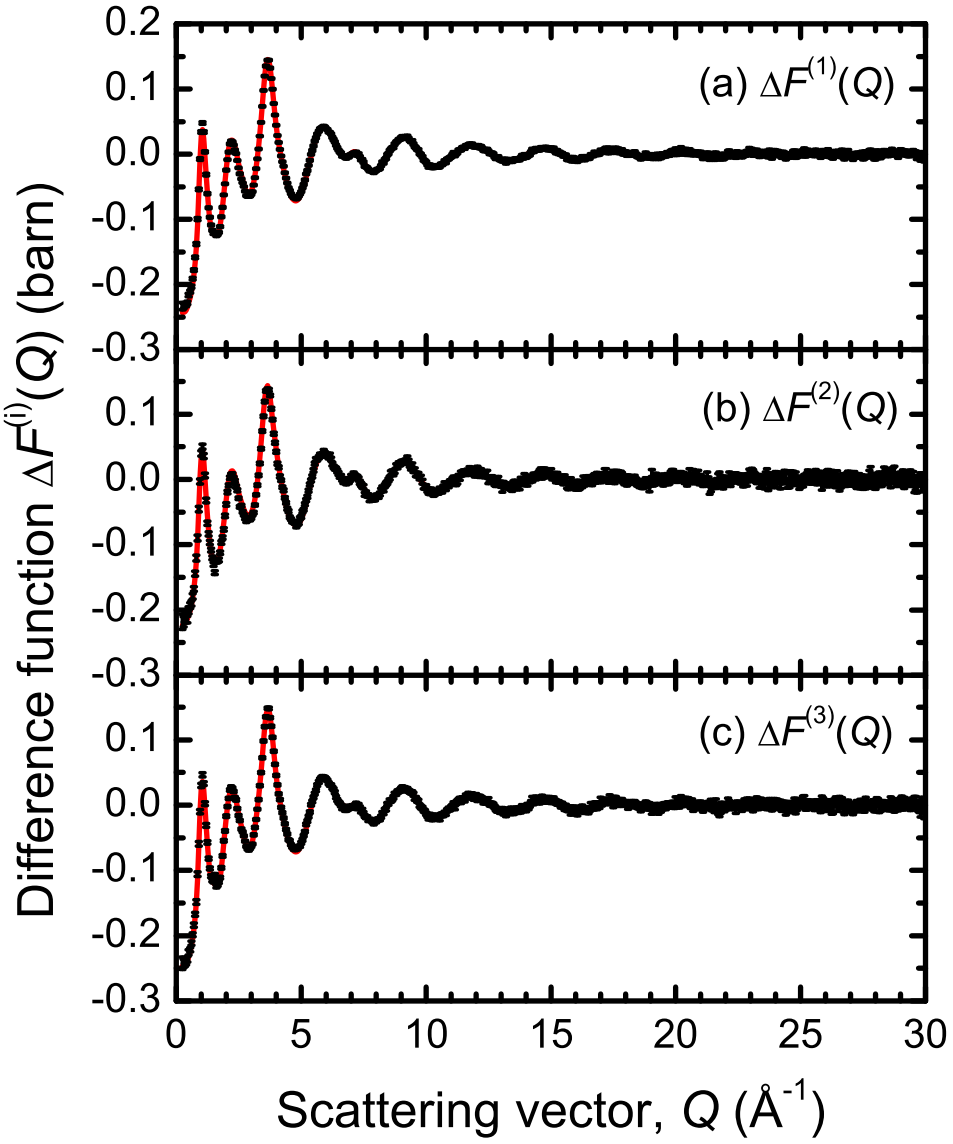

Figure 5.16: Total minus weighted difference functions (a) $\Delta F^{(1)}(Q)$, (b) $\Delta F^{(2)}(Q)$, and (c) $\Delta F^{(3)}(Q)$ for the $(R_2S_3)_{0.07}(Ga_2S_3)_{0.33}(GeS_2)_{0.60}$ glasses. The bars represent the statistical errors and the solid (red) curves are the Fourier back-transforms of the corresponding $\Delta G^{(i)}(r)$ functions, plotted in figure 5.18, after the un-physical low-r oscillations are set to the theoretical $\Delta G^{(i)}(0)$ limits listed in table 5.2.

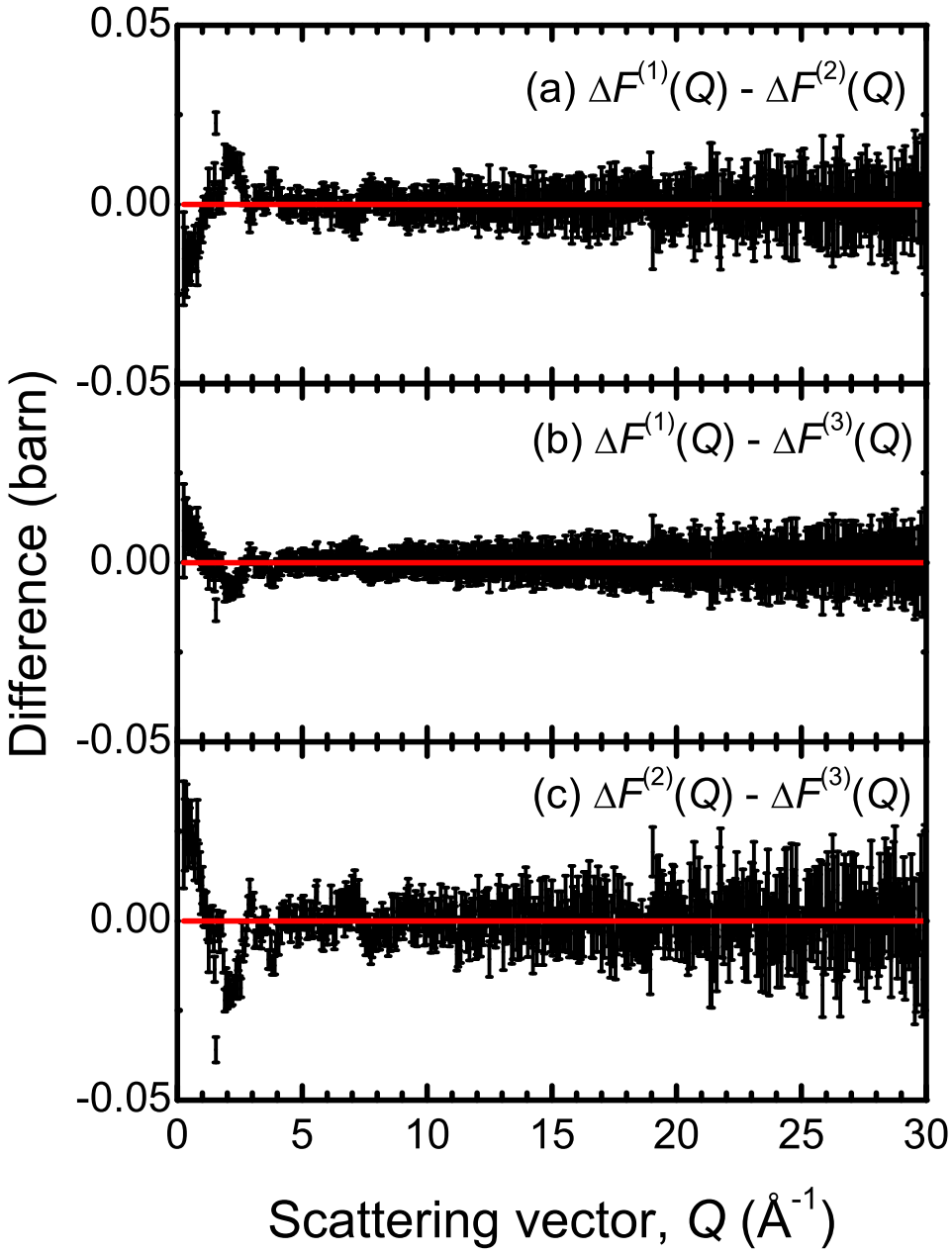

Figure 5.17: Differences between the total minus weighted difference functions plotted in figure 5.16 where (a) $\Delta F^{(1)}(Q) - \Delta F^{(2)}(Q)$, (b) $\Delta F^{(1)}(Q) - \Delta F^{(3)}(Q)$ and (c) $\Delta F^{(2)}(Q) - \Delta F^{(3)}(Q)$ are zero within the statistical errors (represented by the bars) beyond $Q \simeq 5$ Å^{-1}.

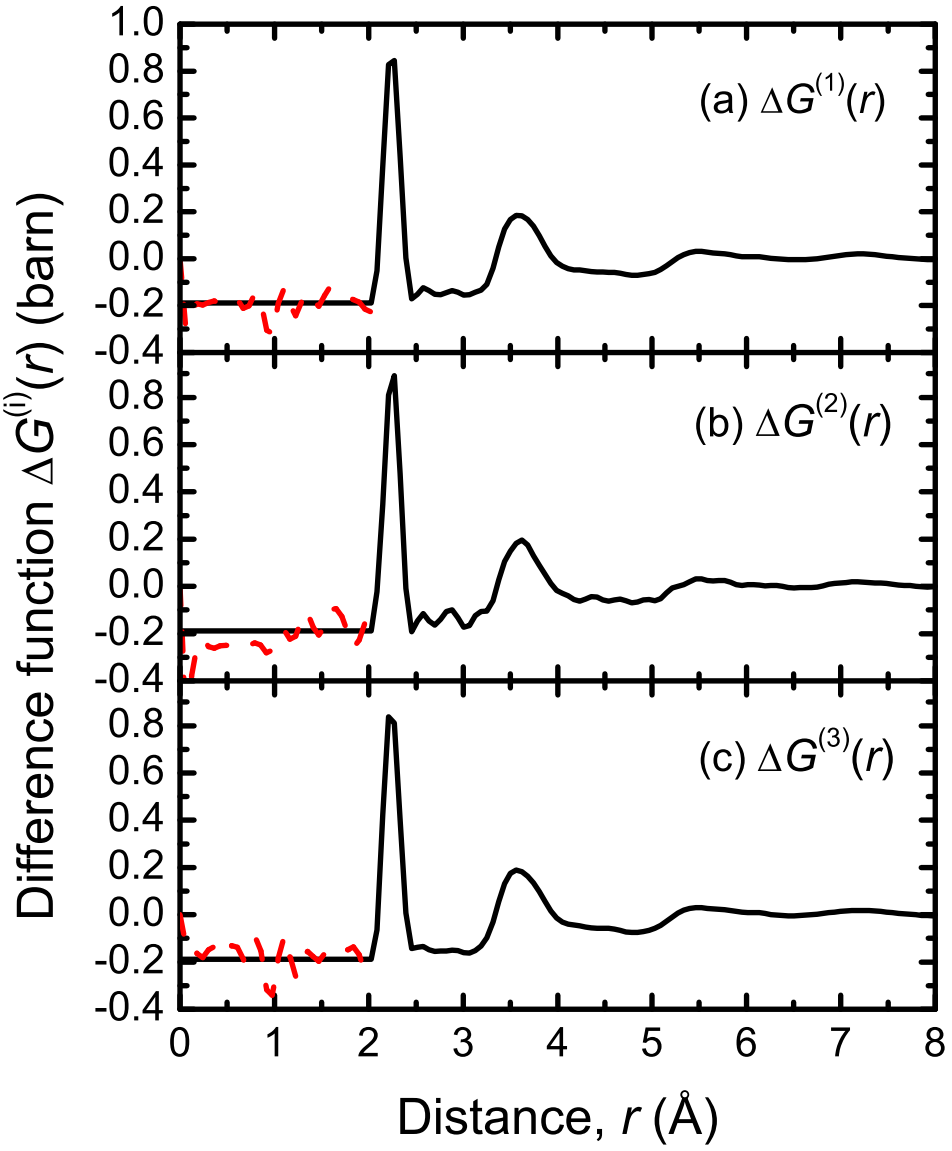

Figure 5.18: Real space total minus weighted difference functions (a) $\Delta G^{(1)}(r)$, (b) $\Delta G^{(2)}(r)$ and (c) $\Delta G^{(3)}(r)$ for the $(R_2S_3)_{0.07}(Ga_2S_3)_{0.33}(GeS_2)_{0.60}$ glasses, as obtained by Fourier transforming the corresponding $\Delta F^{(i)}(Q)$ functions, plotted in figure 5.16, after making a Harwell spline fit [115] to the data and applying a cosine window function between 25 Å^{-1} and 30 Å^{-1}. The dashed (red) curves indicate the extent of the un-physical low-r oscillations.

plotted in figure 5.16. They exhibit an FSDP at $q_1 = 1.05(2)$ Å^{-1} which is higher, relative to the peaks at $q_2 \simeq 2.22(2)$ Å^{-1} and $q_3 = 3.67(2)$ Å^{-1}, by comparison to the $F(Q)$ functions. As plotted in figure 5.17, there are some small differences between the $\Delta F^{(i)}(Q)$ functions at low Q. However, beyond $Q \simeq 5$ Å^{-1} the $\Delta F^{(i)}(Q)$ are identical within the statistical uncertainty. The $\Delta G^{(i)}(r)$ functions are plotted in figure 5.18 and were obtained by Fourier transforming the corresponding $\Delta F^{(i)}(Q)$ functions after making a Harwell spline fit [115] to the data and applying a cosine window function between 25 and 30 Å^{-1}. The R-S peak observed in the $G(r)$ and $\Delta G_R^{(i)}(r)$ functions is not present in these functions, which suggests that the $R-\mu$ correlations have been successfully eliminated. The first peak at $r_1 \simeq 2.24(2)$ Å is attributed to a superposition of the Ge-S and Ga-S correlations, as for the $G(r)$ functions. Assuming the number of homopolar bonds to be negligible, a mean coordination number of $\bar{n}^{\mathrm{S}}_{\mathrm{Ge}} \simeq 4.1(1)$ was obtained from the first peak in the $\Delta G^{(i)}(r)$ functions by integrating over the range $2.02 \leq r$ (Å) ≤ 2.64 and subtracting the contribution to the peak area from the Ga-S correlations, for which $\bar{n}^{\mathrm{S}}_{\mathrm{Ga}} = 4$.

The total x-ray structure factors ${}^{\mathrm{La}}S_X(Q)$, ${}^{\mathrm{Mix}}S_X(Q)$ and ${}^{\mathrm{Ce}}S_X(Q)$ for the R-Ge-Ga-S samples, as measured by x-ray diffraction on the ID15B beamline at the ESRF, are plotted in figure 5.19. As shown by figure 5.20, the difference between the $S_X(Q)$ functions for the three R-Ge-Ga-S samples is zero within the statistical error at all Q values. This confirms that the samples are indeed structurally isomorphic. The total x-ray pair distribution functions ${}^{\mathrm{La}}G_X(r)$, ${}^{\mathrm{Mix}}G_X(r)$ and ${}^{\mathrm{Ce}}G_X(r)$ are plotted in figure 5.21 and were obtained by Fourier transforming the corresponding $S_X(Q)$ functions after truncating at a maximum scattering vector $Q_{\mathrm{max}} = 18$ Å^{-1}. The first peak at $r_1 = 2.25(2)$ Å is attributed to a superposition of the Ge-S and Ga-S correlations, by comparison with the neutron diffraction results. In x-ray diffraction, the form factors for Ga and Ge are virtually identical, since the atomic numbers are $Z(\mathrm{Ga}) = 31$ and $Z(\mathrm{Ge}) = 32$. Therefore, by converting the $S_X(Q)$ function to $F_X(Q)$ and dividing by $2c_{\mathrm{S}}f_{\mathrm{S}}(Q)f_{\mathrm{Ge}}(Q)$, the r-dependent weighting factor is removed

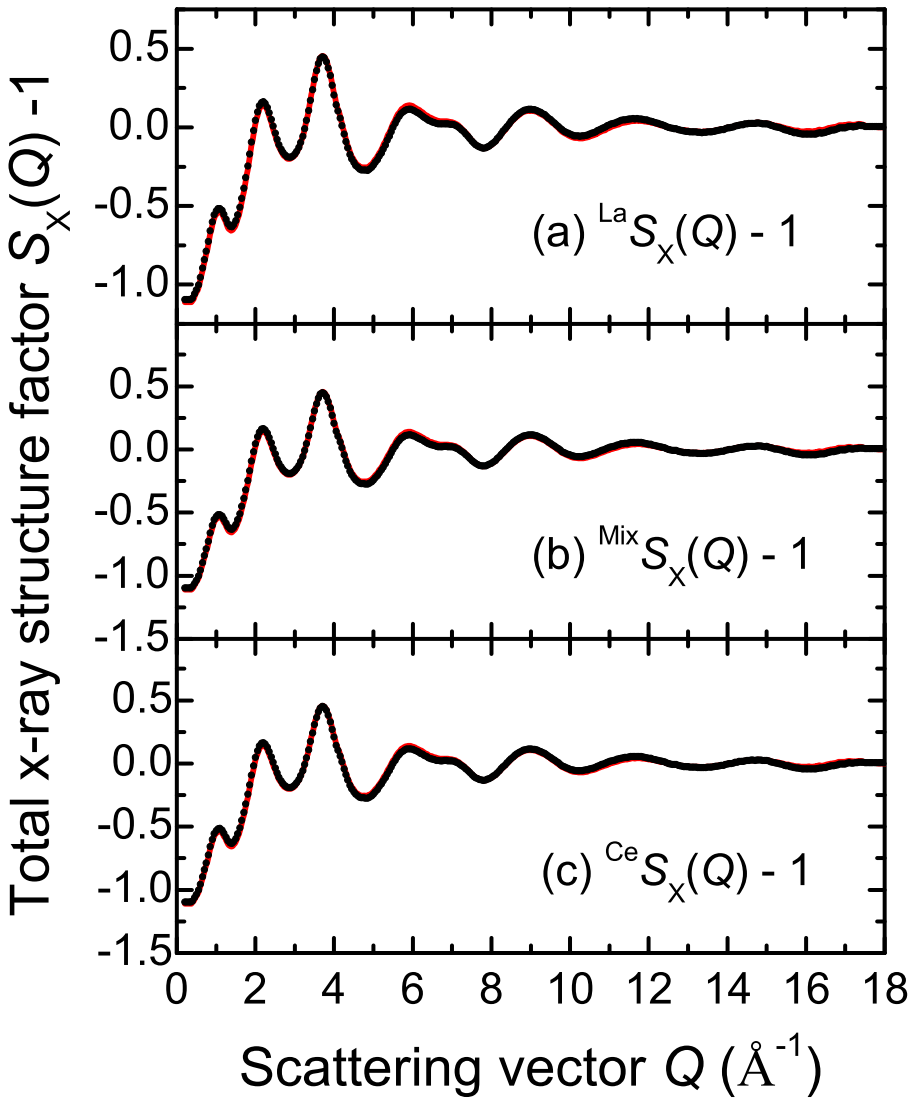

Figure 5.19: The measured total x-ray structure factors (a) $^{\mathrm{La}}S_X(Q)$, (b) $^{\mathrm{Mix}}S_X(Q)$, and (c) $^{\mathrm{Ce}}S_X(Q)$ for the $(R_2\mathrm{S}_3)_{0.07}(\mathrm{Ga}_2\mathrm{S}_3)_{0.33}(\mathrm{GeS}_2)_{0.60}$ glasses as measured by x-ray diffraction on the ID15B beamline at the ESRF. The solid circles represent the measured data points, where the symbol size is larger than the statistical error. The solid (red) curves are the Fourier back-transforms of the corresponding total pair distribution functions $G_X(r)$ of figure 5.21 after the un-physical low-r oscillations are set to the theoretical $G_X(0) = 0$ limit.

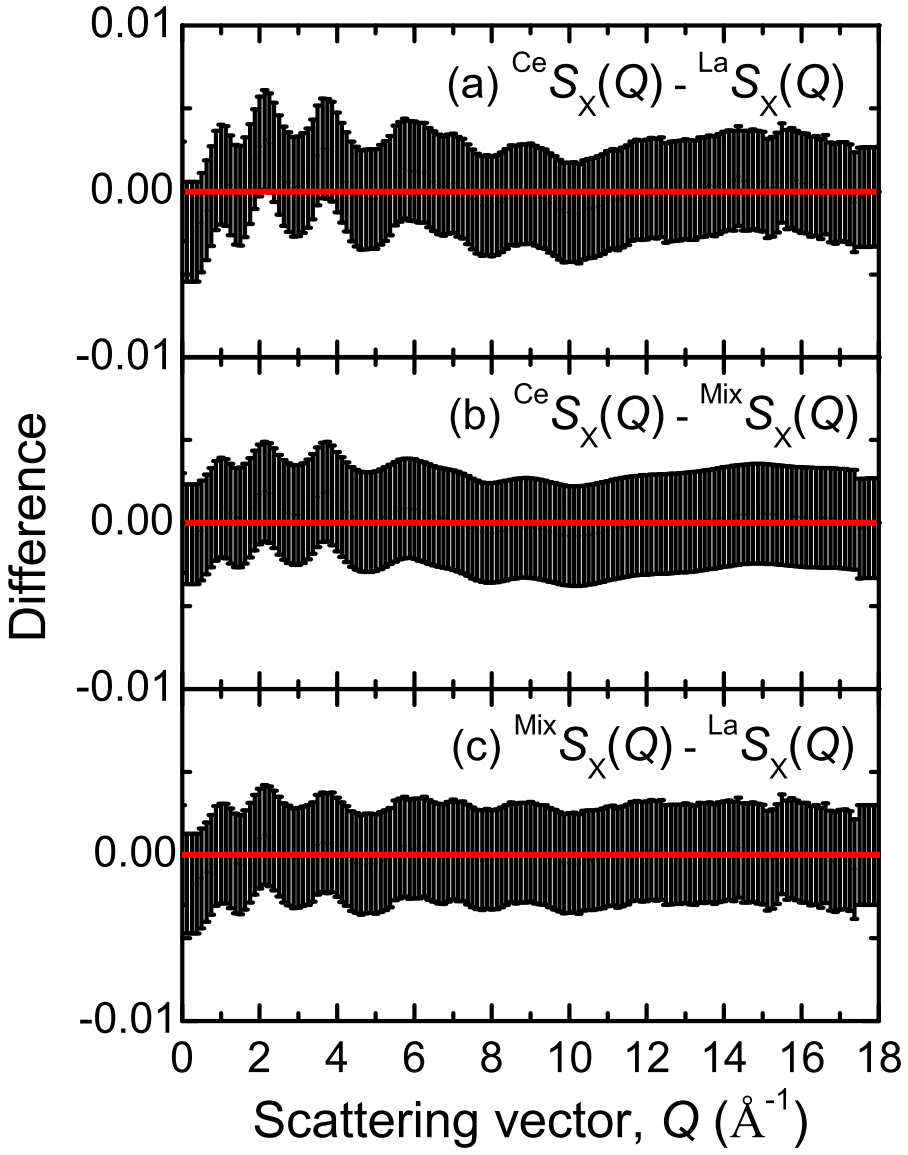

Figure 5.20: Differences between the total x-ray structure factors plotted in figure 5.19 where (a) $^{\mathrm{Ce}}S_X(Q) - ^{\mathrm{La}}S_X(Q)$, (b) $^{\mathrm{Ce}}S_X(Q) - ^{\mathrm{Mix}}S_X(Q)$, and (c) $^{\mathrm{Mix}}S_X(Q) - ^{\mathrm{La}}S_X(Q)$ are zero within the statistical errors (represented by the bars).

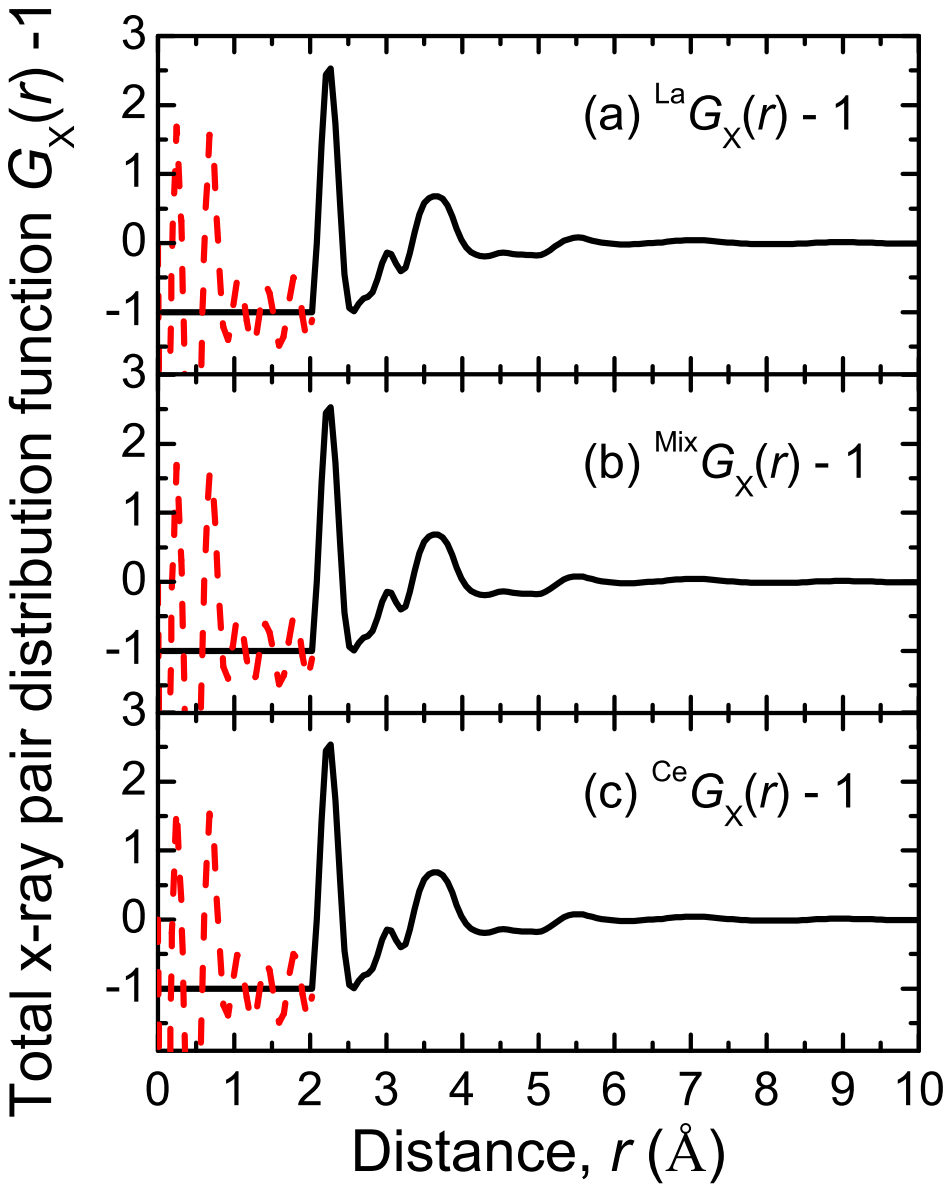

Figure 5.21: Total x-ray pair distribution functions (a) $^{La}G_X(r)$, (b) $^{Mix}G_X(r)$, and (c) $^{Ce}G_X(r)$ obtained by Fourier transforming the corresponding $S_X(Q)$ functions of figure 5.19 after truncating at a maximum scattering vector $Q_{max} = 18$ Å^{-1}. The dashed (red) curves indicate the extent of the un-physical low-r oscillations.

from the $g_{\mathrm{GeS}}(r)$ and $g_{\mathrm{GaS}}(r)$ partial pair distribution functions in the Fourier transform [191]. A coordination number $\bar{n}^{\mathrm{S}}_{\mathrm{Ge}} \simeq 4.0(1)$ was calculated from the first peak in the resulting real space functions by integrating over the range $1.90 \leq r$ (Å) ≤ 2.64 and subtracting the contribution to the peak area from the Ga-S correlations, for which $\bar{n}^{\mathrm{S}}_{\mathrm{Ga}} = 4$ was confirmed by the ^{71}Ga MAS NMR spectrum (see figure 5.6). The second peak in the $G_X(r)$ functions at $r_2 = 3.03(3)$ Å is attributed to the R-S correlations, by comparison with the neutron diffraction results. The peak is much more prominent in the x-ray $G_X(r)$ functions by comparison to the neutron $G(r)$ functions, owing to the greater x-ray scattering power of the high Z rare earth ions by comparison with the matrix species. By converting each $S_X(Q)$ function to $F_X(Q)$ and dividing by $2c_{\mathrm{S}}c_R f_R(Q) f_{\mathrm{S}}(Q)$, consistent values were obtained for the coordination number $\bar{n}^{\mathrm{S}}_R$ from the R-S peak in the resulting Fourier transform by integrating over the range $2.70 \leq r$ (Å) ≤ 3.19 (see table 5.4). The x-ray diffraction data give a mean value of $\bar{n}^{\mathrm{S}}_R = 8.4(2)$.

5.6 Discussion

Very few structural studies have been performed on the glassy R-Ge-Ga-S system and crystal structures of this system are not reported in the literature. Crystal structures are, however, reported for R-Ge-S and R-Ga-S systems containing the rare earth ions R = La, Ce, Pr, Eu, Dy, Ho, Er, Yb or Y, for which the details of the nearest neighbour coordination environment of the rare earth ions are listed in table 5.5. The local structure of R_2S_3-Ga_2S_3-GeS_2 glasses has been studied by EXAFS spectroscopy [186–189, 227] and Raman spectroscopy has also been performed to investigate the solubility mechanism of La^{3+} [158] and Er^{3+} [156] in GeS_2-Ga_2S_3 glasses. The Raman measurements propose a structural model in which the R^{3+} ion acts as a charge compensator to non-bridging S atoms and GaS_4^{-1} tetrahedra in the glass network.

The first peak in the $G(r)$ and $G_X(r)$ functions at $r_1 \simeq 2.25(2)$ Å measured in the present study is attributed to a superposition of Ge-S and Ga-S

Table 5.5: The R-S nearest neighbour distance $r_{R\mathrm{S}}$, average coordination number $\bar{n}^{\mathrm{S}}_{R}$ and the minimum nearest neighbour R-R distance r_{RR} (min) for R-Ge-S or R-Ga-S crystal structures, where R represents a rare earth element La, Ce, Pr, Eu, Dy, Ho, Er, Yb or Y.

Crystal	$r_{R\mathrm{S}}$ (Å)	$\bar{n}^{\mathrm{S}}_{\mathrm{R}}$	$r_{R\mathrm{Ge}}$ (Å)	$r_{R\mathrm{Ga}}$ (Å)	r_{RR} (min) (Å)	Reference
La_2GeS_5	2.84-3.33	8.5	3.77-4.26	–	4.30	[203]
$LaGaS_3$	2.82-3.48	8.3	–	3.50-4.39	4.33	[204]
$Ce_4(GeS_4)_3$	2.86-3.37	9	3.69-4.32	–	4.01	[211]
$Pr_4Ge_3S_{12}$	2.70-3.70	9	3.69-4.08	–	3.99	[212]
Eu_2GeS_4	2.99-3.10	8.5	3.53-4.00	–	4.06	[220]
$EuGa_2S_4$	3.05-3.12	8	–	3.83-3.93	5.10	[221]
$Dy_6Ge_{2.5}S_{14}$	2.68-3.05	7	3.27-4.25	–	4.22	[222]
$Ho_3Ge_{1.25}S_7$	2.69-3.01	7	3.21-4.25	–	4.20	[223]
Er_3GaS_6	2.59-2.96	7	–	3.56-4.40	3.83	[224]
$YbGa_2S_4$	2.99-3.06	8	–	3.74-4.40	4.99	[225]
$Y_3Ge_{1.25}S_7$	2.74-3.02	7	3.23-4.26	–	4.21	[226]

correlations. This is consistent with the bond distances of $r_{\mathrm{GeS}} = 2.21(1)$ Å and $r_{\mathrm{GaS}} = 2.31(1)$ Å measured by EXAFS for $(La_2S_3)_{0.30}(Ga_2S_3)_{0.50}(GeS_2)_{0.20}$ glass [187]. The measured coordination numbers $\bar{n}^{\mathrm{S}}_{\mathrm{Ge}} = 4$ and $\bar{n}^{\mathrm{S}}_{\mathrm{Ga}} = 4$ from the present study are also in agreement with EXAFS results that are invariant with composition [187, 227]. The mean R-S bond distance $r_{R\mathrm{S}} = 3.03(9)$ Å obtained from the present study is in agreement with the range of R-S bond distances found in R-Ge-S and R-Ga-S crystal structures (see table 5.5). The EXAFS measurements give R-S bond distances $r_{\mathrm{LaS}} = 2.990$ Å and $r_{\mathrm{CeS}} = 2.961$ Å in $(R_2S_3)_{0.30}(Ga_2S_3)_{0.50}(GeS_2)_{0.20}$ glass which undergoes an overall reduction of 0.28 Å with the substitution of La by Lu [186]. This is consistent with the reduction in ion radius caused by the lanthanoid contraction and is supported by the reduction in the R-S bond distances reported for crystalline structures as R is changed from La to Y (see table 5.5).

A mean coordination number $\bar{n}^{\mathrm{S}}_{R} = 8.1(2)$ was obtained from the first order difference functions in the neutron diffraction experiment and a mean value of 8.4(2) was obtained from the R-S peak in the total x-ray pair distribution functions. Coordination numbers in the range $7 \leq \bar{n}^{\mathrm{S}}_{R} \leq 8.5$ are reported

in the literature for crystalline La_2GeS_5 [203] and $LaGaS_3$ [204] and, from EXAFS measurements, glassy La_2S_3-Ga_2S_3 [227] and Ce_2S_3-$Ga_2S_3GeS_2$ [186]. The values for the coordination number $\bar{n}_R^S$ compare with characteristic values of $\bar{n}_R^O \simeq 8$ for large rare earth ions in R-P-O [228] and R-Al-Si-O [58] glasses.

5.7 Conclusions

The structure of $(R_2S_3)_{0.07}(Ga_2S_3)_{0.33}(GeS_2)_{0.60}$ glass, where R denotes La, Ce or a 50:50 mixture of the two, was studied using a combination of neutron diffraction, high energy x-ray diffraction and ^{71}Ga MAS NMR. The total x-ray structure factor for the samples are identical at all Q values confirming that the samples are structurally isomorphic. The main resonance in the ^{71}Ga MAS NMR spectrum at $\delta = 250(5)$ ppm is attributed to 4 fold coordinated Ga by comparison with the α and β phases of Ga_2O_3 [196]. This is consistent with the neutron and x-ray diffraction results which give a coordination number of $\bar{n}_{Ge}^S = 4$ when $\bar{n}_{Ga}^S = 4$. Evidence for Ga-Ga homopolar bonds was found in the neutron diffraction results.

A mean nearest neighbour R-S bond distance of $r_{RS} = 3.03(3)$ Å is obtained from the neutron and x-ray diffraction measurements. The first order difference functions $\Delta F_R^{(i)}$ $(i = 1, 2, 3)$ and total x-ray pair distribution functions $G_X(r)$ give coordination numbers $\bar{n}_R^S = 8.1(2)$ and $\bar{n}_R^S = 8.4(2)$, respectively. Since the atomic concentration $c_R = 3.68$ % of the rare earth ions is close to the rare earth solubility limit in this glass system [171], the first order difference functions provide an estimate for the minimum separation of rare earth ions to be $r_{RR} = 4.65(5)$ Å.

6. Structure of La/Ce-Ge-Ga-Se glasses by the method of isomorphic substitution in neutron diffraction

6.1 Introduction

The aim of this experiment is to use the method of isomorphic substitution in neutron diffraction to measure the structure of a R-Ge-Ga-Se glass, where R represents La or Ce. The phase diagram for the La_2Se_3-Ga_2Se_3-$GeSe_2$ system is plotted in figure 6.1 [162], where the glass forming region is extended significantly, by comparison with the sulphide system (see figure 5.1), to approximately 50 mol% Ga_2Se_3 and approximately 25 mol% La_2Se_3. The glass composition $(R_2Se_3)_{0.07}(Ga_2Se_3)_{0.33}(GeSe_2)_{0.60}$ was chosen for investigation to match the sulphide composition studied in chapter 5. This composition also lies well within the glass forming region of figure 6.1 and contains a relatively large atomic fraction of rare earth ion $c_R = 3.68$ % which is required to obtain a measurable scattering intensity contrast for the different rare earth glasses. The structure and properties of the R-Ge-Ga-Se glass will also be compared to the structure of glassy $GeSe_2$ [229] and $(GeSe_2)_{0.87}(Ga_2Se_3)_{0.13}$ as measured by neutron diffraction to investigate the effect on the glass structure of adding Ga_2Se_3 followed by R_2Se_3.

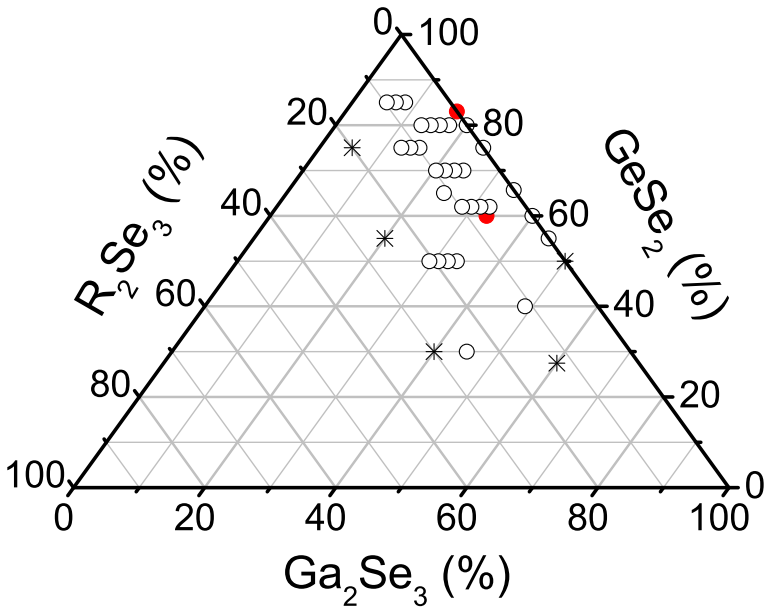

Figure 6.1: The glass forming region for the ternary system R_2Se_3-Ga_2Se_3-$GeSe_2$, where R=La [162]. The open circles denote glass forming compositions, the stars denote partially crystalline compositions and the solid (red) circles denote glass compositions synthesised for this study.

6.2 Theory

As derived in § 2.2, the coherent scattered intensity obtained by a neutron diffraction experiment on a R-Ge-Ga-Se glass is represented by the total structure factor

$$F(Q) = \sum_{\alpha=1}^{n} \sum_{\beta=1}^{n} c_\alpha c_\beta b_\alpha b_\beta [S_{\alpha\beta}(Q) - 1], \tag{6.1}$$

where $n = 4$ is the total number of chemical species denoted by α or β, c_α and b_α represent the atomic fraction and coherent neutron scattering length of chemical species α, respectively, $S_{\alpha\beta}(Q)$ is a Faber-Ziman partial structure factor and Q is the scattering vector. The natural isotopic abundance coherent

neutron scattering lengths are $b_{\mathrm{Se}} = 7.970(9)$ fm, $b_{\mathrm{Ga}} = 7.288(2)$ fm, $b_{\mathrm{Ge}} = 8.185(20)$ fm, $b_{\mathrm{La}} = 8.24(4)$ fm and $b_{\mathrm{Ce}} = 4.84(2)$ fm [30]. Expanding in terms of the partial structure factors $S_{\mu\mu'}(Q)$, that involve only the matrix atom species (Ge, Ga, Se), and the partial structure factors $S_{R\mu}(Q)$ or $S_{RR}(Q)$, that involve the rare earth species R, we can write $F(Q)$ as

$$\begin{aligned} F(Q) &= c_R^2 b_R^2 \left[S_{RR}(Q) - 1\right] + 2c_R c_{\mathrm{Se}} b_R b_{\mathrm{Se}} \left[S_{R\mathrm{Se}}(Q) - 1\right] \\ &+ 2c_R c_{\mathrm{Ge}} b_R b_{\mathrm{Ge}} \left[S_{R\mathrm{Ge}}(Q) - 1\right] + 2c_R c_{\mathrm{Ga}} b_R b_{\mathrm{Ga}} \left[S_{R\mathrm{Ga}}(Q) - 1\right] \\ &+ \sum_{\mu=1}^{m} \sum_{\mu'=1}^{m} c_\mu c_{\mu'} b_\mu b_{\mu'} \left[S_{\mu\mu'}(Q) - 1\right], \end{aligned} \tag{6.2}$$

where $m = 3$ is the total number of matrix atom species denoted by μ or μ'. If the $F(Q)$ functions are measured for samples containing the rare earth isomorphs La^{3+} or Ce^{3+}, for which the neutron scattering lengths $b_{\mathrm{La}} > b_{\mathrm{Ce}}$, then difference function methods can be employed. The $S_{\mu\mu'}(Q)$ partial structure factors may be eliminated by subtracting the two $F(Q)$ functions to yield the first order difference function $\Delta F_R^{(1)}(Q)$, defined as

$$\Delta F_R^{(1)}(Q) \equiv^{\mathrm{La}} F(Q) -^{\mathrm{Ce}} F(Q) = \Delta_{R\mu}^{(1)}(Q) + c_R^2 \left(b_{\mathrm{La}}^2 - b_{\mathrm{Ce}}^2\right) \left[S_{RR}(Q) - 1\right], \tag{6.3}$$

where the matrix to rare earth difference function is given by

$$\begin{aligned} \Delta_{R\mu}^{(1)}(Q) &= 2c_R c_{\mathrm{Se}} b_{\mathrm{Se}} \left(b_{\mathrm{La}} - b_{\mathrm{Ce}}\right) \left[S_{R\mathrm{Se}}(Q) - 1\right] \\ &+ 2c_R c_{\mathrm{Ge}} b_{\mathrm{Ge}} \left(b_{\mathrm{La}} - b_{\mathrm{Ce}}\right) \left[S_{R\mathrm{Ge}}(Q) - 1\right] \\ &+ 2c_R c_{\mathrm{Ga}} b_{\mathrm{Ga}} \left(b_{\mathrm{La}} - b_{\mathrm{Ce}}\right) \left[S_{R\mathrm{Ga}}(Q) - 1\right]. \end{aligned} \tag{6.4}$$

The $S_{R\mu}(Q)$ partial structure factors may be eliminated by subtracting a suitably weighted $\Delta F_R^{(1)}(Q)$ function from the $^{\mathrm{La}}F(Q)$ function to yield the so

Table 6.1: Weighting factors (in millibarn) for the $g_{\alpha\beta}(r)$ partials in the $G(r)$, $\Delta G_R^{(1)}(r)$ and $\Delta G^{(1)}(r)$ functions, together with the limiting values at $r = 0$ (in barn), for glassy $(R_2Se_3)_{0.07}(Ga_2Se_3)_{0.33}(GeSe_2)_{0.60}$ (where R = La or Ce), $GeSe_2$ and $(GeSe_2)_{0.87}(Ga_2Se_3)_{0.13}$.

	$g_{\mathrm{RR}}(r)$	$g_{\mathrm{RSe}}(r)$	$g_{\mathrm{RGe}}(r)$	$g_{\mathrm{RGa}}(r)$	$g_{\mathrm{GeGe}}(r)$	$g_{\mathrm{GeSe}}(r)$	$g_{\mathrm{GeGa}}(r)$	$g_{\mathrm{GaGa}}(r)$	$g_{\mathrm{GaSe}}(r)$	$g_{\mathrm{SeSe}}(r)$	$r = 0$ limit
${}^{\mathrm{La}}G(r)$	0.93(5)	30.7(9)	7.8(3)	7.7(2)	16.5(8)	129(3)	32.59(9)	16.08(2)	127.8(1)	254(2)	-0.623(5)
${}^{\mathrm{Ce}}G(r)$	0.32(2)	18.04(5)	4.60(2)	4.54(1)	16.51(8)	129(3)	32.59(9)	16.08(2)	127.8(1)	254(2)	-0.604(4)
$\Delta G_R^{(1)}(r)$	0.61(5)	12.7(1)	3.23(3)	3.19(3)	0(1)	0(5)	0(1)	0.0(3)	0(1)	0(4)	-0.020(6)
$\Delta G^{(1)}(r)$	-0.5(1)	0(3)	0.0(9)	0.0(6)	17(3)	129(12)	33(3)	16.08(7)	128(3)	254(9)	-0.58(2)
${}^{\mathrm{GeSe_2}}G(r)$	–	–	–	–	74(4)	290(8)	–	–	–	282(6)	-0.65(1)
${}^{\mathrm{GeGaSe}}G(r)$	–	–	–	–	48(4)	227(8)	25.5(6)	3.40(2)	60.7(7)	271(6)	-0.60(1)

called "total minus weighted difference function" given by

$$\begin{aligned}\Delta F^{(1)}(Q) &\equiv {}^{\mathrm{La}}F(Q) - \frac{b_{\mathrm{La}}}{b_{\mathrm{La}} - b_{\mathrm{Ce}}}\Delta F_R^{(1)}(Q) \equiv \frac{b_{\mathrm{La}}\ {}^{\mathrm{Ce}}F(Q) - b_{\mathrm{Ce}}\ {}^{\mathrm{La}}F(Q)}{b_{\mathrm{La}} - b_{\mathrm{Ce}}} \\ &= \sum_{\mu=1}^{m}\sum_{\mu'=1}^{m} c_\mu c_{\mu'} b_\mu b_{\mu'} \left[S_{\mu\mu'}(Q) - 1\right] - c_R^2 b_{\mathrm{La}} b_{\mathrm{Ce}} \left[S_{RR}(Q) - 1\right]. \qquad (6.5)\end{aligned}$$

The real space functions $G(r)$, $\Delta G_R^{(1)}(r)$ and $\Delta G^{(1)}(r)$ are obtained by Fourier transforming the corresponding reciprocal space functions using the relations

$$G(r) = \frac{1}{2\pi^2 r n_0}\int_0^\infty QF(Q)\sin(Qr)\mathrm{d}Q, \qquad (6.6)$$

$$\Delta G_R^{(1)}(r) = \frac{1}{2\pi^2 r n_0}\int_0^\infty Q\Delta F_R^{(1)}(Q)\sin(Qr)\mathrm{d}Q, \qquad (6.7)$$

$$\Delta G^{(1)}(r) = \frac{1}{2\pi^2 r n_0}\int_0^\infty Q\Delta F^{(1)}(Q)\sin(Qr)\mathrm{d}Q, \qquad (6.8)$$

where n_0 is the atomic number density of the glass and r is a distance in real space. The relevant equations for $G(r)$, $\Delta G_R^{(1)}(r)$ and $\Delta G^{(1)}(r)$ are obtained by replacing each $S_{\alpha\beta}(Q)$ by the corresponding partial pair distribution function $g_{\alpha\beta}(r)$ in the equations given for $F(Q)$, $\Delta F_R^{(1)}(r)$ and $\Delta F^{(1)}(r)$, respectively. The theoretical low-r limit of these functions is given by the sum of the weighting factors of the partial pair distribution functions $g_{\alpha\beta}(r)$ as listed in table 6.1. As given in equation 2.12, the coordination number $\bar{n}_\alpha^\beta$ is obtained by integrating over a relevant peak in real space.

6.3 Experimental procedure

6.3.1 Sample preparation

The R-Ge-Ga-Se glasses were prepared by weighing the high purity elements Ge (Aldrich, $\geq$ 3 mm chips, 99.999 %), Ga (Aldrich, 99.9999 %), Se (Aldrich, $\simeq$ 2 mm pellets, 99.999+ %), La (Alpha Aesar, 1 mm thick foil, 99.9 %) and Ce (Alpha Aesar, 1 mm thick foil, 99.9 %) in the correct proportions within

a dry Argon filled glove box at the ISIS facility with levels of $H_2O \leq 2$ ppm and $O_2 \leq 2$ ppm. The Ge and Se elements were powdered using a stainless steel and an agate pestle and mortar, respectively, and the Ga was melted on a hotplate. Strips of La and Ce elements were cut from the supplied foils. The rare earths were incorporated in their elemental form as the corresponding selenides are not readily available from commercial suppliers. Following the procedure outlined in § 5.4.1, the samples were sealed in evacuated silica ampoules and heated in a rocking furnace at a rate of 1 °C min^{-1}, holding for 4 hours at 221 and 685 °C, corresponding to the melting and boiling temperatures of Se, respectively, at 795 or 920 °C, corresponding to the melting temperatures of Ce and La, respectively, and at 937 °C, corresponding to the melting temperature of Ge. Once the final synthesis temperature of 1100 °C had been reached and held for $\geq$ 24 hours, the furnace was rotated vertically and held for a further $\geq$ 12 hours before quenching the glass in an ice-water mixture. Four 3 g batches of glass were prepared to ensure that the vanadium sample container used in the neutron diffraction experiment would be filled. On breaking open the ampoules, the samples came away cleanly from the silica surface. The mean atomic fractions averaged over all of the samples are $c_R = 0.037(1)$, $c_{\mathrm{Ge}} = 0.157(4)$, $c_{\mathrm{Ga}} = 0.174(1)$ and $c_{\mathrm{Se}} = 0.632(3)$, forming the required molar composition $(R_2Se_3)_{0.07}(Ga_2Se_3)_{0.33}(GeSe_2)_{0.60}$.

Figure 6.2: The as quenched *R*-Ge-Ga-Se glasses contained within silica ampoules.

A 3 g batch of glass of composition $(GeSe_2)_{0.87}(Ga_2Se_3)_{0.13}$ was also prepared following the same procedure outlined for the R-Ge-Ga-Se samples using a dry Argon filled glove box environment to fill the silica ampoule, with levels of $H_2O \leq 6$ ppm and $O_2 \leq 30$ ppm, and quenching the ampoule from 1150 °C in an ice-water mixture.

6.3.2 Sample characterisation

Table 6.2: Properties of the $GeSe_2$, $(GeSe_2)_{0.87}(Ga_2Se_3)_{0.13}$ (denoted Ge-Ga-Se) and $(R_2Se_3)_{0.07}(Ga_2Se_3)_{0.33}(GeSe_2)_{0.60}$ glasses (denoted R-Ge-Ga-Se), where R represents La or Ce. The mass density ρ and number density n_0 are listed together with the glass transition temperature T_g, crystallisation temperature T_c and change in heat capacity ΔC_P at T_g as measured by modulated differential scanning calorimetry.

Glass	ρ (g cm^{-3})	n_0 (Å^{-3})	ΔC_P (J g^{-1} °C^{-1})	T_g (°C)	T_c (°C)
$GeSe_2$	4.26(1)	0.0334(1)	0.08(2)	415(2)	487.0(1)
Ge-Ga-Se	4.28(1)	0.0337(1)	0.16(2)	385(2)	460.2(1)
La-Ge-Ga-Se	4.79(1)	0.0367(1)	0.13(2)	403(2)	493.8(1)
Ce-Ge-Ga-Se	4.79(1)	0.0367(1)	–	–	–

The amorphous nature of the R-Ge-Ga-Se samples was confirmed by the absence of crystalline Bragg peaks in the diffraction patterns obtained using a Philips $\theta - 2\theta$ x-ray diffractometer with CuKα radiation of wavelength $\lambda_{K\alpha 1} = 1.54060$ Å and $\lambda_{K\alpha 2} = 1.54439$ Å. The density of each of the samples was measured at the ISIS facility using a Quantachrome helium gas pycnometer and the values are listed in table 6.2 (the density of $GeSe_2$ was taken from Ref. [192]).

The glass transition temperature T_g, crystallisation temperature T_c and change in heat capacity ΔC_p for the glass samples were measured, after the neutron diffraction experiments had been performed, by modulated differential scanning calorimetry (MDSC) using a TA Instruments DSC Q100 machine. The finely powdered samples of mass ≈ 30 mg were contained in crimped aluminium pans and heated over the temperature range $300 \leq T$ °C ≤ 550 at

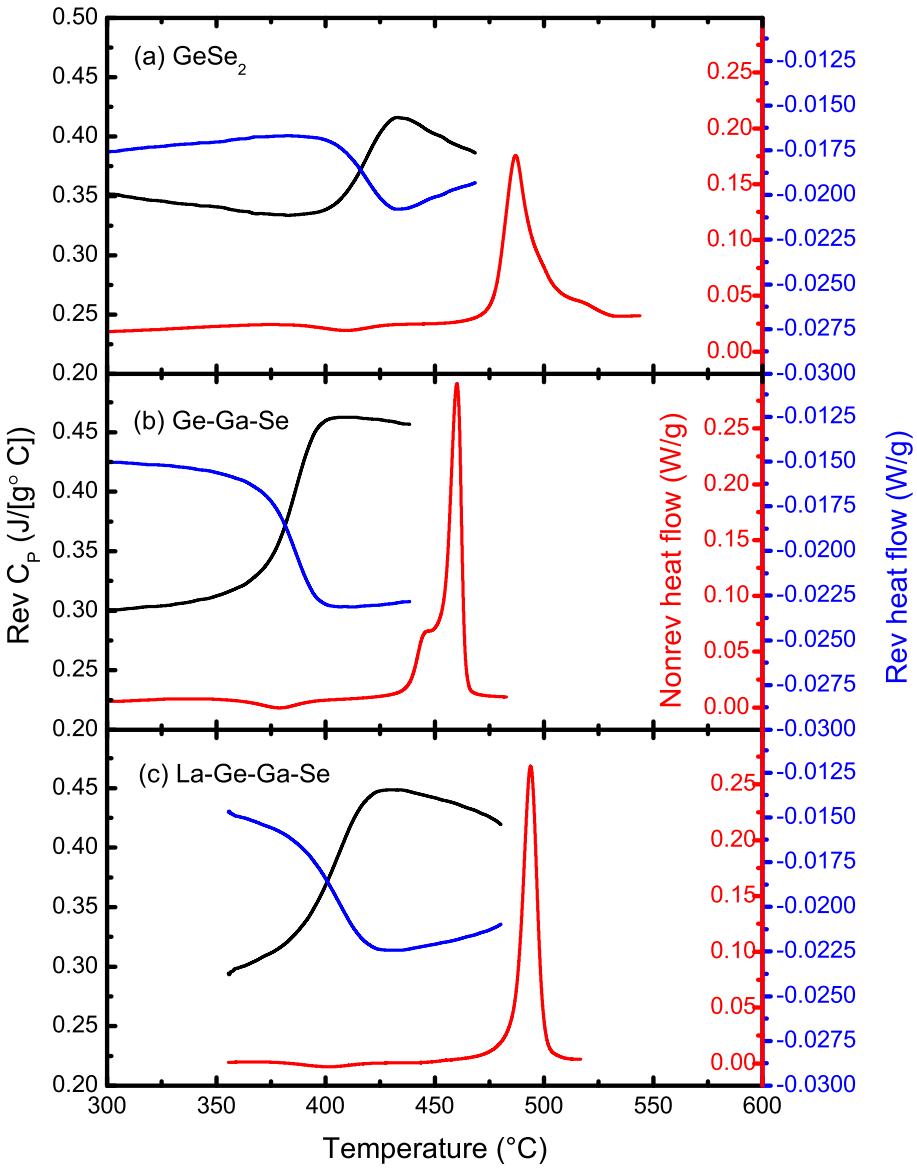

Figure 6.3: Modulated differential scanning calorimetry (MDSC) scans for the glass samples (a) $GeSe_2$, (b) $(GeSe_2)_{0.87}(Ga_2Se_3)_{0.13}$, and (c) $(La_2Se_3)_{0.07}(Ga_2Se_3)_{0.33}(GeSe_2)_{0.60}$, where the blue curve denotes the reversible heat flow, the red curve denotes the non-reversible heat flow and the black curve denotes the reversible heat capacity C_p signal. For clarity, the reversible heat flow and heat capacity signals are truncated before the crystallisation peak.

a rate of 3.00 °C min^{-1} with a temperature modulation of ± 1.00 °C min^{-1}. Nitrogen gas (BOC, Oxygen free), flowing at 50 ml min^{-1}, was used to purge the instrument of moisture and oxygen and to provide efficient heat transfer between the sample pans and the DSC cell contacts. The reversible and non-reversible components of the heat flow and heat capacity C_p were recorded every 0.2 s and are plotted in figure 6.3. The mid-point glass transition temperature T_g was obtained by drawing a tangent line to the data in the transition region of the reversible heat flow to find the point of inflection. The change in heat capacity ΔC_p through T_g was obtained from the observed step in the reversible heat capacity curve. The crystallisation temperature T_c is given by the position of the exothermic peak in the non-reversible heat flow curve. The values of ΔC_P, T_g and T_c are listed in table 6.2.

The glass transition temperature T_g and crystallisation temperature T_c decreases as Ga_2Se_3 is added to $GeSe_2$ glass and subsequently increases with the addition of La_2Se_3. The change in heat capacity ΔC_P in the region of T_g undergoes an increase when Ga_2Se_3 is added to $GeSe_2$ glass and subsequently decreases with the addition of La_2Se_3. These results are consistent with DSC measurements of $(GeS_2)_x(Ga_2Se_3)_{1-x}$ glasses which show a drop in T_g with increasing Ga_2Se_3 content [230, 231] and a subsequent increase in T_g with increasing rare earth content [183]. An analogous effect is also observed in the sulphide system [156, 159, 160].

6.3.3 The neutron diffraction experiments

Neutron diffraction experiments were performed on the *R*-Ge-Ga-Se glasses using the GLAD instrument at the IPNS, described in § 3.2.4, with a maximum scattering vector $Q_{max} = 40.0$ $Å^{-1}$. The coarsely powdered samples were held in cylindrical vanadium containers of 4.64 mm inner diameter and 0.13 mm wall thickness in the GLAD room temperature sample changer (RTSC). Diffraction patterns were taken, alternating between the two samples in their vanadium containers every 864,000 pulses, which, given the IPNS pulse rate of 30 Hz, is equivalent to 8 hours counting time per scan. Since the beam current was

relatively low at 14 to 15 μA, a total counting time of 56 hours per sample was required to obtain reasonable counting statistics. Diffraction patterns were also taken for the empty instrument, empty vanadium containers and a cylindrical vanadium rod of diameter 9.5 mm for calibration purposes. The individual scans showed no deviation outside the statistical variation verifying the diffractometer stability [197]. After eliminating non-functioning or noisy detectors, the ISAW analysis program [232] was used to process the data detector-by-detector, correcting for attenuation, background, multiple scattering and inelasticity effects and normalising to the vanadium standard. The results were then merged and the data set for the Ce sample was corrected for the contribution from Ce^{3+} paramagnetic scattering [36] (see § 2.2.1).

The $(GeSe_2)_{0.87}(Ga_2Se_3)_{0.13}$ glass was measured by neutron diffraction using the GEM instrument at ISIS, described in § 3.2.3, with a maximum scattering vector $Q_{\max} = 49.5$ Å^{-1}. The sample was finely powdered and held in a cylindrical vanadium container of 6.8 mm inner diameter and 0.1 mm wall thickness at ambient temperature (≈ 25 °C). Diffraction patterns were taken for the samples in the vanadium container, the empty vanadium container, the empty instrument and a cylindrical vanadium rod of diameter 8.36 mm. A total run time of 1327.5 μAhr was made to obtain good counting statistics, which at an average ISIS beam current of 170 μA equates to ≈ 8 hours of counting time. After eliminating non-functioning or noisy detectors, the GUDRUN analysis program [111] was used to process the data, correcting detector-by-detector for attenuation, background, multiple scattering, inelasticity effects and normalising to the vanadium standard. The results were then merged to produce the total structure factor ${}^{\mathrm{GeGaSe}}F(Q)$.

Self consistency checks were performed on the data sets to ensure that (i) each measured $F(Q)$ obeys the sum-rule relation (see equation 2.11), (ii) the low-r features in the real space functions oscillate about their theoretical $r = 0$ limit as given in table 6.1 and (iii) the Fourier backtransform of the real space functions after the low-r oscillations are set to the theoretical $r = 0$ limit is in good overall agreement with the original reciprocal space function [113].

6.4 Results

The total structure factors ${}^{\mathrm{La}}F(Q)$ and ${}^{\mathrm{Ce}}F(Q)$ for the R-Ge-Ga-Se glasses, as measured by neutron diffraction on the GLAD instrument at the IPNS, are plotted in figure 6.4. The total pair distribution functions ${}^{\mathrm{La}}G(r)$ and ${}^{\mathrm{Ce}}G(r)$ are plotted in figure 6.5 and were obtained by Fourier transforming the corresponding $F(Q)$ functions after making a Harwell spline fit [115] to the data and applying a cosine window function between 18 and 23 $\mathrm{\AA}^{-1}$. It was necessary to truncate the $F(Q)$ functions at the relatively small maximum scattering vector $Q_{\mathrm{max}} = 23$ $\mathrm{\AA}^{-1}$ to prevent the poor statistical precision in the data sets at higher Q values (see figure 6.10 (c)) leading to un-physical features in the Fourier transforms. The positions of the leading peaks in the $F(Q)$, $G(r)$ and corresponding difference functions are listed in table 6.3 together with the coordination numbers $\bar{n}$, $\bar{n}^{\mathrm{Se}}_{\mathrm{Ge}}$ and $\bar{n}^{\mathrm{Se}}_{R}$ obtained from the real space functions as detailed below.

The $F(Q)$ functions exhibit a first sharp diffraction peak (FSDP), indicative of ordering on intermediate length scales [116], at $q_1 \simeq 1.02(2)$ $\mathrm{\AA}^{-1}$. The FSDP experiences an increase in height with substitution of La by Ce. This is emphasised by the first order difference function $\Delta F^{(1)}_{R}(Q)$ plotted in figure 6.6 which exhibits a trough in this region and must therefore result from one or more of the $S_{RR}(Q)$ and $S_{R\mu}(Q)$ partial structure factors having a trough in this region.

The first peak at $r_1 = 2.38(2)$ Å in the $G(r)$ functions is attributed to a superposition of the nearest neighbour Ge-Se and Ga-Se correlations by comparison with the nearest neighbour distances $2.34 \leq r_{\mathrm{GeSe}}$ (Å) ≤ 2.37 reported for crystalline $GeSe_2$ [233] and $2.32 \leq r_{\mathrm{GaSe}}$ (Å) ≤ 2.48 reported for crystalline Ga_2Se_3 [234, 235]. Assuming that the number of homopolar bonds is negligible, a coordination number of $\bar{n}^{\mathrm{Se}}_{\mathrm{Ge}} = 4.0(1)$ was obtained from the first peak in the $G(r)$ functions by integrating over the range $2.15 \leq r$ (Å) ≤ 2.64 and assuming a contribution to the peak area from Ga-Se correlations where $\bar{n}^{\mathrm{Se}}_{\mathrm{Ga}} = 4$ by comparison with the Ga coordination environment in R-Ge-Ga-S glasses (see chapter 5). The second much smaller peak in the $G(r)$ functions at

Table 6.3: Leading peak positions q_1, q_2 and q_3 for the reciprocal space functions together with the leading peak positions r_1, r_2 and r_3 and coordination numbers $\bar{n}$, $\bar{n}^{\mathrm{Se}}_{\mathrm{Ge}}$ and $\bar{n}^{\mathrm{Se}}_{R}$ for the corresponding real space functions for glassy $(R_2\mathrm{Se}_3)_{0.07}(\mathrm{Ga_2Se_3})_{0.33}(\mathrm{GeSe_2})_{0.60}$ (where R denotes La or Ce), $\mathrm{GeSe_2}$ and $(\mathrm{GeSe_2})_{0.87}(\mathrm{Ga_2Se_3})_{0.13}$.

	q_1 (Å^{-1})	q_2 (Å^{-1})	q_3 (Å^{-1})	$\bar{n}$	$\bar{n}^{\mathrm{Se}}_{\mathrm{Ge}}$	$\bar{n}^{\mathrm{Se}}_{R}$	r_1 (Å)	r_2 (Å)	r_3 (Å)
$^{\mathrm{La}}F(Q)$	1.01(2)	2.06(2)	3.49(2)	2.6(1)	4.0(1)	8.4(9)	2.38(2)	3.09(3)	3.80(5)
$^{\mathrm{Ce}}F(Q)$	1.02(2)	2.05(2)	3.50(2)	2.6(1)	4.0(1)	10.7(13)	2.38(2)	3.13(3)	3.85(5)
$\Delta F^{(1)}_R(Q)$	1.09(2)	2.46(2)	–	–	–	8.0(2)	–	3.05(3)	3.72(5)
$\Delta F^{(1)}(Q)$	1.02(2)	2.04(2)	3.50(2)	2.8(1)	4.0(1)	–	2.37(2)	–	3.87(5)
$^{\mathrm{GeSe_2}}F(Q)$	1.01(2)	2.04(2)	3.51(2)	2.7(1)	4.0(1)	–	2.37(2)	–	3.90(5)
$^{\mathrm{GeGaSe}}F(Q)$	1.00(2)	2.04(2)	3.49(2)	2.8(1)	3.7(1)	–	2.37(2)	–	3.90(5)

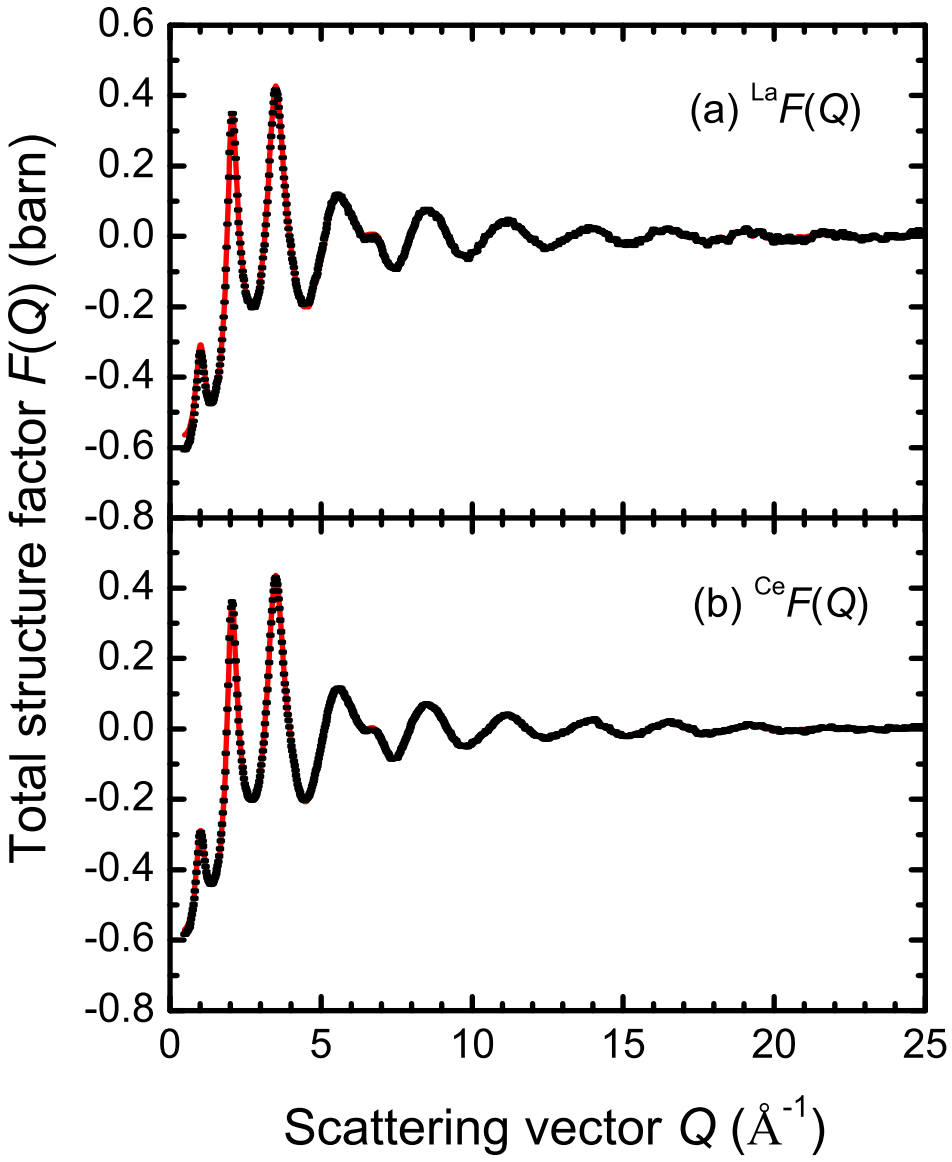

Figure 6.4: The measured total structure factors (a) $^{La}F(Q)$ and (b) $^{Ce}F(Q)$ for the $(R_2Se_3)_{0.07}(Ga_2Se_3)_{0.33}(GeSe_2)_{0.60}$ glasses as measured by neutron diffraction on the GLAD instrument at the IPNS. The bars represent the statistical errors and the solid (red) curves are the Fourier back-transform of the corresponding $G(r)$ functions given in figure 6.5 after the un-physical low-r oscillations are set to the theoretical $G(0)$ limits, as listed in table 6.1.

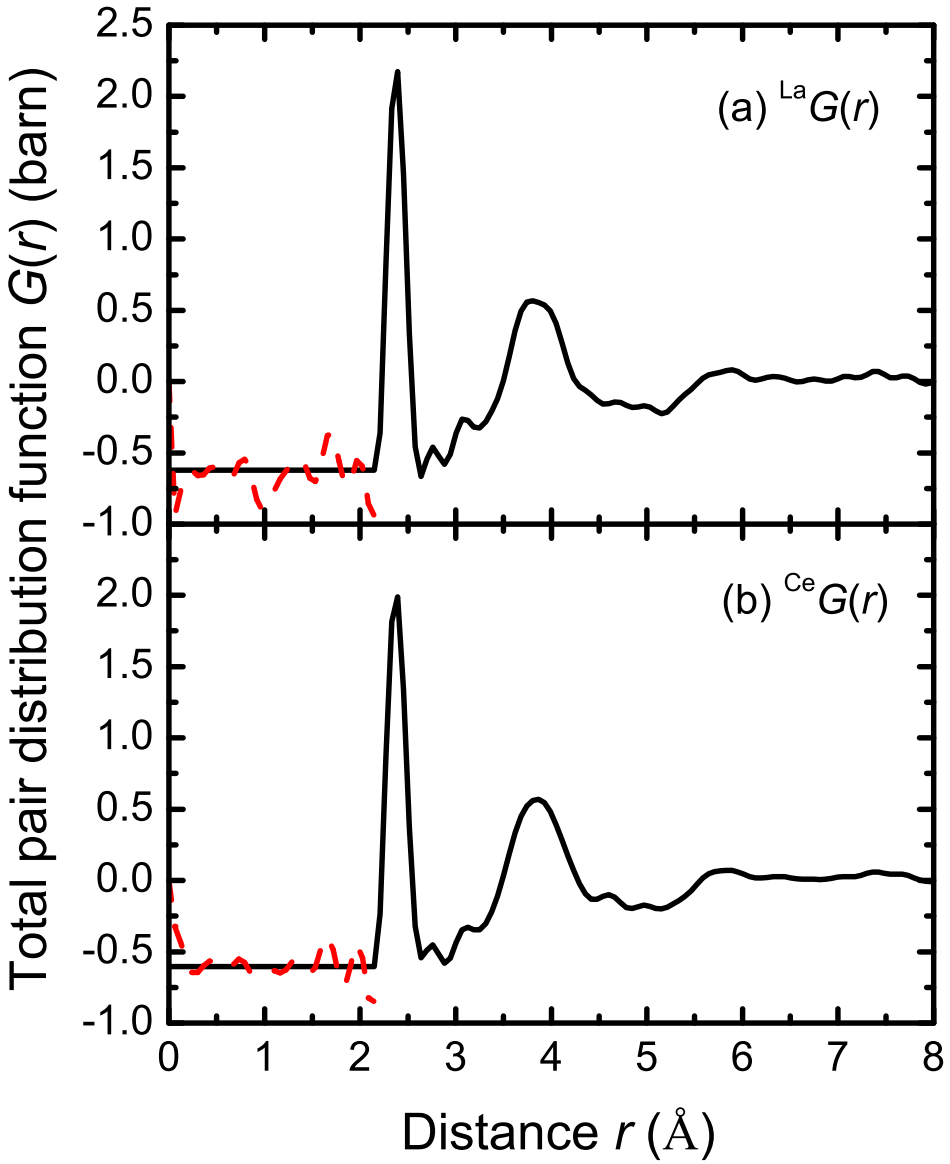

Figure 6.5: The total pair distribution functions (a) $^{La}G(r)$ and (b) $^{Ce}G(r)$ for the $(R_2Se_3)_{0.07}(Ga_2Se_3)_{0.33}(GeSe_2)_{0.60}$ glasses, as obtained by Fourier transforming the corresponding $F(Q)$ functions given in figure 6.4 after making a Harwell spline fit [115] to the data and applying a cosine window function between 18 and 23 Å^{-1}. The dashed (red) curves indicate the extent of the un-physical low-r oscillations.

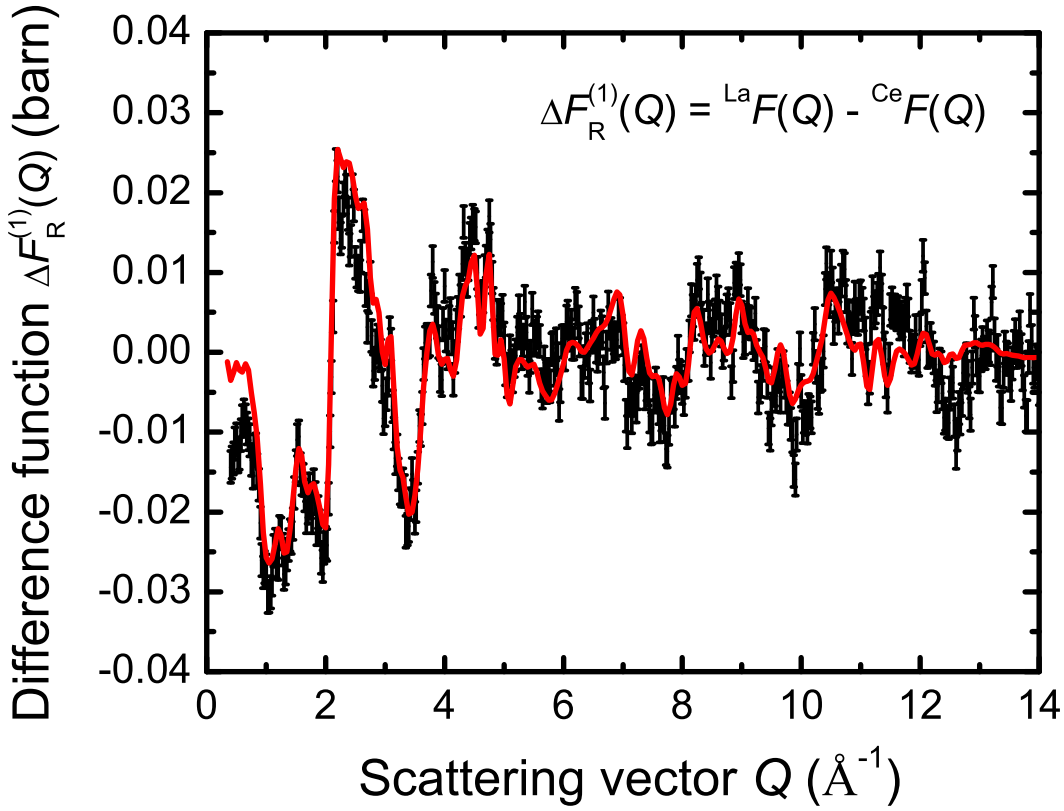

Figure 6.6: First order difference function $\Delta F_R^{(1)}(Q) \equiv^{\mathrm{La}} F(Q) -^{\mathrm{Ce}} F(Q)$ from the total structure factors given in figure 6.4. The bars represent the statistical errors and the solid (red) curve is the Fourier back-transform of the corresponding $\Delta G_R^{(1)}(r)$, shown by the black curve plotted in figure 6.7, after the un-physical low-r oscillations are set to the theoretical $r = 0$ limit (see table 6.1).

$r_2 \simeq 3.09(3)$ Å has greater intensity in the ${}^{\mathrm{La}}G(r)$ function, consistent with this peak arising from correlations involving the rare earth ion since $b_{\mathrm{La}} > b_{\mathrm{Ce}}$. The peak is attributed to the nearest neighbour R-Se correlations by comparison with the range of bond distances $2.93 \leq r_{R\mathrm{Se}}$ (Å) ≤ 3.22 reported in crystalline systems containing R, Ge and Se or R, Ga and Se, where R denotes a large rare earth element (see table 6.4). The coordination number $\bar{n}_R^{\mathrm{Se}}$ was obtained from the R-Se peak in the $G(r)$ functions by integrating over the range $2.88 \leq r$ (Å) ≤ 3.25. However, different values were obtained from each $G(r)$ (see table 6.3) which may indicate that other correlations involving matrix atoms

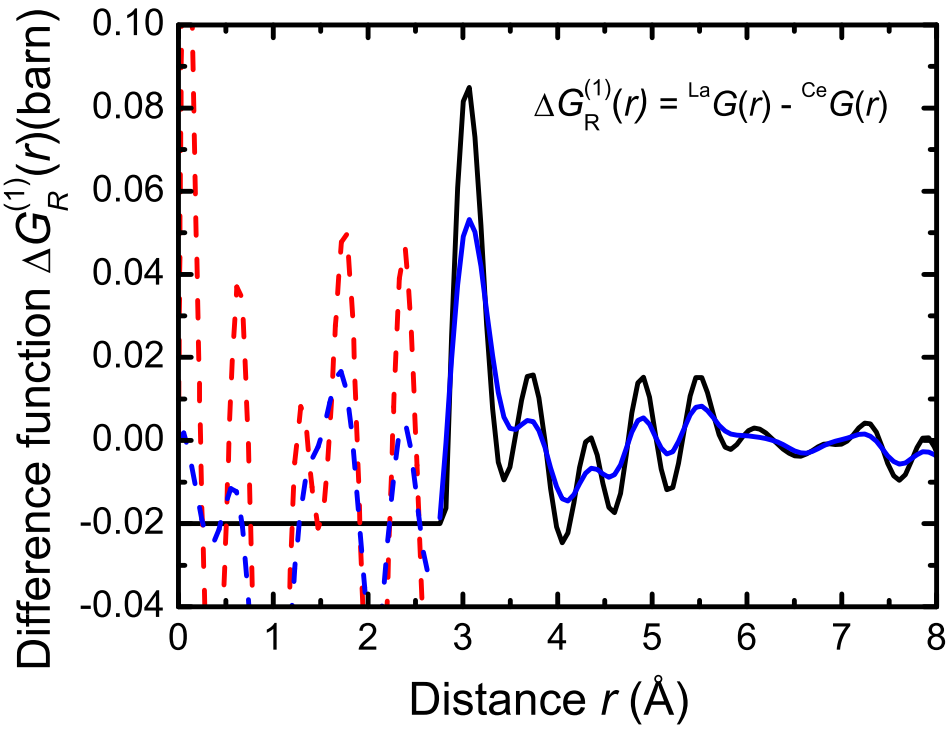

Figure 6.7: First order difference function $\Delta G_R^{(1)}(r)$ obtained by Fourier transforming the $\Delta F_R^{(1)}(Q)$ function in figure 6.6 after making a Harwell spline fit [115] to the data and applying a cosine window function between 10 and 14 Å^{-1} (solid black curve), where the dashed (red) curve indicates the extent of the un-physical low-r oscillations. The $\Delta G_R^{(1)}(r)$ function obtained by Fourier transforming the spline fitted $\Delta F_R^{(1)}(Q)$ truncated at a maximum scattering vector $Q_{\max} = 14$ Å^{-1} using a Lorch [33] modification function is also shown (solid blue curve), where the dashed (blue) curve indicates the extent of the un-physical low-r oscillations.

also contribute to the peak.

The first order difference function $\Delta G_R^{(1)}(r)$ is plotted in figure 6.7 and was obtained by Fourier transforming the $\Delta F_R^{(1)}(Q)$ function after making a Harwell spline fit [115] to the data and applying a cosine window function between 10 and 14 Å^{-1}. The Fourier backtransform of the $\Delta G_R^{(1)}(r)$ function after the un-physical low-r oscillations up to the onset of the first peak at $r_{\text{cut}} = 2.70$ Å are set to the theoretical $\Delta G_R^{(1)}(0)$ limit (listed in table 6.1) is in good overall agreement with the $\Delta F_R^{(1)}(Q)$ function, indicating successful elimination of correlations involving only the matrix atoms (Ge, Ga, Se). The $\Delta G_R^{(1)}(r)$ function exhibits a prominent first peak at $r_2 = 3.05(3)$ Å followed by several subsidiary peaks. To try and distinguish the physical peaks in real space from e.g. Fourier transform artifacts, a Lorch [33] modification function was also applied to the spline fitted $\Delta F_R^{(1)}(Q)$ function truncated at a maximum scattering vector $Q_{\text{max}} = 14$ Å^{-1} (see figure 6.7) prior to Fourier transformation into real space. By comparison with the bond distances reported for large rare earth elements in crystalline systems containing R, Ge and Se or R, Ga and Se (see table 6.4) the first peak in $\Delta G_R^{(1)}(r)$ at $r_2 = 3.05(3)$ Å is attributed to the nearest neighbour R-Se correlations. A coordination number $\bar{n}_R^{\text{Se}} = 8.0(2)$ was obtained from the R-Se peak by integrating over the range $2.88 \leq r$ (Å) ≤ 3.25. The second peak in $\Delta G_R^{(1)}(r)$ at $r_3 = 3.72(5)$ Å is attributed to a superposition of the R-Ge and R-Ga correlations. Although further peaks are present in $\Delta G_R^{(1)}(r)$ it is not possible to unambiguously identify which of these may result from e.g. the R-R correlations.

The total minus weighted difference function $\Delta F^{(1)}(Q)$ is plotted in figure 6.8. The corresponding $\Delta G^{(1)}(r)$ function is plotted in figure 6.9 and was obtained by Fourier transforming the $\Delta F^{(1)}(Q)$ function after making a Harwell spline fit [115] to the data and applying a cosine window function between 18 and 23 Å^{-1}. As for the $G(r)$ functions, the first peak in $\Delta G^{(1)}(r)$ at $r_1 = 2.37(2)$ Å is attributed to a superposition of the Ge-Se and Ga-Se correlations. Assuming that the number of homopolar bonds is negligible, a coordination number of $\bar{n}_{\text{Ge}}^{\text{Se}} = 4.0(1)$ was obtained from the first peak in the

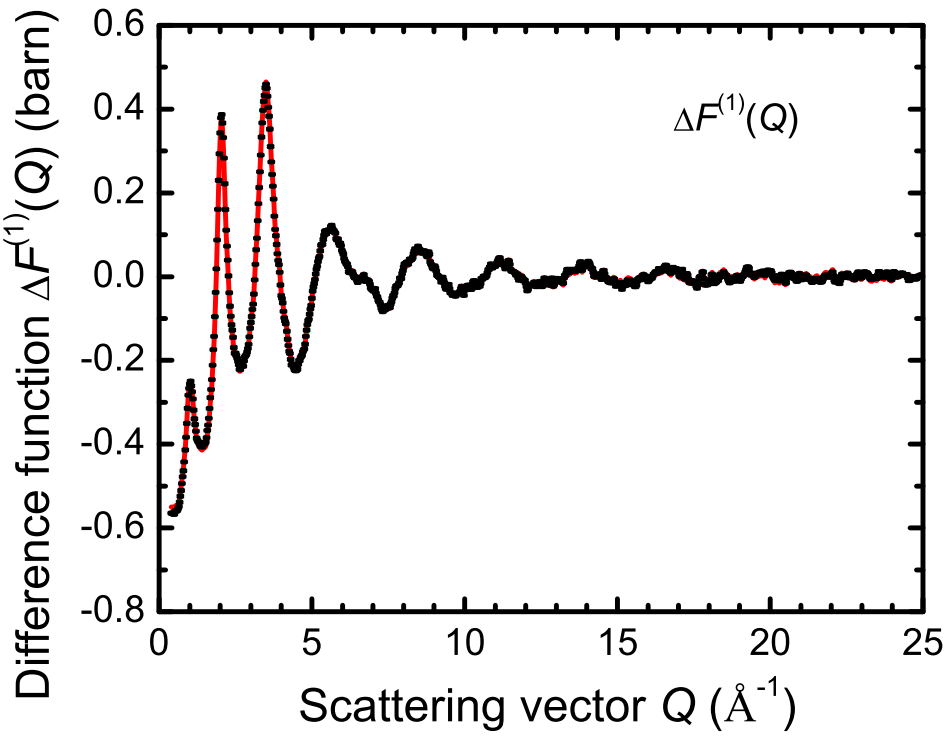

Figure 6.8: The total minus weighted difference function $\Delta F^{(1)}(Q)$ for the $(R_2Se_3)_{0.07}(Ga_2Se_3)_{0.33}(GeSe_2)_{0.60}$ glass. The bars represent the statistical errors and the solid (red) curve is the Fourier back-transform of the corresponding $\Delta G^{(1)}(r)$ function given in figure 6.9 after the un-physical low-r oscillations are set to the theoretical $r = 0$ limit (see table 6.1).

$\Delta G^{(1)}(r)$ function by integrating over the range $2.09 \leq r$ (Å) ≤ 2.70 assuming a contribution to the peak area from Ga-Se correlations where $\bar{n}^{\mathrm{Se}}_{\mathrm{Ga}} = 4$. Despite the fact that the R-μ correlations are eliminated in the total minus weighted difference function, a shoulder is present in $\Delta G^{(1)}(r)$ at $r \simeq 3.1$ Å although it is not as prominent as the feature observed in the $G(r)$ functions (see figure 6.5). This shoulder may therefore result from matrix-matrix atom correlations e.g. the Ge-Ge distance for edge sharing $GeSe_4$ tetrahedra occurs at 3.02(2) Å in $GeSe_2$ glass. By comparison with the structure of $GeSe_2$ glass [192], the peak at $r_3 = 3.87(5)$ Å can be attributed to Se-Se correlations and

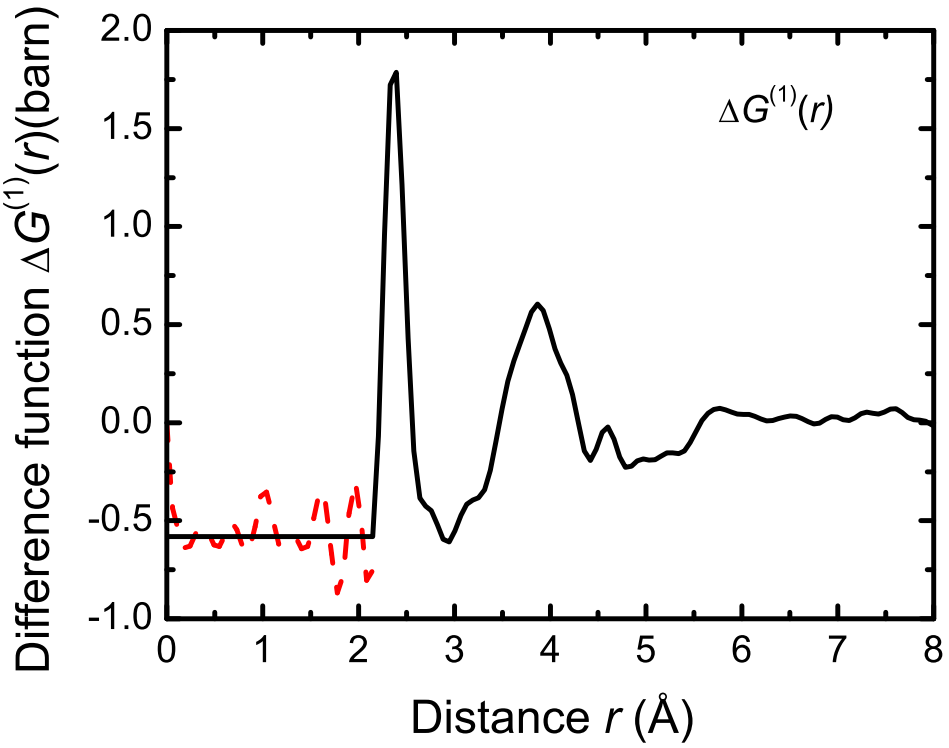

Figure 6.9: The total minus weighted difference function $\Delta G^{(1)}(r)$ obtained by Fourier transforming the $\Delta F^{(1)}(Q)$ function given in figure 6.8 after making a Harwell spline fit [115] to the data and applying a cosine window function between 18 and 23 Å^{-1}. The dashed (red) curve indicates the extent of the un-physical low-r oscillations.

the shoulder on this peak at $r \simeq 3.6$ Å can attributed to Ge-Ge correlations for corner shared tetrahedra. The small peak at $r_4 = 4.59$ Å is difficult to identify. Although it occurs at a distance consistent with the nearest neighbour R-R correlations reported in crystalline systems containing R, Ge and Se or R, Ga and Se (see table 6.4), no distinct peak is apparent at this distance in the $\Delta G_R^{(1)}(r)$ function. The R-R correlations also have a negative weighting in $\Delta G^{(1)}(r)$ (see table 6.1) and hence any contribution from the R-R correlations should appear as a trough.

The total structure factors obtained using the GEM instrument, denoted

$^{GeSe_2}F(Q)$ for the $GeSe_2$ glass (as measured by Zeidler [229]) and $^{GeGaSe}F(Q)$ for the $(GeSe_2)_{0.87}(Ga_2Se_3)_{0.13}$ glass, are plotted in figure 6.10 together with the $^{La}F(Q)$ and $\Delta F^{(1)}(Q)$ functions for the $(R_2Se_3)_{0.07}(Ga_2Se_3)_{0.33}(GeSe_2)_{0.60}$ glass. Small but distinct changes are observed in the structure of $GeSe_2$ on the addition of Ga_2Se_3 followed by La_2Se_3. Specifically, the FSDP, which is present at $q_1 \simeq 1.01$ Å^{-1} in all three $F(Q)$ functions undergoes a progressive reduction in intensity from $^{GeSe_2}F(Q)$ to $^{GeGaSe}F(Q)$ to $\Delta F^{(1)}(Q)$ to $^{La}F(Q)$. In $GeSe_2$ glass the FSDP arises predominantly from the Ge-Ge correlations [192].

The total pair distribution functions $^{GeSe_2}G(r)$ are $^{GeGaSe}G(r)$ are plotted in figure 6.11, together with $^{La}G(r)$ and $\Delta G^{(1)}(r)$. All of these functions were obtained in an identical manner, i.e. by Fourier transforming the corresponding reciprocal space functions after making a Harwell spline fit [115] to the data and applying a cosine window function between 18 and 23 Å^{-1}. The first peak in $^{GeSe_2}G(r)$ at $r_1 = 2.37(2)$ Å has a majority contribution from the nearest neighbour Ge-Se correlations [192]. The peak is broadened and experiences a reduction in height with the addition of Ga_2Se_3 followed by La_2Se_3, although its position is maintained. The total pair distribution functions $^{GeSe_2}G(r)$ and $^{GeGaSe}G(r)$ are also plotted in figure 6.12 but were this time obtained by Fourier transforming the corresponding spline fitted $F(Q)$ functions after applying a cosine window function between 30 and 40 Å^{-1}. It is evident by comparing figure 6.11 with figure 6.12 that Fourier transforming the $F(Q)$ functions at the higher $Q_{max} = 40$ Å^{-1} substantially improves the peak resolution in real space but no change is observed in the peak positions. Assuming that the number of homopolar bonds is negligible, a coordination number $\bar{n}^{Se}_{Ge} = 4.0(1)$ was obtained from the first peak in the $^{GeSe_2}G(r)$ function by integrating over the range $2.21 \leq r$ (Å) ≤ 2.58. The peak at $r_3 = 3.90(5)$ Å is attributed to Se-Se correlations by comparison with the first major peak in the measured $g_{SeSe}(r)$ partial pair distribution function [192]. A shoulder is also apparent on this peak at $r \simeq 3.6$ Å and is attributed to the Ge-Ge correlations for corner shared $GeSe_4$ tetrahedra by comparison with the first major peak in the measured $g_{GeGe}(r)$ partial pair distribution function [192].

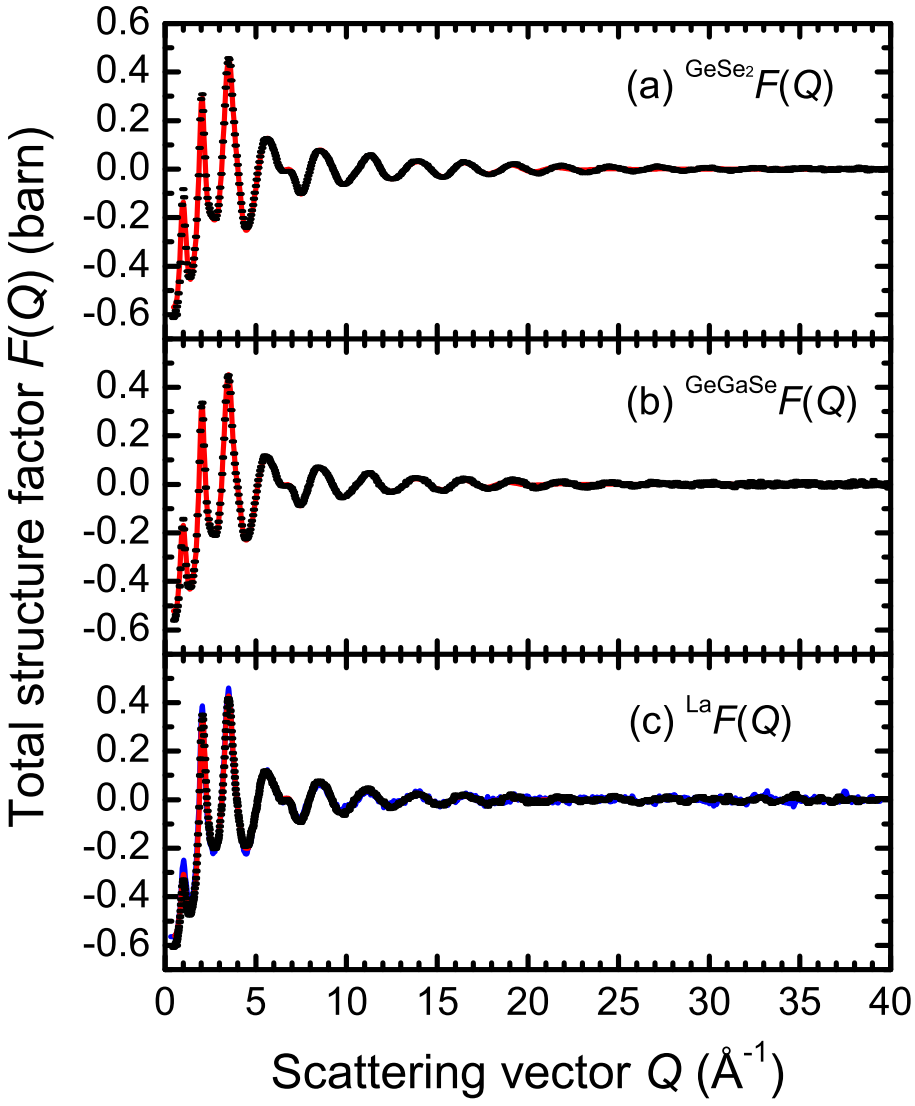

Figure 6.10: The total structure factors (a) ${}^{GeSe_2}F(Q)$ for the $GeSe_2$ glass measured using the GEM instrument [229], (b) ${}^{GeGaSe}F(Q)$ for the $(GeSe_2)_{0.87}(Ga_2Se_3)_{0.13}$ glass measured using the GEM instrument, and (c) ${}^{La}F(Q)$ for the $(La_2Se_3)_{0.07}(Ga_2Se_3)_{0.33}(GeSe_2)_{0.60}$ glass measured using the GLAD instrument (taken from figure 6.4). The bars represent the statistical errors and the solid (red) curves are the Fourier back-transforms of the corresponding $G(r)$ functions plotted in figure 6.11 after the low-r oscillations are set to the theoretical $r = 0$ limit (see table 6.1). The solid (blue) curve in (c) shows the total minus weighted difference function $\Delta F^{(1)}(Q)$ taken from figure 6.8.

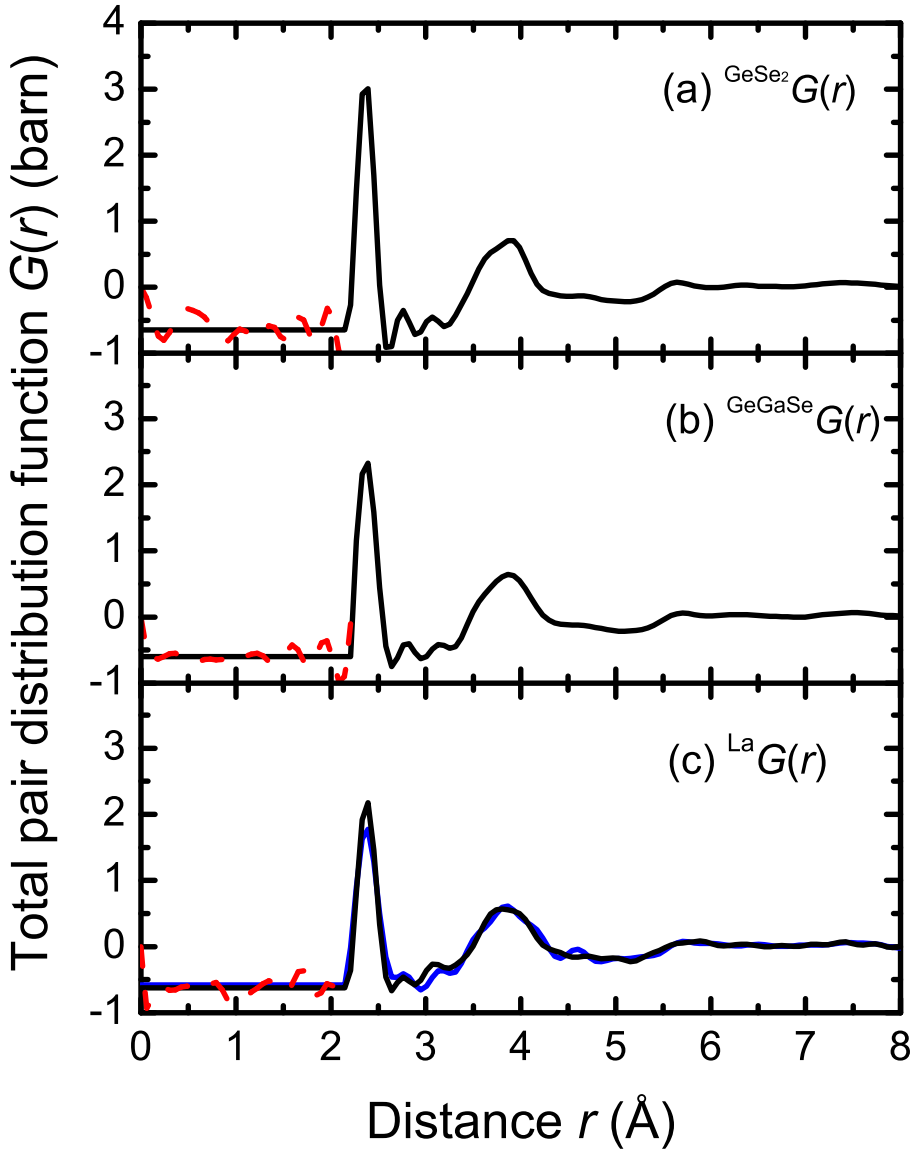

Figure 6.11: The total pair distribution functions (a) $^{GeSe_2}G(r)$ for glassy $GeSe_2$, (b) $^{GeGaSe}G(r)$ for glassy $(GeSe_2)_{0.87}(Ga_2Se_3)_{0.13}$ and (c) $^{La}G(r)$ for glassy $(La_2Se_3)_{0.07}(GeSe_2)_{0.60}(Ga_2Se_3)_{0.33}$ (taken from figure 6.5) as obtained by Fourier transforming the corresponding $F(Q)$ functions in figure 6.10 after making a Harwell spline fit [115] to the data and applying a cosine window function between 18 and 23 $Å^{-1}$. The dashed (red) curves indicate the extent of the un-physical low-r oscillations. The solid (blue) curve in (c) shows the total minus weighted difference function $\Delta G^{(1)}(r)$ taken from figure 6.9.

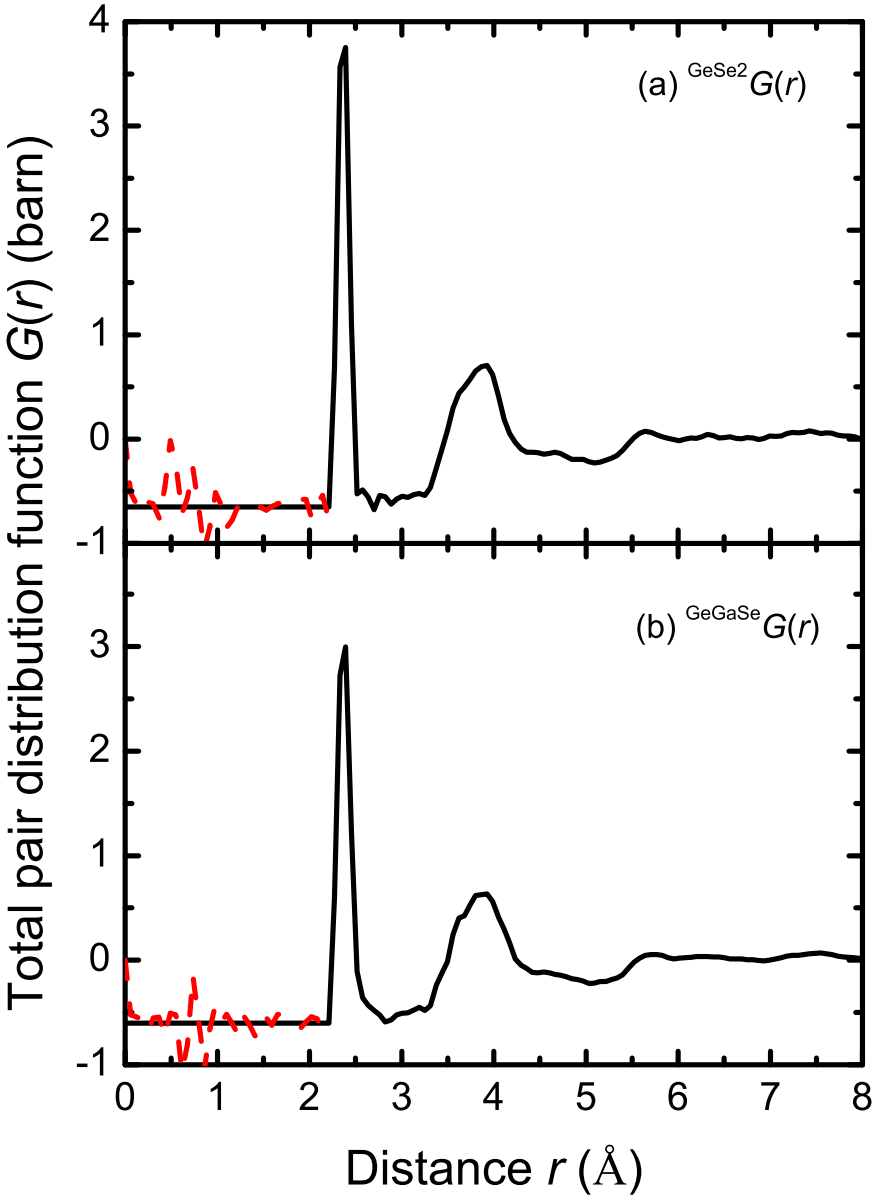

Figure 6.12: The total pair distribution functions (a) ${}^{\mathrm{GeSe_2}}G(r)$ for glassy $GeSe_2$ and (b) ${}^{\mathrm{GeGaSe}}G(r)$ for glassy $(GeSe_2)_{0.87}(Ga_2Se_3)_{0.13}$ as obtained by Fourier transforming the corresponding $F(Q)$ functions in figure 6.10 after making a Harwell spline fit [115] to the data and applying a cosine window function between 30 and 40 $\mathrm{Å}^{-1}$. The dashed (red) curves indicate the extent of the un-physical low-r oscillations.

As for the R-Ge-Ga-Se glasses, the first peak at $r_1 = 2.37(2)$ Å in the $^{\mathrm{GeGaSe}}G(r)$ function is attributed to a superposition of Ge-Se and Ga-Se correlations. A coordination number of $\bar{n}^{\mathrm{Se}}_{\mathrm{Ge}} = 3.7(1)$ was obtained from the first peak in the $^{\mathrm{GeGaSe}}G(r)$ function by integrating over the range $2.21 \leq r$ (Å) ≤ 2.88 and, as for the $^{\mathrm{La}}G(r)$ function, subtracting the contribution from the Ga-Se correlations for which it was assumed that $\bar{n}^{\mathrm{Se}}_{\mathrm{Ga}} = 4$. By comparison with $GeSe_2$ [192] and crystalline Ga_2Se_3 [234, 235] the peak at $r_3 = 3.90(5)$ Å is attributed to a superposition of Se-Se and Ga-Ga correlations. The shoulder at $r \simeq 3.6$ Å is attributed to Ge-Ge correlations for corner shared $GeSe_4$ tetrahedra [192]. Also, although no peak is apparent, there is a finite intensity at $r \simeq 3.05$ Å which may arise from other matrix-matrix atom correlations, for example the Ge-Ge nearest neighbour distance $r_{\mathrm{GeGe}} = 3.02(2)$ Å for edge sharing $GeSe_4$ tetrahedra [192]. A shoulder is also present at $r \simeq 2.55$ Å on the first peak in the $^{\mathrm{GeGaSe}}G(r)$ function by comparison with $^{\mathrm{GeSe_2}}G(r)$, which can help to explain the broadening of the first peak in the $^{\mathrm{La}}G(r)$, $^{\mathrm{Ce}}G(r)$ and $\Delta G^{(1)}(r)$ functions. The nearest neighbour Ge-Se and Ga-Se distances in crystalline systems containing R, Ge and Se [236–241] and R, Ga and Se [242], where R denotes a large rare earth element, are comparable to the distances reported for $GeSe_2$ [233] and Ga_2Se_3 [234, 235] and hence this shoulder cannot be attributed to these correlations. However, it may indicate the existence of Ga-Ga homopolar bonds by comparison with the range of nearest neighbour Ga-Ga bond distances $2.44 \leq r_{\mathrm{GaGa}}$ Å ≤ 2.82 reported for liquid Ga [213–218] and $r_{\mathrm{GaGa}} = 2.48$ Å reported for crystalline Ga [219].

6.5 Discussion

As for the sulphide system (see chapter 5) few structural studies have been performed on the glassy R-Ge-Ga-Se system and crystal structures of this system are not reported in the literature. Some information on the nearest neighbour coordination environment of the rare earth ions can nevertheless be gained from other systems containing R, Ge and Se or R, Ga and Se (see table 6.4).

Table 6.4: The R-Se nearest neighbour distance $r_{R\mathrm{Se}}$, average coordination number $\bar{n}_R^{\mathrm{Se}}$ and the minimum nearest neighbour R-R distance r_{RR} (min) for crystal structures containing R-Ge-Se or R-Ga-Se, where R represents a rare earth element La, Ce, Pr, Nd or Eu.

Crystal	$r_{R\mathrm{Se}}$ (Å)	$\bar{n}_{\mathrm{R}}^{\mathrm{Se}}$	$r_{R\mathrm{Ge}}$ (Å)	$r_{R\mathrm{Ga}}$ (Å)	r_{RR} (min) (Å)	Ref.
$La_3CuGeSe_7$	2.99-3.22	8	3.88	–	4.54	[236]
$LaKGeSe_4$	3.02-3.21	8	3.62-4.30	–	4.64	[237]
$Ce_3CuGeSe_7$	2.97-3.19	8	3.86	–	4.51	[238]
$CeKGeSe_4$	3.01-3.20	7	3.60-4.30	–	4.63	[239]
$Pr_3CuGeSe_7$	2.94-3.18	8	3.83	–	4.48	[238]
$PrKGeSe_4$	2.99-3.16	7	3.59-4.27	–	4.62	[240]
$Nd_3CuGeSe_7$	2.93-3.17	8	3.82	–	4.47	[238]
$EuGa_2Se_4$	3.18-3.23	8	–	3.98-4.08	5.44	[242]
Eu_2GeSe_4	3.10-3.31	7	3.70-4.32	–	4.20	[241]

The first peak in the ${}^{\mathrm{GeSe_2}}G(r)$ function at $r_1 = 2.37(2)$ Å for $GeSe_2$ glass is attributed to nearest neighbour Ge-Se correlations and gives a coordination number $\bar{n}_{\mathrm{Ge}}^{\mathrm{Se}} = 4.0(1)$. The first peak in the $G(r)$ functions for the R-Ge-Ga-Se glasses at $r_1 = 2.38(2)$ Å is attributed to a superposition of Ge-Se and Ga-Se correlations and also gives a coordination number $\bar{n}_{\mathrm{Ge}}^{\mathrm{Se}} = 4.0(1)$ if we assume that $\bar{n}_{\mathrm{Ga}}^{\mathrm{Se}} = 4$. These results should not, however, be taken to be an indication of complete chemical ordering. For example, in the case of glassy $GeSe_2$ a substantial number of structural defects in the form of Ge-Ge and Se-Se homopolar bonds are known to exist [192] giving rise to correlations at $r_{\mathrm{GeGe}} = 2.42$ Å and $r_{\mathrm{SeSe}} = 2.32(2)$ Å. Also, the measured $G(r)$ functions for the glasses containing Ga_2Se_3 exhibit a shoulder in the first peak at $r \simeq 2.55$ Å. The shoulder may be attributed to nearest neighbour Ga-Ga correlations by comparison with typical Ga-Ga bond distances [213–219]. All of these homopolar bond distances are within the integration range used to calculate $\bar{n}_{\mathrm{Ge}}^{\mathrm{Se}}$. However, if we consider the case for $GeSe_2$, the coherent neutron scattering lengths for Ge and Se of natural isotopic abundance are comparable and hence the $G(r)$ function for $GeSe_2$ measured by neutron diffraction is effectively equivalent to the Bhatia Thornton [243] number-number partial pair distribution function

$g_{\mathrm{NN}}(r)$ which makes no distinction between the chemical species occupying the scattering sites. The mean coordination number irrespective of species type is given by [244]

$$\begin{aligned} \bar{n} &= 4\pi n_0 \int_{r_i}^{r_j} r^2 g_{\mathrm{NN}}(r)\mathrm{d}r \\ &= c_{\mathrm{Ge}}(\bar{n}_{\mathrm{Ge}}^{\mathrm{Ge}} + \bar{n}_{\mathrm{Ge}}^{\mathrm{Se}}) + c_{\mathrm{Se}}(\bar{n}_{\mathrm{Se}}^{\mathrm{Se}} + \bar{n}_{\mathrm{Se}}^{\mathrm{Ge}}). \end{aligned} \tag{6.9}$$

There are two contrasting models for chemical ordering in Ge-Se networks, namely the random covalent network (RCN) model and the chemically ordered network (CON) model [244]. In the RCN model, the distribution of Ge-Ge, Se-Se and Ge-Se bonds is purely statistical and the coordination numbers $\bar{n}_{\mathrm{Ge}}^{\mathrm{Ge}} = 8c_{\mathrm{Ge}}/(1+c_{\mathrm{Ge}})$, $\bar{n}_{\mathrm{Se}}^{\mathrm{Se}} = 2(1-c_{\mathrm{Ge}})/(1+c_{\mathrm{Ge}})$ and $\bar{n}_{\mathrm{Ge}}^{\mathrm{Se}} = 4(1-c_{\mathrm{Ge}})/(1+c_{\mathrm{Ge}})$. In the CON model and at the stoichiometric composition, i.e. $c_{\mathrm{Ge}} = 1/3$, only Ge-Se bonds are permitted and the network is completely ordered giving coordination numbers of $\bar{n}_{\mathrm{Ge}}^{\mathrm{Ge}} = 0$, $\bar{n}_{\mathrm{Se}}^{\mathrm{Se}} = 0$ and $\bar{n}_{\mathrm{Ge}}^{\mathrm{Se}} = 4$. However, both the RCN and CON models give the same mean coordination number $\bar{n} = 2(c_{\mathrm{Ge}} + 1)$ provided the z=8-n rule (see § 5.1.3) is satisfied, i.e. Ge is four-fold coordinated and Se is two-fold coordinated. Hence for $GeSe_2$ the mean coordination number $\bar{n} = 2.67$ regardless of whether or not homopolar bonds exist.[1] A mean coordination number $\bar{n} = 2.7(1)$ is obtained by integrating over the first peak in the measured ${}^{\mathrm{GeSe_2}}G(r)$ function which is consistent with the calculated value. Similarly, the mean matrix atom coordination number for the Ge-Ga-Se and R-Ge-Ga-Se glasses is given by

$$\bar{n} = c_{\mathrm{Ge}}(\bar{n}_{\mathrm{Ge}}^{\mathrm{Ge}} + \bar{n}_{\mathrm{Ge}}^{\mathrm{Ga}} + \bar{n}_{\mathrm{Ge}}^{\mathrm{Se}}) + c_{\mathrm{Ga}}(\bar{n}_{\mathrm{Ga}}^{\mathrm{Ge}} + \bar{n}_{\mathrm{Ga}}^{\mathrm{Ga}} + \bar{n}_{\mathrm{Ga}}^{\mathrm{Se}}) + c_{\mathrm{Se}}(\bar{n}_{\mathrm{Se}}^{\mathrm{Ge}} + \bar{n}_{\mathrm{Se}}^{\mathrm{Ga}} + \bar{n}_{\mathrm{Se}}^{\mathrm{Se}}). \tag{6.10}$$

If we assume the CON model the mean coordination number is calculated using

$$\bar{n} = 4c_{\mathrm{Ge}} + 4c_{\mathrm{Ga}} + 2c_{\mathrm{Se}} \tag{6.11}$$

[1] This result does not apply for Ge-S networks, as studied in chapter 5, since the total structure factor measured by neutron diffraction does not directly yield $g_{\mathrm{NN}}(r)$ due to the large contrast between the coherent neutron scattering lengths of Ge and S.

giving $\bar{n} = 2.70$ for glassy $(GeSe_2)_{0.87}(Ga_2Se_3)_{0.13}$ and $\bar{n} = 2.59$ for glassy $(R_2Se_3)_{0.07}(Ga_2Se_3)_{0.33}(GeSe_2)_{0.60}$. As given in table 6.3 the experimental values for $\bar{n}$ are similar to the calculated values, although some discrepancy is expected due to the difference in the coherent neutron scattering lengths $b_{Ga} = 7.288(2)$ fm cf. $b_{Ge} = 8.185(20)$ fm and $b_{Se} = 7.970(9)$ fm [30].

The nearest neighbour R-Se bond length $r_{R\mathrm{Se}} = 3.05(3)$ Å and coordination number $\bar{n}_R^{\mathrm{Se}} = 8.0(2)$, obtained from the first order difference function $\Delta F_R^{(1)}(Q)$, are in agreement with the local coordination environment for large rare earth elements reported for crystalline materials containing R, Ge and Se or R, Ga, Se (see table 6.4). The R-Se peak is more prominent than the R-S peak in $G(r)$ for the sulphide glass (see chapter 5) which is consistent with the greater coherent neutron scattering length of selenium, i.e. $b_{Se} = 7.970(9)$ fm cf. $b_S = 2.84(1)$ fm [30].

6.6 Conclusions

The method of isomorphic substitution in neutron diffraction was used to study the structure of $(R_2Se_3)_{0.07}(Ga_2Se_3)_{0.33}(GeSe_2)_{0.60}$ glasses, where R denotes La or Ce. The structure of this material is based on a network of $GeSe_4$ and $GaSe_4$ tetrahedra. The first order difference function $\Delta G_R^{(1)}(Q)$ gives a nearest neighbour R-Se bond length $r_{R\mathrm{Se}} = 3.05(3)$ Å and coordination number $\bar{n}_R^{\mathrm{Se}} = 8.0(2)$.

7. Structure of Y/Ho-Ge-Ga-Se glasses by the method of isomorphic substitution in x-ray diffraction

7.1 Introduction

The aim of this experiment is to use the method of isomorphic substitution in high energy x-ray diffraction to measure the structure of a R-Ge-Ga-Se glass, where R represents Ho or Y. The $(R_2Se_3)_{0.07}(Ga_2Se_3)_{0.33}(GeSe_2)_{0.60}$ glass was chosen for investigation to match the composition of the sulphide and selenide glasses studied in chapters 5 and 6. The rare earth ions Ho^{3+} and Y^{3+} are suitable x-ray isomorphs since they have identical ionic radii (0.901 cf. 0.900 Å) [121] and comparable structural chemistry as indicated by their Pettifor chemical parameters (0.6825 cf. 0.66) [147]. The x-ray form factors of these elements are, however, substantially different where the atomic numbers are $Z(\mathrm{Ho}) = 67$ and $Z(\mathrm{Y}) = 39$.

7.2 Theory

As given in equation 2.17, the coherent scattered intensity measured in an x-ray diffraction experiment on a R-Ge-Ga-Se glass is represented by the total

x-ray structure factor

$$F_X(Q) = \sum_{\alpha=1}^{n}\sum_{\beta=1}^{n} c_\alpha c_\beta f_\alpha(Q) f_\beta(Q)[S_{\alpha\beta}(Q) - 1], \tag{7.1}$$

where $n = 4$ is the total number of chemical species denoted by α or β, c_α and $f_\alpha(Q)$ represent the atomic fraction and atomic form factor of chemical species α, respectively, $S_{\alpha\beta}(Q)$ is a Faber-Ziman partial structure factor and Q is the scattering vector. This intensity is often written in terms of the total x-ray structure factor $S_X(Q)$ which oscillates about unity at large Q values and is given by

$$S_X(Q) = \frac{F_X(Q)}{\left(\sum_{\alpha=1}^{n} c_\alpha f_\alpha(Q)\right)^2} + 1. \tag{7.2}$$

Expanding $F_X(Q)$ in terms of the partial structure factors $S_{\mu\mu'}(Q)$, that involve only the matrix species (Ge, Ga, Se), and the partial structure factors $S_{R\mu}(Q)$ or $S_{RR}(Q)$, that involve only the rare earth species R, we can write

$$\begin{aligned} F_X(Q) &= c_R^2 f_R(Q)^2 \left[S_{RR}(Q) - 1\right] + 2c_R c_{\mathrm{Se}} f_R(Q) f_{\mathrm{Se}}(Q) \left[S_{R\mathrm{Se}}(Q) - 1\right] \\ &+ 2c_R c_{\mathrm{Ge}} f_R(Q) f_{\mathrm{Ge}}(Q) \left[S_{R\mathrm{Ge}}(Q) - 1\right] \\ &+ 2c_R c_{\mathrm{Ga}} f_R(Q) f_{\mathrm{Ga}}(Q) \left[S_{R\mathrm{Ga}}(Q) - 1\right] \\ &+ \sum_{\mu\mu'} c_\mu c_{\mu'} f_\mu(Q) f_{\mu'}(Q) \left[S_{\mu\mu'}(Q) - 1\right], \end{aligned} \tag{7.3}$$

where $m = 3$ is the total number of matrix atom species denoted by μ or μ'. By measuring the $F_X(Q)$ function for samples containing the rare earth ions Ho^{3+} or Y^{3+}, where the atomic form factor $f_{\mathrm{Ho}}(Q) > f_{\mathrm{Y}}(Q)$, the difference function methods described in § 2.4 can be employed. The $S_{\mu\mu'}(Q)$ partial structure factors may be eliminated by subtracting the two $F_X(Q)$ functions to give the x-ray first order difference function

$$\begin{aligned} \Delta_X F_R^{(1)}(Q) &\equiv {}^{\mathrm{Ho}}F_X(Q) - {}^{\mathrm{Y}}F_X(Q) \\ &= \Delta_{R\mu}^{(1)}(Q) + c_R^2 \left(f_{\mathrm{Ho}}(Q)^2 - f_{\mathrm{Y}}(Q)^2\right) \left[S_{RR}(Q) - 1\right], \end{aligned} \tag{7.4}$$

where the rare earth to matrix atom difference function is given by

$$\begin{aligned}\Delta^{(1)}_{R\mu}(Q) &= 2c_Rc_{\rm Se}f_{\rm Se}(Q)\left(f_{\rm Ho}(Q)-f_{\rm Y}(Q)\right)\left[S_{R{\rm Se}}(Q)-1\right] \\ &+ 2c_Rc_{\rm Ge}f_{\rm Ge}(Q)\left(f_{\rm Ho}(Q)-f_{\rm Y}(Q)\right)\left[S_{R{\rm Ge}}(Q)-1\right] \\ &+ 2c_Rc_{\rm Ga}f_{\rm Ga}(Q)\left(f_{\rm Ho}(Q)-f_{\rm Y}(Q)\right)\left[S_{R{\rm Ga}}(Q)-1\right].\end{aligned} \tag{7.5}$$

The normalised x-ray first order difference function is obtained by dividing by the sum of the weighting factors of the correlations such that

$$\Delta_X S^{(1)}_R(Q) = \frac{\Delta_X F^{(1)}_R(Q)}{w^{(1)}_R(Q)} + 1, \tag{7.6}$$

where

$$\begin{aligned}w^{(1)}_R(Q) &= c_R^2\left[f_{\rm Ho}(Q)^2 - f_{\rm Y}(Q)^2\right] + 2c_Rc_{\rm Ge}f_{\rm Ge}(Q)\left[f_{\rm Ho}(Q)-f_{\rm Y}(Q)\right] \\ &+ 2c_Rc_{\rm Ga}f_{\rm Ga}(Q)\left[f_{\rm Ho}(Q)-f_{\rm Y}(Q)\right] + 2c_Rc_{\rm Se}f_{\rm Se}(Q)\left[f_{\rm Ho}(Q)-f_{\rm Y}(Q)\right].\end{aligned} \tag{7.7}$$

The $S_{R\mu}(Q)$ partial structure factors may be eliminated by subtracting a suitably weighted $\Delta_X F^{(1)}_R(Q)$ function from the ${}^{\rm Ho}F_X(Q)$ function to give the so called "x-ray total minus weighted difference function" given by

$$\begin{aligned}\Delta_X F^{(1)}(Q) &\equiv {}^{\rm Ho}F_X(Q) - \frac{f_{\rm Ho}(Q)}{f_{\rm Ho}(Q)-f_{\rm Y}(Q)}\Delta_X F^{(1)}_R(Q) \\ &\equiv \frac{f_{\rm Ho}(Q)\ {}^{\rm Y}F_X(Q) - f_{\rm Y}(Q)\ {}^{\rm Ho}F_X(Q)}{f_{\rm Ho}(Q)-f_{\rm Y}(Q)} \\ &= \sum_{\mu=1}^{m}\sum_{\mu'=1}^{m} c_\mu c_{\mu'} f_\mu(Q) f_{\mu'}(Q)\left[S_{\mu\mu'}(Q)-1\right] \\ &- c_R^2 f_{\rm Ho}(Q) f_{\rm Y}(Q)\left[S_{RR}(Q)-1\right].\end{aligned} \tag{7.8}$$

The normalised x-ray total minus weighted difference function is obtained by dividing by the sum of the weighting factors of the correlations such that

$$\Delta_X S^{(1)}(Q) = \frac{\Delta_X F^{(1)}(Q)}{w^{(1)}(Q)} + 1, \tag{7.9}$$

where

$$w^{(1)}(Q) = \sum_{\mu=1}^{m}\sum_{\mu'=1}^{m} c_\mu c_{\mu'} f_\mu(Q) f_{\mu'}(Q) - c_R^2 f_{\mathrm{Ho}}(Q) f_{\mathrm{Y}}(Q). \tag{7.10}$$

The real space functions $G_X(r)$, $\Delta_X G_R^{(1)}(r)$ and $\Delta_X G^{(1)}(r)$ are obtained by Fourier transforming the corresponding reciprocal space functions using the relations

$$G_X(r) = \frac{1}{2\pi^2 r n_0}\int_0^\infty Q S_X(Q)\sin(Qr)\mathrm{d}Q, \tag{7.11}$$

$$\Delta_X G_R^{(1)}(r) = \frac{1}{2\pi^2 r n_0}\int_0^\infty Q \Delta_X S_R^{(1)}(Q)\sin(Qr)\mathrm{d}Q, \tag{7.12}$$

$$\Delta_X G^{(1)}(r) = \frac{1}{2\pi^2 r n_0}\int_0^\infty Q \Delta_X S^{(1)}(Q)\sin(Qr)\mathrm{d}Q, \tag{7.13}$$

where n_0 is the atomic number density of the glass and r is a distance in real space. The relevant equations for $G_X(r)$, $\Delta_X G_R^{(1)}(r)$ and $\Delta_X G^{(1)}(r)$ are obtained by replacing each $S_{\alpha\beta}(Q)$ by the corresponding partial pair distribution function $g_{\alpha\beta}(r)$ in the equations given for $F_X(Q)$, $\Delta_X F_R^{(1)}(Q)$ and $\Delta_X F^{(1)}(Q)$, respectively. Because the partial structure factors are weighted by Q-dependant form factors, the $g_{\alpha\beta}(r)$ correlations are convoluted by the Fourier transform of the form factors in real space. The coordination number $\bar{n}_\alpha^\beta$ cannot therefore be calculated by directly integrating over the relevant peaks in real space. Instead, if there is a clearly defined peak in $G_X(r)$ that can be assigned to a particular $g_{\alpha\beta}(r)$, the $F_X(Q)$ function is divided by the weighting factor for the relevant $S_{\alpha\beta}(Q)$ function such that in the Fourier transform the r-dependent weighting factor is removed from the $g_{\alpha\beta}(r)$ function of interest [191].

7.3 Experimental procedure

7.3.1 Glass preparation

The R-Ge-Ga-Se glasses were prepared by weighing the high purity starting constituents Ge (Aldrich, $\geq$ 3 mm chips, 99.999 %), Ga (Aldrich, 99.9999 %), Se (Aldrich, $\simeq$ 2 mm pellets, 99.999 + %), Y (Aldrich, pieces 99.9 %) and Ho (Aldrich, pieces 99.9 %) in the correct proportions within a dry Argon filled glove box with levels of $H_2O \leq 6$ ppm and $O_2 \leq 30$ ppm. The Ge and Se elements were powdered using a stainless steel and an agate pestle and mortar, respectively, and the Ga was melted on a hotplate. Following the procedure outlined in § 5.4.1, the samples were sealed in evacuated silica ampoules and heated in a rocking furnace at a rate of 1 °C min^{-1}, holding for 4 hours at 221 and 685 °C, corresponding to the melting and boiling temperatures of Se, respectively, and at 937 °C, corresponding to the melting temperature of Ge. Once the final synthesis temperature of 1100 °C had been reached and held for $\geq$ 24 hours, the furnace was rotated vertically and held for a further $\geq$ 12 hours before quenching the glass in ice water. Photographs of the prepared glasses in their silica ampoules are shown in figure 7.1. Since x-ray diffraction experiments require small samples only one 3 g batch of each glass was made. On breaking open the ampoules, the samples came away cleanly from the silica surface. The mean atomic fractions averaged over the samples are $c_R = 0.037(1)$, $c_{\mathrm{Ge}} = 0.156(1)$, $c_{\mathrm{Ga}} = 0.174(1)$ and $c_{\mathrm{Se}} = 0.633(1)$, forming the required molar composition $(R_2Se_3)_{0.07}(Ga_2Se_3)_{0.33}(GeSe_2)_{0.60}$.

7.3.2 Sample characterisation

The density of the samples was measured at the ISIS facility using a Quantachrome helium gas pycnometer and the values are listed in table 6.2.

The glass transition temperature T_g, crystallisation temperature T_c and change in heat capacity ΔC_p of the samples were measured by modulated differential scanning calorimetry (MDSC) using a TA Instruments DSC Q100 ma-

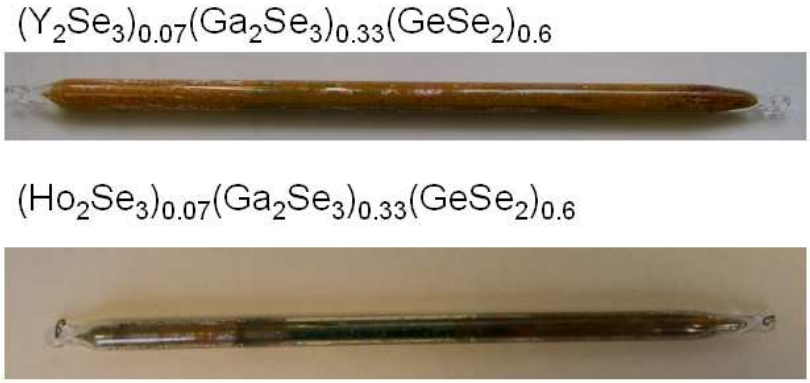

Figure 7.1: The as quenched R-Ge-Ga-Se glasses contained within silica ampoules.

Table 7.1: Properties of the $(R_2Se_3)_{0.07}(Ga_2Se_3)_{0.33}(GeSe_2)_{0.60}$ glasses where R represents Ho or Y. The mass density ρ and number density n_0 are listed together with the glass transition temperature T_g, crystallisation temperature T_c, and change in heat capacity ΔC_P at T_g as measured by modulated differential scanning calorimetry.

R	ρ (g cm^{-3})	n_0 (Å^{-3})	ΔC_P (J g^{-1} °C^{-1})	T_g (°C)	T_c (°C)
Ho	4.81(1)	0.0370(8)	0.16(2)	405(2)	475.23(1)
Y	4.78(1)	0.0377(8)	0.17(2)	405(2)	475.76(1)

chine. The finely powdered samples of mass ≈ 30 mg were contained in crimped aluminium pans and heated over the temperature range $300 \leq T$ (°C) ≤ 550 at a rate of 3.00 °C min^{-1} with a temperature modulation of ± 1.00 °C min^{-1}. Nitrogen gas (BOC, Oxygen free), flowing at 25 ml min^{-1}, was used to purge the instrument of moisture and oxygen and to provide efficient heat transfer between the sample pans and the DSC cell contacts. The reversible and non-reversible components of the heat flow and heat capacity C_p were recorded every 0.2 s and are plotted in figure 7.2. The mid-point glass transition temperature T_g was obtained by drawing a tangent line to the data in the transition region of the reversible heat flow to find the point of inflection. The change in heat capacity ΔC_p through T_g was obtained from the observed step in the reversible heat capacity curve. The crystallisation temperature T_c is given by

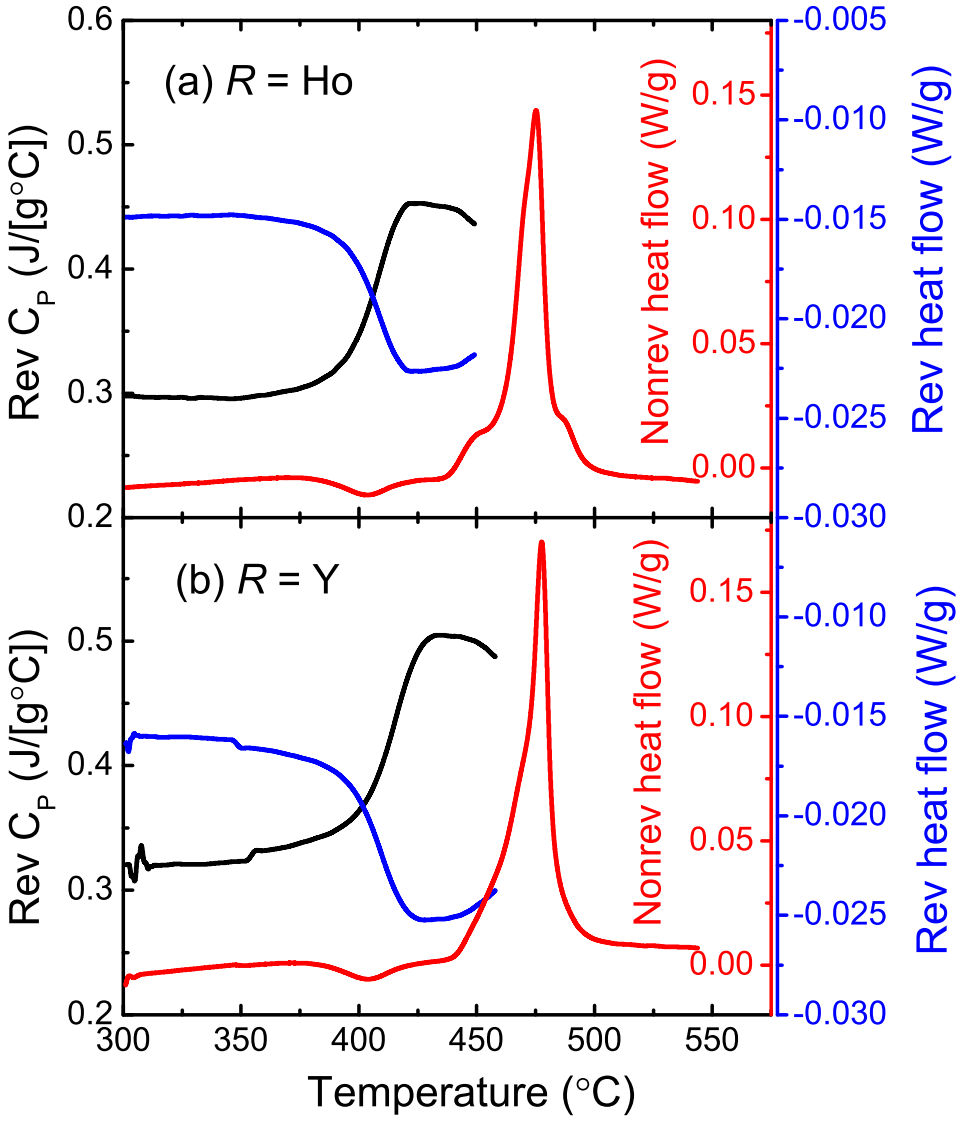

Figure 7.2: Modulated differential scanning calorimetry (MDSC) scans for the $(R_2Se_3)_{0.07}(Ga_2Se_3)_{0.33}(GeSe_2)_{0.60}$ glasses where (a) R = Ho and (b) R = Y. The blue curves denote the reversible heat flow, the red curves denote the non-reversible heat flow and the black curves denote the reversible heat capacity C_p signal. For clarity, the reversible heat flow and heat capacity signals are truncated before the crystallisation peak.

the position of the exothermic peak in the non-reversible heat flow curve. The values of ΔC_P, T_g and T_c are listed in table 7.1.

7.3.3 The 11-ID-C x-ray diffraction experiments

High energy x-ray diffraction experiments were performed on the R-Ge-Ga-Se glasses by Benmore and Qiang [245] using the 11-ID-C beamline at the APS, described in § 3.5.1, using a single element Ge solid state detector with an incident beam of energy 115 keV. The finely powdered samples were held in a washer and sealed each side with kapton 77-80 tape to give an approximate slab geometry with a sample thickness of 1.5 mm. Diffraction patterns were taken at ambient temperature ($\approx$ 25 °C) for the samples in the kapton container, the empty kapton container, the empty instrument and a lead slab of comparable geometry to the sample. Using the ISOMERX program [246], the data sets were normalised to the incident monitor counts and corrected for detector deadtime and deviation of the vertical scanning path taken by the detector from a circle centred at the sample position. Following the procedure detailed in § 3.7 the data sets were corrected for background scattering and attenuation effects and scaled to fit the sum of the Compton scattering cross section (given in Ref. [200]) and self scattering $\sum_\alpha c_\alpha f_\alpha(Q)^2$ contributions at high Q values, where the neutral atom form factors $f_\alpha(Q)$ were taken from Ref. [201]. The fit is plotted in figure 7.3 and was performed over the region $4 \leq Q(\text{Å}^{-1}) \leq 25$. The Compton scattering contribution was subtracted to obtain the Rayleigh-Thomson differential scattering cross-section from which the total x-ray structure factor $S_X(Q)$ was obtained. Self consistency checks were performed on the data sets to ensure that the low-r features in $G(r)$ oscillate about the theoretical $G_X(0) = 0$ limit and that the Fourier backtransform of $G_X(r)$, after the low-r oscillations are set to the theoretical $G_X(0) = 0$ limit, are in good overall agreement with the original $S_X(Q)$ function.

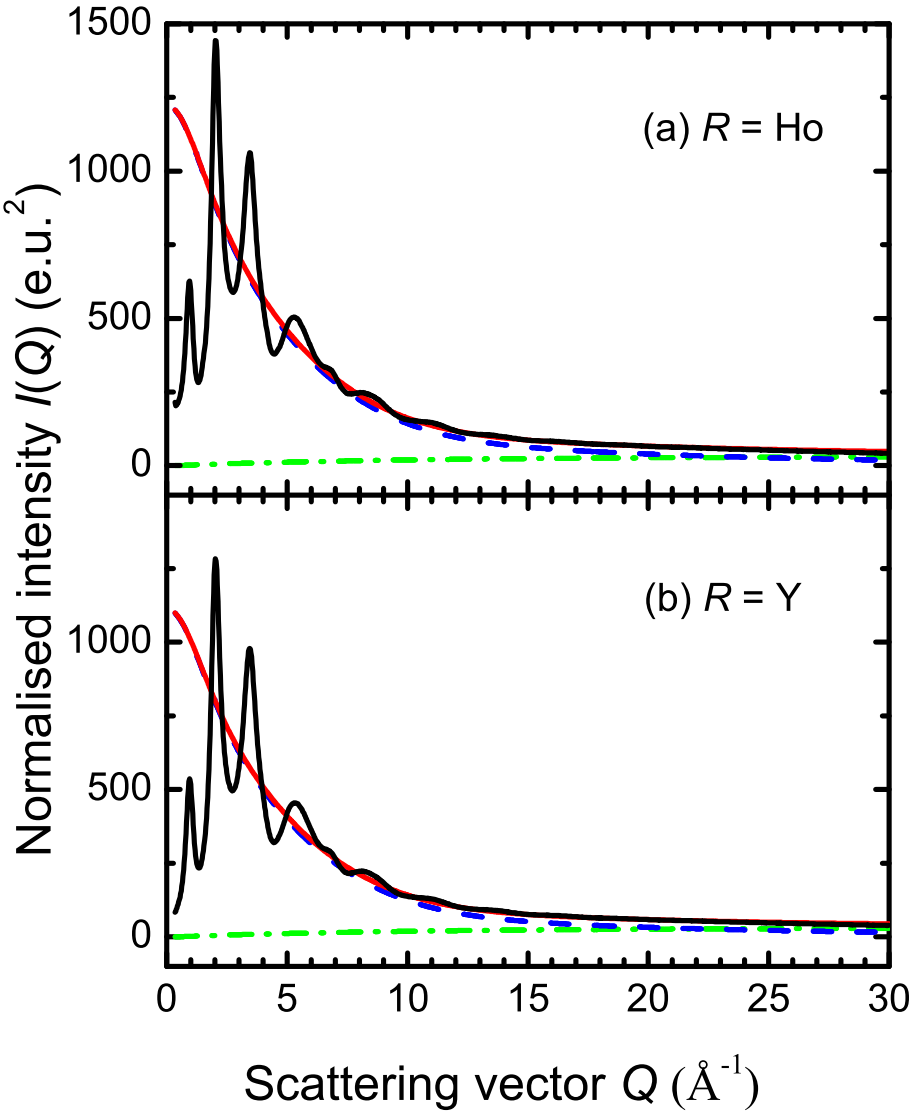

Figure 7.3: Contributions to the total x-ray scattered intensity for the $(R_2Se_3)_{0.07}(Ga_2Se_3)_{0.33}(GeSe_2)_{0.60}$ glasses, where (a) R = Ho and (b) R = Y, as measured on the 11-ID-C beamline at the APS. The dashed (blue) curves show the self scattering, the chained (green) curves show the Compton scattering, the solid (red) curves show the sum of the self scattering and Compton scattering and the solid (black) curves show the x-ray diffraction data that have been normalised by fitting to the sum of the self scattering and Compton scattering intensities.

7.4 Results

The total x-ray structure factors ${}^{\mathrm{Ho}}S_X(Q)$ and ${}^{\mathrm{Y}}S_X(Q)$ for the R-Ge-Ga-Se glasses, as measured by x-ray diffraction on the 11-ID-C beamline at the APS, are plotted in figure 7.4. The total x-ray pair distribution functions ${}^{\mathrm{Ho}}G_X(r)$ and ${}^{\mathrm{Y}}G_X(r)$ are plotted in figure 7.5 and were obtained by Fourier transforming the corresponding $S_X(Q)$ functions after making a Harwell spline fit [115] to the data and applying a cosine window function between 20 and 22 $\mathrm{\AA}^{-1}$. The positions of the leading peaks in the $S_X(Q)$, $G_X(r)$ and corresponding difference functions are listed in table 7.2 together with the coordination numbers $\bar{n}^{\mathrm{Se}}_{\mathrm{Ge}}$ and $\bar{n}^{\mathrm{Se}}_{\mathrm{R}}$ as obtained from the real space functions using the methods detailed below.

The $S_X(Q)$ functions exhibit a first sharp diffraction peak (FSDP), indicative of ordering on an intermediate length scale [116], at $q_1 \simeq 0.95(2)$ $\mathrm{\AA}^{-1}$. The first peak at $r_1 = 2.39(2)$ Å in the $G_X(r)$ functions is attributed to a superposition of the nearest neighbour Ge-Se and Ga-Se correlations by comparison with the nearest neighbour distances $2.34 \leq r_{\mathrm{GeSe}}$ (Å) ≤ 2.37 reported for crystalline $GeSe_2$ [233] and $2.32 \leq r_{\mathrm{GaSe}}$ (Å) ≤ 2.48 reported for crystalline Ga_2Se_3 [234, 235]. Since the x-ray atomic form factors for Ge and Ga are very similar, the r-dependent weighting factors were removed from the $g_{\mathrm{GeSe}}(r)$ and $g_{\mathrm{GaSe}}(r)$ partial pair distribution functions by Fourier transforming the function $F_X(Q)/2c_{\mathrm{Se}}f_{\mathrm{Se}}(Q)f_{\mathrm{Ge}}(Q)$. Hence, a coordination number $\bar{n}^{\mathrm{Se}}_{\mathrm{Ge}} = 3.9(1)$ was calculated from the first peak in the resulting real space function by integrating over the range $2.15 \leq r$ (Å) ≤ 2.64 and assuming a contribution to the peak area from Ga-Se correlations, where $\bar{n}^{\mathrm{Se}}_{\mathrm{Ga}} = 4$. The second smaller peak in the $G_X(r)$ functions at a mean distance $r_2 = 2.99(3)$ Å is less prominent in the glass containing Y. This is consistent with the peak having a contribution from correlations involving the rare earth ions since $f_{\mathrm{Ho}}(Q) > f_{\mathrm{Y}}(Q)$. The most likely contribution is from the nearest neighbour R-Se correlations by comparison with the range of bond distances $2.80 \leq r_{R\mathrm{Se}}$ (Å) ≤ 3.31 reported in crystalline systems containing R, Ge and Se or R, Ga and Se, where R denotes a small rare earth element (see table 7.3). The r-dependent weight-

Table 7.2: Leading peak positions q_1, q_2 and q_3 for the reciprocal space functions for the $(R_2Se_3)_{0.07}(Ga_2Se_3)_{0.33}(GeSe_2)_{0.60}$ glasses, where R denotes Ho or Y, as measured by x-ray diffraction on the 11-ID-C beamline at the APS. The leading peak positions r_1, r_2, r_3 and r_4 for the corresponding real space functions are also given together with the coordination numbers $\bar{n}^{\mathrm{Se}}_{\mathrm{Ge}}$ and $\bar{n}^{\mathrm{Se}}_{R}$.

	q_1 (Å^{-1})	q_2 (Å^{-1})	q_3 (Å^{-1})	$\bar{n}^{\mathrm{Se}}_{\mathrm{Ge}}$	$\bar{n}^{\mathrm{Se}}_{R}$	r_1 (Å)	r_2 (Å)	r_3 (Å)	r_4 (Å)
$^{\mathrm{Ho}}S_X(Q)$	0.95(2)	2.04(2)	3.47(2)	3.9(1)	8.9(9)	2.39(2)	2.95(3)	3.87(5)	–
$^{\mathrm{Y}}S_X(Q)$	0.96(2)	2.04(2)	3.47(2)	3.9(1)	10.7(9)	2.39(2)	3.03(3)	3.88(5)	–
$\Delta S^{(1)}_R(Q)$	1.19(2)	2.16(2)	–	–	5.0(2)	–	2.93(3)	3.70(5)	4.40(5)
$\Delta S^{(1)}(Q)$	0.98(2)	2.02(2)	3.44(2)	4.1(1)	–	2.39(2)	–	3.89(5)	–

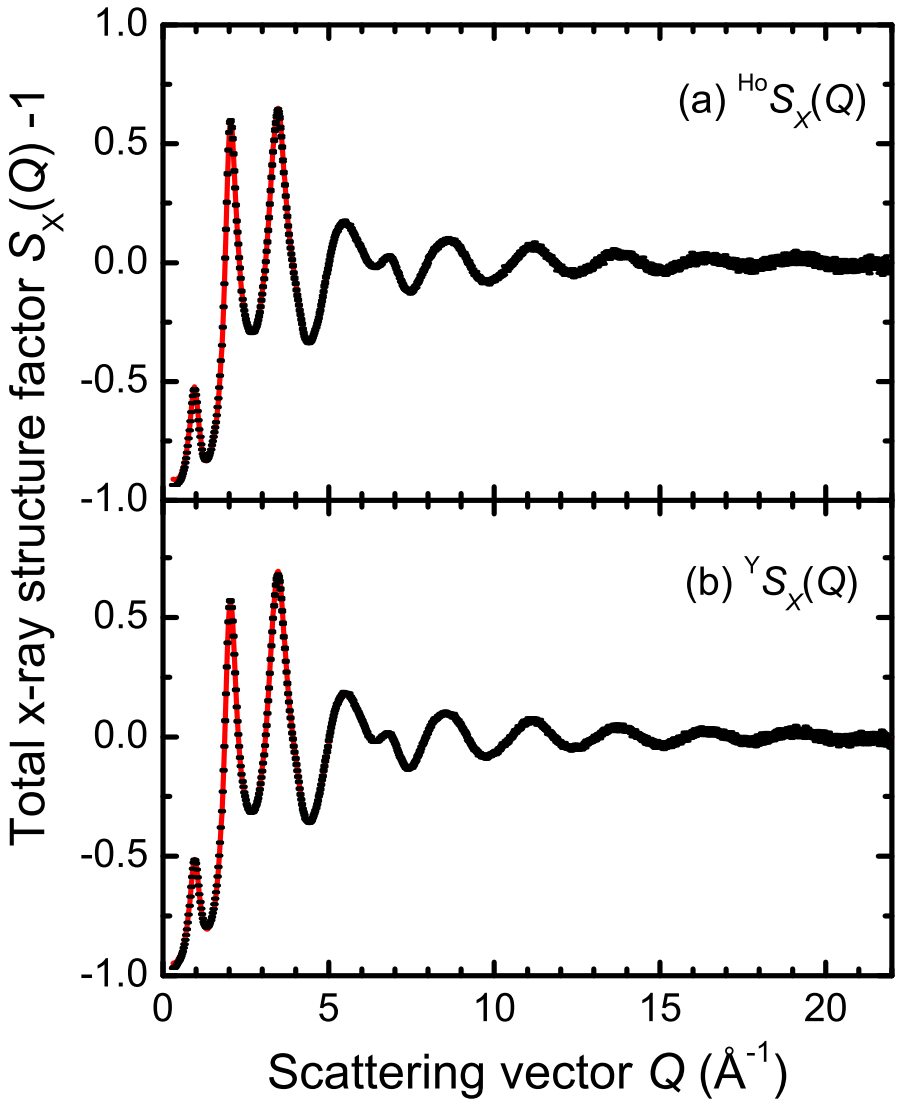

Figure 7.4: The total x-ray structure factors (a) $^{Ho}S_X(Q)$ and (b) $^{Y}S_X(Q)$ for the $(R_2Se_3)_{0.07}(Ga_2Se_3)_{0.33}(GeSe_2)_{0.60}$ glasses as measured by x-ray diffraction on the 11-ID-C beamline at the APS. The bars represent the statistical errors and the solid (red) curves are the Fourier back-transforms of the corresponding $G_X(r)$ functions given in figure 7.5 after the un-physical low-r oscillations are set to the theoretical $G_X(0) = 0$ limit.

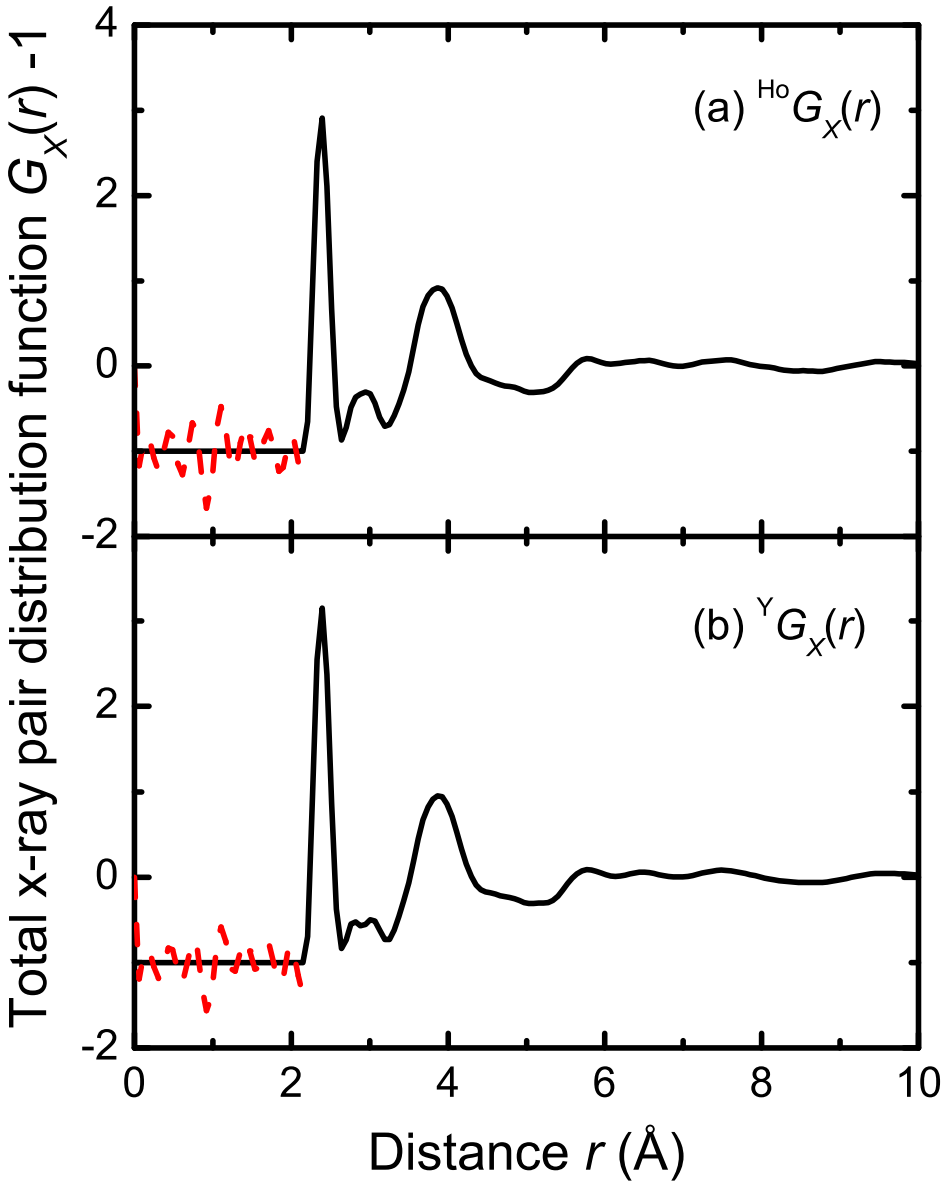

Figure 7.5: Total x-ray pair distribution functions (a) $^{\mathrm{Ho}}G_X(r)$ and (b) $^{\mathrm{Y}}G_X(r)$ for the $(R_2\mathrm{Se}_3)_{0.07}(\mathrm{Ga}_2\mathrm{Se}_3)_{0.33}(\mathrm{GeSe}_2)_{0.60}$ glasses, obtained by Fourier transforming the corresponding $S_X(Q)$ functions shown in figure 7.4 after making a Harwell spline fit [115] to the data and applying a cosine window function between 20 and 22 $\mathrm{Å}^{-1}$. The dashed (red) curves denote the extent of the un-physical low-r oscillations.

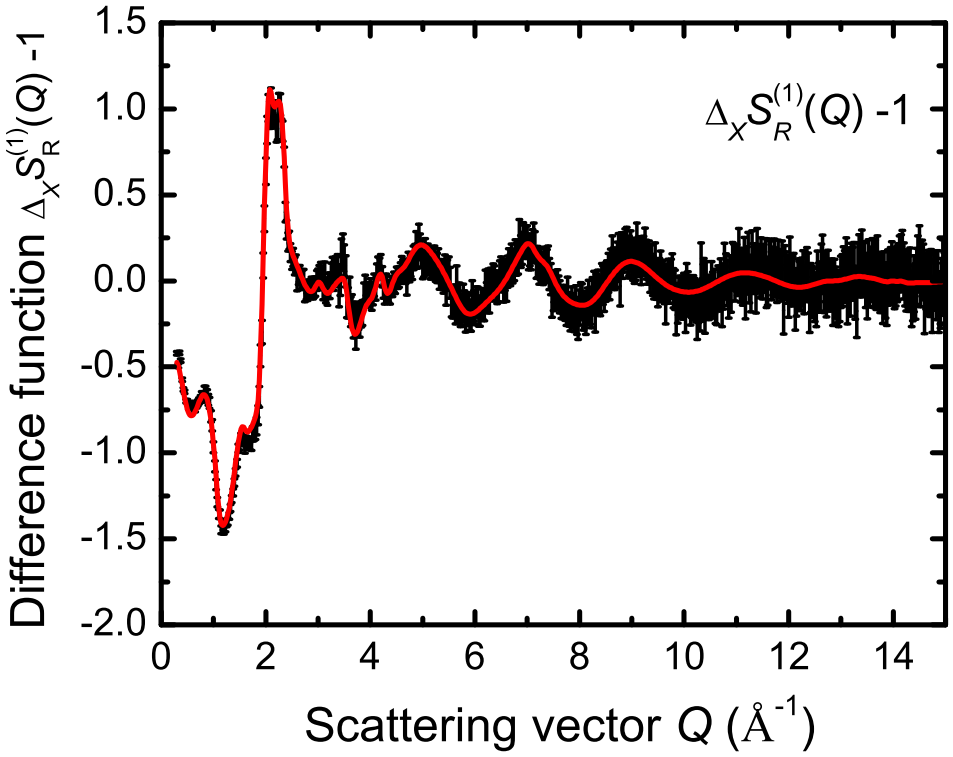

Figure 7.6: The x-ray first order difference function $\Delta_X S_R^{(1)}(Q)$. The bars represent the statistical errors and the solid (red) curve is the Fourier back-transform of the $\Delta_X G_R^{(1)}(r)$ function shown in figure 7.7, after the un-physical low-r oscillations are set to the theoretical $\Delta_X G_R^{(1)}(0) = 0$ limit.

ing factor was removed from the $g_{R\mathrm{Se}}(r)$ partial pair distribution function by Fourier transforming the function $F_X(Q)/2c_R c_{\mathrm{Se}} f_R(Q) f_{\mathrm{Se}}(Q)$. Hence, the coordination number $\bar{n}_R^{\mathrm{Se}}$ was obtained from the peak at $r \simeq 2.99$ Å in the resulting real space functions by integrating over the range $2.64 \leq r$ (Å) ≤ 3.19. Different values of $\bar{n}_R^{\mathrm{Se}}$ were obtained for the Ho and Y samples (see table 7.2) which indicates that other correlations involving matrix atoms also contribute to the peak. On closer inspection of the $^{\mathrm{Ho}}G(r)$ and $^{\mathrm{Y}}G(r)$ functions it is possible to see that there are in fact two peaks at $r \simeq 2.80$ Å and $r \simeq 3.05$ Å. This is most apparent for $^{\mathrm{Y}}G(r)$ in which the R-Se correlations are less strongly weighted.

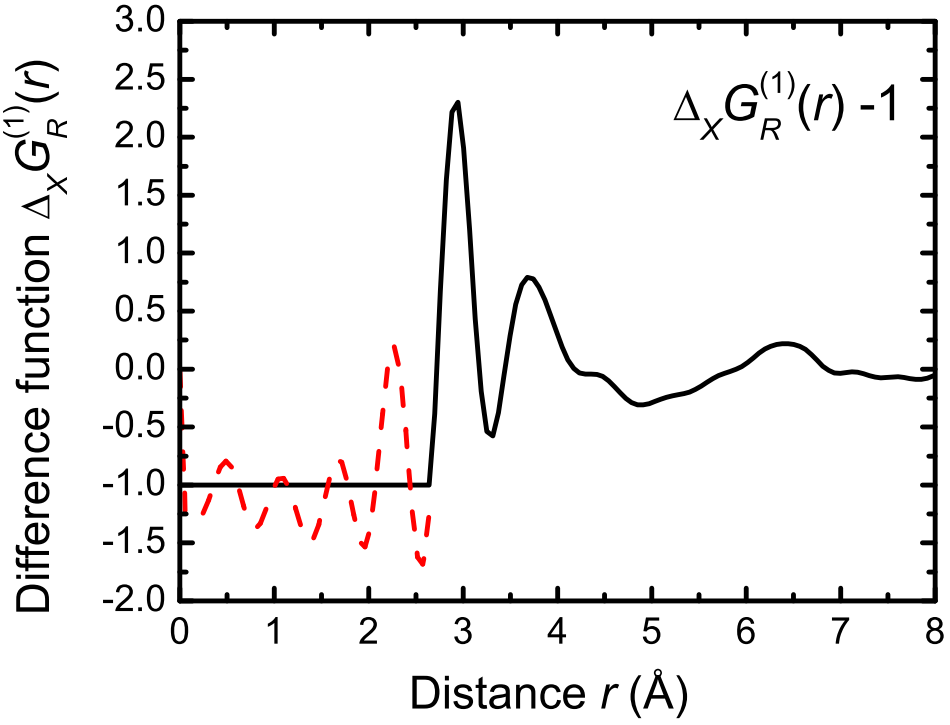

Figure 7.7: The x-ray first order difference function $\Delta_X G_R^{(1)}(r)$ obtained by Fourier transforming the $\Delta_X S_R^{(1)}(Q)$ function in figure 7.6 after making a Harwell spline fit [115] to the data and applying a cosine window function between 10 and 15 Å^{-1}. The dashed (red) curve indicates the extent of the un-physical low-r oscillations.

The x-ray first order difference function $\Delta_X S_R^{(1)}(Q)$ is plotted in figure 7.6 and shows a clear contrast between the measured $S_X(Q)$ functions. The real space difference function $\Delta_X G_R^{(1)}(Q)$ is plotted in figure 7.7 and was obtained by Fourier transforming the $\Delta_X S_R^{(1)}(Q)$ function after making a Harwell spline fit [115] to the data and applying a cosine window function between 10 and 15 Å^{-1}. By comparison with the bond distances reported for small rare earth elements in crystalline systems containing R, Ge and Se or R, Ga and Se (see table 7.3) the prominent first peak in $\Delta_X G_R^{(1)}(r)$ at $r_2 = 2.93(3)$ Å is attributed to the nearest neighbour R-Se correlations. The second peak

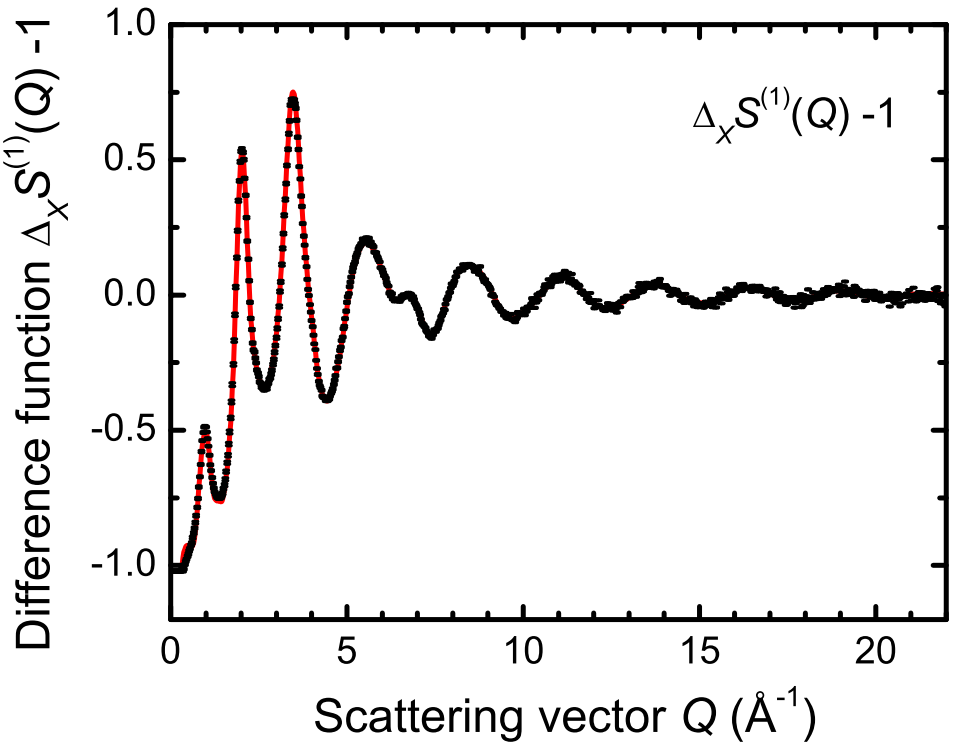

Figure 7.8: The x-ray total minus weighted difference function $\Delta_X S^{(1)}(Q)$. The bars represent the statistical errors and the solid (red) curve is the Fourier back-transform of the corresponding $\Delta_X G^{(1)}(r)$ function, shown by the black curve in figure 7.9 after the un-physical low-r oscillations are set to the theoretical $\Delta_X G^{(1)}(0) = 0$ limit.

at $r_3 = 3.70(5)$ Å is attributed to a superposition of R-Ge and R-Ga correlations and the shoulder at $r_4 = 4.40(5)$ Å is consistent with the nearest neighbour R-R distance. The r-dependent weighting factor was removed from the $g_{R\mathrm{Se}}(r)$ partial pair distribution function by Fourier transforming the function $\Delta_X F_R^{(1)}(Q)/2c_R c_{\mathrm{Se}} f_{\mathrm{Se}}(Q)\,[f_{\mathrm{Ho}}(Q) - f_{\mathrm{Y}}(Q)]$. Hence, a coordination number $\bar{n}_R^{\mathrm{Se}} = 5.0(2)$ was obtained from the R-Se peak in the resulting real space function by integrating over the range $2.64 \leq r$ (Å) ≤ 3.31.

The x-ray total minus weighted difference function $\Delta_X S^{(1)}(Q)$ is plotted in figure 7.8 and exhibits an FSDP at $q_1 = 0.98(2)$ Å^{-1}. The $\Delta_X G^{(1)}(r)$

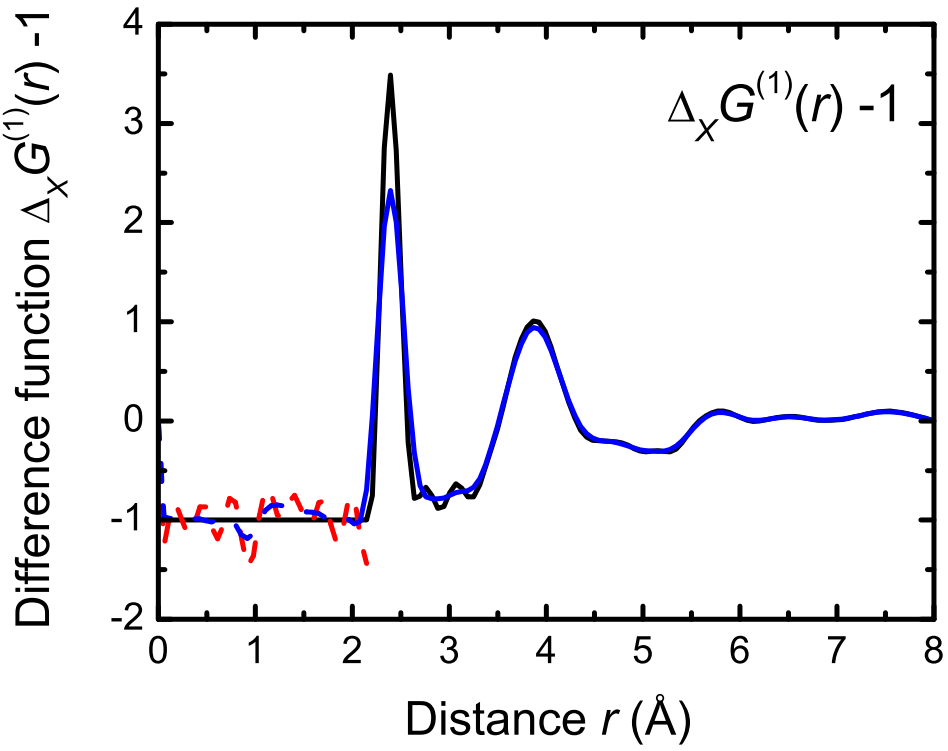

Figure 7.9: The x-ray total minus weighted difference function $\Delta_X G^{(1)}(r)$ obtained by Fourier transforming the $\Delta_X S^{(1)}(Q)$ function shown in figure 7.8 after making a Harwell spline fit [115] to the data and applying a cosine window function between 20 and 22 Å^{-1}, where the dashed (red) curve indicates the extent of the un-physical low-r oscillations. The $\Delta_X G^{(1)}(r)$ function obtained by Fourier transforming the spline fitted $\Delta_X S^{(1)}(Q)$ function truncated at a maximum scattering vector $Q_{\max} = 22$ Å^{-1} using a Lorch [33] modification function is also shown (solid blue curve), where the dashed (blue) curve indicates the extent of the un-physical low-r oscillations.

function is plotted in figure 7.9 and was obtained by Fourier transforming the $\Delta_X S^{(1)}(Q)$ function after making a Harwell spline fit [115] to the data and applying a cosine window function between 20 and 22 Å^{-1}. The first peak at $r_1 = 2.39(2)$ Å is attributed to a superposition of Ge-Se and Ga-Se correlations and, as for the $G_X(r)$ functions, a coordination number of $\bar{n}^{\rm Se}_{\rm Ge} = 4.1(1)$ was obtained from the first peak in the Fourier transform of the function $\Delta_X F^{(1)}(Q)/2c_{\rm Se}f_{\rm Se}(Q)f_{\rm Ge}(Q)$ by integrating over the range $2.15 \leq r$ (Å) ≤ 2.64 and assuming a contribution to the peak area from Ga-Se correlations, where $\bar{n}^{\rm Se}_{\rm Ga} = 4$.

The prominent peak at $r = 2.99(3)$ Å that was observed in the $G_X(r)$ functions and attributed largely to the R-Se correlations is not present in $\Delta_X G^{(1)}(r)$. However, although no peak is apparent, there is a finite intensity at $r \simeq 3.05$ Å which remains even after the data was smoothed by applying a Lorch [33] modification function to $\Delta_X S^{(1)}(Q)$ in order to reduce the appearance of the Fourier transform truncation artifacts (see figure 7.9). The finite intensity may therefore arise from other matrix-matrix atom correlations, for example the Ge-Ge nearest neighbour distance $r_{\rm GeGe} = 3.02(2)$ Å for edge sharing $GeSe_4$ tetrahedra [192].

7.5 Discussion

Table 7.3: The R-Se nearest neighbour distance $r_{R\rm Se}$, average coordination number $\bar{n}^{\rm Se}_R$ and the minimum nearest neighbour R-R distance r_{RR} (min) for crystal structures containing R, Ge and Se or R, Ga and Se, where R represents a rare earth element Eu, Gd, Tb, Dy or Y.

Crystal	$r_{R\rm Se}$ (Å)	$\bar{n}^{\rm Se}_{\rm R}$	$r_{R\rm Ge}$ (Å)	$r_{R\rm Ga}$ (Å)	r_{RR} (min) (Å)	Ref.
$EuGa_2Se_4$	3.18-3.23	8	–	3.98-4.08	5.44	[242]
Eu_2GeSe_4	3.10-3.31	7	3.70-4.32	–	4.20	[241]
$Gd_3CuGeSe_7$	2.95-3.11	8	3.78-4.48	–	4.44	[238]
$Tb_3CuGeSe_7$	2.91-3.16	8	3.78-4.47	–	4.41	[238]
$Dy_3CuGeSe_7$	2.85-3.15	8	3.75-4.50	–	4.39	[247]
$Y_3CuGeSe_7$	2.80-3.10	8	3.75-4.50	–	4.41	[248]

Few structural studies have been performed on the glassy R-Ge-Ga-Se system and crystal structures of this system are not reported in the literature. Some information on the nearest neighbour coordination environment of the rare earth ions can nevertheless be gained from other systems containing R, Ge and Se or R, Ga and Se, as listed in table 6.4. Coordination numbers reported for other systems containing small rare earth ions include, e.g. $\bar{n}_R^{\mathrm{O}} = 6$ in crystalline $R\mathrm{P_3O_9}$ [228], $\bar{n}_R^{\mathrm{Cl}} = 6$ in molten $\mathrm{YCl_3}$ [249] and $\bar{n}_R^{\mathrm{I}} = 5$ in molten $\mathrm{ScI_3}$ [250]. A coordination number $\bar{n}_{\mathrm{Yb}}^{\mathrm{S}} = 5$ has also been reported for $(\mathrm{Yb_2S_3})_{0.10}(\mathrm{La_2S_3})_{0.20}(\mathrm{Ga_2S_3})_{0.50}(\mathrm{GeS_2})_{0.20}$ glass using EXAFS [186]. However, the coordination number $\bar{n}_R^{\mathrm{Se}} = 5.0(2)$ obtained from the first order difference function $\Delta_X G_R^{(1)}(r)$ in the present study is not expected as it is inconsistent with the values of $\bar{n}_R^{\mathrm{Se}} \simeq 8$ reported for the crystalline systems in table 6.4.

7.6 Conclusions

The method of isomorphic substitution in x-ray diffraction was used to study the structure of $(R_2\mathrm{Se_3})_{0.07}(\mathrm{Ga_2Se_3})_{0.33}(\mathrm{GeSe_2})_{0.60}$ glasses, where R denotes Ho or Y. The structure of this material is based on a network of $\mathrm{GeSe_4}$ and $\mathrm{GaSe_4}$ tetrahedra. The first order difference function $\Delta_X G_R^{(1)}(r)$ gives a nearest neighbour R-Se bond length $r_{R\mathrm{Se}} = 2.93(3)$ Å but gives an unexpectedly small coordination number of $\bar{n}_R^{\mathrm{Se}} = 5.0(2)$. An estimate for the minimum R-R separation at a distance $r_{RR} = 4.40(5)$ Å was also obtained from the $\Delta_X G_R^{(1)}(r)$ function.

8. Structure of GeO_2 glass at high pressure I

The work presented in this chapter is also reported in Refs. [191] and [251].

8.1 Introduction

Under the extreme pressures and temperatures experienced deep inside planetary interiors, crystalline materials can undergo large structural and physical changes and form distinct polymorphic structures [252–256]. Similar changes may also be observed in liquids and amorphous solids, forming distinct polyamorphic phases of the same stoichiometry but different local structure and density [13, 14]. In order to investigate the structural transformations and properties of materials at such extreme conditions, *in situ* diffraction and spectroscopy methods are typically employed using diamond anvil cells which are capable of pressures of up to ≈ 400 GPa [46–48]. However, diamond anvil cells prohibit the application of neutron diffraction methods due to the small sample size. Instead, the larger volume Paris-Edinburgh cell, described in § 3.3, can be employed up to pressures of 30 GPa [49, 50].

Silica, SiO_2, is the most abundant compound present within the crust and upper mantle of the Earth and terrestrial planets [258–261]. The structural transformations of crystalline and amorphous silicate minerals and melts and the associated changes of physical properties, e.g. compressibility, thermal expansivity and viscosity, govern some major geophysical principles. These in-

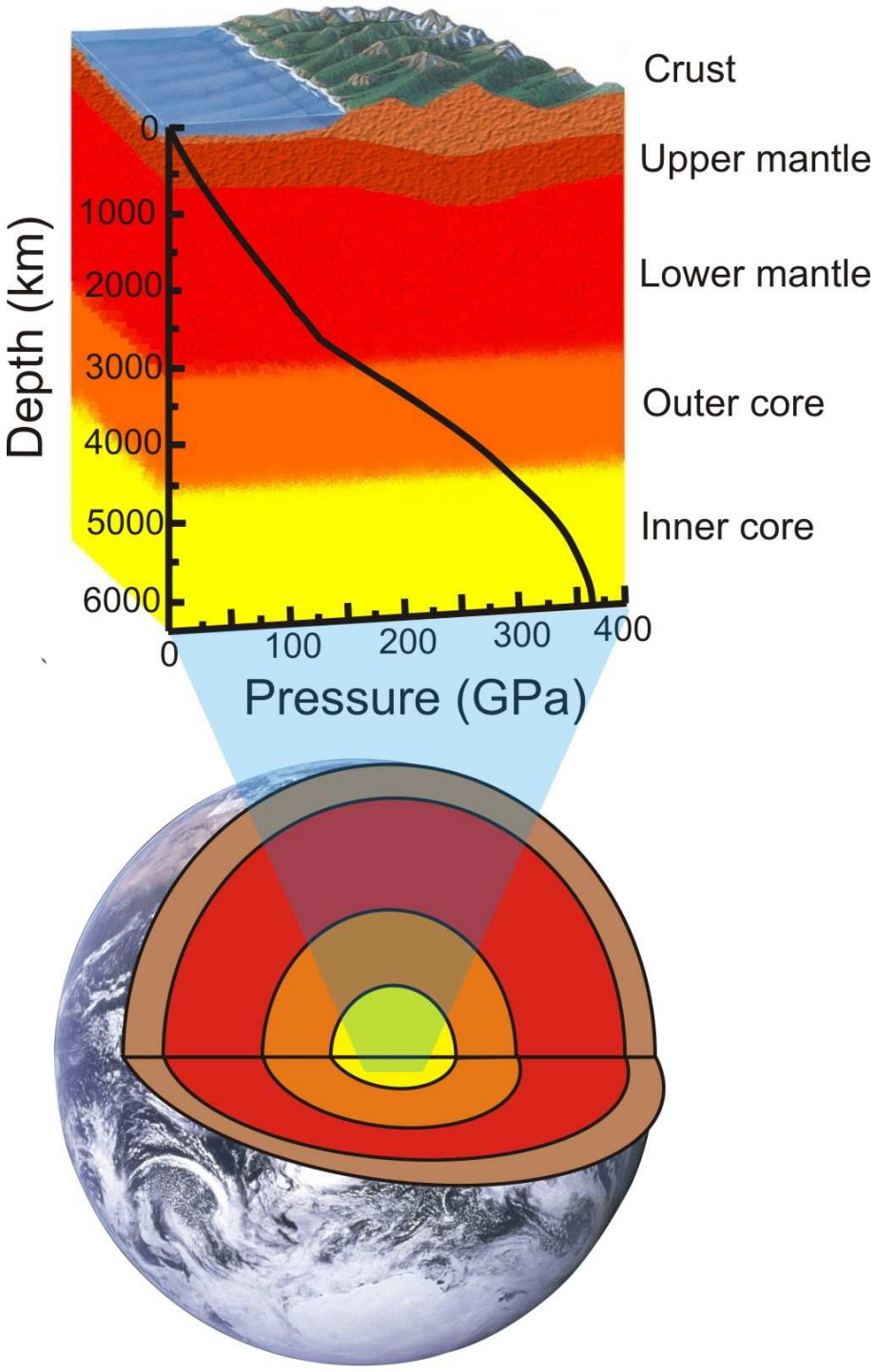

Figure 8.1: Cross section of the Earth's interior with a plot of depth vs. pressure data from the Preliminary Reference Earth Model (PREM) of Dziewonski and Anderson [257] overlaid.

clude deep-earthquake faulting which results from the interaction of the subducted solid state lithosphere and mantle [262, 263], the differentiation and evolution of the composition of planetary interiors [264–267], and the response of the Earth's crust and mantle to meteorite impacts [267–269]. At ambient pressure the most common polymorph of SiO_2 is α-quartz in which the Si atoms are 4-fold coordinated by oxygen [270–272]. At elevated pressure and temperature α-quartz transforms to Stischovite, in which the Si atoms are 6-fold coordinated [261, 273, 274]. A similar transformation from 4-fold to 6-fold coordinated Si has been observed in silica glass at pressures up to 50 GPa [265, 275–280]. As illustrated in figure 8.1, this pressure corresponds to depths within the Earth's crust and mantle of greater than 1000 km. Due to the challenging nature of high pressure experiments and the inherent structural disorder of silica glass, the pressure induced structural transformation mechanism of silica glass is not yet fully understood [278].

Germania (GeO_2) is in many respects a structural analogue of silica [281] and serves as a model compound to study the polyamorphic structures of these binary network glass forming systems. For example, a variety of spectroscopic [282–284] and diffraction [285–287] studies have shown that high pressure structural transformations take place in glassy GeO_2, that are analogous to those in glassy SiO_2, with 6-fold coordinated Ge being reported from *in situ* x-ray diffraction measurements [285] at the much lower and more experimentally accessible pressure of 15 GPa. The previously reported neutron diffraction data sets are, however, limited to a maximum pressure of 5 GPa and have large statistical uncertainties [285].

The aim of this investigation is, therefore, to develop *in situ* high pressure neutron diffraction methods to obtain high quality measurements of the total structure factor of GeO_2 glass, improving upon the neutron diffraction measurements previously obtained [285] and opening up a new realm of experimental possibility for measuring the structure of glasses at high pressure. This includes making isotopic substitution experiments feasible, the results of which would help to elucidate the mechanisms by which high pressure structural transformations occur in glasses.

8.2 Theory

As derived in § 2.2, the coherent scattered intensity measured in a neutron diffraction experiment on a multicomponent glass system is represented by the total structure factor $F(Q)$, defined as

$$F(Q) = \sum_{\alpha=1}^{n}\sum_{\beta=1}^{n} c_\alpha c_\beta b_\alpha b_\beta [S_{\alpha\beta}(Q) - 1], \tag{8.1}$$

where n denotes the total number of chemical species α or β, c_α and b_α represent the atomic fraction and coherent neutron scattering length of chemical species α, respectively, $S_{\alpha\beta}(Q)$ is a Faber-Ziman partial structure factor and Q is the scattering vector. The coherent neutron scattering lengths for GeO_2 glass are $b_{\mathrm{Ge}} = 8.185(20)$ fm and $b_{\mathrm{O}} = 5.803(4)$ fm [30]. The total structure factor can therefore be written as

$$F(Q) = A[S_{\mathrm{GeGe}}(Q) - 1] + B[S_{\mathrm{OO}}(Q) - 1] + C[S_{\mathrm{GeO}}(Q) - 1], \tag{8.2}$$

where $A = c_{\mathrm{Ge}}^2 b_{\mathrm{Ge}}^2 = 0.0744(4)$ barn, $B = c_{\mathrm{O}}^2 b_{\mathrm{O}}^2 = 0.1497(5)$ barn and $C = 2c_{\mathrm{Ge}}c_{\mathrm{O}}b_{\mathrm{Ge}}b_{\mathrm{O}} = 0.2111(5)$ barn. The corresponding real space information is given by the total pair distribution function $G(r)$ which is obtained by the Fourier transform

$$\begin{aligned} G(r) &= \frac{1}{2\pi^2 r n_0}\int_0^\infty QF(Q)\sin(Qr)\mathrm{d}Q \\ &= \sum_{\alpha=1}^{n}\sum_{\beta=1}^{n} c_\alpha c_\beta b_\alpha b_\beta [g_{\alpha\beta}(r) - 1] \\ &= A[g_{\mathrm{GeGe}}(r) - 1] + B[g_{\mathrm{OO}}(r) - 1] + C[g_{\mathrm{GeO}}(r) - 1], \end{aligned} \tag{8.3}$$

where n_0 denotes the atomic number density, $g_{\alpha\beta}(r)$ is a partial pair distribution function and r is a distance in real space. As defined in equation 2.12, the coordination number $\bar{n}_{\mathrm{Ge}}^{\mathrm{O}}$ is determined by integrating over the nearest neighbour peak in $G(r)$, for which it is assumed that only the $g_{\mathrm{GeO}}(r)$ correlations

contribute. The theoretical $G(0)$ limit is defined by

$$G(0) = -\sum_{\alpha=1}^{n}\sum_{\beta=1}^{n} c_\alpha c_\beta b_\alpha b_\beta. \tag{8.4}$$

For GeO_2 glass $G(0) = -0.4352(9)$ barn.

In an x-ray diffraction experiment, the scattered intensity is conventionally denoted by the total x-ray structure factor $S_X(Q)$ which, within the independent atom approximation, is given by

$$\begin{aligned} S_X(Q) - 1 &= \frac{F_X(Q)}{\left[\sum_\alpha c_\alpha f_\alpha(Q)\right]^2} \\ &= \frac{1}{\left[\sum_\alpha c_\alpha f_\alpha(Q)\right]^2} \sum_{\alpha=1}^{N}\sum_{\beta=1}^{N} c_\alpha f_\alpha(Q) c_\beta f_\beta(Q) \left[S_{\alpha\beta}(Q) - 1\right], \end{aligned} \tag{8.5}$$

where $f_\alpha(Q)$ represents the Q dependent neutral atom form factor for atomic species α. The total x-ray pair distribution function $G_X(r)$ is obtained by Fourier transforming the $S_X(Q)$ function. However, because the partial structure factors are weighted by Q-dependant form factors, the $g_{\alpha\beta}(r)$ correlations are convoluted by the Fourier transform of the form factors in real space. The coordination number cannot therefore be calculated by integrating over the first peak in $G_X(r)$. Instead, provided the nearest neighbour peak in the $G_X(r)$ function arises solely from the Ge-O correlations, the $F_X(Q)$ function is divided by the weighting factor for the $S_{\mathrm{GeO}}(Q)$ function, i.e. $2c_{\mathrm{Ge}}f_{\mathrm{Ge}}(Q)c_{\mathrm{O}}f_{\mathrm{O}}(Q)$, such that in the Fourier transform the r-dependent weighting factor is removed from the $g_{\mathrm{GeO}}(r)$ partial pair distribution function [191].

8.3 Neutron diffraction study A

The structural transformations that occur in GeO_2 glass at high pressures are not retained upon decompression [286]. Therefore, high pressure diffraction experiments must be performed *in situ*. The objective of this experiment was to assess the operation of a Paris-Edinburgh press installed for the first time

on the D4C instrument at the ILL, France, described in § 3.2.1, to measure accurate diffraction patterns for GeO_2 glass at high pressures. The VX5 variant Paris-Edinburgh press was used since it has only two support pillars and therefore avoids unwanted scattering and attenuation effects. By mounting the press in transmission geometry a large range of scattering angles 2θ is accessible to the D4C detector array. An incident neutron wavelength of $\simeq 0.7$ Å provides an optimum incident neutron flux and enables the use of cadmium (Cd), an excellent neutron absorber at this wavelength, as an effective shielding material to reduce background scattering from the Paris-Edinburgh cell assembly and anvils. The high incident neutron flux and very high counting stability of the D4C instrument are vital in order to obtain accurate diffraction patterns from the very small sample volume (< 0.05 cm^3) which is limited by the geometry of the cell.

8.3.1 Experimental procedure

Glass preparation

The GeO_2 glass was made by heating ≈ 3 g of powdered Germanium (IV) Oxide (Alfa Aesar, 99.9999%) contained in a 10% Rhodium Platinum crucible in air at 1600°C. After ≈ 30 min the crucible was removed from the furnace and placed onto a nitrogen cooled brass block where liquid nitrogen was poured over the melt to increase the quench rate. The resulting transparent, colourless sample was annealed at a temperature of 600°C [288]. Unfortunately this temperature is 20 °C above the highest reported T_g of GeO_2 [289] and hence the sample experienced some re-crystallisation during annealing. Since GeO_2 is hygroscopic, the glass sample was stored in a desiccator containing silica gel (BDH, granules) until immediately prior to the experiment. For the *in situ* neutron diffraction experiments, a pre-compressed pellet was formed to ensure a large sample packing fraction thus reducing the number of voids in the powder and improving the pressure response of the cell to the applied force. The pellet was formed by Klotz [290] at the Pierre & Marie Curie University,

Paris using finely powdered GeO_2 glass which was compressed using a powder press die of identical geometry to the single toroid sample cell (see figure 3.9). The resulting pellet was extremely fragile and, after removing from the powder press, the middle section disintegrated. Additional fine powder was therefore added to bulk out the sample for the diffraction experiment giving a total sample mass of ≈ 0.2 g.

Modulated Differential Scanning Calorimetry

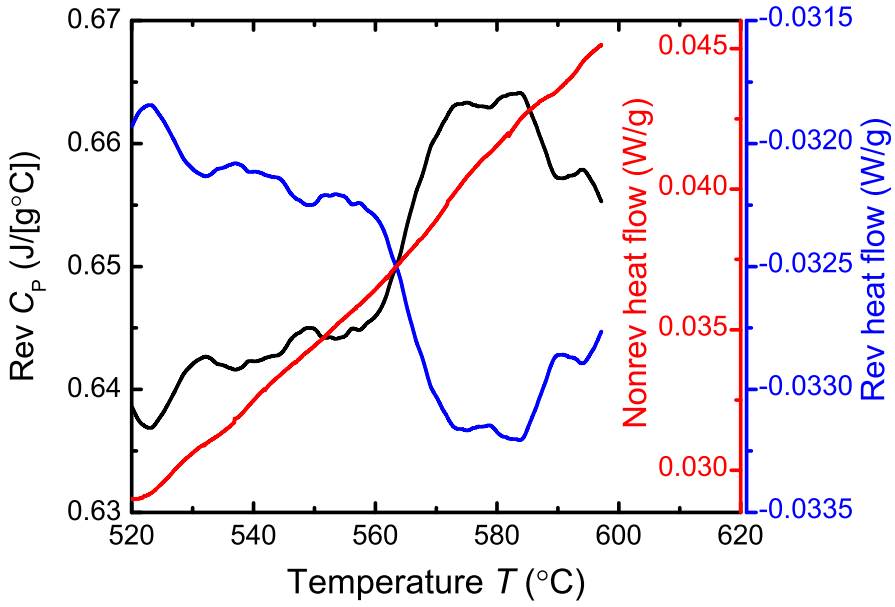

Figure 8.2: Modulated differential scanning calorimetry (MDSC) scans for GeO_2 glass, where the blue curve denotes the reversible heat flow, the red curve denotes the non-reversible heat flow and the black curve denotes the reversible heat capacity C_p signal.

The glass transition temperature T_g and change in heat capacity ΔC_p for the GeO_2 glass was measured by modulated differential scanning calorimetry (MDSC) using a TA Instruments DSC Q100 machine. The T_g for GeO_2 has been previously reported at several temperatures namely 476 [291], 550 [292],

560 [293] and 580 °C [289]. Since the upper limit of the operating temperature of the standard TA Refrigerated Cooling System (RCS) is only 550 °C, a TA Finned Air Cooling System (FACS) was installed to enable temperature modulation up to 725 °C. The sample and reference pans were constructed from gold (0.025 mm thick foil, Aldrich, 99.99%) with a flat circular base of 5 mm diameter and walls of 2 mm height. The sample and reference pans had identical masses (within ± 0.5 mg) and were both annealed in a furnace at 750 °C for 3 hours prior to the experiment to relieve any residual internal stress in the gold structure that could lead to fluctuations in the MDSC baseline.

A finely powdered sample of GeO_2 glass of mass 17.18 mg was loaded into the annealed gold sample pan. An annealed gold lid was placed on top of the powder and crimped with the walls of the pan to ensure good thermal contact over the entire sample. The sample was first equilibrated at 150 °C for 2 hours to remove any adsorbed H_2O and then heated over the temperature range $400 \leq T$ °C ≤ 700 at a rate of 3.00 °C min^{-1} with a temperature modulation of ± 0.5 °C every 100 s. Nitrogen gas (BOC, Oxygen free), flowing at 50 ml min^{-1}, was used to purge the instrument of moisture and oxygen and to provide efficient heat transfer between the sample pans and the DSC cell contacts. A nitrogen gas line was also used to provide cooling gas for the FACS and a desktop fan was used to cool the bell jar assembly of the MDSC head to assist heat dissipation. The reversible and non-reversible components of the heat flow and heat capacity C_p were recorded every 0.2 s and are plotted in figure 8.2. Unlike the standard RCS, the FACS is not designed for routine MDSC experiments and hence the temperature modulation was not so precisely defined. The results were therefore extremely difficult to obtain as large fluctuations were observed in the baseline of the DSC signals. Nevertheless an endothermic step is observed in the reversible heat flow signal in the expected region for the glass transition. A mid-point glass transition temperature of $T_g = 566(2)$ °C was obtained by drawing a tangent line to the data in the transition region of the reversible heat flow to find the point of inflection. A change in heat capacity through T_g of $\Delta C_p = 0.018(5)$ Jg^{-1} $°C^{-1}$ was obtained from the observed step in the reversible heat capacity curve. The small ΔC_p is

typical of open network systems and the mean value of $C_p \approx 0.65(1)$ Jg^{-1} $°C^{-1}$ is comparable to a value of $C_p \approx 0.7$ Jg^{-1} $°C^{-1}$ reported by Angell [8].

The neutron diffraction experiment

The VX5 variant Paris Edinburgh press used for the *in situ* high pressure neutron diffraction experiments is shown in figure 8.3. The monochromatic neutron beam, with an incident wavelength of 0.69566(7) Å and beam width of 11 mm, was collimated using boron carbide ($^{10}B_4C$) flags set to give a beam height of 4 mm centered on the GeO_2 glass pellet encapsulated between the single toroid cubic boron nitride (BN) anvils by a null scattering Ti-Zr gasket, denoted gasket 1. The neutron beam, incident on the edge of the gasket, was further collimated to the separation h of the BN anvils, determined by the thickness of the Ti-Zr gasket, defining a cylindrical sample geometry for the incident and scattered beam (see figure 8.4). At ambient pressure the sample height and diameter were 1.6 mm and 6 mm, respectively. The relatively large height of the incident neutron beam, by comparison with the sample height, was chosen to account for the vertical displacement of the compression anvil upon the application of pressure and to ensure the sample remained fully illuminated by the neutron beam.

The pressure was applied using a hydraulic pump. The force F on the compression anvil is given by

$$F = pA = Lg, \tag{8.6}$$

where p denotes the oil pressure, $A = 66.5$ cm^2 is the piston cross section for the VX5 variant Paris-Edinburgh press, L is the applied load and $g = 9.80665$ m s^{-2} is the standard acceleration due to gravity. A nominal load of 1.0 tonne was first applied, to ensure the sample and gasket took the shape of the anvils, before performing an ambient pressure diffraction experiment on the GeO_2 glass. Further high pressure experiments were performed, applying loads at ≈ 20 tonne intervals up to 101.7 tonne. To obtain reasonable counting

Figure 8.3: The VX5 variant Paris-Edinburgh press assembly mounted in transmission geometry prior to installation on the D4C instrument for study A, orientated such that the compression anvil is on top. The neutron beam is incident from the left hand side and is collimated by the $^{10}B_4C$ flags shown, which define a beam height of 4 mm centered on the sample position at ambient pressure.

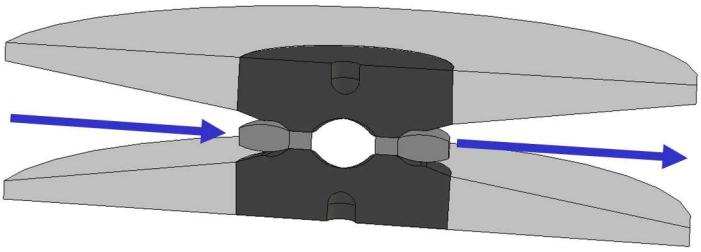

Figure 8.4: A cross section of the single toroid pressure cell used at D4C. In transmission geometry, the neutron beam, as shown by the arrows, is incident on the edge of the null scattering Ti-Zr gasket, which encapsulates the sample between the boron nitride anvils, and scatters from the sample and gasket into the D4C detectors.

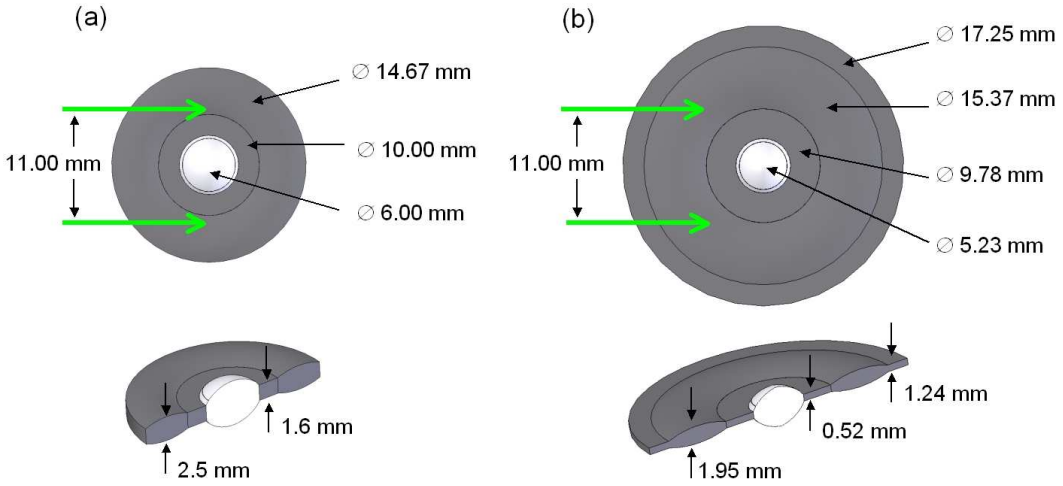

Figure 8.5: The dimensions of the sample and null scattering Ti-Zr gasket from study A at (a) ambient pressure and (b) recovered from 101.7 tonne. The green arrows indicate the width of the incident neutron beam. Equation 8.9 was used to calculate the maximum pressure $P_0 = 8.6(5)$ GPa on the sample from the outer radius of the recovered gasket $r_g = 8.625$ mm (see figure 8.7).

statistics, neutrons were counted for 4.0 hr in the ambient pressure measurement and for up to 8.5 hr in the higher pressure experiments (see table 8.1). On recovery back to ambient pressure the GeO_2 sample had compacted into a transparent solid. The recovered gasket was deformed, as shown in figure 8.5, by comparison to the dimensions of the gasket at ambient pressure.

To characterise the gasket scattering, ambient pressure diffraction patterns were measured for an uncompressed empty Ti-Zr gasket, denoted gasket 2, and the empty Ti-Zr gasket recovered from the 101.7 tonne experiment, denoted gasket 3. To assist in the data normalisation at different pressures, ambient pressure diffraction patterns were measured for large (V pellet 1) and small (V pellet 2) vanadium pellets in gaskets 2 and 3, respectively (see table 8.1). The vanadium pellets were machined from a vanadium rod (Alfa Aesar, 99.5 %) to the single toroid anvil profile with the height of the cylindrical section measuring 1.6 mm for V pellet 1 and 1.2 mm for V pellet 2. A diffraction pattern was also measured with the anvils separated by 1.5 mm to assist in estimating the background scattering and, to examine the effect of sample self-

Table 8.1: Details of the experimental runs. The load L on the piston was determined using equation 8.6 at the corresponding oil pressure p. The separation h of the anvils was determined by the thickness of the gaskets and was either measured or, for the *in situ* pressure measurements marked by †, was estimated by using a linear extrapolation procedure (see § 8.3.2). Note, the anvil separation at the highest pressure is smaller than the thickness of the recovered gasket, due to relaxation of the gasket on recovery. The neutron counting time t is also listed.

Sample	Gasket	h (mm)	p (bar)	L (tonne)	t (hr)
GeO_2 glass	1	1.6	15	1.0	4.0
GeO_2 glass	1	1.2 †	300	20.3	4.5
GeO_2 glass	1	0.9 †	600	40.7	6.5
GeO_2 glass	1	0.7 †	900	61.0	8.5
GeO_2 glass	1	0.5 †	1200	81.4	8.0
GeO_2 glass	1	0.4 †	1500	101.7	7.0
Empty uncompressed gasket	2	1.6	15	1.0	6.5
Empty recovered gasket	3	0.52	15	1.0	6.0
V pellet 1	2	1.6	15	1.0	4.0
V pellet 2	3	0.52	15	1.0	4.0
Cd pellet 1	2	1.6	15	1.0	1.0
Cd pellet 2	3	0.52	15	1.0	1.0
Empty anvils	–	1.5	–	–	1.0

Gasket 1 : used to encapsulate the sample
Gasket 2 : uncompressed gasket
Gasket 3 : gasket 1 recovered from 101.5 tonne

shielding on the background count rate at small scattering angles, diffraction patterns were measured for large (Cd pellet 1) and small (Cd pellet 2) cadmium pellets in gaskets 2 and 3, respectively (see table 8.1). The cadmium pellets were formed from Cd foil compacted in a press to the single toroid anvil profile with the height of the cylindrical section measuring 1.6 mm for Cd pellet 1 and 1.0 mm for Cd pellet 2. For these background and calibration runs, a nominal load of 1.0 tonne was applied to ensure the gasket was seated tightly in the anvils, giving an effective sample height equal to the thickness of the gasket used.

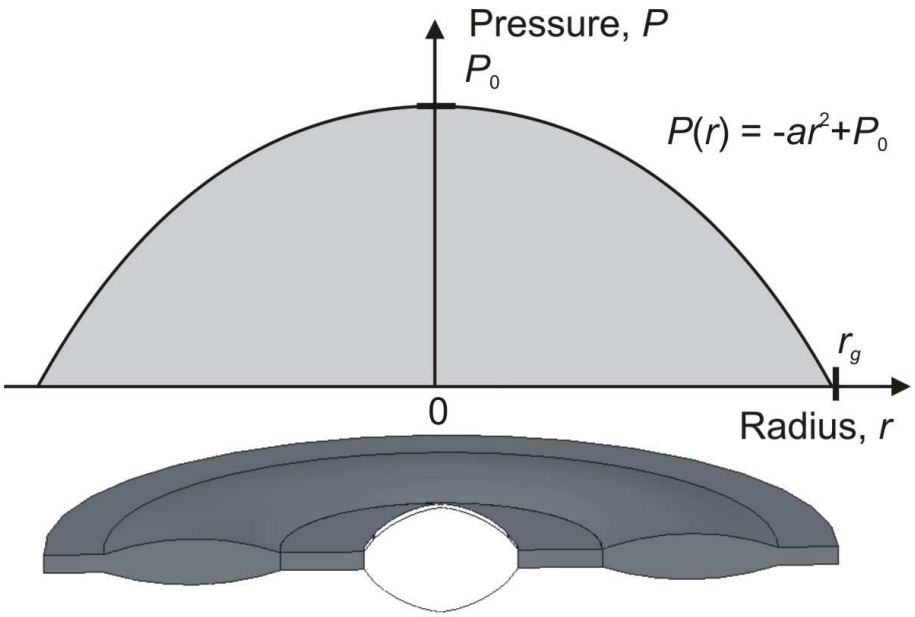

Figure 8.6: An illustration of the pressure gradient across the sample and gasket assembly during a high pressure experiment. The pressure P at radius r can be expressed by the function $P(r) = -ar^2 + P_0$, where P_0 is the pressure at the sample position and a is a constant.

During the high pressure experiments, there is a large pressure gradient across the sample and gasket assembly. As illustrated in figure 8.6, the pressure P at a specified radius r from the centre of the sample and gasket assembly can be approximated by the function [45]

$$P(r) = -ar^2 + P_0, \tag{8.7}$$

where P_0 is the maximum pressure at the sample position. The boundary conditions are $P(r = 0) = P_0$ and $P(r_{\rm g}) = P_0 - ar_{\rm g}^2 = 0$, where r_g is the outer radius of the gasket, giving $a = \frac{P_0}{r_{\rm g}^2}$. The total force F applied to the sample and gasket assembly is determined by

$$F = \int_0^{r_{\rm g}} 2\pi r {\rm d}r P(r). \tag{8.8}$$

Table 8.2: The pressure P_0 at each load L together, with the corresponding number density n_0 and sum rule S, given by equation 2.11, for GeO_2 glass and the number density n_0(Ti-Zr) for the null scattering Ti-Zr gasket, measured using the archimedes method at ambient pressure and estimated using equation 8.17 at pressure P_g (given by equation 8.10) experienced across the gasket.

L (tonne)	P_0 (GPa)	n_0 (Å^{-3})	S (barn Å^{-3})	$P_{\rm g}$ (GPa)	n_0(Ti-Zr) (Å^{-3})
1.0	0	0.0629(3)	-0.540(8)	0	0.0511(9)
20.3	1.2(5)	0.0664(9)	-0.570(8)	0.5(5)	0.0513(9)
40.7	3.1(5)	0.0719(9)	-0.618(8)	1.4(5)	0.0517(9)
61.0	4.9(5)	0.0774(9)	-0.665(8)	2.3(5)	0.0522(9)
81.4	6.8(5)	0.0845(9)	-0.726(8)	3.1(5)	0.0525(9)
101.7	8.6(5)	0.0872(9)	-0.749(8)	4.0(5)	0.0529(9)

Solving this equation gives

$$P_0 = \frac{2F}{\pi r_{\rm g}^2} = \frac{2g}{\pi r_{\rm g}^2} L. \tag{8.9}$$

The maximum sample pressure of $P_0 = 8.6(5)$ GPa attained in the experiment was determined from equation 8.9, where the radius of the gasket was $r_{\rm g} = 8.625$ mm after recovery from $L = F/g = 101.7$ tonne (see figure 8.5). The pressure on the sample during each experiment, given in table 8.2, was estimated from figure 8.7 by assuming a linear relationship between load and pressure (see equation 8.9), after application of an initial load of ≥ 7 tonne. Before this load the gasket deforms to the shape of the anvils but pressure is not applied to the sample.

Estimated values for the average pressure P_g experienced across the gasket for each pressure P_0 are listed in table 8.2 and were calculated using

$$P_{\rm g} = \frac{P(r_{\rm g}) - P(r'_{\rm g})}{2}, \tag{8.10}$$

where $r'_{\rm g}$ denotes the inner radius of the gasket and the pressure $P(r'_{\rm g})$ was calculated from equation 8.7. This is, however, a crude method as the pressure does not vary linearly with r. At radius r'_g the total force applied to the gasket

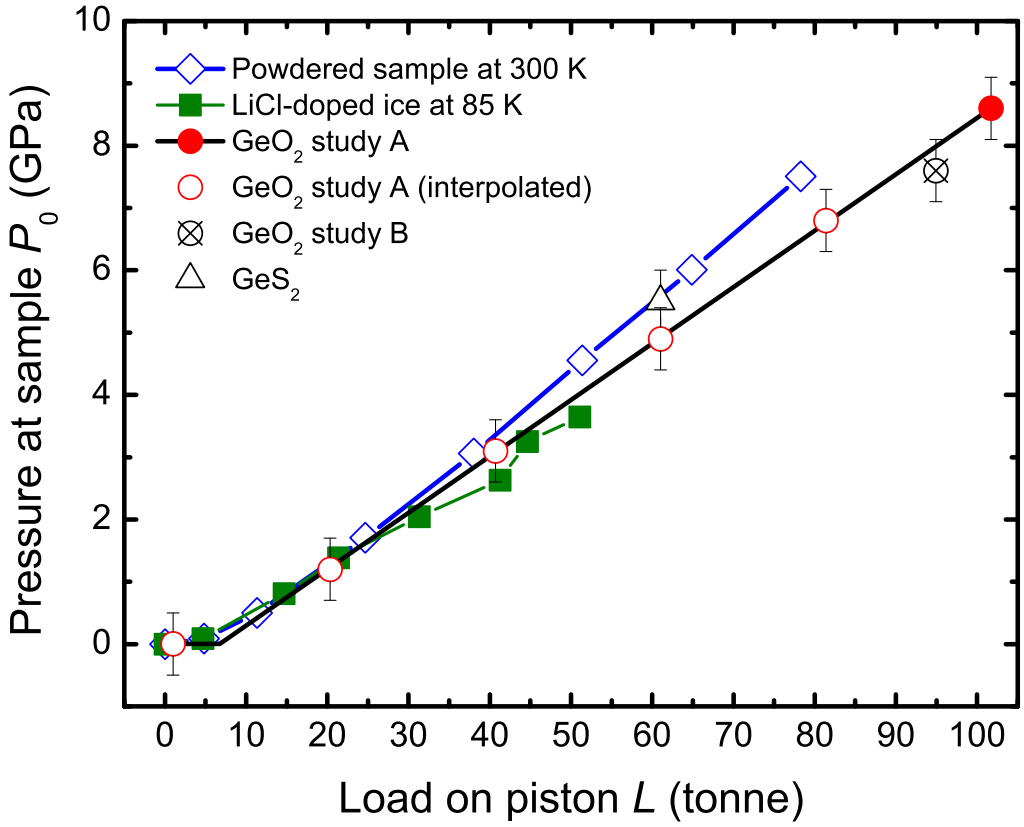

Figure 8.7: Load L applied to the VX5 variant Paris-Edinburgh cell piston versus pressure P_0 at the sample position from measurements of powdered samples at 300 K [294] (open blue diamonds), LiCl-doped ice at 85 K [294] (solid green squares), GeO_2 glass after applying equation 8.9 using the radius of the recovered gasket from $L = 101.7$ tonne (solid red circle) and by using the radius of recovered gaskets from subsequent measurements of GeO_2 glass in study B (crossed black circle) (see § 8.5) and GeS_2 glass [191] (open black triangle). The other data points (open red circles) were obtained after assuming a linear relationship between load and pressure between an initial load of ≥ 7 tonne (before which $P_0 = 0$ GPa) and the load of 101.7 tonne (see the text).

and sample assembly is given by

$$F = \int_0^{r_g'} 2\pi r \mathrm{d}r P(r) \tag{8.11}$$

which can be solved to give

$$F(r_g') = \pi P_0 \left[r_g'^2 - \frac{r_g'^4}{2r_g^2} \right]. \tag{8.12}$$

As given in equation 8.9, the total force applied at radius r_g is given by

$$F(r_g) = \frac{1}{2}\pi r_g^2 P_0. \tag{8.13}$$

The force applied across the gasket only is therefore given by

$$F_g = F(r_g) - F(r_g') = \pi P_0 r_g^2 \left[\frac{1}{2} - \left(\frac{r_g'}{r_g} \right)^2 + \frac{1}{2} \left(\frac{r_g'}{r_g} \right)^4 \right]. \tag{8.14}$$

Since the area of the gasket

$$A_g = \pi r_g^2 - \pi r_g'^2 \tag{8.15}$$

the pressure across the gasket can be calculated using

$$P_g = \frac{P_0 r_g^2}{(r_g^2 - r_g'^2)} \left[\frac{1}{2} - \left(\frac{r_g'}{r_g} \right)^2 + \frac{1}{2} \left(\frac{r_g'}{r_g} \right)^4 \right]. \tag{8.16}$$

In the current study, the two methods of calculating P_g represented by equations 8.10 and 8.16 give comparable values within ≈ 3 %.

The number density of GeO_2 glass at each pressure is listed in table 8.2. These values were obtained by interpolating between the measured density values of Hong *et al.* [287] (see figure 8.8), which are in good agreement with the equation of state (EOS) for GeO_2 glass given by Tsiok *et al.* [297].

The density of the gasket is also required to correctly determine the atten-

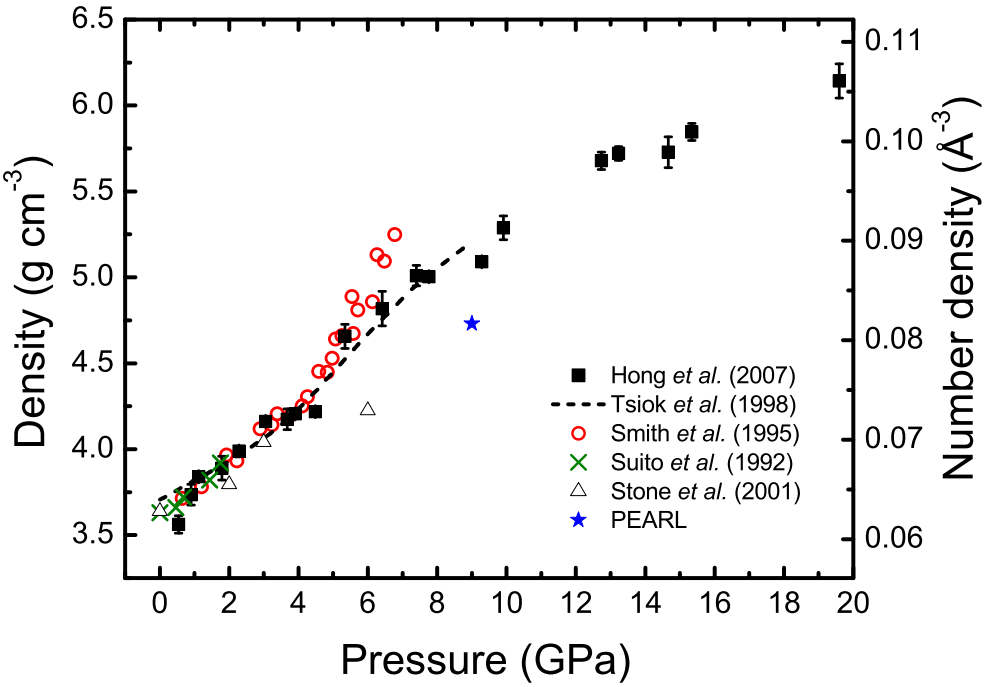

Figure 8.8: The mass density ρ and corresponding number density n_0 for GeO_2 glass from *in situ* measurements by Hong *et al.* [287] (solid black squares), Smith *et al.* [295] (open red circles) and Suitio *et al.* [296] (green crosses), together with the equation of state given by Tsiok *et al.* [297] (dashed black curve). The values for samples recovered to ambient conditions from high pressure by Stone *et al.* [298] (open black triangles) and for a sample recovered from 9.0 GPa as measured *in situ* using the PEARL instrument (blue star), as detailed in chapter 9, are also plotted.

uation coefficients and to make accurate data corrections, as detailed in the following section. However, the EOS for the null scattering Ti-Zr alloy has not previously been determined, although the high pressure crystal structures of Ti [299, 302], Zr [300] and the equiatomic TiZr alloy [301, 303] have been studied. At room temperature, the equiatomic alloy exists in the α-phase and transforms to the denser ω-phase at $\approx$ 12 GPa [301]. According to Vegard's law the density ρ of a simple metallic alloy such as TiZr, in which the components Ti and Zr are completely soluble [303], can be deduced from a linear combination of the density of the individual components, i.e. $\rho(\text{Ti-Zr}) = c_{\text{Ti}}\rho(\text{Ti}) + c_{\text{Zr}}\rho(\text{Zr})$,

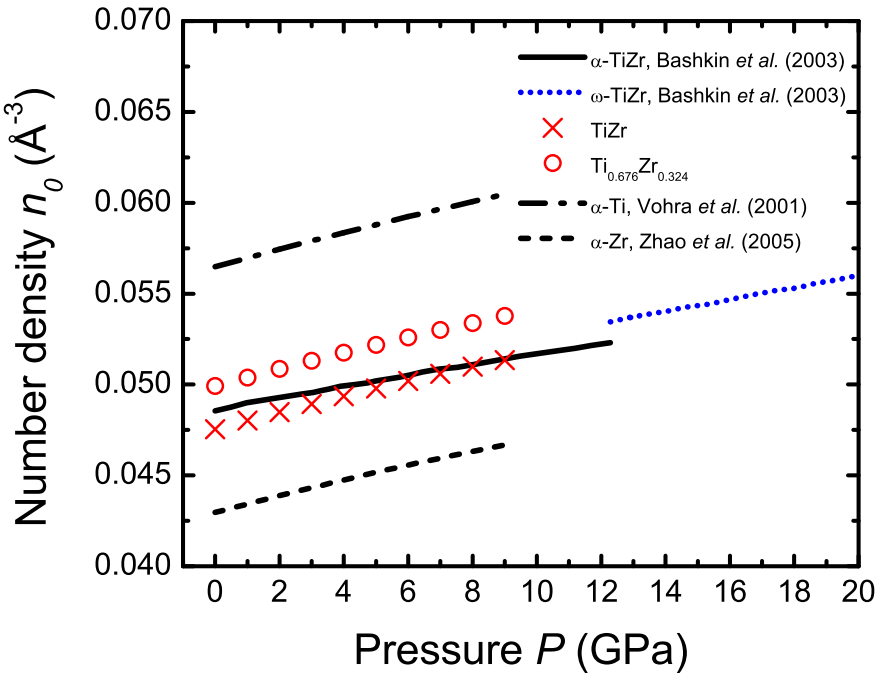

Figure 8.9: The number density as a function of pressure at room temperature for α-Ti [299] (short dashed black curve), α-Zr [300] (chained black curve), equiatomic α-TiZr [301] (solid black curve), equiatomic ω-TiZr [301] (dotted blue curve), an equiatomic linear combination of α-Ti and α-Zr (red crosses) and a null scattering linear combination of α-Ti and α-Zr, i.e. $Ti_{0.676}Zr_{0.324}$ (open circles).

where c_{Ti} and c_{Zr} denote the atomic fraction of Ti and Zr, respectively. Combining the room temperature EOS for α-Ti [299] and α-Zr [300] with equal weighting reproduces the EOS for equiatomic α-TiZr [301] within 2 % (see figure 8.9).

The coherent neutron scattering lengths for Ti and Zr are $-3.438(2)$ and 7.16(3) fm, respectively [30]. Therefore, the null scattering composition is $Ti_{0.676}Zr_{0.324}$. The ambient pressure number density n_0(Ti-Zr) = 0.0511(5) Å^{-1} was measured for a null scattering Ti-Zr gasket using the Archimedes method. This value is in agreement with that previously measured by Howells [304]. Combining the room temperature EOS for α-Ti [299] and α-Zr [300] using the

atomic fractions for the null scattering alloy reproduces the measured value within 2 % (see figure 8.9). Since the EOS for the null scattering Ti-Zr alloy has not previously been determined, experimentally or otherwise, Vegard's law was employed to estimate the density of the null scattering Ti-Zr alloy at pressures greater than ambient using the pressure dependance of the number density of Ti and Zr such that

$$n_0(\text{Ti-Zr}) = 0.676 n_0(\text{Ti}) + 0.324 n_0(\text{Zr}). \tag{8.17}$$

The values for the number density for the null scattering Ti-Zr at each pressure P_g experienced by the gasket are given in table 8.2.

8.3.2 Data analysis procedure

The measured diffraction patterns are plotted in figure 8.10. The scattered intensity from the Ti-Zr gasket constitutes a large proportion of the total scattering at each pressure with a comparable level of intensity arising from empty Ti-Zr gasket 2 as from the measurement of GeO_2 glass at ambient pressure. The scattered intensity from the anvils is relatively small at low scattering angles but leads to significant steps in the measured diffraction patterns at higher scattering angles. By comparison with the empty Ti-Zr gasket measurements, the cadmium measurements show a small reduction in the scattered intensity at low scattering angles. In practice, the self-shielding correction using the cadmium measurements was not performed. Despite the large contributions to the GeO_2 diffraction patterns from the gasket and anvils, the total structure factors $F(Q)$ were successfully extracted from the measured intensities using the following analysis procedure, which proved to be essential for correcting the data sets and was developed to account for the pressure dependent sample and gasket geometry and associated background and attenuation factors.

In the high pressure diffraction experiments, neutrons were incident on the edge of the null scattering Ti-Zr gasket which encapsulates the sample (see figure 8.4). The scattering from the Ti-Zr gasket and anvils is large and must be suitably corrected for. However, the background scattering and ge-

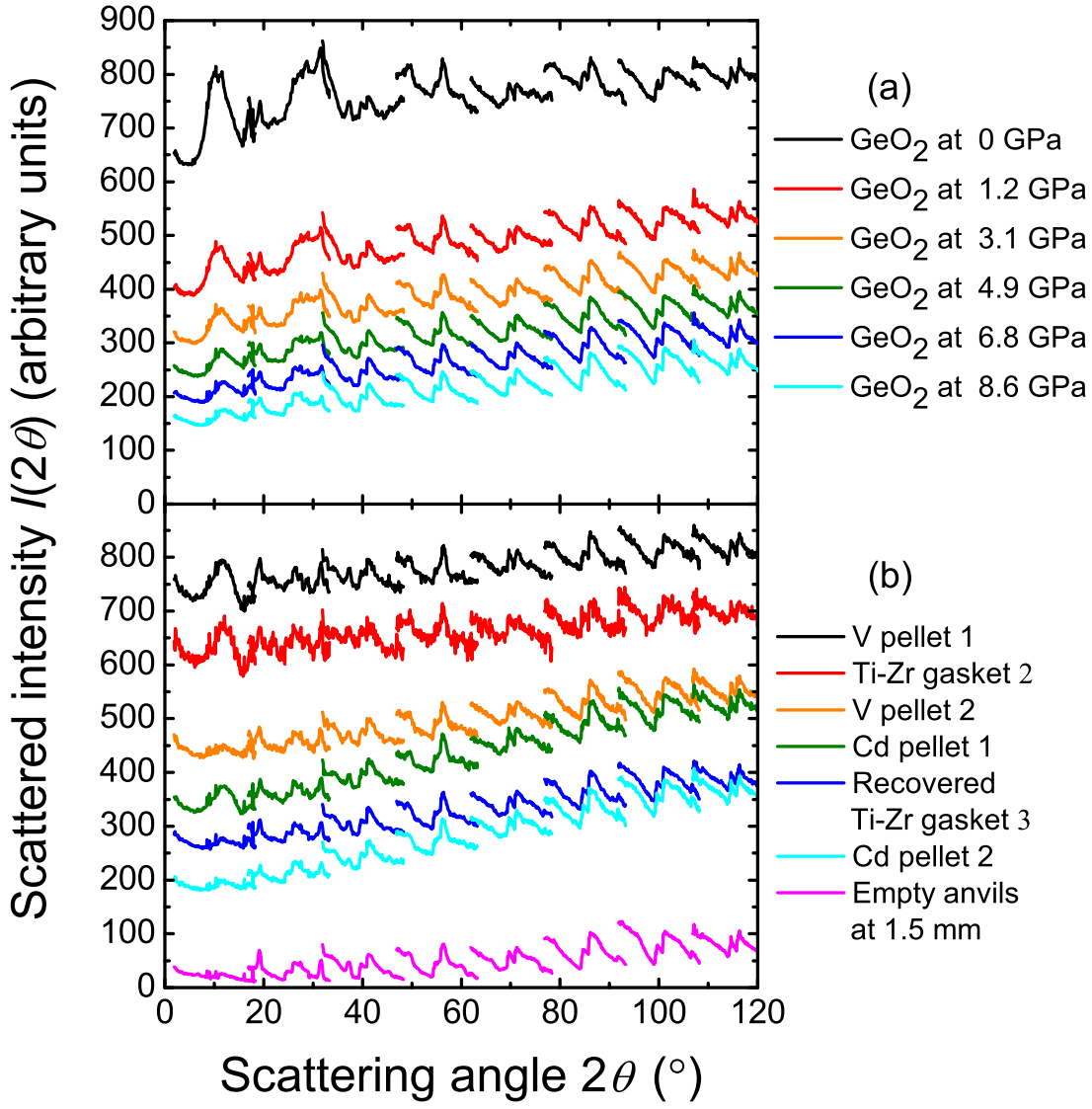

Figure 8.10: The measured *in situ* neutron diffraction patterns. (a) GeO_2 glass contained within Ti-Zr gasket 1 at ambient pressure (black), 1.2 GPa (red), 3.1 GPa (orange), 4.9 GPa (green), 6.8 GPa (blue) and 8.6 GPa (cyan). (b) V pellet 1 within Ti-Zr gasket 2 (black), empty Ti-Zr gasket 2 (red), V pellet 2 in recovered Ti-Zr gasket 3 (orange), Cd pellet 1 in Ti-Zr gasket 2 (green), empty recovered Ti-Zr gasket 3 (gasket 1 recovered from 8.6 GPa) (blue), Cd pellet 2 in recovered Ti-Zr gasket 3 (cyan), and empty anvils separated by 1.5 mm (magenta).

ometry of the sample and gasket are not explicitly known as a function of pressure. A linear combination of the ambient pressure diffraction patterns for an uncompressed empty gasket (i.e. gasket 2), denoted $I^E_{C'}(\theta)$, and an empty gasket recovered from the pressure experiment (i.e. gasket 3), denoted $I^E_{C''}(\theta)$, is therefore made to approximate the contribution from the gasket to the total scattering at each pressure. The contribution to the total scattering from the instrument and pressure cell can be quantified by using the scattered intensity from the anvils with no sample or gasket present, denoted $I^B_{SC}(\theta)$. The measured sample intensity $I^E_{SC}(\theta)$, corrected for pressure cell background and gasket scattering, is given by

$$\begin{aligned} I'_{SC}(\theta) &= (I^E_{SC}(\theta) - I^B_{SC}(\theta)) \\ &- \frac{A_{C,SC}(\theta)}{A_{C,C}(\theta)}\left[x(I^E_{C'}(\theta) - I^B_{SC}(\theta)) + (1-x)(I^E_{C''}(\theta) - I^B_{SC}(\theta))\right] \\ &= I^E_{SC}(\theta) - A_1(\theta)I^E_{C'}(\theta) - A_2(\theta)I^E_{C''}(\theta) - A_3(\theta)I^B_{SC}(\theta), \end{aligned} \tag{8.18}$$

where $0 \leq x \leq 1$. The values of the coefficients $A_1(\theta)$, $A_2(\theta)$ and $A_3(\theta)$ are given by

$$A_1(\theta) = x\frac{A_{C,SC}(\theta)}{A_{C,C}(\theta)}, \tag{8.19}$$

$$A_2(\theta) = (1-x)\frac{A_{C,SC}(\theta)}{A_{C,C}(\theta)}, \tag{8.20}$$

$$A_3(\theta) = 1 - \frac{A_{C,SC}(\theta)}{A_{C,C}(\theta)}. \tag{8.21}$$

The attenuation factors $A_{i,j}(\theta)$, calculated for the sample and gasket geometry at ambient pressure, are plotted in figure 8.11. In practice, the θ dependence of the attenuation factor $\frac{A_{C,SC}(\theta)}{A_{C,C}(\theta)}$ was neglected and the exact values for $A_1(\theta)$, $A_2(\theta)$ and $A_3(\theta)$ were allowed to vary from their theoretical values to ensure that the contributions from the gasket and anvil scattering were eliminated

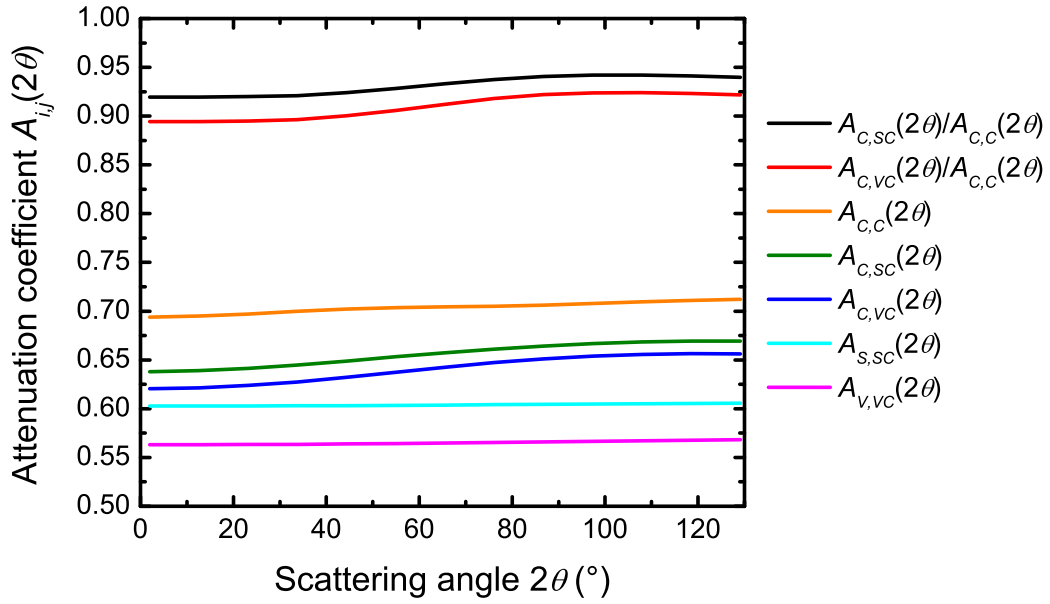

Figure 8.11: The 2θ dependence of the attenuation coefficients $A_{C,SC}(2\theta)/A_{C,C}(2\theta)$ (black), $A_{C,VC}(2\theta)/A_{C,C}(2\theta)$ (red), $A_{C,C}(2\theta)$ (orange), $A_{C,SC}(2\theta)$ (green), $A_{C,VC}(2\theta)$ (blue), $A_{S,SC}(2\theta)$ (cyan), and $A_{V,VC}(2\theta)$ (magenta) calculated using the GUDRUN program [111] for GeO_2 glass and vanadium samples encapsulated in uncompressed null scattering Ti-Zr gaskets in cylindrical geometry defined by the dimensions of the gasket at ambient pressure (see figure 8.5 (a)) with an incident neutron wavelength of 0.69566(7) Å.

i.e. the coefficients $A_1(\theta)$, $A_2(\theta)$ and $A_3(\theta)$ did not necessarily sum to unity.

As shown by equation 3.27, the differential scattering cross section for a sample in a container is given by

$$\left[\frac{\mathrm{d}\sigma}{\mathrm{d}\Omega}(\theta)\right]_S = \frac{1}{N_S A_{S,SC}(\theta)}\left[\left(\frac{I^*_{SC}(\theta)}{a(\theta)} - M_{SC}(\theta)\right) - \frac{A_{C,SC}(\theta)}{A_{C,C}(\theta)}\left(\frac{I^*_{C}(\theta)}{a(\theta)} - M_{C}(\theta)\right)\right] \tag{8.22}$$

where N_S denotes the number of sample nuclei in the neutron beam, $M_{SC}(\theta)$ and $M_C(\theta)$ denote the multiple scattering cross sections for the sample and the container, respectively, and $I^*_{SC}(\theta)$ and $I^*_C(\theta)$ denote the background corrected

intensities measured for the sample and container, respectively. In equation 8.18, the container and background scattering has already been corrected for and hence

$$I'_{SC}(\theta) \equiv I^*_{SC}(\theta) - \frac{A_{C,SC}(\theta)}{A_{C,C}(\theta)} I^*_C(\theta). \tag{8.23}$$

Equation 8.22 can therefore be re-written in terms of $I'_{SC}(\theta)$ where

$$\left[\frac{\mathrm{d}\sigma}{\mathrm{d}\Omega}(\theta)\right]_S = \frac{1}{N_S A_{S,SC}(\theta)} \left[\frac{I'_{SC}(\theta)}{a(\theta)} - \left(M_{SC}(\theta) - \frac{A_{C,SC}(\theta)}{A_{C,C}(\theta)} M_C(\theta)\right)\right]. \tag{8.24}$$

When a vanadium pellet is used as the sample, equation 8.24 is written as

$$\left[\frac{\mathrm{d}\sigma}{\mathrm{d}\Omega}(\theta)\right]_V = \frac{1}{N_V A_{V,VC}(\theta)} \left[\frac{I'_{VC}(\theta)}{a(\theta)} - \left(M_{VC}(\theta) - \frac{A_{C,VC}(\theta)}{A_{C,C}(\theta)} M_C(\theta)\right)\right] \tag{8.25}$$

where N_V is the total number of vanadium nuclei in the neutron beam and the measured intensity $I'_{VC}(\theta)$ for the vanadium pellet, corrected for background and gasket scattering, is given by

$$I'_{VC}(\theta) = I^E_{VC}(\theta) - \frac{A_{C,VC}(\theta)}{A_{C,C}(\theta)} I^E_C(\theta). \tag{8.26}$$

From equation 3.12

$$\left[\frac{\mathrm{d}\sigma}{\mathrm{d}\Omega}(\theta)\right]_V = b^2_{\mathrm{inc},V}(1 + P_V(\theta)), \tag{8.27}$$

where $b_{\mathrm{inc},V}$ is the bound incoherent scattering length of vanadium and $P_V(Q)$ is the vanadium Placzek [31] inelasticity correction term. By using equations 8.25 and 8.27, the normalisation factor $a(\theta)$ is then obtained from the relation

$$a(\theta) = \frac{I'_{VC}(\theta)}{N_V A_{V,VC}(\theta) b^2_{\mathrm{inc},V}(1 + P_V(\theta)) + M_{VC}(\theta) - \frac{A_{C,VC}(\theta)}{A_{C,C}(\theta)} M_C(\theta)}. \tag{8.28}$$

Since the sample geometry is not explicitly known as a function of pressure, the vanadium diffraction intensity at each intermediate pressure point was approximated by a linear combination of the ambient pressure diffraction

patterns taken for a piece of vanadium matching the ambient pressure cell geometry (i.e. V pellet 1) and a piece of vanadium that approximates the sample geometry at higher pressures (i.e. V pellet 2). A linear fit was made to the resultant vanadium intensity to ensure smooth overlap between the individual detector groups following the vanadium normalisation.

The total number of nuclei in the beam N_S or N_V, the attenuation factors $A_{S,SC}(\theta)$, $A_{C,SC}(\theta)$, $A_{C,C}(\theta)$ and $A_{V,VC}(\theta)$, and the multiple scattering cross sections $M_{SC}(\theta)$, $M_{VC}(\theta)$ and $M_C(\theta)$, are all dependent upon the sample and gasket geometry. The radii of the sample and gasket at each intermediate pressure were determined by interpolating between the dimensions of the gasket at ambient pressure and the dimensions of the gasket recovered from 8.6(5) GPa (see figure 8.5). The values for the thickness of the gasket and hence the anvil separation at each pressure are listed in table 8.1 and were also determined by assuming a linear relationship with increasing pressure. However, the Ti-Zr gaskets relax on recovery from high pressure and hence the thickness of the recovered gasket is not the same as the *in situ* thickness at the highest pressure. The measured thickness of the recovered gasket $h = 0.52$ mm was therefore estimated as corresponding to the gasket thickness at ≈ 6 GPa. A linear fit to the gasket thickness between 0 and 6 GPa was thus extrapolated to find h at the highest pressure points. In the specific experimental geometry used, the incident neutron beam width was smaller than the outer diameter of the gasket and the attenuation coefficients for this geometry were calculated using the GUDRUN program [111]. The CYLMULTOF program was used to calculate the multiple scattering cross sections defined by Soper and Egelstaff [55].

As shown by equation 2.5, the total structure factor $F(Q)$ is extracted from the measured differential scattering cross-section by using the relation

$$\frac{1}{N_S}\left[\frac{\mathrm{d}\sigma}{\mathrm{d}\Omega}(Q)\right]_S = F(Q) + \sum_{\alpha}^{n} c_\alpha(\bar{b}^2_{\mathrm{coh},\alpha} + \bar{b}^2_{\mathrm{inc},\alpha})(1 + P_\alpha(Q)) \tag{8.29}$$

where c_α denotes the atomic fraction of each chemical species α in the system,

$\bar{b}_{\mathrm{coh},\alpha}$ and $\bar{b}_{\mathrm{inc},\alpha}$ are the coherent and incoherent neutron scattering lengths for chemical species α, respectively, and $P_\alpha(Q)$ is the Placzek [31] (inelasticity) correction for species α. The approximations made in calculating the sample geometry and vanadium diffraction intensities at each pressure point and the uncertainty of ± 0.5 GPa in the pressure necessitate the application of an additional scaling factor to ensure correct data normalisation. Self consistency checks were performed on the data sets thus obtained to ensure that (i) each measured $F(Q)$ obeys the sum-rule relation (see equation 2.11), the values of which are given in table 8.2, (ii) the low-r features in $G(r)$ oscillate about the theoretical $G(0) = -0.4352(9)$ barn limit and (iii) the Fourier backtransform of $G(r)$ after the low-r oscillations are set to the theoretical $G(0)$ limit are in good overall agreement with the original $F(Q)$ function [113].

8.4 Results

Table 8.3: The leading peak positions q_1, q_2 and q_3 in the measured $F(Q)$ functions for GeO_2 glass at pressure P_0, together with the leading peak positions r_1, r_2, r_3 and coordination number $\bar{n}^{\mathrm{O}}_{\mathrm{Ge}}$ for the corresponding $G(r)$ functions.

	$F(Q)$			$G(r)$			
P_0 (GPa)	q_1 (Å^{-1})	q_2 (Å^{-1})	q_3 (Å^{-1})	$\bar{n}^{\mathrm{O}}_{\mathrm{Ge}}$	r_1 (Å)	r_2 (Å)	r_3 (Å)
0	1.55(2)	2.65(2)	4.48(5)	4.0(1)	1.72(2)	2.85(3)	4.41(5)
1.2(5)	1.52(2)	2.42(2)	4.57(5)	4.0(1)	1.73(2)	2.98(3)	4.34(5)
3.1(5)	1.62(2)	2.52(2)	4.52(5)	4.1(1)	1.73(2)	3.01(3)	4.34(5)
4.9(5)	1.81(2)	2.72(2)	4.61(5)	4.1(1)	1.73(2)	2.85(3)	4.35(5)
6.8(5)	1.92(2)	2.78(2)	4.69(5)	4.5(1)	1.75(2)	2.93(3)	4.26(5)
8.6(5)	2.09(2)	2.77(2)	4.54(5)	4.9(1)	1.77(2)	2.90(3)	4.21(5)

The total structure factors $F(Q)$ for GeO_2 glass measured by *in situ* neutron diffraction using the Paris-Edinburgh cell at various pressures up to 8.6(5) GPa are plotted in figure 8.12. The $F(Q)$ functions have good counting statistics although the data sets at the highest pressures, specifically 6.8(5) and 8.6(5) GPa, display distinct steps and sharp anomalies which show that the

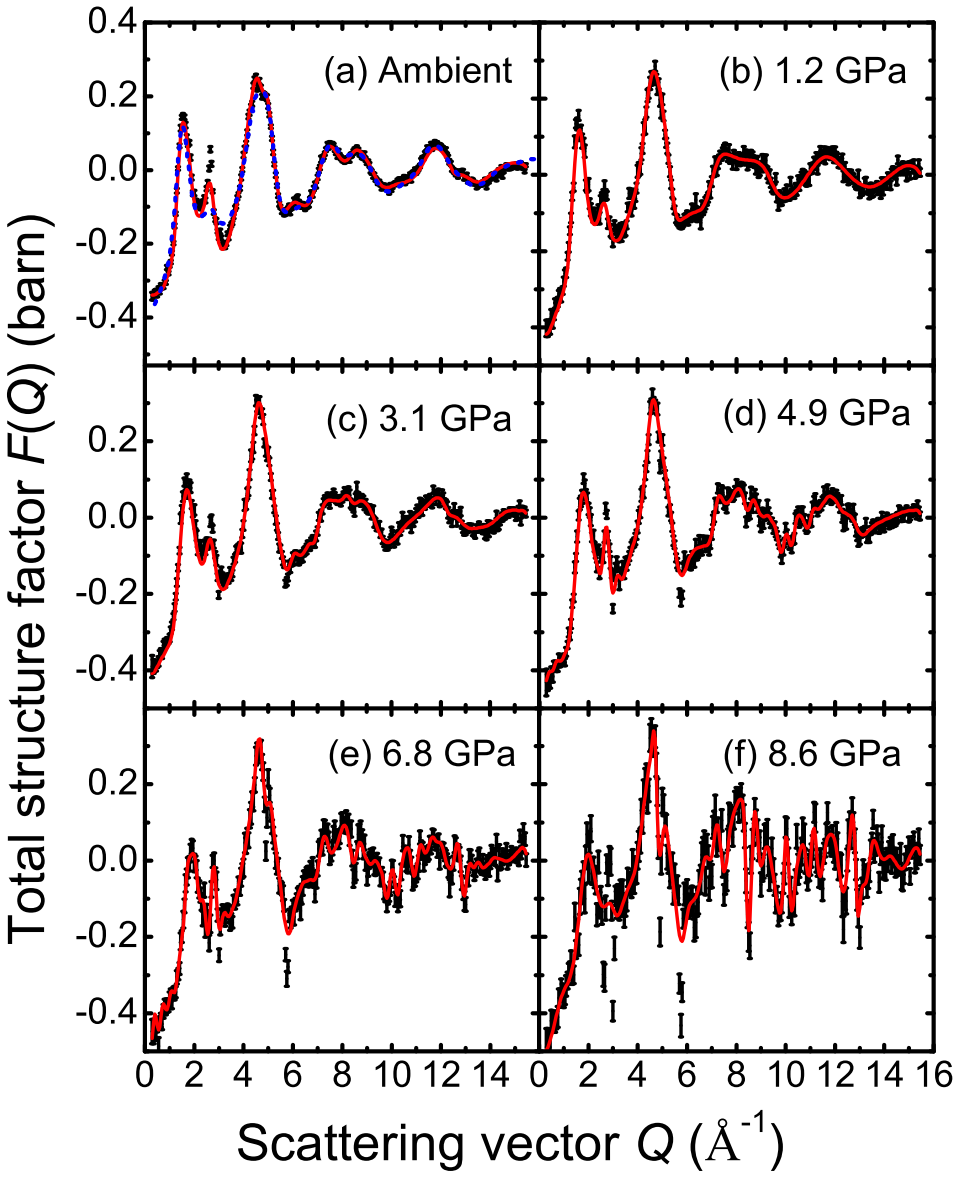

Figure 8.12: Total structure factors $F(Q)$ for GeO_2 glass at (a) ambient pressure, (b) 1.2(5) GPa, (c) 3.1(5) GPa, (d) 4.9(5) GPa, (e) 6.8(5) GPa and (f) 8.6(5) GPa. The bars represent the statistical errors and the solid (red) curves are the Fourier back transforms of the $G(r)$ functions plotted in figure 8.13 after the un-physical low-r oscillations are set to the $G(0) = -0.4352(9)$ barn limit. The dashed (blue) curve in (a) is the $F(Q)$ for GeO_2 glass measured at D4C using a conventional neutron diffraction set-up [305].

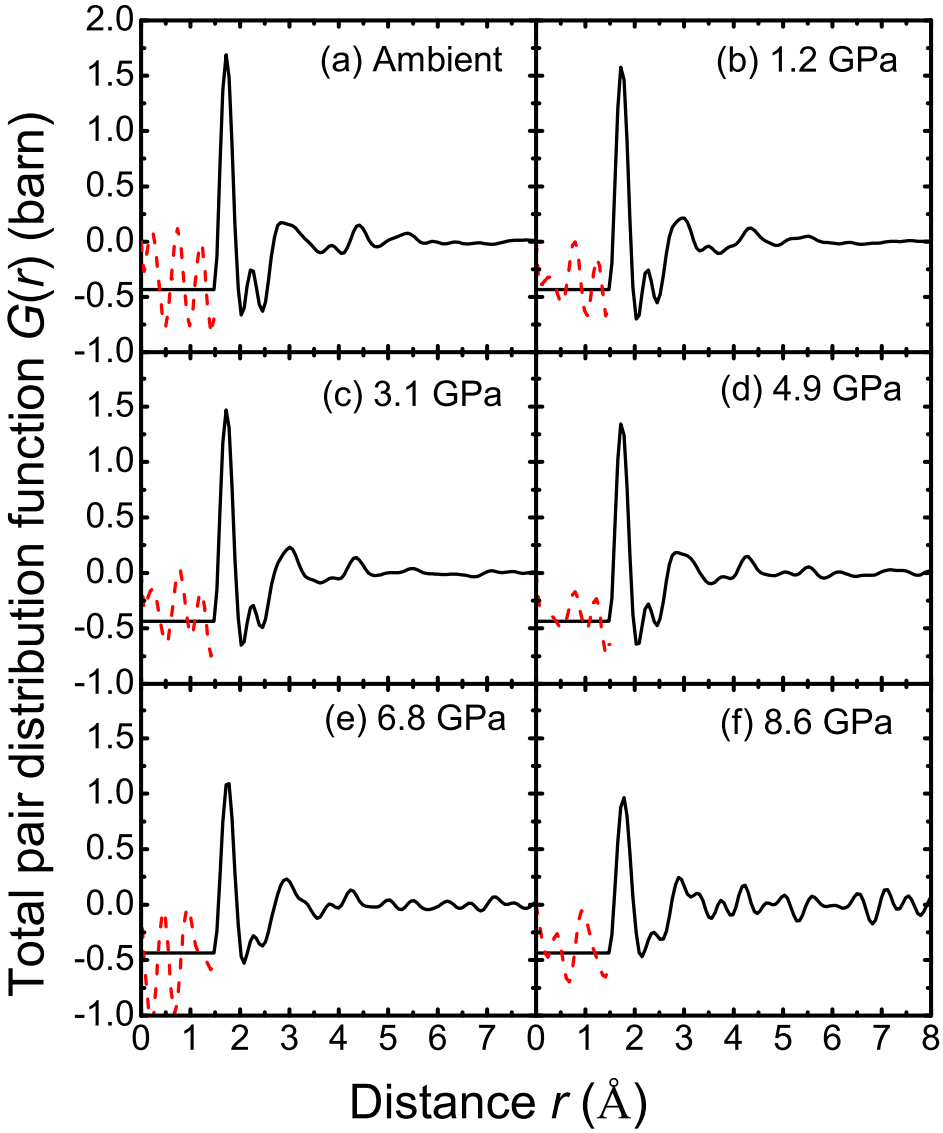

Figure 8.13: Total pair distribution functions $G(r)$ for GeO_2 glass at (a) ambient pressure, (b) 1.2(5) GPa, (c) 3.1(5) GPa, (d) 4.9(5) GPa, (e) 6.8(5) GPa and (f) 8.6(5) GPa, as obtained by Fourier transforming the corresponding $F(Q)$ functions plotted in figure 8.12 after making a Harwell spline fit [115] to the data with $Q_{max} = 15.45$ Å^{-1}. The dashed (red) curves indicate the extent of the un-physical low-r oscillations.

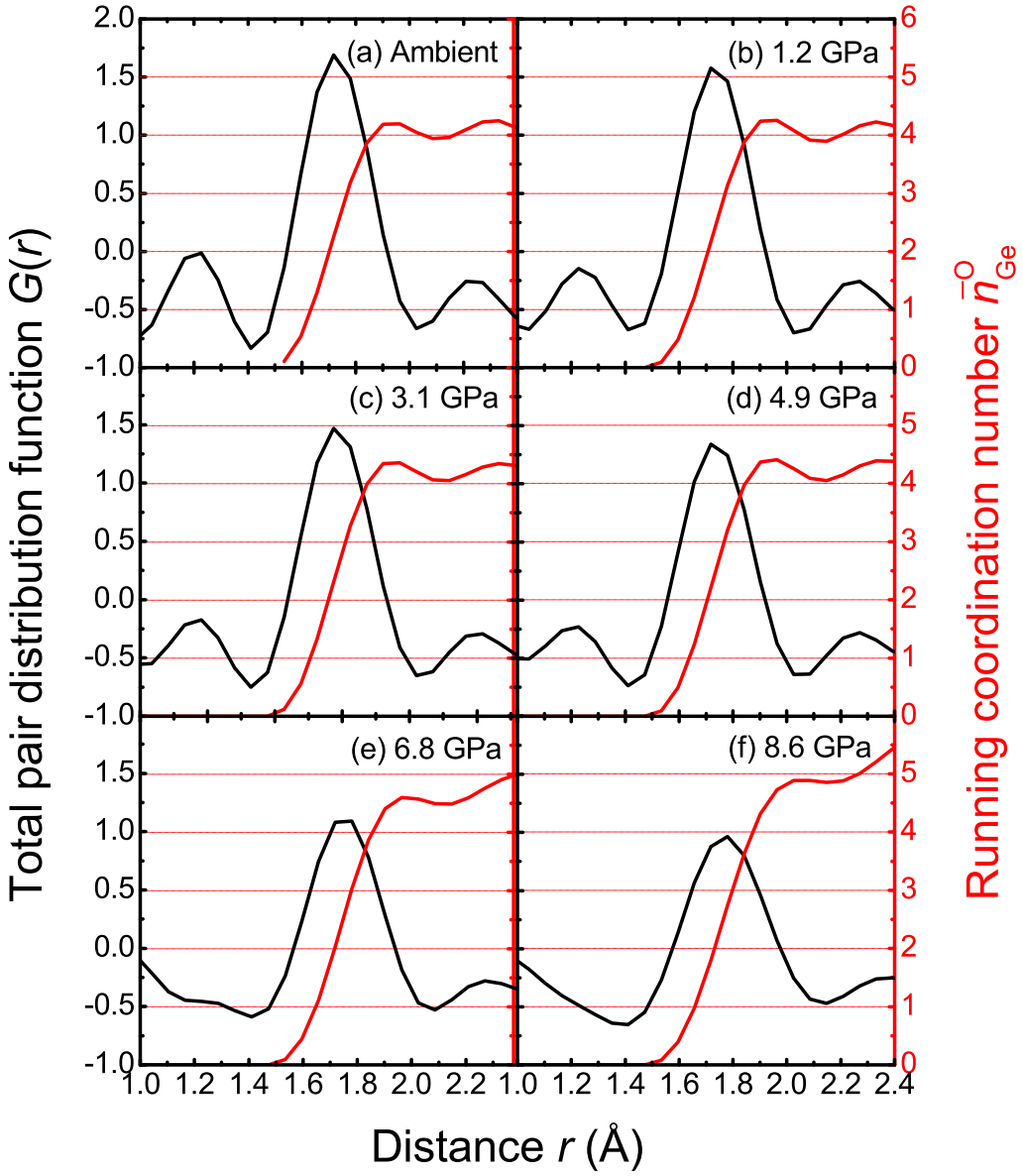

Figure 8.14: Running coordination number $\bar{n}^{O}_{Ge}$ (red curves) obtained by integrating over the nearest neighbour peak of the total pair distribution function $G(r)$ given in figure 8.13 (black curves) for GeO_2 glass at (a) ambient pressure, (b) 1.2(5) GPa, (c) 3.1(5) GPa, (d) 4.9(5) GPa, (e) 6.8(5) GPa and (f) 8.6(5) GPa.

background correction is insufficient. The total pair distribution functions $G(r)$ at the various pressures are plotted in figure 8.13 and were obtained by Fourier transforming the corresponding $F(Q)$ functions after making a Harwell spline fit [115] to the data with $Q_{\max} = 15.45$ Å^{-1}. The first peak in real space, at $r_1 = 1.72(2)$ Å in the ambient pressure $G(r)$, is attributed to the nearest neighbour Ge-O correlations [305]. The running coordination number $\bar{n}^{\mathrm{O}}_{\mathrm{Ge}}$ at each pressure, obtained by integrating over the region of the first peak in the corresponding $G(r)$ function, are plotted in figure 8.14. The second peak in real space, at $r_2 = 2.85(3)$ Å in the ambient pressure $G(r)$, is attributed to O-O correlations by comparison with the measured partial pair distribution functions [305, 306] which give the nearest neighbour O-O distance at $r_{\mathrm{OO}} = 2.83(1)$ Å. It is not possible to resolve the nearest neighbour Ge-Ge distance expected at $r_{\mathrm{GeGe}} = 3.16(1)$ Å [306]. The positions of the leading peaks in the $F(Q)$ and $G(r)$ functions together with $\bar{n}^{\mathrm{O}}_{\mathrm{Ge}}$, which was taken as the value of the running coordination number at the first minimum in $G(r)$ following the first peak, are listed in table 8.3.

As shown figure 8.12 (a), the measured *in situ* ambient pressure $F(Q)$ is in good agreement with the $F(Q)$ function for $^{\mathrm{nat}}GeO_2$ glass previously obtained at D4C using a conventional neutron diffraction set-up with a much larger sample volume [305], with the exception of a sharp Bragg peak at 2.65(2) Å^{-1} in the former which was due to a partial re-crystallisation of the sample during synthesis. The first sharp diffraction peak (FSDP) at 1.55(2) Å^{-1} is a characteristic of intermediate range ordering in network glasses [306] and arises from cage-like structures that enclose open regions in the network of corner shared GeO_4 tetrahedral structural units [285, 286]. With increasing pressure the FSDP undergoes a clear reduction in intensity and shifts towards higher Q values.

In real space, the Ge-O peak at 1.72(2) Å yields a coordination number $\bar{n}^{\mathrm{O}}_{\mathrm{Ge}} = 4.0(1)$ at ambient pressure. There is no change in the $\bar{n}^{\mathrm{O}}_{\mathrm{Ge}}$ coordination number until the pressure is increased beyond $\approx$ 5 GPa. At 8.6 GPa $\bar{n}^{\mathrm{O}}_{\mathrm{Ge}} = 4.9(1)$ which suggests the coexistence of GeO_4 tetrahedra with either

GeO_5 pentahedra, GeO_6 octahedra or even a mixture of all three structural units. The observed increase in $\bar{n}^{O}_{Ge}$ is accompanied by an increase in the nearest neighbour Ge-O bond distance r_{GeO} from 1.72(2) Å at ambient pressure to 1.77(2) Å at 8.6(5) GPa. This distance is within the range of bond distances for GeO_5 pentahedra of $1.82 \leq r_{GeO}$ (Å) ≤ 1.93 in germanate glasses [307, 308] and $1.77 \leq r_{GeO}$ (Å) ≤ 1.97 in crystalline $K_2Ge_8O_{17}$ [309].

8.4.1 Discussion

Despite the small size of the sample in the PE cell (< 0.05 cm^3) the statistical errors are relatively small and the data could be corrected for background scattering. However, the data correction procedure is more difficult at higher pressures due to background scattering from the anvil and press assembly. Nevertheless, notable structural changes were observed with increasing pressure, specifically in the position and intensity of the FSDP and in the coordination number and nearest neighbour bond distance. A reduction of the background scattering, and hence an improvement in the quality of the measured diffraction patterns, is the subject of a further study which is presented in the next section.

8.5 Neutron diffraction study B

The previous study A showed that the measurement of accurate *in situ* high pressure neutron diffraction patterns for GeO_2 glass is possible using the Paris-Edinburgh press mounted on the D4C diffractometer. However, although successful at low pressures, the data correction procedure is more difficult at higher pressures due to the large background scattering intensity from the anvil and press assembly by comparison to the inherently diffuse scattering from the glass sample. The objective of this investigation is to reduce the background scattering from the anvil and press assembly by improving the neutron shielding and to thus obtain high quality diffraction patterns at high pressures, of suitable caliber for future application of the method of isotopic substitution in neutron diffraction to measure the partial structure factors of liquid and glassy materials.

8.5.1 Experimental procedure

Glass preparation

The GeO_2 glass was made by heating ≈ 1.35 g of powdered Germanium (IV) Oxide (99.9999%) contained in a platinum crucible (supported by an alumina crucible) in air at 1400°C. After ≈ 2 hr, the crucible was removed from the furnace and placed on a copper block to cool to room temperature. Neutron diffraction experiments were previously performed on this glass [305, 306] and the coarsely powdered sample was stored under dry conditions for a period of ≈ 2 yr. To avoid excessive exposure to atmospheric H_2O, the following pelleting process was performed immediately prior to the experiment. A piece of the GeO_2 glass was powdered using an agate pestle and mortar and pre-compacted into a pellet, matching the geometry of the single toroid anvils, using the tungsten carbide die illustrated in figure 8.15. The finely powdered GeO_2 glass was filled into the die and compressed using a powder press at the ILL facility with an applied load of 3 tonne for ≈ 30 min. The pressure ϱ

applied to the powder is related to the load l according to the relation

$$\varrho = \frac{lg}{A} \tag{8.30}$$

where A is the area of the die and $g = 9.80665$ ms^{-2} is the standard acceleration due to gravity. The die has a diameter of 6 mm and therefore the pre-compaction process applied a pressure of $\varrho \approx 1$ GPa to the sample. The distance D shown in figure 8.15 was measured before and after compression and additional powder added where appropriate until the difference between the measured values of D was equal to 1.6 mm, i.e. the thickness of the gasket. The pre-compacted pellet was extremely fragile and the middle section disintegrated after removing it from the powder press. Additional fine powder was therefore added to bulk out the sample for the diffraction experiment. The total mass of the pellet was ≈ 0.3 g which was larger than the mass of sample used in study A.

The neutron diffraction experiment

In situ high pressure neutron diffraction experiments were conducted on the glassy GeO_2 pellet using the VX5 variant Paris-Edinburgh press mounted in transmission geometry on the D4C diffractometer at the ILL, France. In contrast to experiment A, the press was orientated such that the compression anvil was situated at the bottom of the press for improved accessibility during sample loading. The monochromatic neutron beam, of incident wavelength 0.69599(7) Å and width of 11 mm, was collimated using $^{10}B_4C$ flags set to 4 mm centered on the GeO_2 glass pellet encapsulated between the single toroid BN anvils by a null scattering Ti-Zr gasket, denoted gasket 4. As in study A, the neutron beam was incident on the edge of the gasket (see figure 8.4) and was further collimated to the separation h of the BN anvils, determined by the thickness of the Ti-Zr gasket, defining a cylindrical sample geometry for the incident and scattered beam with a height and diameter of 1.6 mm and 6 mm, respectively, at ambient pressure. Cadmium (Cd) foil of thickness 0.3 mm was

Table 8.4: Details of the experimental runs. The load L on the piston was determined using equation 8.6 at the corresponding oil pressure p. The separation h of the anvils was determined by the thickness of the gaskets and was either measured or, for the *in situ* pressure measurements marked by †, was estimated by using a linear extrapolation procedure (see § 8.3.2). Note, the anvil separation at the highest pressure is smaller than the thickness of the recovered gasket, due to relaxation of the gasket on recovery. The neutron counting time t is also listed.

Sample	Gasket	h (mm)	p (bar)	L (tonne)	t (hr)
GeO_2	4	1.6	100	6.8	5.5
GeO_2	4	1.0 †	450	30.5	8.5
GeO_2	4	0.8 †	750	50.9	7.5
GeO_2	4	0.7 †	900	61.0	7.0
GeO_2	4	0.6 †	1050	71.2	10.0
GeO_2	4	0.4 †	1400	94.9	10.0
Ordinary empty gasket	5	1.6	0	0	9.0
Empty recovered gasket	3	0.52	100	6.8	9.0
Empty recovered gasket	6	0.56	500	33.9	9.0
V pellet 1	5	1.6	100	6.8	5.5
V pellet 2	3	0.52	100	6.8	4.0
Cd pellet 1	5	1.6	15	1.0	1.0
Cd pellet 2	3	0.52	15	1.0	1.0
Closed anvils	–	0	–	–	1.0
No anvils	–	–	–	–	0.5

Gasket 3 : gasket 1 recovered from 101.5 tonne (see study A)
Gasket 4 : used to encapsulate the sample
Gasket 5 : uncompressed gasket
Gasket 6 : gasket 4 recovered from 94.9 tonne

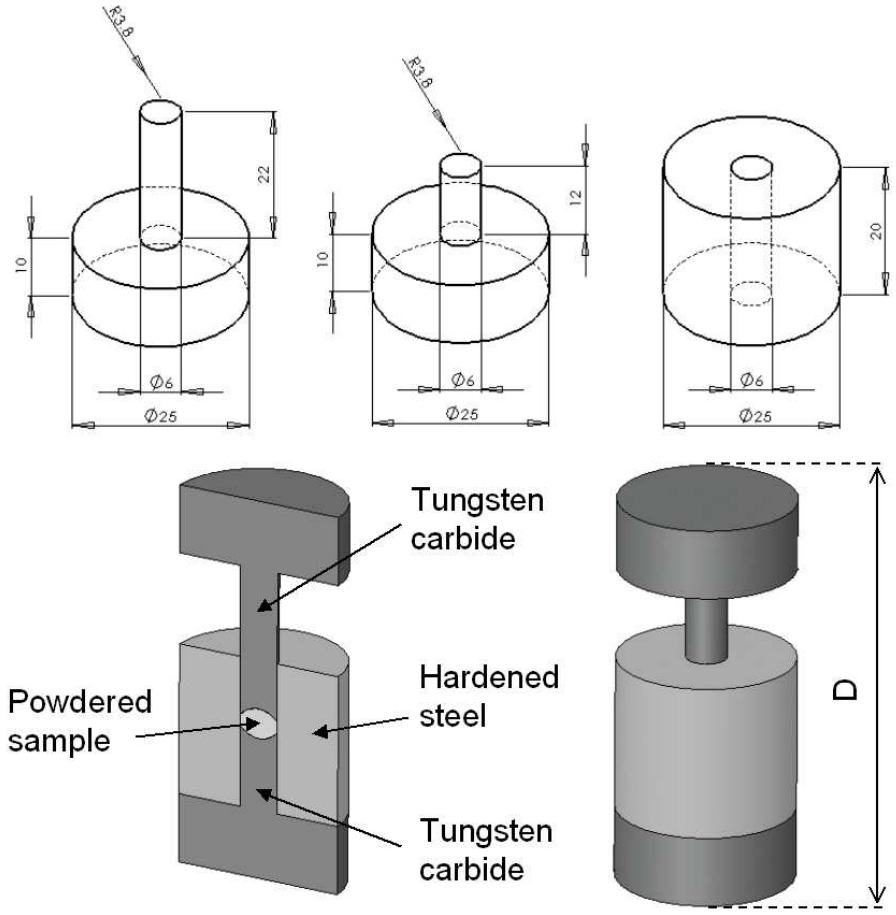

Figure 8.15: Schematic of the tungsten carbide powder press dies used to form the pre-compressed powder pellet. Dimension units are in mm.

used as shielding material on the anvils and further extensive Cd shielding was attached to the press assembly facing the incident beam, including the support pillars and collimation flags, as shown in figure 8.16, to reduce the background scattering. A Cd mask was used to shield the edges of the incident beam aperture to the instrument belljar.

A hydraulic pump was used to apply force to the compression anvil and compress the sample and gasket assembly. A nominal load of 6.8 tonne was first applied to ensure the sample and gasket were seated tightly between the anvils. An ambient pressure neutron diffraction experiment on the GeO_2

Figure 8.16: The VX5 Paris-Edinburgh press assembly mounted in transmission geometry prior to installation on the D4C instrument for study B. The press is orientated such that the compression anvil is at the bottom for improved accessibility during sample loading. Note the extensive use of Cd shielding on the anvils, press assembly and $^{10}B_4C$ incident beam collimation flags.

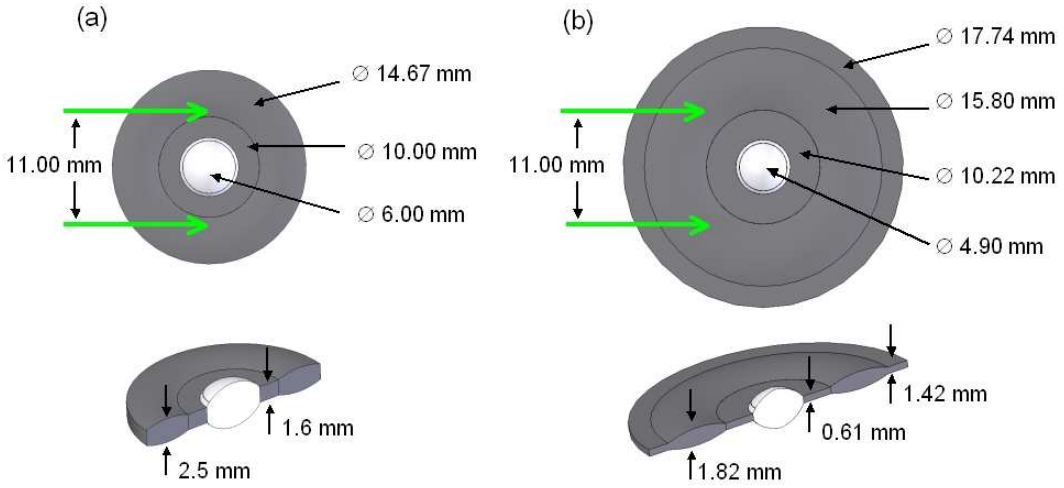

Figure 8.17: The dimensions of the sample and null scattering Ti-Zr gasket from study B at (a) ambient pressure and (b) recovered from 94.9 tonne. The green arrows indicate the width of the incident neutron beam. Equation 8.9 was used to calculate the maximum pressure $P_0 = 8.0(5)$ GPa on the sample from the outer radius of the recovered gasket $r_g = 8.87$ mm (see figure 8.7).

glass was performed and five further high pressure diffraction experiments were made on the GeO_2 glass up to a maximum load of 94.9 tonne. To obtain reasonable counting statistics, neutrons were counted for 6.0 hr in the ambient pressure measurement and up to 10.0 hr for the higher pressure experiments (see table 8.4). On recovery back to ambient pressure the GeO_2 sample had compacted into a transparent solid. The recovered gasket was deformed, as shown in figure 8.17, by comparison to the dimensions of the gasket at ambient pressure.

To assist the data correction procedures detailed in § 8.3.2, ambient pressure measurements were also made for an uncompressed empty Ti-Zr gasket, denoted gasket 5, the Ti-Zr gasket 3 recovered from the 101.7 tonne experiment in study A, and the closed empty anvils. In order to more accurately approximate the gasket scattering contribution to the diffraction pattern for GeO_2 glass at the highest pressure point, the Ti-Zr gasket recovered from the 94.9 tonne experiment in the present study B, denoted gasket 6, was also

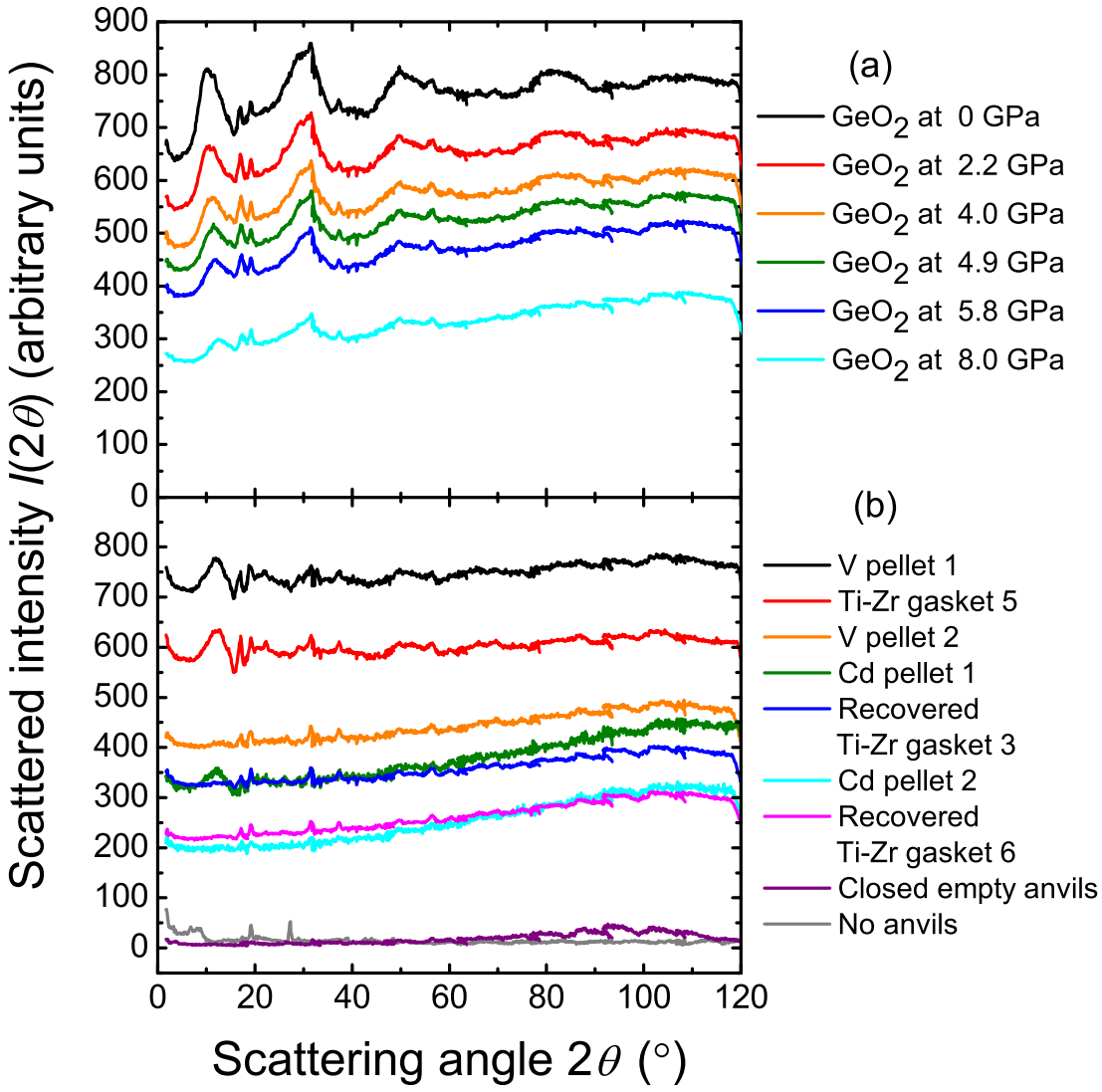

Figure 8.18: The measured *in situ* neutron diffraction patterns. (a) GeO_2 glass contained within Ti-Zr gasket 4 at ambient pressure (black), 2.2 GPa (red), 4.0 GPa (orange), 4.9 GPa (green), 5.8 GPa (blue) and 8.0 GPa (cyan). (b) V pellet 1 in Ti-Zr gasket 5 (black), empty Ti-Zr gasket 5 (red), V pellet 2 in Ti-Zr gasket 3 (orange), Cd pellet 1 in Ti-Zr gasket 5 (green), empty Ti-Zr gasket 3 (recovered from 8.6 GPa in study A) (blue), Cd pellet 2 in recovered Ti-Zr gasket 3 (cyan), empty Ti-Zr gasket 6 (recovered from 8.0 GPa experiment in study B) (magenta), closed empty anvils (purple), and the background with the anvils removed (grey).

Table 8.5: The pressure P_0 at each load L together, with the corresponding number density n_0 and sum rule S, given by equation 2.11, for GeO_2 glass and the number density n_0(Ti-Zr) for the null scattering Ti-Zr gasket, given by equation 8.17, at the corresponding pressure P_g, given by equation 8.10.

L (tonne)	P_0 (GPa)	n_0 (Å^{-3})	S (barn Å^{-3})	P_g (GPa)	n_0(Ti-Zr) (Å^{-3})
6.8	0	0.0629(3)	-0.540(8)	0	0.0511(9)
30.5	2.2(5)	0.0684(9)	-0.588(8)	1.0(5)	0.0516(9)
50.9	4.0(5)	0.0726(9)	-0.624(8)	1.8(5)	0.0519(9)
61.0	4.9(5)	0.0774(9)	-0.665(8)	2.3(5)	0.0522(9)
71.2	5.8(5)	0.0816(9)	-0.701(8)	2.7(5)	0.0523(9)
94.9	8.0(5)	0.0866(9)	-0.744(8)	3.7(5)	0.0528(9)

measured with an additional applied load of 33.9 tonne. To assist in the data normalisation and to examine the effect of sample self-shielding on the background scattering, additional ambient pressure diffraction patterns were measured for the large and small vanadium and cadmium pellets, used in the previous study A, in the uncompressed Ti-Zr gasket 5 (large pellets) or the recovered Ti-Zr gasket 3 (small pellets) (see table 8.4).

The diffraction data were analysed according to the procedure outlined in § 8.3.2, where the maximum sample pressure $P_0 = 8.0(5)$ GPa and the intermediate pressure points listed in table 8.5 were obtained from the pressure-load curve plotted in figure 8.7. The measured diffraction patterns are plotted in figure 8.18 and show a significant reduction in the background scattering by comparison with the measured intensities in study A (see figure 8.10). The ambient pressure diffraction patterns for empty Ti-Zr gasket 5 and the empty recovered Ti-Zr gasket 3 have the same relative levels of intensity seen for empty gasket 2 and the same empty recovered gasket 3 measured in study A, respectively. However, the un-physical steps in the diffraction patterns observed in study A have now been virtually eliminated by the improved use of Cd shielding. The scattered intensity from the GeO_2 glass at 8.0(5) GPa has experienced an approximate 2-fold increase by comparison with the scattered intensity from the GeO_2 glass at 8.6(5) GPa in study A, resulting from

a greater number of scattering centers in the neutron beam owing to a greater quantity of GeO_2 powder being added to bulk out the powder pellet. The greatest contribution to the background in the sample measurements is due to scattering from the Ti-Zr gasket which, despite its null scattering composition, contains some small but sharp features. The remaining background, which is most significant at higher scattering angles, results largely from the anvils. This is clearly evident from the lack of intensity at higher scattering angles for the no anvils measurement. The cadmium measurements show a significant reduction in the scattered intensity from the Ti-Zr gaskets at all scattering angles. However, the self-shielding correction using the cadmium measurements was not performed.

The corresponding sum rule for GeO_2 glass, the GeO_2 number density, pressure on the gasket and null scattering Ti-Zr number density, are listed in table 8.5 and were obtained by the same methods given in § 8.3.1.

X-ray diffraction experiment

High energy x-ray diffraction experiments were performed by Barnes [310] on an uncompressed piece of GeO_2 glass and the sample recovered from 8.0(5) GPa using the ID11 beamline at the ESRF, France, with an incident wavelength of 0.1220 Å and a charge-coupled device (CCD) detection system. Two dimensional diffraction patterns were taken for the samples and instrument background at two sample to detector distances of 160 and 300 mm with an acquisition time of 20 s per scan. The scattering vector Q scale was calibrated with reference to the Bragg peaks in the diffraction pattern for crystalline Si. The FIT2D [199] analysis program was used to correct the data for geometrical effects, such as non-orthogonality of the detector relative to the incident beam, and polarisation of the incident beam before integrating over the two dimensional regions to produce a one dimensional diffraction pattern. The detector regions covered by the beam stop or bad pixels were masked off such that they did not influence the results of the integration. The data was corrected for background scattering and, following the procedure detailed in § 3.7, fitted

to the sum of the Compton scattering cross section (given in Ref. [200]) and self scattering $\sum_\alpha c_\alpha f_\alpha(Q)^2$ contributions at high Q values, where the neutral atom form factors $f_\alpha(Q)$ were taken from Ref. [201]. The Compton scattering contribution was subtracted to obtain the Rayleigh-Thomson differential scattering cross-section, from which the total x-ray structure factor $S_X(Q)$ was obtained. The number density of the uncompressed GeO_2 sample was taken to be 0.0629(3) $Å^{-3}$, as in the neutron diffraction experiments. The number density of the densified sample was estimated as 0.0773 $Å^{-3}$ from the mean value of the number density of samples recovered from 6 GPa (measured by Stone *et al.* [298]) and 9 GPa (as recovered from the study in the next chapter measured at the ISIS facility), shown in figure 8.8.

8.5.2 Results

Table 8.6: The leading peak positions q_1, q_2 and q_3 in the measured $F(Q)$ functions for GeO_2 glass at pressure P_0, together with the leading peak positions r_1, r_2, r_3 and coordination number $\bar{n}^{O}_{Ge}$ from the corresponding $G(r)$ functions.

	$F(Q)$			$G(r)$			
P_0 (GPa)	q_1 ($Å^{-1}$)	q_2 ($Å^{-1}$)	q_3 ($Å^{-1}$)	$\bar{n}^{O}_{Ge}$	r_1 (Å)	r_2 (Å)	r_3 (Å)
0	1.53(2)	2.80(2)	4.63(5)	4.0(1)	1.74(2)	2.78(3)	4.40(5)
2.2(5)	1.60(2)	2.65(2)	4.60(5)	3.9(1)	1.73(2)	2.84(3)	4.38(5)
4.0(5)	1.71(2)	2.71(2)	4.70(5)	4.0(1)	1.73(2)	2.84(3)	4.36(5)
4.9(5)	1.80(2)	2.73(2)	4.61(5)	4.2(1)	1.73(2)	3.00(3)	4.30(5)
5.8(5)	1.82(2)	2.72(2)	4.62(5)	4.3(1)	1.74(2)	2.79(3)	4.33(5)
8.0(5)	1.96(2)	2.81(2)	4.66(5)	4.5(1)	1.75(2)	2.79(3)	4.31(5)

The total structure factors $F(Q)$ for GeO_2 glass measured by *in situ* neutron diffraction using the Paris-Edinburgh cell at various pressures up to 8.0(5) GPa are plotted in figure 8.19 and the position and height of the FSDP is given in figure 8.20. The $F(Q)$ functions have excellent counting statistics and are suitably corrected for the background scattering even at the highest pressures. There is no evidence of the crystalline Bragg peak at 2.65(2) $Å^{-1}$ that was observed in study A. As shown in figure 8.19 (a), the measured *in situ*

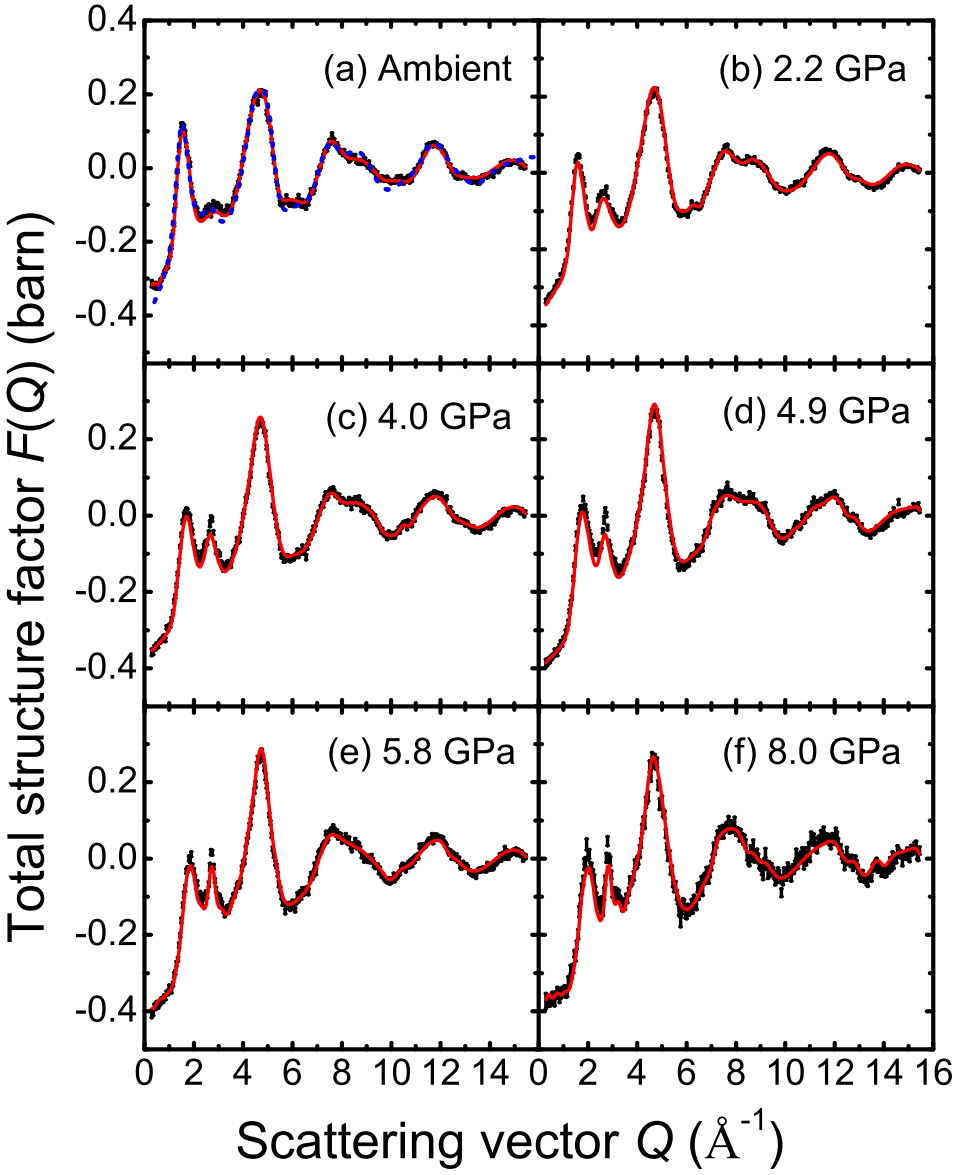

Figure 8.19: Total structure factors $F(Q)$ for GeO_2 glass at (a) ambient pressure, (b) 2.2(5) GPa, (c) 4.0(5) GPa, (d) 4.9(5) GPa, (e) 5.8(5) GPa and (f) 8.0(5) GPa. The bars represent the statistical errors and the solid red curves are the Fourier back transforms of the corresponding $G(r)$ functions plotted in figure 8.21 after the un-physical low-r oscillations are set to the $G(0) = -0.4352(9)$ barn limit. The dashed (blue) curve in (a) is the $F(Q)$ for GeO_2 glass measured at D4C using a conventional neutron diffraction set-up [305].

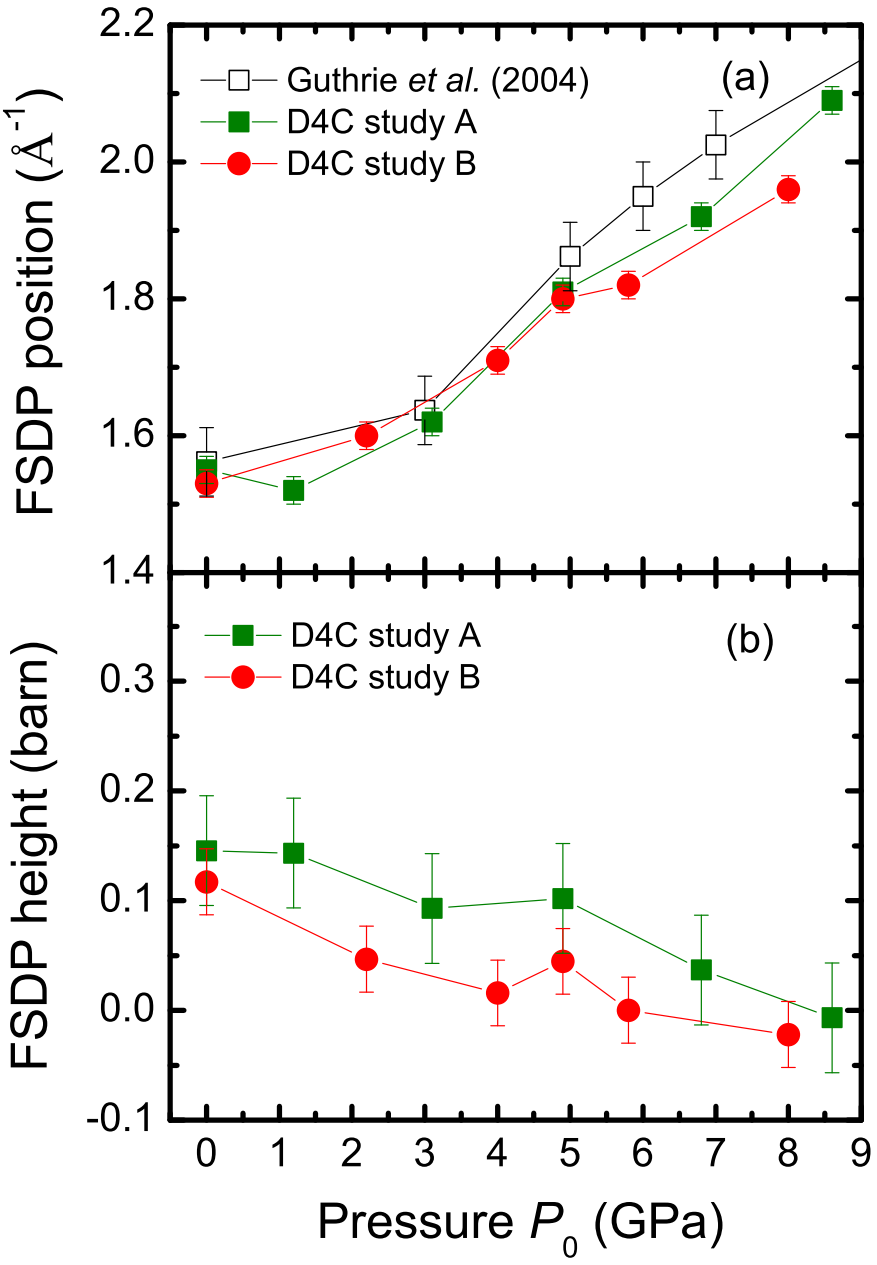

Figure 8.20: (a) Position and (b) height of the First Sharp Diffraction Peak (FSDP) as a function of pressure from the $F(Q)$ functions measured at D4C in study A (solid green squares) and study B (solid red circles). The open squares in (a) are the results taken from the x-ray diffraction study by Guthrie *et al.*[285].

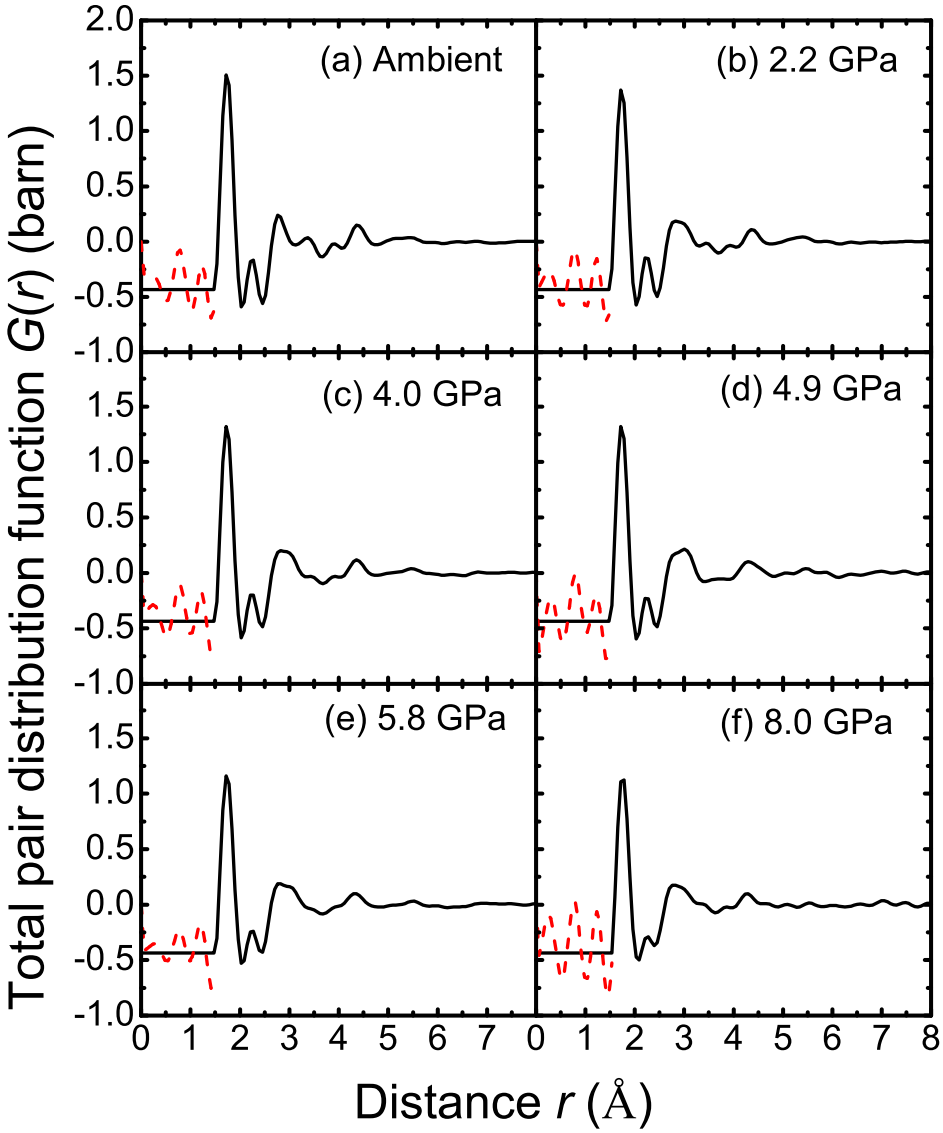

Figure 8.21: Total pair distribution functions $G(r)$ for GeO_2 glass at (a) ambient pressure, (b) 2.2(5) GPa, (c) 4.0(5) GPa, (d) 4.9(5) GPa, (e) 5.8(5) GPa and (f) 8.0(5) GPa, as obtained by Fourier transforming the corresponding $F(Q)$ functions plotted in figure 8.19 after making a Harwell spline fit [115] to the data with $Q_{max} = 15.45$ Å^{-1}. The dashed (red) curves indicate the extent of the un-physical low-r oscillations.

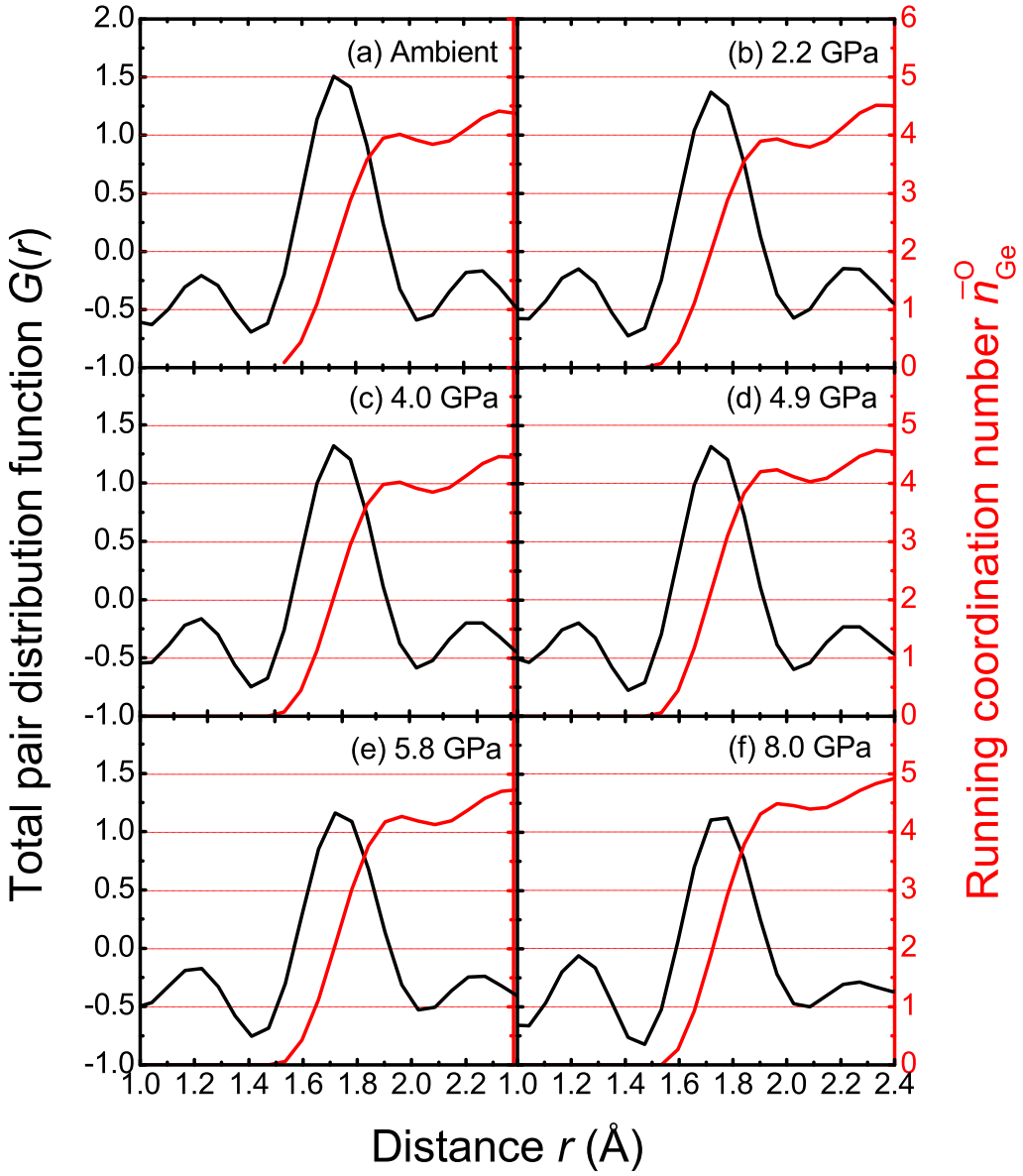

Figure 8.22: Running coordination number $\bar{n}^{O}_{Ge}$ (red curves) obtained by integrating over the nearest neighbour peak of the total pair distribution function $G(r)$ given in figure 8.21 (black curves) for GeO_2 glass at (a) ambient pressure, (b) 2.2(5) GPa, (c) 4.0(5) GPa, (d) 4.9(5) GPa, (e) 5.8(5) GPa and (f) 8.0(5) GPa.

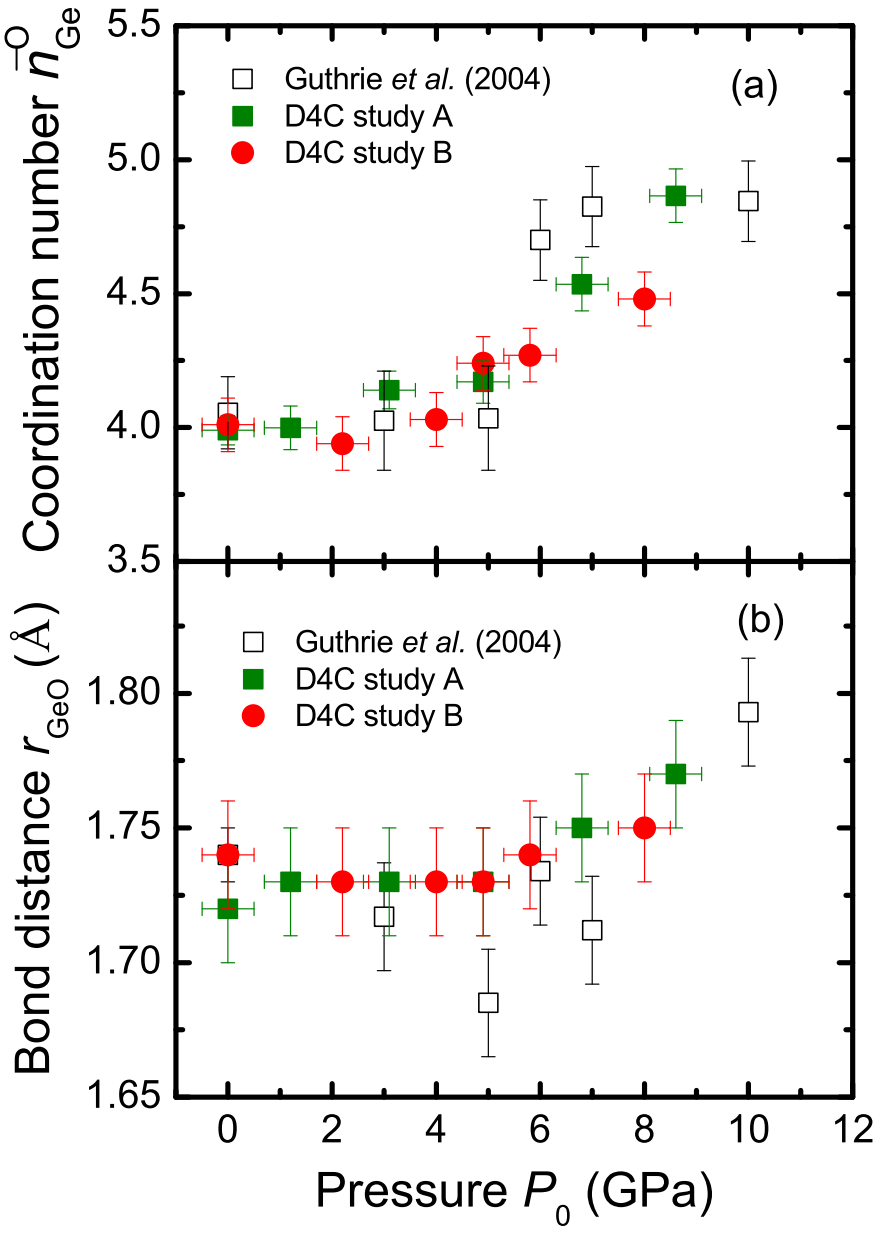

Figure 8.23: (a) Coordination number $\bar{n}^{O}_{Ge}$ and (b) nearest neighbour peak position r_{GeO} as a function of pressure for GeO_2 glass as measured using D4C in study A (solid red circles) and study B (solid green squares). The open squares are the results taken from the x-ray diffraction study by Guthrie *et al.* [285].

ambient pressure $F(Q)$ is in good overall agreement with the $F(Q)$ function obtained for $^{nat}GeO_2$ glass [305] in a conventional neutron diffraction experiment using D4C which indicates that pre-compression of the powder pellet had little effect on the structure of the illuminated portion of the glass. The total pair distribution functions $G(r)$ at the various pressures are plotted in figure 8.21 and were obtained by Fourier transforming the corresponding $F(Q)$ functions after making a Harwell spline fit [115] to the data with $Q_{max} = 15.45$ Å^{-1}. The first peaks in the ambient pressure real space $G(r)$ function at $r_1 = 1.74(2)$ Å and $r_2 = 2.78(3)$ Å are attributed to the nearest neighbour Ge-O and O-O correlations, respectively [306]. The running coordination numbers $\bar{n}^{O}_{Ge}$ at each pressure, obtained by integrating over the region of the first peak in the corresponding $G(r)$ function, are plotted in figure 8.22. The positions of the leading peaks in the $F(Q)$ and $G(r)$ functions together with $\bar{n}^{O}_{Ge}$, which was taken to be the value of the running coordination number at the first minimum in $G(r)$ following the first peak, are listed in table 8.6.

Changes are observed in the position and height of the FSDP with increasing pressure (see figure 8.20). The FSDP at 1.53(2) Å^{-1} in the ambient pressure $F(Q)$ is indicative of ordering on intermediate length scales and undergoes the same reduction in intensity and shift to higher Q values with pressure that was observed in study A. The position of the FSDP as a function of pressure is also consistent with the x-ray diffraction measurements of Guthrie *et al.* [285]. A notable increase in intensity of the principle peak at ≈ 2.8 Å^{-1} is observed with increasing pressure, which was not as apparent in study A due to the crystalline Bragg peak that was present in this region. An increase is also observed in the height of the third peak with increasing pressure. As shown in figure 8.23, at pressures up to ≈ 5 GPa the coordination number $\bar{n}^{O}_{Ge}$ remains at four. With a further increase of pressure, the coordination number increases to $\bar{n}^{O}_{Ge} = 4.5(1)$ at 8.0(5) GPa. The nearest neighbour Ge-O peak position r_{GeO} in $G(r)$ experiences a small increase from 1.74(2) Å at ambient pressure to 1.75(2) Å at 8.0(5) GPa. This increase is consistent with the results obtained from study A which give $r_{GeO} = 1.77(2)$ Å at 8.6(2) GPa.

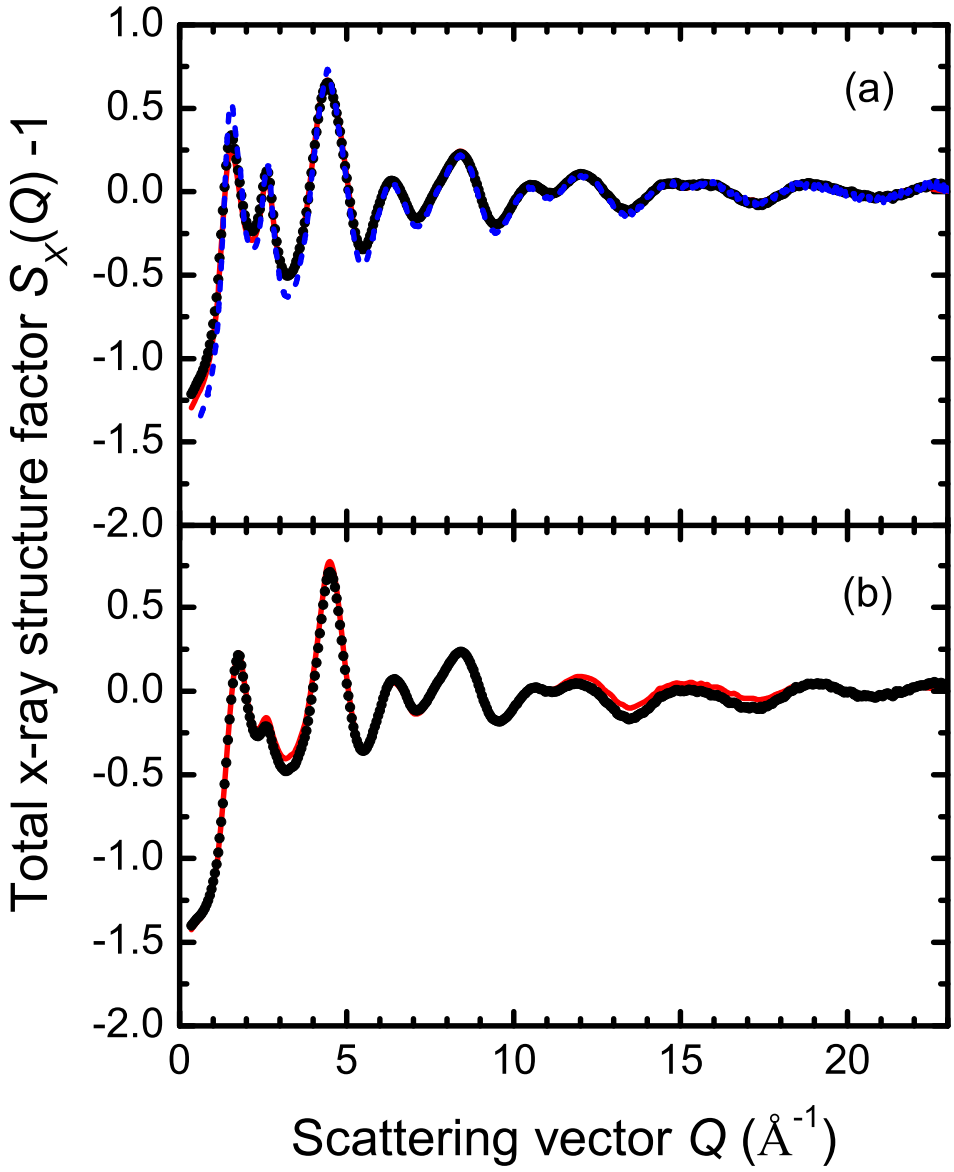

Figure 8.24: The total x-ray structure factors $S_X(Q)$ for (a) uncompressed GeO_2 glass and (b) the GeO_2 glass recovered from the 8.0(5) GPa neutron diffraction experiment. The solid (black) circles are the data points and the solid (red) curves are the Fourier backtransforms of the corresponding $G_X(r)$ functions in figure 8.25 after the un-physical low-r oscillations have been set to the theoretical $G_X(0) = 0$ limit. The dashed (blue) curve in (a) is the $S_X(Q)$ function for ordinary GeO_2 glass measured by Sampath *et al.* [286].

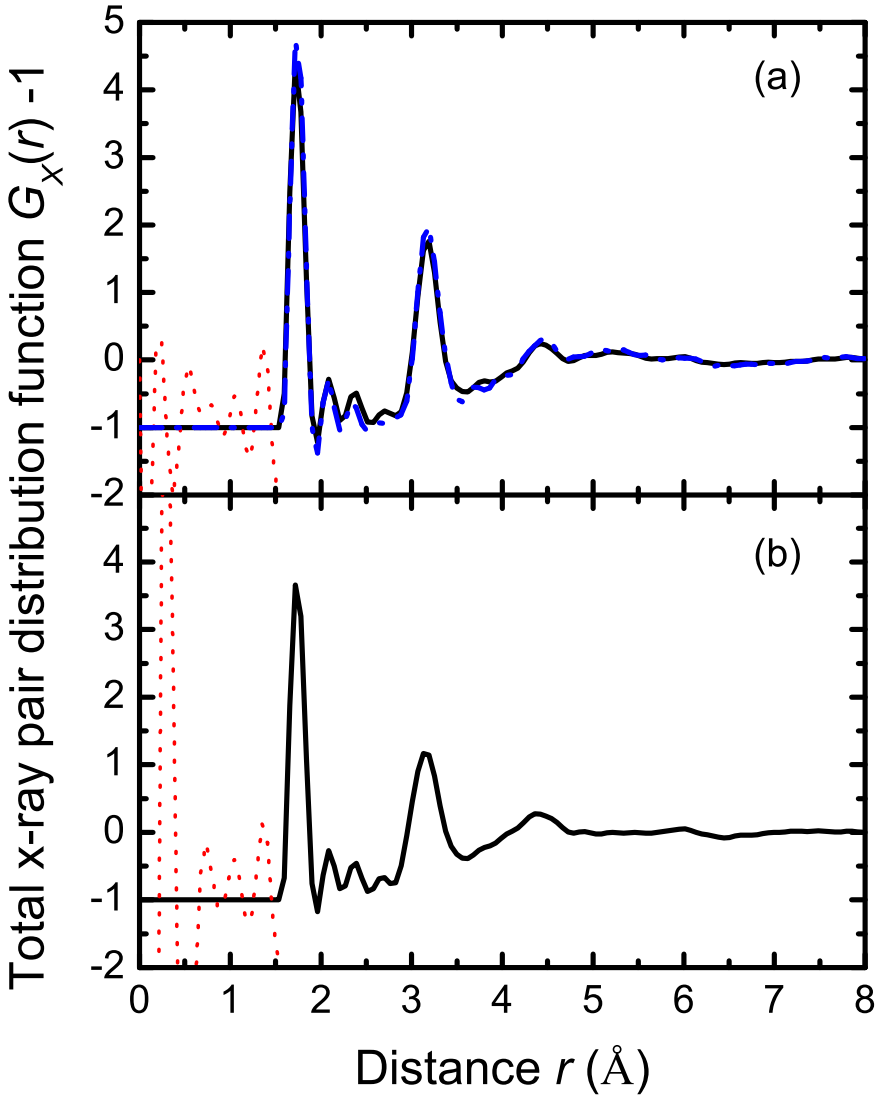

Figure 8.25: The total x-ray pair distribution functions $G_X(r)$ for (a) uncompressed GeO_2 glass and (b) the GeO_2 glass recovered from the 8.0(5) GPa neutron diffraction experiment, obtained by Fourier transforming the corresponding $S_X(Q)$ functions given in figure 8.24 after making a Harwell spline fit [115] to the data and applying a cosine window function between 21 and 23 Å^{-1}. The dotted (red) curves indicate the extent of the un-physical low-r oscillations. The chained (blue) curve in (a) represents the $G_X(r)$ function obtained by Fourier transforming the $S_X(Q)$ function of Sampath *et al.* [286] after truncating at a maximum scattering vector $Q_{\max} = 23$ Å^{-1}.

Table 8.7: The leading peak positions q_1, q_2 and q_3 in the measured $S_X(Q)$ functions plotted in figure 8.24 for uncompressed GeO_2 glass and the densified glass recovered from a pressure $P_0 = 8.0(5)$ GPa from the neutron diffraction experiment. The leading real space peak positions r_1, r_2 and r_3 from the corresponding $G_X(r)$ functions plotted in figure 8.25 and the coordination number $\bar{n}^{O}_{Ge}$ are also listed.

	$S_X(Q)$			$G_X(r)$				Ref.
P_0 (GPa)	q_1 (Å^{-1})	q_2 (Å^{-1})	q_3 (Å^{-1})	$\bar{n}^{O}_{Ge}$	r_1 (Å)	r_2 (Å)	r_3 (Å)	
0	1.54(2)	2.63(2)	4.42(3)	4.1(2)	1.73(2)	3.17(3)	4.42(5)	a
0	1.54(2)	2.63(2)	4.43(3)	4.3(2)	1.74(2)	3.17(3)	4.47(5)	b
8.0(5)	1.77(2)	2.68(2)	4.50(3)	4.4(2)	1.74(2)	3.15(3)	4.38(5)	a

[a] This study (ID11); [b] Sampath *et al.* [286]

The total x-ray structure factors $S_X(Q)$ for the uncompressed GeO_2 glass and the densified glass recovered from the 8.0(5) GPa neutron diffraction experiment are shown in figure 8.24. The total x-ray pair distribution functions $G_X(r)$ are plotted in figure 8.25 and were obtained by Fourier transforming the corresponding $S_X(Q)$ functions after making a Harwell spline fit [115] to the data and applying a cosine window function between 21 and 23 Å^{-1}. As for the neutron diffraction results, the first peak in the $G(r)$ function of the uncompressed sample at $r_1 = 1.73(2)$ Å is attributed to the nearest neighbour Ge-O correlations. The second peak at $r_2 = 3.17(3)$ Å is, however, at a greater distance than $r_2 = 2.78(3)$ Å which was found using neutron diffraction and attributed to the nearest neighbour O-O correlations. This is because oxygen is much less strongly probed using x-rays and the peak is instead attributed to the nearest neighbour Ge-Ge correlations which have a reported distance of $r_{GeGe} = 3.16(1)$ Å [306]. The positions of the leading peaks in reciprocal and real space are listed in table 8.7 together with the coordination number $\bar{n}^{O}_{Ge}$.

The measured $S_X(Q)$ for the uncompressed glass is in reasonable overall agreement with the $S_X(Q)$ previously measured by Sampath *et al.* [286] (see figure 8.24 (a)) with the exception of the slightly sharper FSDP at 1.54(2) Å^{-1} in the latter study. The position of the FSDP is shifted to 1.77(2) Å^{-1} in the $S_X(Q)$ for the sample recovered from 8.0(5) GPa and the peak experiences a

reduction in height. The principal peak has also shifted from 2.63(2) Å^{-1} for the uncompressed sample to 2.68(2) Å^{-1} for the recovered sample, accompanied by a large reduction in the peak height. A small increase in the height of the third reciprocal space peak is also observed for the recovered sample. The changes observed for all three reciprocal space peaks are consistent with previous x-ray and neutron diffraction measurements of pre-densified GeO_2 glass [286, 298]. Stone *et al.* [298] report the FSDP position at 1.796(2) Å^{-1} for a sample recovered from 6 GPa.

The coordination number $\bar{n}^{\text{O}}_{\text{Ge}}$ experiences an increase from 4.1(2) for the uncompressed sample to 4.4(2) for the sample recovered from 8.0 GPa, which would indicate a similar local structure as in the *in situ* measurement at 8.0 GPa where $\bar{n}^{\text{O}}_{\text{Ge}} = 4.5(1)$. However, this is in disagreement with the value of $\bar{n}^{\text{O}}_{\text{Ge}} = 4$ previously reported for GeO_2 glass recovered from 6 GPa [298] and 10 GPa [286] which suggest that any higher coordinated structural units present *in situ* at high pressure revert back to tetrahedral units on decompression. The discrepancy in $\bar{n}^{\text{O}}_{\text{Ge}}$ could be due to the finite maximum scattering vector $Q_{\text{max}} = 23$ Å^{-1} which leads to a broadening of the nearest neighbour peak in real space after Fourier transformation and un-physical 'truncation ripples' in this region [4]. For example, Sampath *et al.* [286] measured the $S_X(Q)$ for uncompressed GeO_2 glass to a maximum $Q_{\text{max}} = 32.8$ Å^{-1}. Fourier transforming their $S_X(Q)$ using this extended Q_{max} value gives a coordination number $\bar{n}^{\text{O}}_{\text{Ge}} = 4.0(2)$. However, Fourier transforming the same $S_X(Q)$ function after truncating at $Q_{\text{max}} = 23$ Å^{-1}, as shown in figures 8.24 (a) and 8.25 (a), leads to a coordination number $\bar{n}^{\text{O}}_{\text{Ge}} = 4.3(2)$ (see table 8.7). It is noted, however, that the ID11 diffraction experiments of the present work were performed on the recovered sample only ≈ 2 hr following decompression. The measured coordination number $\bar{n}^{\text{O}}_{\text{Ge}} = 4.4(2)$ for GeO_2 glass recovered from 8.0 GPa may therefore indicate that the structure of this material takes some time to relax after decompression.

8.5.3 Discussion

The measured diffraction patterns for GeO_2 glass are of excellent quality and are a significant improvement on both the diffraction patterns taken for study A and on the previous *in situ* neutron diffraction work by Guthrie *et al.* [285] in which the final data sets are limited to a maximum pressure of 5 GPa and have large statistical uncertainties, as shown in figure 8.26. The results are consistent with the x-ray diffraction results of Guthrie *et al.* [285] in that the coordination number $\bar{n}^{O}_{Ge}$, which is plotted as a function of pressure in figure 8.23, remains constant until ≈ 5 GPa after which it increases, eventually reaching a value of ≈ 4.9 in the vicinity of 9 GPa [285].

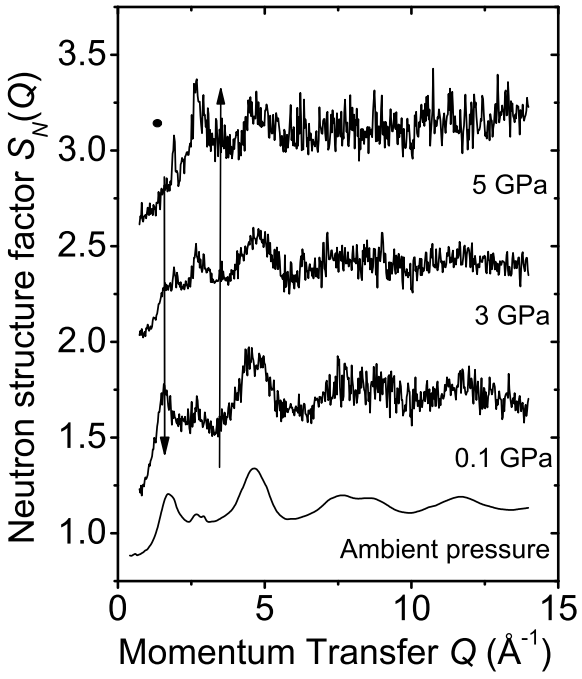

Figure 8.26: The neutron total structure factors $S_N(Q)$ as published by Guthrie *et al.* [285] at 0, 3 and 5 GPa. The authors applied a filter to exclude sharp features more than 3 standard deviations above neighboring data points. The authors also found a weak crystalline contamination, indicated by •, which was attributed to 2-3 % of the α-phase of GeO_2.

The changes in the height and position of the FSDP in the measured $F(Q)$ functions with increasing pressure, shown in figure 8.20, suggest a substantial change in the way the structural motifs are connected with increasing pressure. The FSDP arises from the packing of the structural units on an intermediate range which has a periodicity given by $2\pi/q_1$. Hence, the observed reduction in intensity and increase in position of the FSDP with increasing pressure suggests a denser packing of the structural units accompanied by a reduction in the periodicity associated with the intermediate range ordering. The observed changes in the FSDP with initial application of pressure can therefore be understood in terms of a reduction in size and eventual collapse of the cage-like structures that enclose open regions of the network of corner shared GeO_4 structural units [285, 286]. The increase in coordination number $\bar{n}^{\mathrm{O}}_{\mathrm{Ge}}$ from 4.0(2) to 4.9(2) with increasing pressure in the region between 5 GPa and 9 GPa shows that, following the collapse of the open network regions, a change in the nature of the basic structural motifs occurs as oxygen atoms are forced into close proximity to the GeO_4 tetrahedra. This results in the formation of structural units with higher coordination numbers. However, since the $G(r)$ functions only provide average values for the coordination number, it is not possible to tell whether the observed rise in coordination number results from the formation of GeO_5 pentahedra, GeO_6 octahedra or a mixture of the two. The formation of GeO_5 polyhedra is likely as they are known to exist in germanate glasses [307, 308, 311] and crystalline $K_2Ge_8O_{17}$ [309]. Further investigations using e.g. molecular dynamics simulations will help to resolve this issue.

The x-ray diffraction results of Guthrie *et al.* [285] suggest a further increase in the Ge-O coordination number, leading to the formation of GeO_6 octahedra at 15 GPa. A detailed examination of the structural transformations that take place in GeO_2 glass will be given in the next chapter, where the results of *in situ* high pressure diffraction experiments up to 14 GPa using the PEARL instrument at the ISIS facility, UK, are presented.

8.6 Conclusions

The results from studies A and B prove that high quality *in situ* high pressure neutron diffraction patterns can be measured using the Paris-Edinburgh press on the D4C diffractometer. An analysis procedure was developed to account for the gasket and background scattering at each pressure point and improved neutron shielding has led to the extraction of neutron diffraction total structure factors $F(Q)$ at pressures up to 8 GPa that are of superior quality to previous diffraction measurements [285]. Additional improvements could be made to further reduce the contribution to the background scattering from the anvils by focussing a narrower neutron beam onto the sample position and allowing the entire press assembly to move vertically in order to maintain the sample position at the center of the incident neutron beam. The diffraction patterns measured for GeO_2 glass are of suitable calibre to enable future application of the method of isotopic substitution in neutron diffraction to measure the partial structure factors of liquid and glassy materials under high pressure.

In order to fully investigate the pressure induced structural transformations in GeO_2 glass that are expected to take place, measurements need to be taken at higher pressures than are attainable using single toroid cubic boron nitride anvils. Instead, sintered diamond and double toroid anvils can be employed, which have a greater pressure response with respect to the applied load. The use of sintered diamond anvils on the D4C instrument will be the subject of future studies. However, the results of high pressure experiments up to 14 GPa on GeO_2 glass using sintered diamond single and double toroid anvils on the PEARL instrument at ISIS are reported in the following chapter.

9. Structure of GeO_2 glass at high pressure II

9.1 Introduction

In chapter 8, the structure of GeO_2 glass was studied at high pressure using a reactor source diffractometer and showed distinct changes in the structure on an intermediate length scale and an increase in the local coordination number $\bar{n}^{O}_{Ge}$ from 4 at ambient pressure to 4.9(1) at 8.6(5) GPa. A further structural transformation in GeO_2 to a 6-fold coordinated octahedral glass has been observed at 15 GPa using *in situ* diamond anvil cell x-ray diffraction measurements [285]. The objective of this investigation is to obtain neutron diffraction measurements of GeO_2 glass at a similar pressure. The experiments in chapter 8 were limited to a maximum pressure of 8.6(5) GPa by the performance of the cubic boron nitride single toroid anvils. Higher pressures are attainable using sintered diamond anvils and by using the double toroid anvil profile, as are typically employed on the PEARL instrument at the ISIS facility, UK, which is described in § 3.2.5. However, the PEARL instrument is optimised for crystallography, has limited accessibility to low scattering angles and high pressure experiments typically exhibit large contributions from the background and anvil scattering. This chapter presents the results obtained from significant improvements in the shielding, collimation and experimental methods used on PEARL to obtain, for the first time, high quality and correctly normalised *in situ* neutron total structure factors for an amorphous material.

9.2 Theory

As derived in § 2.2, the coherent scattered intensity measured in a neutron diffraction experiment on a multicomponent glass system is represented by the total structure factor $F(Q)$ defined as

$$F(Q) = \sum_{\alpha=1}^{n}\sum_{\beta=1}^{n} c_\alpha c_\beta b_\alpha b_\beta [S_{\alpha\beta}(Q) - 1], \tag{9.1}$$

where n is the total number of atomic species denoted by α or β, c_α and b_α represent the atomic fraction and coherent neutron scattering length of atomic species α, respectively, $S_{\alpha\beta}(Q)$ is a Faber-Ziman partial structure factor and Q is the scattering vector. The coherent neutron scattering lengths for GeO_2 glass are $b_{\mathrm{Ge}} = 8.185(20)$ fm and $b_{\mathrm{O}} = 5.803(4)$ fm [30]. The total structure factor can therefore be written as

$$F(Q) = A[S_{\mathrm{GeGe}}(Q) - 1] + B[S_{\mathrm{OO}}(Q) - 1] + C[S_{\mathrm{GeO}}(Q) - 1], \tag{9.2}$$

where $A = c_{\mathrm{Ge}}^2 b_{\mathrm{Ge}}^2 = 0.0744(4)$ barn, $B = c_{\mathrm{O}}^2 b_{\mathrm{O}}^2 = 0.1497(5)$ barn and $C = 2c_{\mathrm{Ge}}c_{\mathrm{O}}b_{\mathrm{Ge}}b_{\mathrm{O}} = 0.2111(5)$ barn. The corresponding real space information is given by the total pair distribution function $G(r)$ which is obtained by the Fourier transform

$$\begin{aligned} G(r) &= \frac{1}{2\pi^2 r n_0}\int_0^\infty QF(Q)\sin(Qr)\mathrm{d}Q \\ &= \sum_{\alpha=1}^{n}\sum_{\beta=1}^{n} c_\alpha c_\beta b_\alpha b_\beta [g_{\alpha\beta}(r) - 1] \\ &= A[g_{\mathrm{GeGe}}(r) - 1] + B[g_{\mathrm{OO}}(r) - 1] + C[g_{\mathrm{GeO}}(r) - 1], \end{aligned} \tag{9.3}$$

where n_0 denotes the atomic number density, $g_{\alpha\beta}(r)$ is a partial pair distribution function and r is a distance in real space. As defined in equation 2.12, the coordination number $\bar{n}_{\mathrm{Ge}}^{\mathrm{O}}$ is determined by integrating over the nearest neighbour peak in $G(r)$, for which it is assumed that only the $g_{\mathrm{GeO}}(r)$ correlations

contribute. The theoretical $G(0)$ limit is given by

$$G(0) = -\sum_{\alpha=1}^{n}\sum_{\beta=1}^{n} c_\alpha c_\beta b_\alpha b_\beta. \tag{9.4}$$

For GeO_2 glass $G(0) = -0.4352(9)$ barn.

In x-ray diffraction experiments the scattering lengths are Q dependent such that the partial structure factors have Q dependent weighting factors and the total x-ray structure factor is given by

$$F_X(Q) = \sum_{\alpha=1}^{n}\sum_{\beta=1}^{n} c_\alpha f_\alpha(Q) c_\beta f_\beta(Q) \left[S_{\alpha\beta}(Q) - 1\right], \tag{9.5}$$

where $f_{\mathrm{Ge}}(Q)$ and $f_{\mathrm{O}}(Q)$ are the atomic form factors for Ge and O, respectively, and are tabulated in Ref. [201]. It is therefore convenient to define the normalised total neutron structure factor $S_N(Q)$ for GeO_2 glass as

$$S_N(Q) = \frac{F(Q) + \langle b\rangle^2}{\langle b\rangle^2}, \tag{9.6}$$

where the average scattering length $\langle b\rangle = c_{\mathrm{Ge}} b_{\mathrm{Ge}} + c_{\mathrm{O}} b_{\mathrm{O}}$. Similarly, the normalised total x-ray structure factor $S_X(Q)$ for GeO_2 glass is defined by

$$S_X(Q) = \frac{F_X(Q) + \langle f(Q)\rangle^2}{\langle f(Q)\rangle^2}, \tag{9.7}$$

where the average form factor $\langle f(Q)\rangle = c_{\mathrm{Ge}} f_{\mathrm{Ge}}(Q) + c_{\mathrm{O}} f_{\mathrm{O}}(Q)$.

9.3 Experimental procedure

9.3.1 Sample preparation

The GeO_2 glass was prepared by heating $\approx$ 5 g of powdered Germanium (IV) Oxide (Alfa Aesar, 99.9999%) contained in a platinum crucible, with a 10 % rhodium reinforced rim, in air at 1600 °C. After $\approx$ 20 min the crucible

was removed from the furnace, placed onto a nitrogen cooled brass block and liquid nitrogen was poured over the melt. The crucible was warmed to room temperature using a heat gun to avoid condensation of atmospheric H_2O on the hygroscopic GeO_2 glass. The clear glass was removed from the crucible in one piece and stored in a desiccator containing silica gel (BDH, granules).

Table 9.1: Properties of the pellets prepared for high pressure neutron diffraction measurements on the PEARL instrument using single toroid (ST) or double toroid (DT) sintered diamond anvils. The GeO_2 pellets were either formed from compressed powders or solid pieces ground to shape. The vanadium (V) pellets were either formed from compressed powders or foils. The powder and foil pellets were pre-compressed in dies of suitable geometry at the listed applied load in a powder press.

Pellet	Sample	Type	Geometry	Load (tonne)	Mass (g)
1	GeO_2	powder	ST	8	0.22(1)
2	GeO_2	solid	ST	–	0.24(1)
3	GeO_2	solid	DT	–	0.12269(5)
4	GeO_2	solid	DT	–	0.12146(5)
A	V	powder	ST	1	0.390(1)
B	V	powder	ST	1	0.390(1)
C	V	powder	ST	1	0.390(1)
D	V	foil	DT	0.75	0.2053(5)
E	V	foil	DT	0.75	0.2061(5)

Several pellets of GeO_2 glass and vanadium, matching the geometry of the single toroid or double toroid anvils, were formed as listed in table 9.1. The pre-compressed GeO_2 pellet 1 and vanadium pellets A, B and C, made for the single toroid anvil experiments, were formed using powdered GeO_2 glass and V powder following the method outlined in § 8.5.1 using a SPECAC powder press at the ISIS facility. The GeO_2 powder pellet 1 was extremely fragile and, after removing from the powder press, the middle section disintegrated. Additional fine powder was therefore added to bulk out the sample for the diffraction experiment. For the double toroid anvil experiments, the vanadium pellets D and E were formed from pieces of V foil which were tightly rolled and compressed in the powder press using a die made from hardened steel.

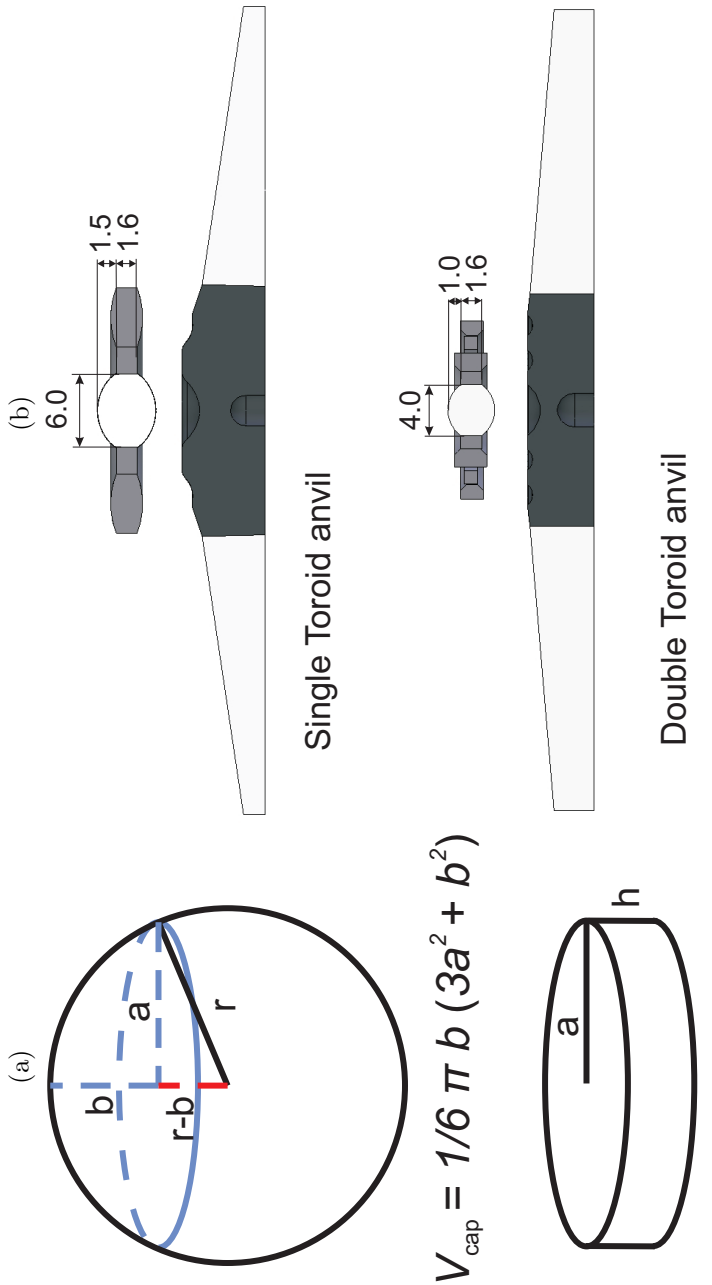

Figure 9.1: Defining the geometry and dimensions of the samples used in the single toroid and double toroid anvil experiments.

The solid GeO_2 glass pellets 2, 3 and 4, matching the geometry of the single or double toroid anvils, were formed by grinding a large solid piece of glass into a cylinder of either 6 mm or 4 mm diameter, as appropriate, using a dremmel with a rotary grinding stone attachment. To form the required pellet profile, the ends of the cylindrical pieces of GeO_2 glass were polished, using diamond paste, against faulty anvils of the correct geometry rotating on a polishing wheel. The precise pellet mass required for the anvil geometries was calculated from the sample density and the combined volume of the two spherical caps and the cylindrical middle sections of the pellets. This is illustrated in figure 9.1, where the volume of a spherical cap V_{cap} and the volume of a cylinder V_{cyl} are given by

$$V_{\text{cap}} = \frac{1}{6}\pi b(3a^2 + b^2), \tag{9.8}$$

and

$$V_{\text{cyl}} = \pi a^2 h, \tag{9.9}$$

where a denotes the radius of the cylinder cross-section and cap base, b denotes the height of the cap and h denotes the height of the cylinder. The precise sample volume for the single toroid anvil was therefore determined as 91.1847 mm^3 using $a = 3.0$ mm, $b = 1.5$ mm and $h = 1.6$ mm. Similarly, the precise sample volume for the double toroid anvil was determined as 33.7198 mm^3 using $a = 2.0$ mm, $b = 1.0$ mm and $h = 1.6$ mm. These values were confirmed by making three-dimensional Solidworks models of the pellets. Taking the density of GeO_2 glass as 3.643 g cm^{-3} [306] and vanadium as 6.110g cm^{-3}, the ideal mass of the GeO_2 glass pellets was calculated as 0.33218 g for use in the single toroid anvils and 0.12284 g for use in the double toroid anvils. The ideal mass of the vanadium pellets was calculated as 0.55714 g for use in the single toroid anvils and 0.20603 g for use in the double toroid anvils. The mass of the pellets for the double toroid anvil experiments were matched, within 2 %, to the theoretically ideal sample mass.

9.3.2 The single toroid anvil neutron diffraction experiments

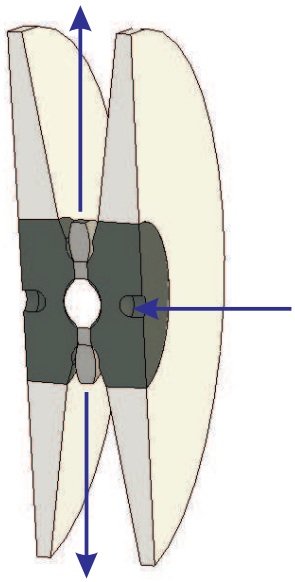

Figure 9.2: Single toroid anvil cross-section in the PEARL transverse geometry. The incident and scattered neutron beam directions are indicated by the blue arrows.

In situ high pressure neutron diffraction experiments were conducted on GeO_2 glass using a V4 variant Paris-Edinburgh press mounted in transverse geometry on the PEARL instrument at the ISIS facility, UK, with Los Alamos type single toroid sintered diamond anvils. In this set-up the incident neutrons are directed through one of the anvils along the compression axis of the cell and the sample is encapsulated by a null scattering Ti-Zr gasket assembly, as shown in figure 9.2. A semi-automated hydraulic pump system was used to apply force to the compression anvil and compress the sample and gasket assembly. In order to ensure the anvils were centered at the same position in the incident beam at each pressure, a remotely controlled motorised system was used to move the press assembly and centre the anvils on fixed cross hairs, as monitored by a live feed from a video camera (see figure 9.3).

(a) Ambient pressure

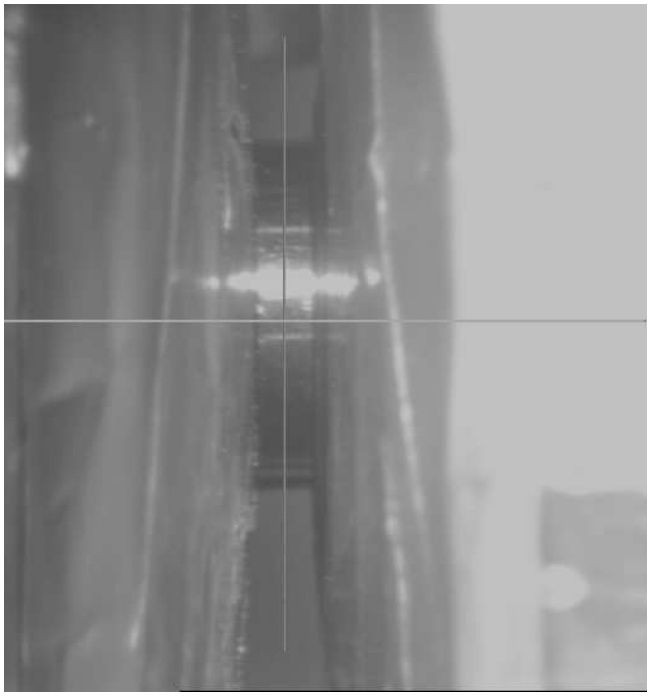

(b) 9.0(5) GPa

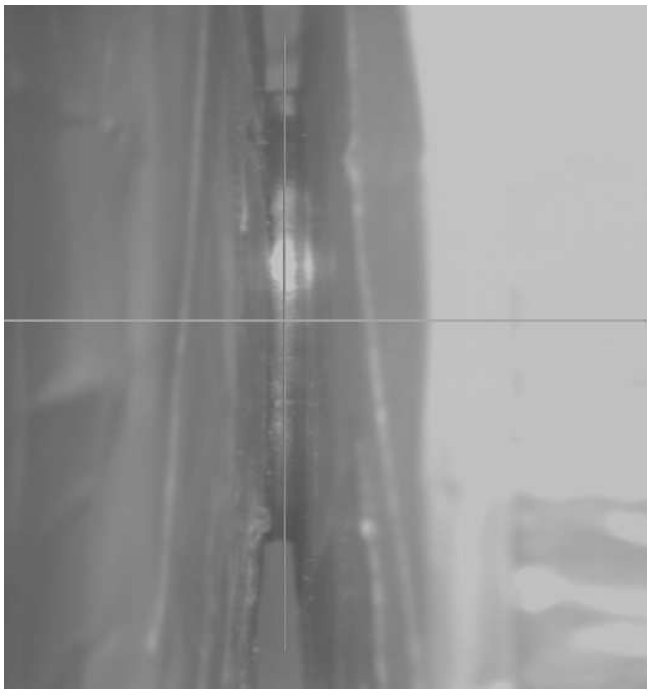

Figure 9.3: *In situ* images of the pressure cell set up at (a) ambient pressure and (b) 9.0(5) GPa.

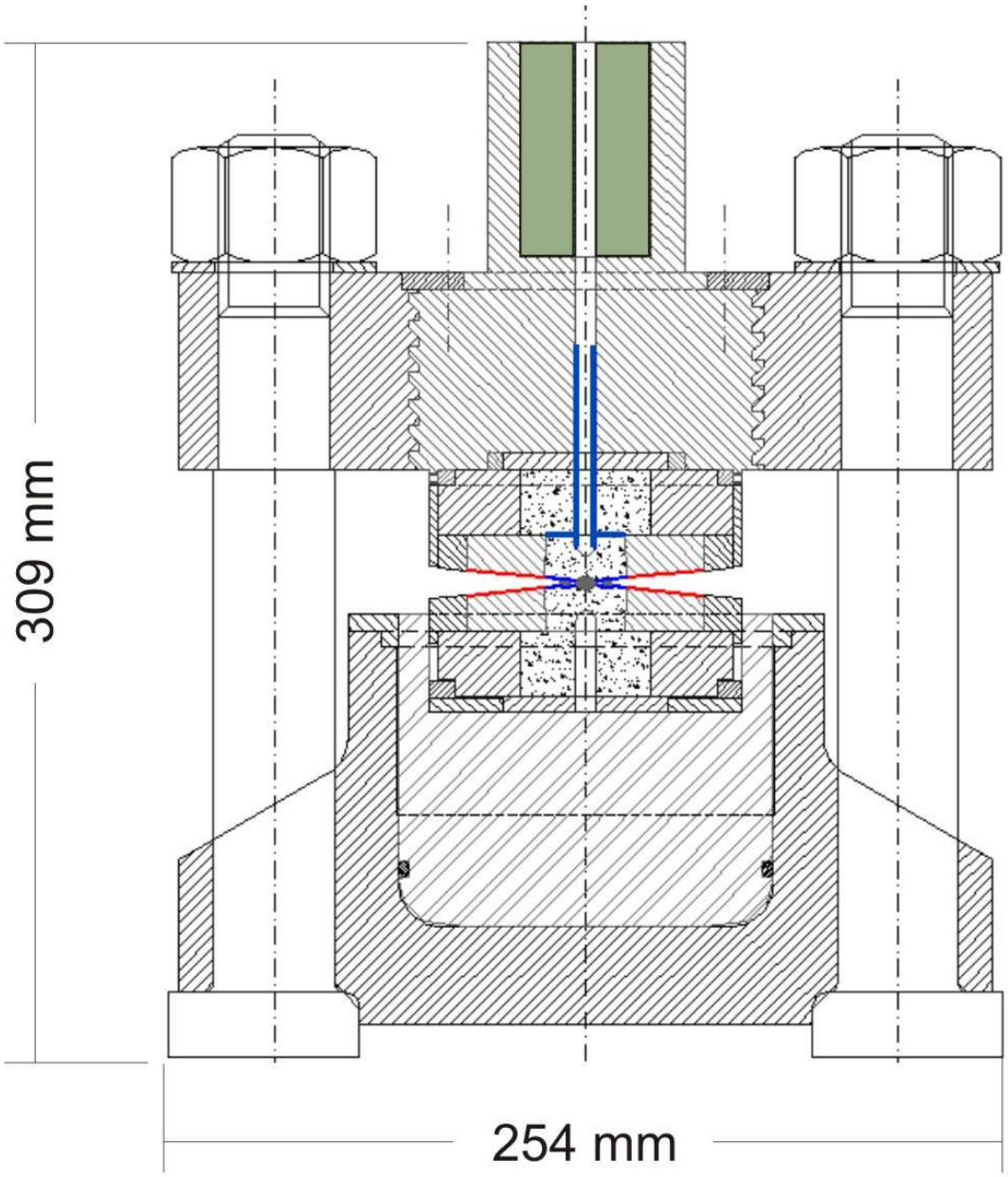

Figure 9.4: V3 variant Paris-Edinburgh cell with Los Alamos type single toroid anvils [45]. A V4 variant cell was used in the single toroid anvil experiment, however the geometry of the cell assemblies are identical. The boron nitride collimator is marked by the green regions, the Gd collimation and shielding is marked by the blue regions, and the cadmium shielding is marked by the red regions.

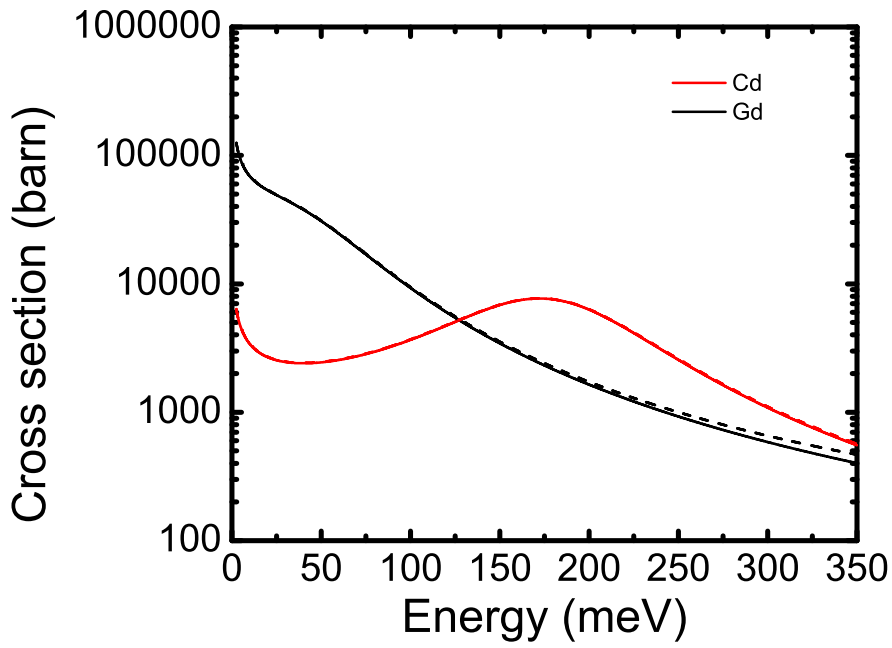

Figure 9.5: Cross sections for Gd and Cd, of naturally occurring isotopic abundance, as a function of the energy of incident neutrons at the PEARL instrument (ISIS). Values were obtained from the Nuclear Data Evaluation Lab [312] using the Evaluated Nuclear Data File (ENDF) [313]. The solid and dashed red curves are the absorption and total cross sections for Cd, respectively. The solid and dashed black curves are the absorption and total cross sections for Gd, respectively.

A significant contribution to the background intensity arises from Bragg scattering from the sintered diamond anvils. These diamond Bragg features are pressure dependent and it is therefore difficult to accurately extract the diffuse scattering of an amorphous sample. Improved shielding and incident neutron beam collimation, as detailed below and illustrated in figure 9.4, were incorporated into the press assembly in order to significantly reduce the background scattering contributions. The cross sections for Gadolinium (Gd) and Cadmium (Cd), in their naturally occurring isotopic abundance, are plotted in figure 9.5. Both elements exhibit very large absorption cross sections over

the energy range of incident neutrons used at the PEARL instrument. The absorption cross section is, however, much higher for Gd at low neutron energies and higher for Cd at high neutron energies. A combination of foils of both elements was therefore used as shielding material. The incident neutron beam was collimated by a 3.5 mm diameter aperture through a cylindrical block of sintered hexagonal boron nitride. A Gd tube of 3.5 mm outer diameter and 3.44 mm inner diameter was used to further collimate the incident neutrons near the sample position. In order to reduce the neutron scattering paths directly from the diamond anvils to the detectors, 0.03 mm Gd foils were incorporated between the Ti-Zr gasket assembly and anvils and 0.25 mm Cd foils were attached to the anvil binding rings. The neutrons diffracted by the sample exit the cell through the Ti-Zr gasket and impinge on detector banks set at 90° to the incident beam. To further reduce the contribution from anvil scattering, an effective scattered beam collimation was achieved by summing only those detector pixels encompassing a narrow 2θ range of 90 ± 3.5 °. The resulting Q-range is hence limited to $1.55 \leq Q(\text{Å}^{-1}) \leq 19.6$. A comparison between measurements of a Ti-Zr gasket in the pressure cell with and without the Gd collimation and shielding is shown in figure 9.6 and clearly illustrates the effectiveness of the Gd in reducing the intensity of the diamond Bragg peaks and other more broad background features.

Diffraction patterns were taken for the GeO_2 glass pellets 1 and 2 at ambient pressure and three loads up to 125 tonnes, as listed in table 9.2. Additional measurements were made for an empty Ti-Zr gasket at ambient pressure and the vanadium pellets A, B and C at various applied loads for data correction and normalisation purposes, as described in § 9.4. The intensities for each detector group were saved at regular intervals (every 170 μAhr) and no deviation between each scan was observed outside the statistical variation, verifying the diffractometer stability [197]. In order to attain acceptable counting statistics, considering the small size of the sample in the neutron beam, a total run time equivalent to $\approx$ 2700 μAhr per sample was made, which at an average ISIS beam current of 170 μA equates to $\approx$ 16 hours of neutron counting time for

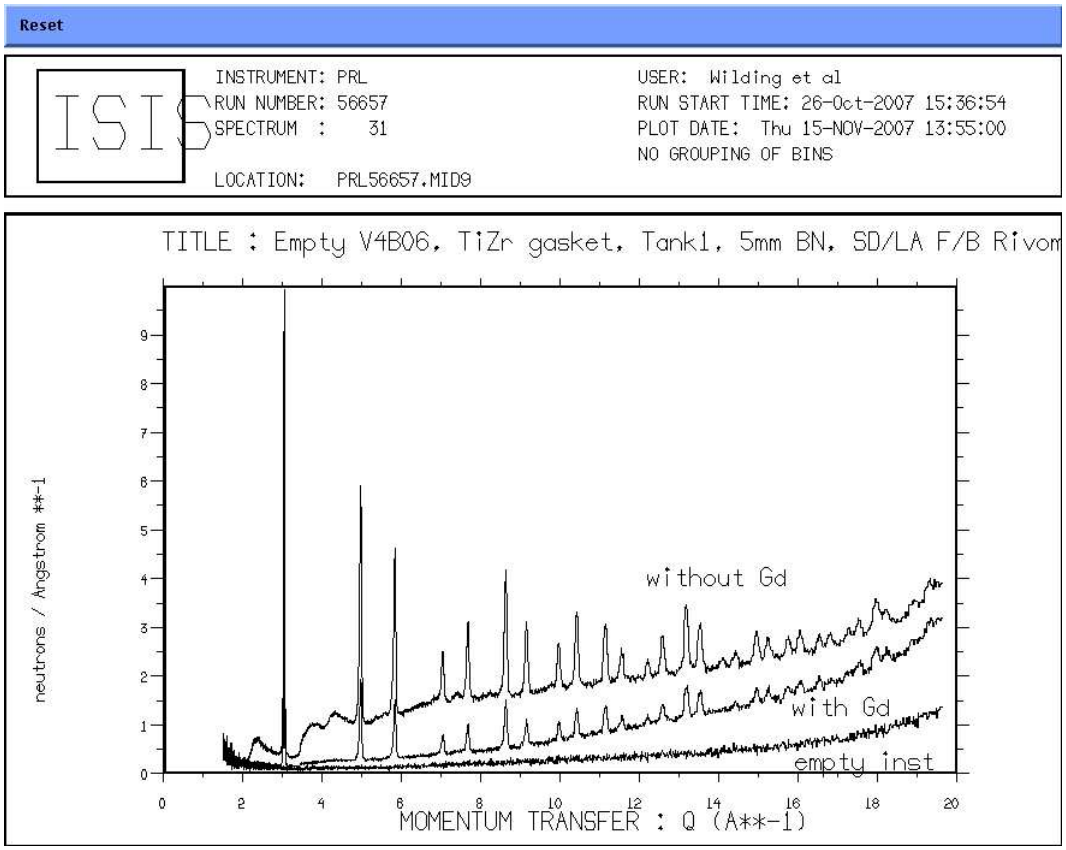

Figure 9.6: A comparison between the scattered intensity from a Ti-Zr gasket in the Paris-Edinburgh press with and without the Gd collimation and shielding (see the text) together with the background measurement for the empty instrument.

the sample at each pressure.

The measured diffraction patterns were focussed i.e. the raw time of flight data sets for each run were first normalised to the incident neutron flux and corrected for the relative efficiency of each detector pixel. This was obtained from the diffraction pattern measured for a vanadium sphere, normalised to the incident flux, which should be a constant with respect to 2θ for each incident neutron energy provided each detector pixel is at the same distance from the sphere and subtends the same solid angle. The data sets were then summed to give a single diffraction pattern as a function of Q. The total structure factor

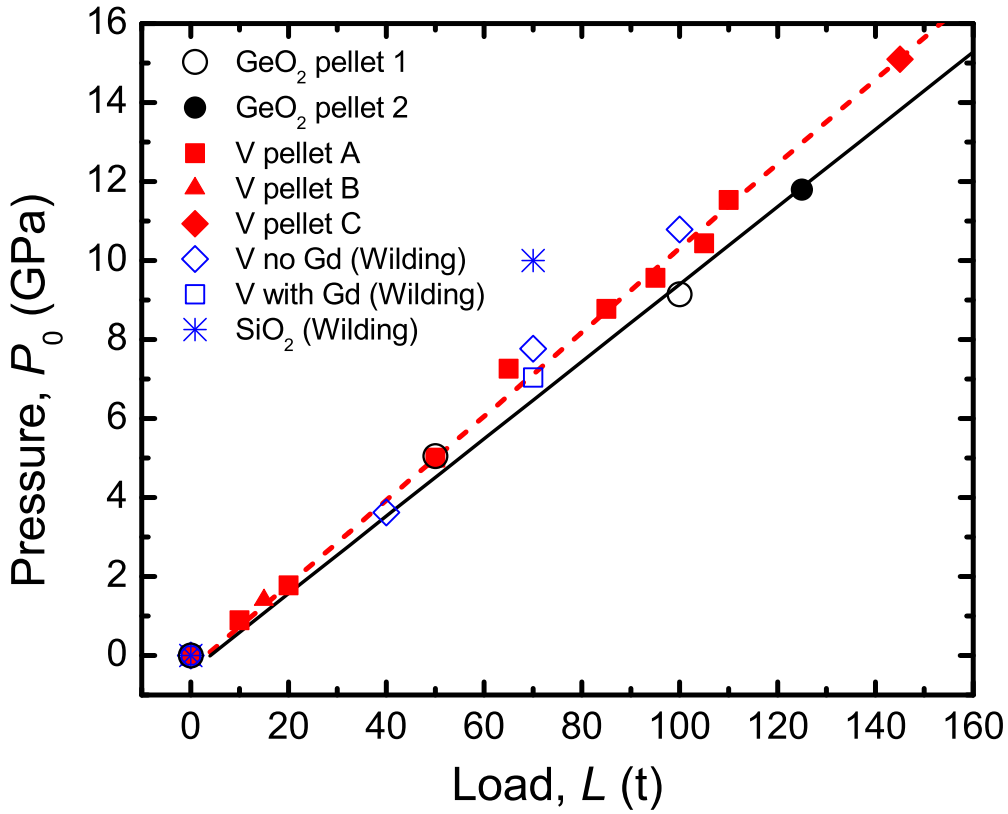

Figure 9.7: The pressure at each experimental load using the single toroid sintered diamond anvils as obtained by making a Rietveld refinement to the diamond anvil Bragg peaks and calibrated to the known equation of state for crystalline ice VII [314]. The refined data points correspond to GeO_2 pellet 1 (open black circles), vanadium pellet A (solid red squares), vanadium pellet B (solid red triangles), vanadium pellet without Gd collimation from Wilding [315] (open blue diamonds), vanadium pellet with Gd collimation from Wilding [315] (open blue squares) and SiO_2 glass from Wilding [315] (blue star). The GeO_2 pellet 2 (solid black circle) and vanadium pellet C (solid red diamond) data points were obtained after making a linear fit to the refined data points as shown by the solid black line for GeO_2 and the dashed red line for vanadium.

$F(Q)$ for the GeO_2 glass at each pressure was then obtained using the data correction and normalisation procedures detailed in § 9.4.

The pressure P_0 on the GeO_2 and vanadium pellets at each applied load L is plotted in figure 9.7. The calibration curves were calculated by making a Rietveld refinement to the diamond anvil Bragg peaks in the focussed data sets which gave the diamond unit cell volume [314]. This was compared with the volume of crystalline ice VII compressed in the same type of single toroid anvil cell and, since ice VII has a known equation of state [316], the diamond unit cell volume was determined as a function of pressure. A linear fit was made to the GeO_2 and vanadium data in figure 9.7 to obtain the pressure on GeO_2 pellet 2 and vanadium pellet C measured at the highest applied loads. As in the preceding chapter, the number density of the GeO_2 glass at each pressure was determined from the experimental data taken by Hong *et al.* [287] and is listed in table 9.2.

Table 9.2: Applied load L and pressure P_0 on the GeO_2 glass pellets 1, 2 or 4 using sintered diamond anvils with single toroid (ST) or double toroid (DT) geometry, listed together with the atomic number density n_0 of the pressurised GeO_2 glass.

L (tonne)	P_0 (GPa)	geometry	pellet	n_0 (Å^{-3})
0	Ambient	ST	1	0.0629(3)
50	5.0(5)	ST	1	0.0774(9)
100	9.0(5)	ST	1	0.0876(9)
125	11.5(5)	ST	2	0.0946(9)
120	14(1)	DT	4	0.0988(9)

9.3.3 The double toroid anvil neutron diffraction experiment

In situ neutron diffraction experiments were conducted on GeO_2 glass using a V3 variant Paris-Edinburgh press mounted in transverse geometry on the PEARL instrument at the ISIS facility, UK, with double toroid sintered dia-

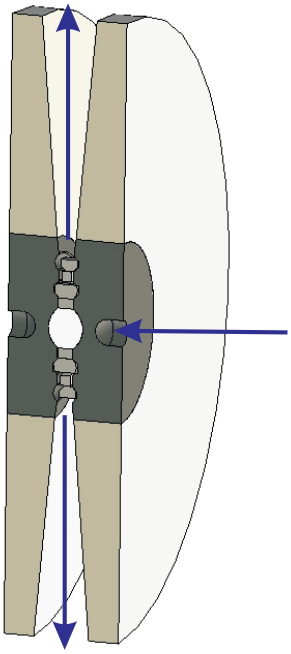

Figure 9.8: Double toroid anvil cross-section in the PEARL transverse geometry. The incident and scattered neutron beam directions are indicated by the blue arrows.

mond anvils. The GeO_2 glass sample was encapsulated in the cell by a null scattering Ti-Zr gasket assembly, as shown in figure 9.8. Diffraction patterns were taken for GeO_2 pellet 3 and vanadium pellet D at loads of 115 tonne and 120 tonne, respectively, with the same collimation and shielding used in the single toroid anvil experiments shown in figure 9.4. Further diffraction patterns were taken for GeO_2 pellet 4 and vanadium pellet E at loads of 120 tonne and 85 tonne, respectively, with the Gd foils removed from between the anvil and gasket assembly in order to increase the scattered signal from the sample. Additional diffraction patterns were taken for an empty Ti-Zr gasket at ambient pressure.

The pressure calibration plot for the double toroid sintered diamond anvils is given in figure 9.9 and was obtained from previous measurements by the Edinburgh High Pressure research group [317]. From these measurements, the sample pressure at the applied load of 120 tonne was estimated to be

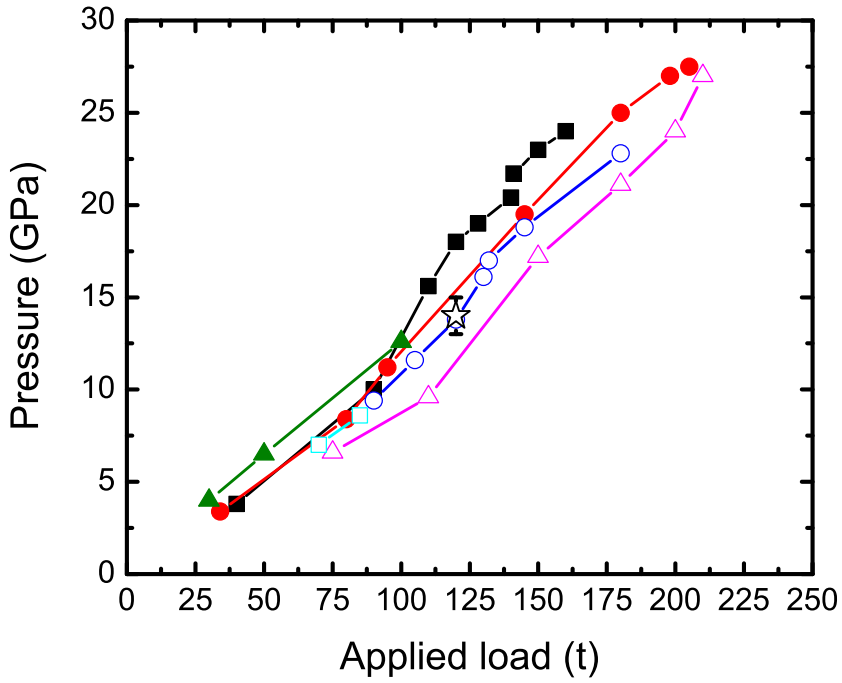

Figure 9.9: Pressure versus load calibration plot for the double toroid De Beers sintered diamond anvils [317]. The five separate curves indicate different loadings of ice. The estimated pressure of 14(1) GPa for the 120 tonne applied load is indicated by the star and was chosen to approximately correspond to the average of the calibration points.

14(1) GPa. A total of ≈ 3300 μAhr was collected on the sample at 14(1) GPa, equating to ≈ 20 hours of neutron counting time, owing to the very small size of the sample. As in the single toroid anvil experiments, the data sets were checked for detector stability and focussed. The total structure factor $F(Q)$ for the GeO_2 glass at 14(1) GPa was then extracted using the data correction and normalisation procedures detailed in § 9.4. The number density of the GeO_2 glass at 14(1) GPa is listed in table 9.2.

9.4 Data analysis procedure

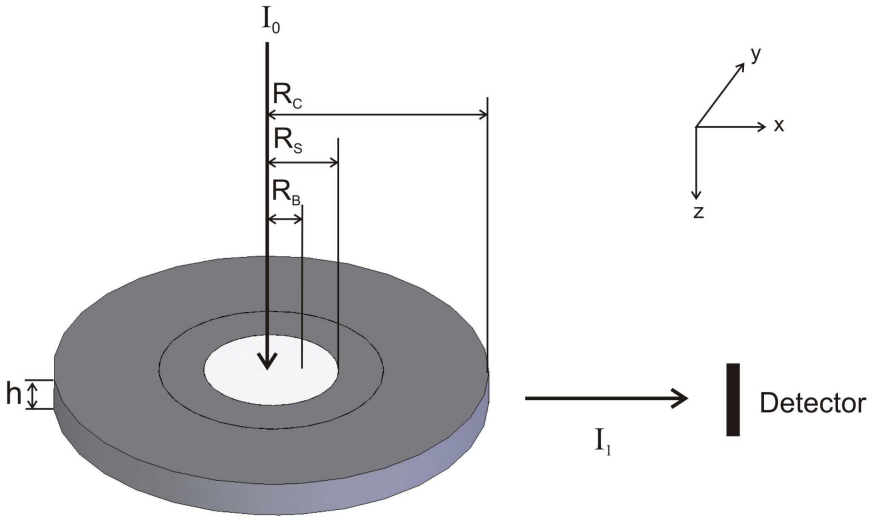

Figure 9.10: Defining the PEARL geometry. The neutron beam with radius R_B and intensity I_0 is incident along the z-axis. The neutrons scatter from the sample of radius R_S through the Ti-Zr gasket of radius R_C into the detector along the x-axis at 90° to the incident beam.

In a neutron diffraction experiment using a Paris-Edinburgh press in transverse geometry, neutrons are incident through the compression axis of the anvil and scatter from the sample through the null scattering Ti-Zr gasket. This defines a cylindrical sample geometry for the scattered beam with a height given by the separation of the anvils (see figure 9.10). On PEARL the data sets are collected in a small angular range at $2\theta \simeq 90°$. The Q-dependence of the scattered intensity is thus obtained by varying the incident wavelength λ where $Q = (4\pi/\lambda)\sin(\theta)$. For the sample, the differential scattering cross section per atom at a fixed incident neutron wavelength is given by

$$\left[\frac{\mathrm{d}\sigma}{\mathrm{d}\Omega}(Q)\right]_S = \frac{1}{N_S A_{S,SC}(Q)}\left[\frac{I'_{SC}(Q)}{a(Q)} - M_{SC}(Q)\right], \tag{9.10}$$

where $I'_{SC}(\theta)$ denotes the measured scattered intensity from the sample in a Ti-Zr gasket corrected for background (e.g. anvil) scattering, $a(Q)$ is the calibration factor, N_S denotes the number of sample nuclei in the incident neutron beam, $M_{SC}(Q)$ denotes the multiple scattering cross-section for the sample in the Ti-Zr gasket, and $A_{S,SC}(Q)$ denotes the attenuation coefficient for the incident neutron beam scattered by the sample and attenuated by the sample and gasket. For the PEARL geometry $A_{S,SC}(Q)$ is given by [318]

$$A_{S,SC}(Q) = \frac{4}{\pi}\frac{1}{R_B h}\frac{(1-e^{-\mu_S h})}{\mu_S^2}\int_0^{\pi/2} \mathrm{d}\theta \sin(\theta)\,[\chi]\,, \tag{9.11}$$

where

$$\chi = e^{-(\mu_S-\mu_C)(R_S^2-R_B^2\cos^2\theta)^{1/2}} e^{-\mu_C(R_C^2-R_B^2\cos^2\theta)^{1/2}} \sinh(\mu_S R_B \sin\theta), \tag{9.12}$$

μ_S and μ_C are the attenuation coefficients of the sample and the Ti-Zr gasket, respectively, R_B is the radius of the incident neutron beam, R_S is the radius of the sample and R_C is the radius of the gasket (see figure 9.10).

Similarly, the differential scattering cross section per atom for a vanadium pellet contained in a Ti-Zr gasket is given by

$$\left[\frac{\mathrm{d}\sigma}{\mathrm{d}\Omega}(Q)\right]_V = \frac{1}{N_V A_{V,VC}(Q)}\left[\frac{I'_{VC}(Q)}{a(Q)} - M_{VC}(Q)\right], \tag{9.13}$$

where the subscript V denotes vanadium. The calibration factor $a(Q)$ can be defined in terms of the vanadium differential scattering cross section according to

$$a(Q) = \frac{1}{\left[N_V A_{V,VC}(Q)\left[\frac{\mathrm{d}\sigma}{\mathrm{d}\Omega}(Q)\right]_V + M_{VC}(Q)\right]} I'_{VC}(Q). \tag{9.14}$$

Since the coherent scattering from vanadium is negligible, the differential scattering cross section for vanadium depends only upon the incoherent scattering length $b_{\mathrm{inc,V}}$. Equation 9.14 can therefore be re-written as

$$a(Q) = \frac{1}{\left[N_V A_{V,VC}(Q) b_{\mathrm{inc},V}^2 (1+P_V(Q)) + M_{VC}(Q)\right]} I'_{VC}(Q), \tag{9.15}$$

where $P_V(Q)$ is the Placzek [31] (inelasticity) correction for vanadium. By substituting equation 9.15 into equation 9.10 and using equation 2.5 it follows that

$$\begin{aligned}\left[\frac{\mathrm{d}\sigma}{\mathrm{d}\Omega}(Q)\right]_S &= F(Q) + \sum_{\alpha}^{n} c_\alpha (b_{\mathrm{coh},\alpha}^2 + b_{\mathrm{inc},\alpha}^2)(1 + P_\alpha(Q)) \\ &= \frac{I'_{SC}(Q)}{I'_{VC}(Q)} \frac{\left[N_V A_{V,VC}(Q) b_{\mathrm{inc},V}^2 \left[1 + P_V(Q)\right] + M_{VC}(Q)\right] - M_{SC}(Q)}{N_S A_{S,SC}(Q)}\end{aligned} \tag{9.16}$$

where c_α denotes the atomic fraction, $b_{\mathrm{coh},\alpha}$ and $b_{\mathrm{inc},\alpha}$ are the coherent and incoherent neutron scattering lengths, respectively, and $P_\alpha(Q)$ is the Placzek [31] (inelasticity) correction, for each chemical species α in the system.

The attenuation coefficients $A_{i,j}(Q)$ for the sample and vanadium are plotted in figure 9.11 and were calculated using equation 9.11 for the transverse geometry used on PEARL [318] for the sample and gasket assembly in the single toroid anvil geometry at ambient pressure for a fixed scattering angle $2\theta = 90^\circ$ and the PEARL incident neutron wavelength range of $0.45 \leq \lambda_n(\text{Å}) \leq 5.73$. The PLATOM routine in the ATLAS suite of programs [319] was used to calculate the inelasticity correction for the sample and vanadium for the same scattering angle and incident neutron wavelength range, the results of which are also plotted in figure 9.11. The attenuation coefficients $A_{i,j}(Q)$ exhibit a relatively large dependency on Q. However, as shown in figure 9.11, the coefficient $[A_{V,VC}(Q)/A_{S,SC}(Q)]b_{\mathrm{inc,V}}^2[1 + P_{\mathrm{V}}(Q)]$ used in equation 9.16 exhibits a significantly smaller Q dependency.

The sample geometry and background intensity is not explicitly known as a function of pressure. The background scattering at each pressure was therefore estimated from the measured scattered intensity $I_C^E(Q)$ for an empty Ti-Zr gasket at ambient pressure such that

$$I'_{SC}(Q) = I_{SC}^E(Q) - mI_C^E(Q), \tag{9.17}$$

$$I'_{VC}(Q) = I_{VC}^E(Q) - nI_C^E(Q), \tag{9.18}$$

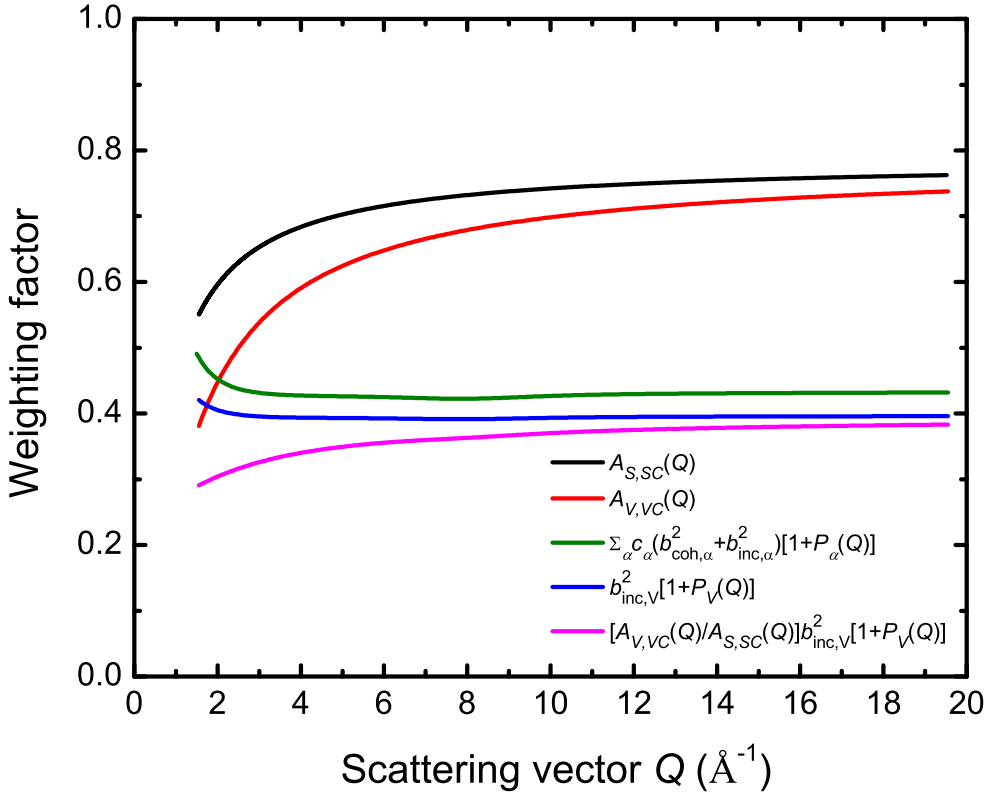

Figure 9.11: The attenuation coefficients $A_{S,SC}(Q)$ (black) and $A_{V,VC}(Q)$ (red), the Placzek [31] corrections $\sum_\alpha c_\alpha(b^2_{\mathrm{coh},\alpha} + b^2_{\mathrm{inc},\alpha})[1 + P_\alpha(Q)]$ for GeO_2 (green) and $b^2_{\mathrm{inc,V}}\,[1 + P_{\mathrm{V}}(Q)]$ for vanadium (blue), and the coefficient $[A_{V,VC}(Q)/A_{S,SC}(Q)]\,b^2_{\mathrm{inc},\alpha}[1 + P_{\mathrm{V}}(Q)]$ (magenta). The attenuation coefficients were calculated using equation 9.11 for the transverse geometry used on PEARL for the sample and vanadium encapsulated in a Ti-Zr gasket in the single toroid anvil geometry at ambient pressure for a scattering angle $2\theta = 90°$ and an incident neutron wavelength range of $0.45 \leq \lambda_n\ (\text{Å}) \leq 5.73$. The Placzek [31] corrections were calculated using the PLATOM routine [319].

where m and n are scaling factors chosen to ensure that the diamond Bragg peak contributions to the intensities $I^E_{SC}(Q)$ and $I^E_{VC}(Q)$ are either eliminated or minimised. When using a Paris-Edinburgh press it is important to match the geometry of the sample and vanadium in the Ti-Zr gasket at each pressure point so that the correct calibration factor $a(Q)$ can be found from the vanadium measurement. In practice, the load applied to the vanadium was therefore varied until the ratio

$$\frac{I'_{SC}(Q)}{I'_{VC}(Q)} = \frac{I^E_{SC}(Q) - mI^E_C(Q)}{I^E_{VC}(Q) - nI^E_C(Q)} \tag{9.19}$$

had a minimal slope at large Q values. This is illustrated in figure 9.12 where the data set for glassy GeO_2 at 9.0(5) GPa is normalised using (a) the vanadium data at 1.5(5) GPa and (b) the vanadium data at 11.5(5) GPa. The data sets were then analysed using equation 9.16 which can be re-written as

$$F(Q) = W(Q)\left(\frac{I^E_{SC}(Q) - mI^E_C(Q)}{I^E_{VC}(Q) - nI^E_C(Q)}\right) - Z(Q), \tag{9.20}$$

where

$$W(Q) = \frac{N_V A_{V,VC}(Q) b^2_{\mathrm{inc},V}(1 + P_V(Q)) + M_{VC}(Q)}{N_S A_{S,SC}(Q)} \tag{9.21}$$

and

$$Z(Q) = \frac{M_{SC}(Q)}{N_S A_{S,SC}(Q)} - \sum_{\alpha}^{n} c_\alpha (b^2_{\mathrm{coh},\alpha} + b^2_{\mathrm{inc},\alpha})(1 + P_\alpha(Q)). \tag{9.22}$$

In view of the empirical approach used to find the calibration factor $a(Q)$, as a first approximation the factors $W(Q)$ and $Z(Q)$ in equation 9.20 were assumed to be Q-independent. The constant Z in equation 9.20 therefore displaces the data to ensure $F(Q)$ oscillates about zero at high Q values and the constant W is an overall scaling factor to ensure correct data normalisation, i.e. the low-r features in $G(r)$ should oscillate about the theoretical $G(0)$ limit and the Fourier backtransform of $G(r)$, after the low-r features are set to the theoretical $G(0)$ limit, should be in good overall agreement with the original $F(Q)$.

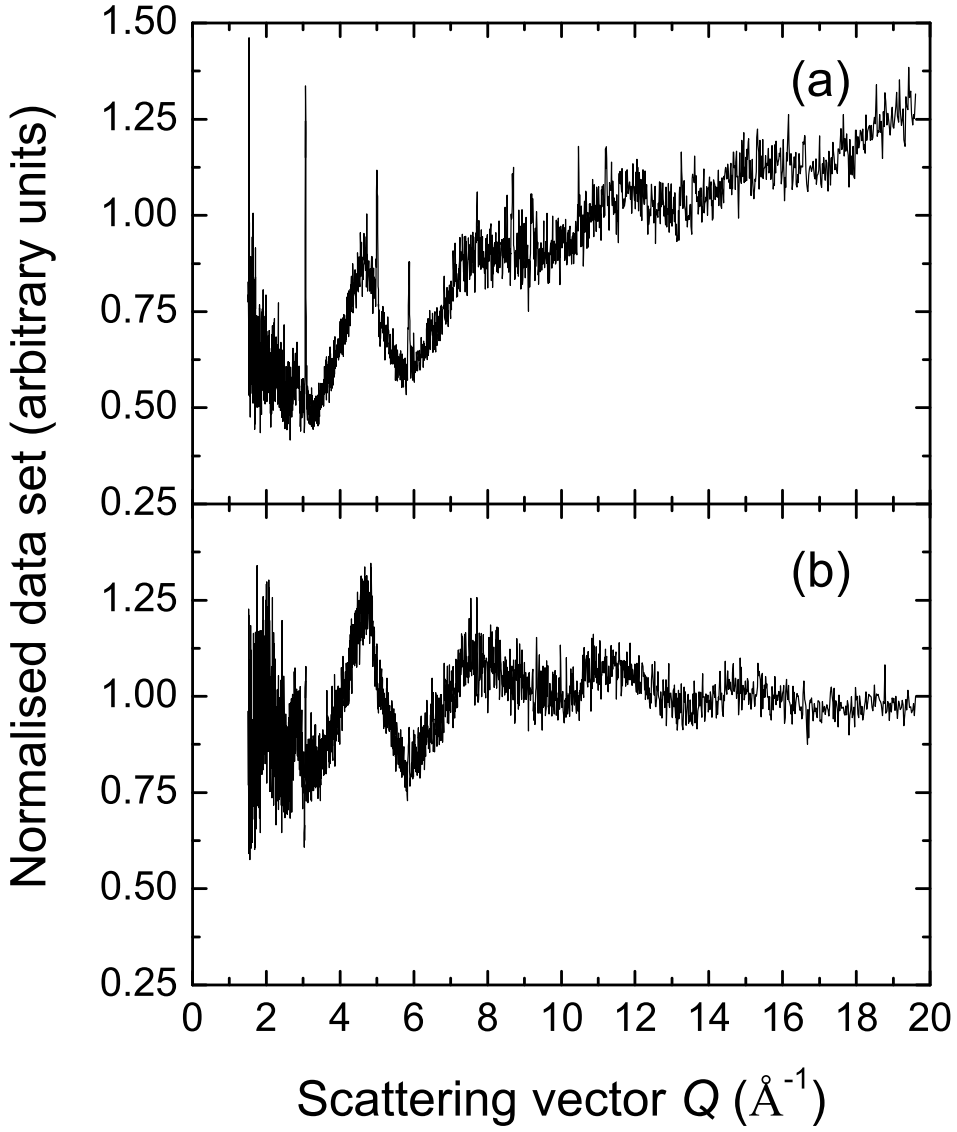

Figure 9.12: The data set for glassy GeO_2 at 9.0(5) GPa normalised according to equation 9.19 using (a) the vanadium data at 1.5(5) GPa where $m = 0.3$ and $n = 0.7$, and (b) the vanadium data at 11.5(5) GPa where $m = 0.3$ and $n = 0.2$. Despite adjusting the values of m and n it did not prove possible to eliminate the diamond Bragg peaks in (a) using the incorrect vanadium normalisation standard.

As mentioned above, a procedure was adopted in the diffraction experiments whereby the vanadium pellet was pressurised until the normalised data set for the sample given by equation 9.19 oscillated about a constant level at high Q values. At ambient pressure and temperature, the bulk modulus for vanadium $B(\mathrm{V}) = 157.12$ GPa [320] and for GeO_2 glass $B(GeO_2) = 23.81$ GPa [295]. Hence vanadium is less compressible than GeO_2 glass. So a greater load is required on the vanadium by comparison with the sample in order to reproduce the same scattering geometry, assuming that the GeO_2 and vanadium pellets have the same starting volume. This was observed in the single toroid anvil measurements in which a greater load was required on the vanadium pellet in order to give normalised sample data sets with no slope. However, the opposite effect was observed in the double toroid anvil measurement where the load required on the vanadium to eliminate the slope on the normalised sample data sets was significantly smaller than the load on the sample. The reason for this is at present unsure.

The measured diffraction intensities for the empty Ti-Zr gasket, GeO_2 glass and vanadium pellets at the various pressures using the single toroid anvils are plotted in figures 9.13 to 9.16 together with the background corrected intensities $I'_{SC}(Q) = I^E_{SC}(Q) - mI^E_C(Q)$ and $I'_{VC}(Q) = I^E_{VC}(Q) - nI^E_C(Q)$ and the preliminary normalised data sets $\left[I^E_{SC}(Q) - mI^E_C(Q)\right] / \left[I^E_{VC}(Q) - nI^E_C(Q)\right]$, where, as noted above, the scaling factors m and n were chosen to eliminate or minimise the contribution to the diffraction patterns from the diamond anvil Bragg peaks.

The raw data sets obtained from the high pressure experiments using double toroid anvils with and without the Gd foils in place are plotted in figures 9.17 (a) and (c), respectively. Very little structure is present above the background scattering in the diffraction pattern taken for GeO_2 glass with the Gd foil in place and there is a large residual slope on the data when normalised using the scattering from a vanadium pellet measured in the same set up (see figure 9.17 (b)). Upon removing the Gd foil between the anvil and gasket assembly, the sample scattering is more apparent above the background scattering.

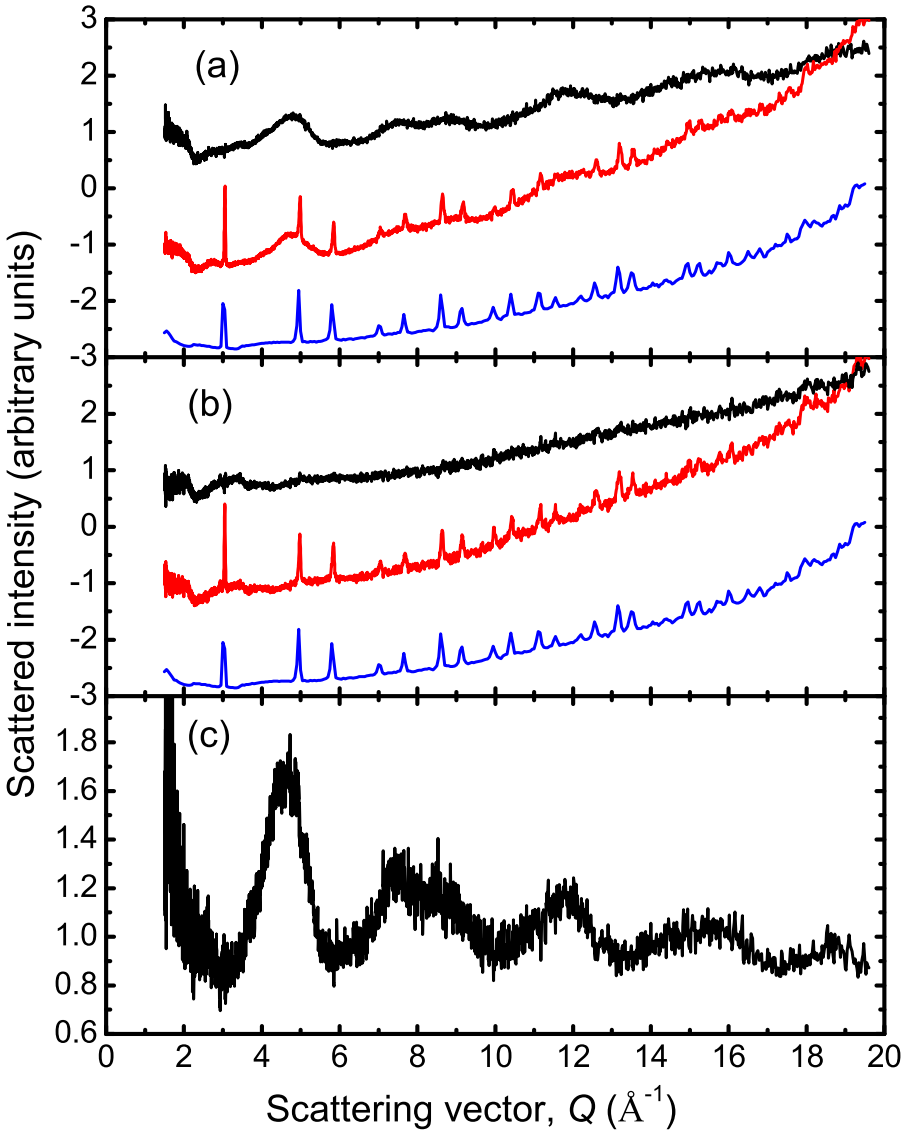

Figure 9.13: (a) The background corrected intensity $I'_{SC}(Q) = I^E_{SC}(Q) - 0.93I^E_C(Q)$ for GeO_2 glass at ambient pressure (black curve) compared with the measured intensities $I^E_{SC}(Q) - 2$ for the sample (red curve) and $I^E_C(Q) - 3$ for the empty Ti-Zr gasket (blue curve). (b) The background corrected intensity $I'_{VC}(Q) = I^E_{VC}(Q) - 0.70I^E_C(Q)$ for vanadium at 1.5(5) GPa (black curve) compared with the measured intensities $I^E_{VC}(Q) - 2$ for the vanadium (red curve) and $I^E_C(Q) - 3$ for the empty Ti-Zr gasket (blue curve). (c) The preliminary normalised data set $\left[I^E_{SC}(Q) - 0.93I^E_C(Q)\right] / \left[I^E_{VC}(Q) - 0.70I^E_C(Q)\right]$.

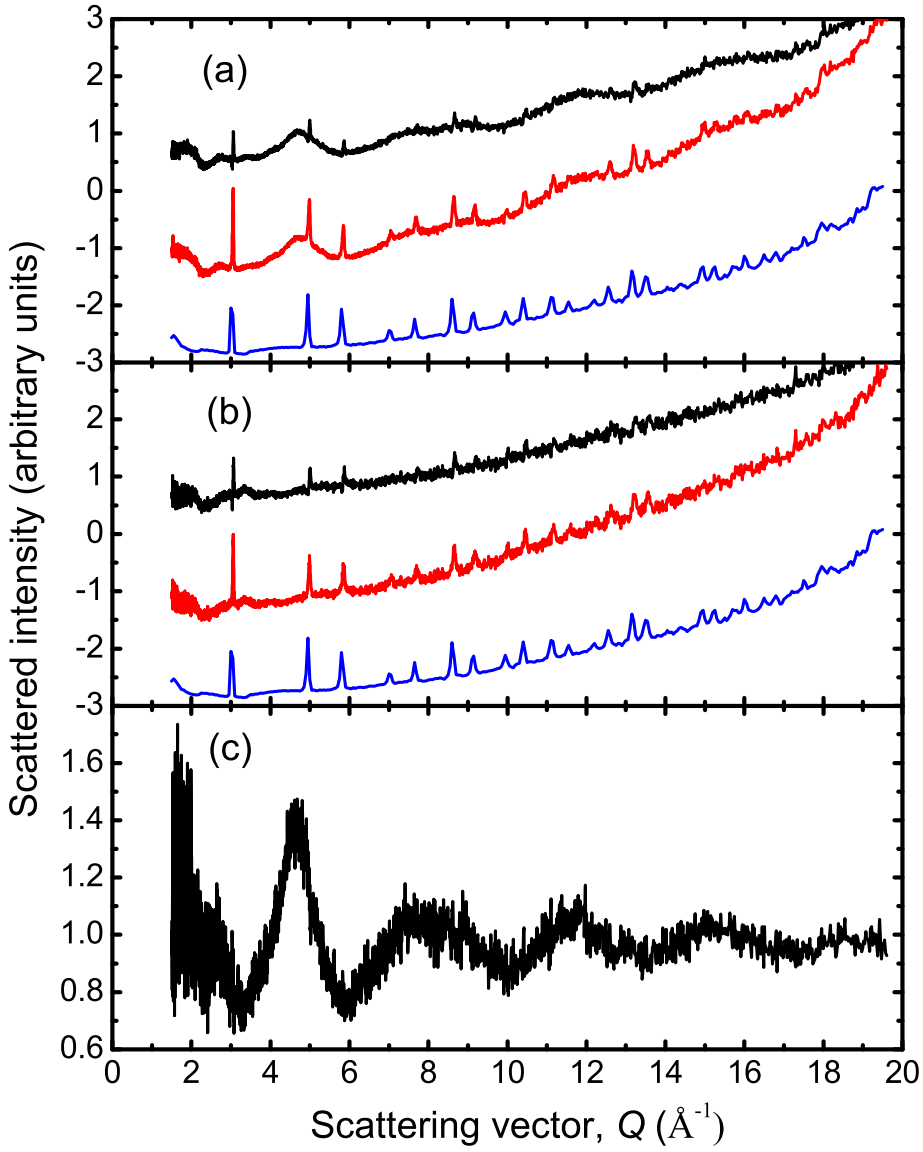

Figure 9.14: (a) The background corrected intensity $I'_{SC}(Q) = I^E_{SC}(Q) - 0.56I^E_C(Q)$ for GeO_2 glass at 5.0(5) GPa (black curve) compared with the measured intensities $I^E_{SC}(Q) - 2$ for the sample (red curve) and $I^E_C(Q) - 3$ for the empty Ti-Zr gasket (blue curve). (b) The background corrected intensity $I'_{VC}(Q) = I^E_{VC}(Q) - 0.45I^E_C(Q)$ for vanadium at 7.0(5) GPa (black curve) compared with the measured intensities $I^E_{VC}(Q) - 2$ for the vanadium (red curve) and $I^E_C(Q) - 3$ for the empty Ti-Zr gasket (blue curve). (c) The preliminary normalised data set $\left[I^E_{SC}(Q) - 0.56I^E_C(Q)\right] / \left[I^E_{VC}(Q) - 0.45I^E_C(Q)\right]$.

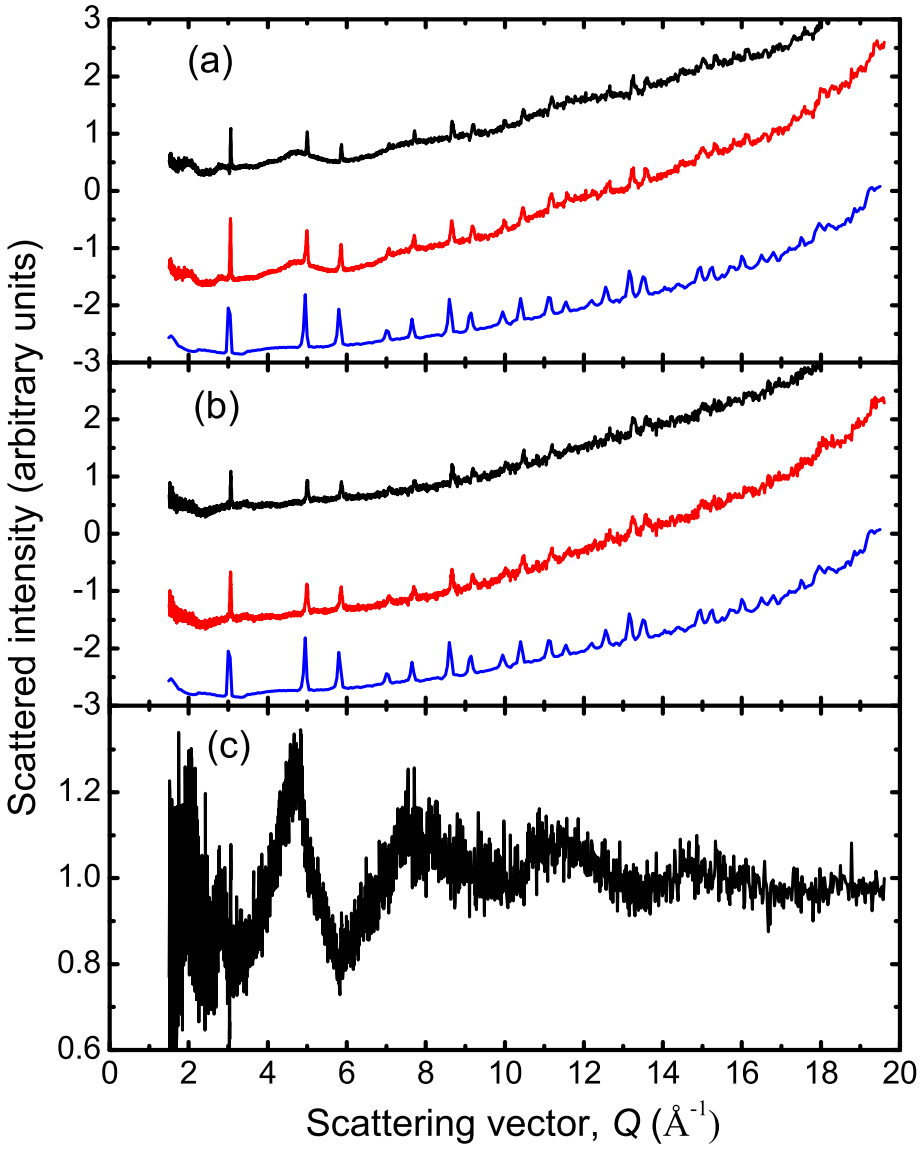

Figure 9.15: (a) The background corrected intensity $I'_{SC}(Q) = I^E_{SC}(Q) - 0.30I^E_C(Q)$ for GeO_2 glass at 9.0(5) GPa (black curve) compared with the measured intensities $I^E_{SC}(Q) - 2$ for the sample (red curve) and $I^E_C(Q) - 3$ for the empty Ti-Zr gasket (blue curve). (b) The background corrected intensity $I'_{VC}(Q) = I^E_{VC}(Q) - 0.20I^E_C(Q)$ for vanadium at 11.5(5) GPa (black curve) compared with the measured intensities $I^E_{VC}(Q) - 2$ for the vanadium (red curve) and $I^E_C(Q) - 3$ for the empty Ti-Zr gasket (blue curve). (c) The preliminary normalised data set $\left[I^E_{SC}(Q) - 0.30I^E_C(Q)\right] / \left[I^E_{VC}(Q) - 0.20I^E_C(Q)\right]$.

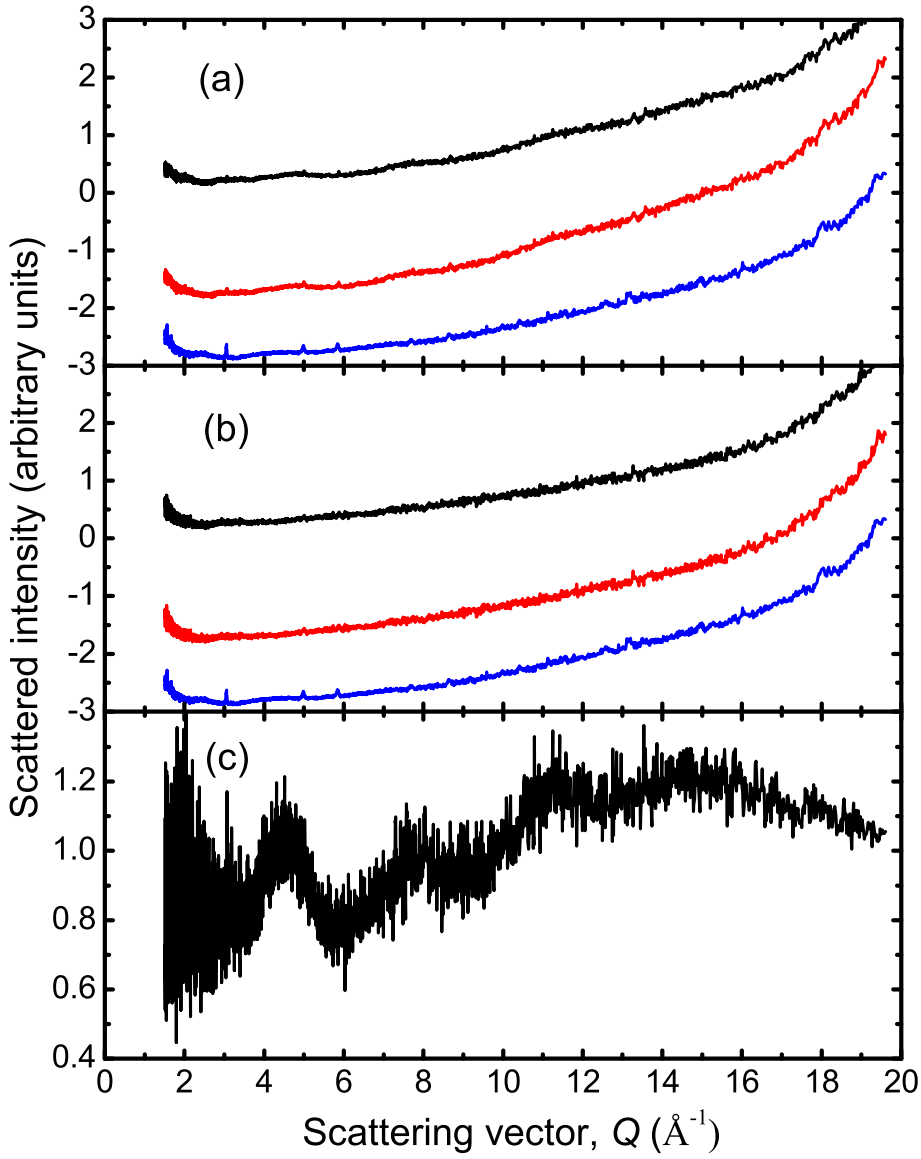

Figure 9.16: (a) The background corrected intensity $I'_{SC}(Q) = I^E_{SC}(Q) - 0.25I^E_C(Q)$ for GeO_2 glass at 11.5(5) GPa (black curve) compared with the measured intensities $I^E_{SC}(Q) - 2$ for the sample (red curve) and $I^E_C(Q) - 3$ for the empty Ti-Zr gasket (blue curve). (b) The background corrected intensity $I'_{VC}(Q) = I^E_{VC}(Q) - 0.15I^E_C(Q)$ for vanadium at 15.0(5) GPa (black curve) compared with the measured intensities $I^E_{VC}(Q) - 2$ for the vanadium (red curve) and $I^E_C(Q) - 3$ for the empty Ti-Zr gasket (blue curve). (c) The preliminary normalised data set $\left[I^E_{SC}(Q) - 0.25I^E_C(Q)\right] / \left[I^E_{VC}(Q) - 0.15I^E_C(Q)\right]$.

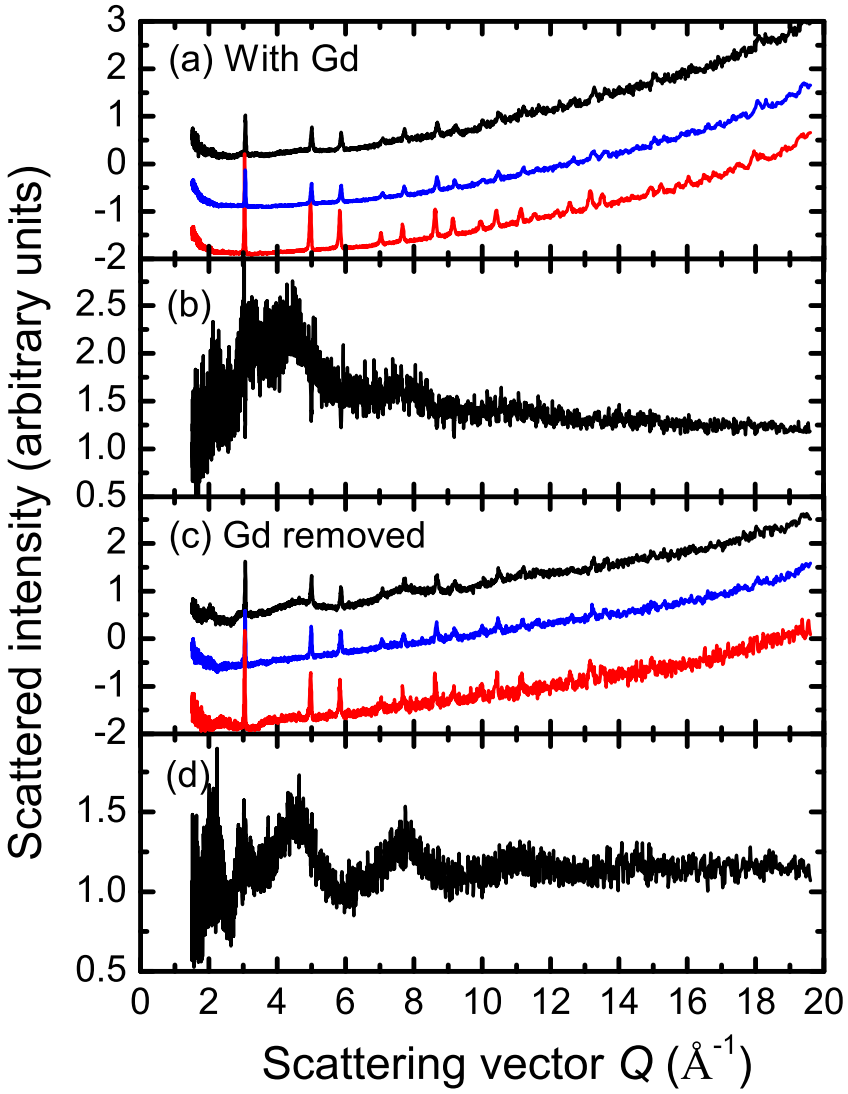

Figure 9.17: The double toroid anvil high pressure data sets. (a) The scattered intensities for GeO_2 glass at 14(1) GPa (black curve) with the corresponding vanadium (blue curve) and empty Ti-Zr gasket (red curve) data sets displaced by -1 and -2, respectively, with the Gd foils in place. (b) The normalised sample scattering from (a) using the method detailed in § 9.4. (c) The scattered intensities for GeO_2 glass at 14(1) GPa (black curve) with the corresponding vanadium (blue curve) and empty Ti-Zr gasket (red curve) data sets displaced by -1 and -2, respectively, with the Gd foils removed. (d) The normalised sample scattering from (c) using the method detailed in § 9.4.

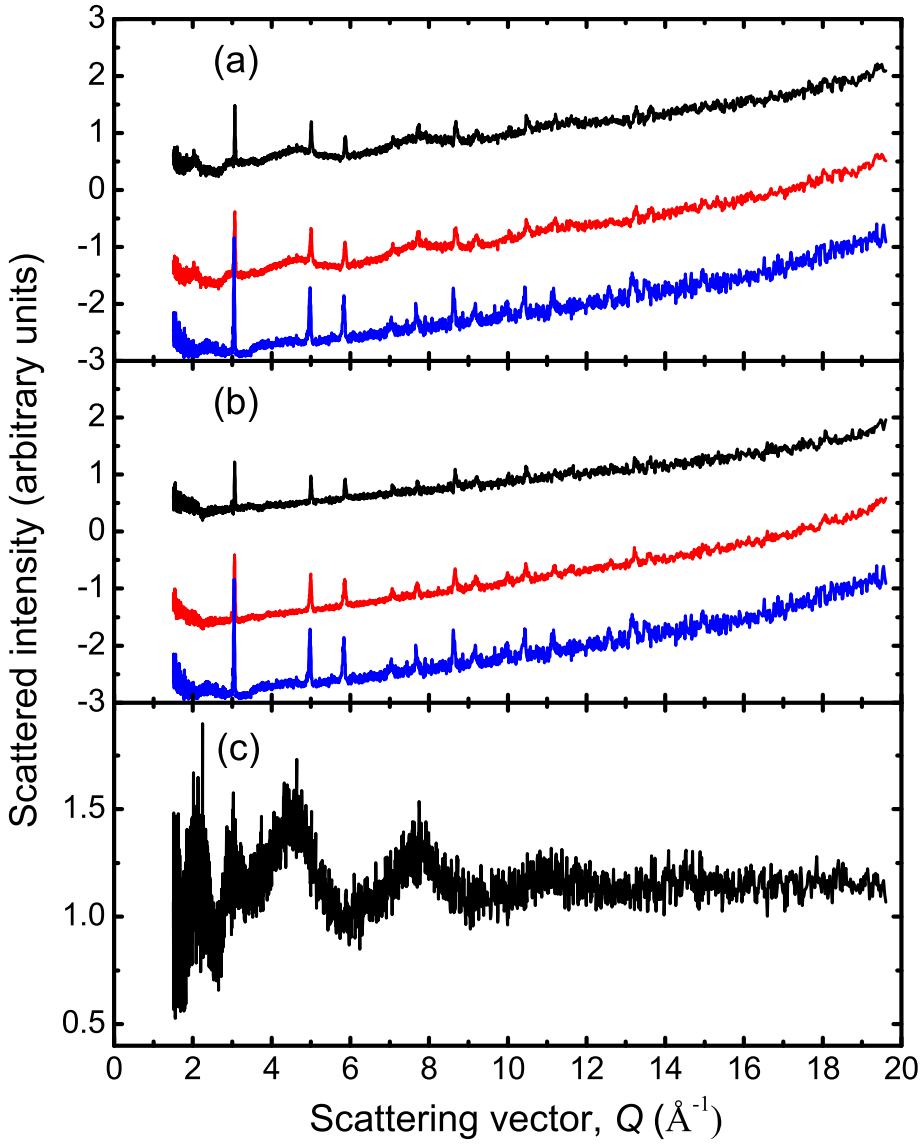

Figure 9.18: (a) The background corrected intensity $I'_{SC}(Q) = I^E_{SC}(Q) - 0.20I^E_C(Q)$ for GeO_2 glass at 14(1) GPa (black curve) compared with the measured intensities $I^E_{SC}(Q) - 2$ for the sample (red curve) and $I^E_C(Q) - 3$ for the empty Ti-Zr gasket (blue curve). (b) The background corrected intensity $I'_{VC}(Q) = I^E_{VC}(Q) - 0.30I^E_C(Q)$ for vanadium at 9.0(5) GPa (black curve) compared with the measured intensities $I^E_{VC}(Q) - 2$ for the vanadium (red curve) and $I^E_C(Q) - 3$ for the empty Ti-Zr gasket (blue curve). (c) The preliminary normalised data set $\left[I^E_{SC}(Q) - 0.20I^E_C(Q)\right] / \left[I^E_{VC}(Q) - 0.30I^E_C(Q)\right]$.

There is, however, an increase in the Bragg scattering from the diamond anvils although this effect is small due to the close proximity of the anvils to each other which increases the effectiveness of the Cd shielding in preventing scattering paths from the sintered diamond anvils to the detectors. This data set can be adequately corrected and normalised to the scattering from a vanadium pellet measured in the same set up (see figure 9.17 (d)). For completeness, the final background corrected intensities and the preliminary normalised data set for the double toroid anvil experiment are plotted in figure 9.18.

It is not easy to obtain the scaling factor W in equation 9.20. The reason for this is the limited accessible Q range of the PEARL instrument which leads to a truncation of the diffraction patterns at a relatively large minimum Q value of 1.55 Å^{-1}. Therefore, the Fourier transform of the reciprocal space data sets will be affected by the method used to extrapolate this data to low Q. Also, this is the same region of Q that is most sensitive to problems with the data normalisation. Several methods were therefore employed to extrapolate the data sets to low Q values, and their effectiveness was examined.

Method (i) involved setting the $F(Q)$ functions for $0 \leq Q \leq 1.55$ Å^{-1} to the $F(0)$ limiting value. This was obtained by making a linear fit to the low-Q region of the $F(Q)$ function for GeO_2 glass measured under ambient conditions in a conventional neutron diffraction experiment [305] (see figure 9.19) for which a value for $F(0) = -0.387$ barn is obtained. The $F(0)$ limit may also be estimated by adopting the Bhatia Thornton [243] formalism in which the total structure factor is defined by

$$F(Q) = \langle b \rangle^2 S_{NN}(Q) + (b_{\text{Ge}} - b_{\text{O}})^2 S_{CC}(Q) + 2\langle b \rangle (b_{\text{Ge}} - b_{\text{O}}) S_{NC}(Q) - (c_{\text{Ge}} b_{\text{Ge}}^2 + c_{\text{O}} b_{\text{O}}^2), \tag{9.23}$$

where $S_{NN}(Q)$, $S_{CC}(Q)$ and $S_{NC}(Q)$ denote the number-number, concentration-concentration and number-concentration partial structure factors, respectively. Assuming that GeO_2 is an ionic material, then $S_{CC}(0) = S_{NC}(0) = 0$ and $S_{NN}(0) = n_0 k_{\text{B}} T \chi_T$, where n_0 is the number density, k_B is the Boltzmann constant, T is the absolute temperature and $\chi_T = 0.042$ GPa^{-1} is the isother-

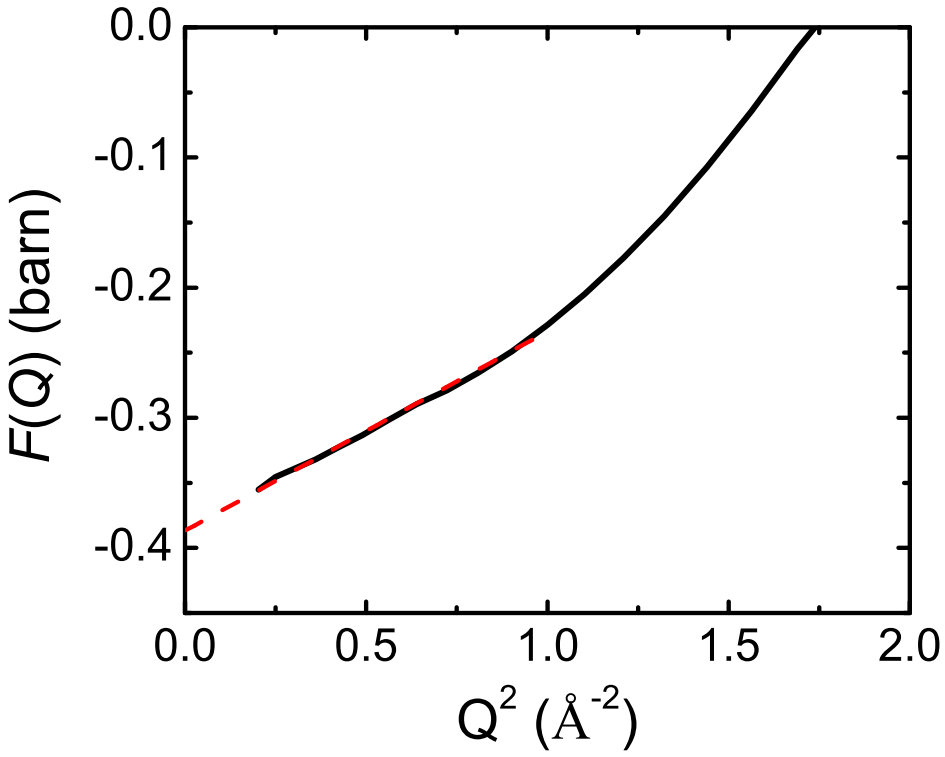

Figure 9.19: Linear fit to the $F(Q)$ function for GeO_2 glass at ambient pressure as measured by Salmon *et al.* [305]. The solid (black) curve shows the $F(Q)$ and the dashed (red) curve shows the linear fit at low-Q which gives $F(0) = -0.387$ barn.

mal compressibility at ambient pressure [295]. The theoretical $F(0)$ value is then calculated to be

$$F(0) = \langle b \rangle^2 n_0 k_B T \chi_T - \left(c_{Ge} b_{Ge}^2 + c_O b_O^2 \right) = -0.4478 \text{ barn}. \tag{9.24}$$

This value deviates from the experimental value but is comparable in magnitude. This discrepancy may be due to the ionic approximation, since GeO_2 is a covalent material, or could be due to experimental uncertainty in the low Q region of the measured $F(Q)$ function. The isothermal compressibility χ_T is

pressure dependent [295] but this makes no significant change to the theoretical value of $F(0)$ at the pressures obtained in the present study.

Method (ii) involved taking the data for $0 \leq Q \leq 1.55$ Å^{-1} from the $F(Q)$ function for GeO_2 glass measured under ambient conditions in a conventional neutron diffraction experiment [305] after scaling this data such that the First Sharp Diffraction Peak (FSDP) fits the visible part of the FSDP in a PEARL data set.

Method (iii) used the data for $0 \leq Q \leq 1.55$ Å^{-1} from the $F(Q)$ functions measured at comparable pressures using the D4C instrument, as given in chapter 8, after scaling this data such that the First Sharp Diffraction Peak (FSDP) fits the visible part of the FSDP in a PEARL data set.

The final method (iv) involved simply setting the $F(Q)$ functions to zero for Q values up to $0 \leq Q \leq 1.55$ Å^{-1}.

The total structure factors $F(Q)$ for GeO_2 glass at the various pressures, each normalised by applying the four distinct low-Q extrapolation methods, are plotted in figures 9.20 to 9.24. The nearest neighbour region of the corresponding total pair distribution functions $G(r)$, obtained by Fourier transforming the $F(Q)$ functions after making a Harwell spline fit [115], are also plotted together with the running coordination number. It is clear that setting the low-Q data to zero leads to a severe over-scaling of $F(Q)$ in order to ensure agreement between $F(Q)$ and the Fourier backtransform. Method (i) was eventually adopted to produce the final data sets, i.e. the low-Q data points were set equal to the $F(0) = -0.387$ barn limit as extrapolated from the published ambient pressure $F(Q)$ [305], since the coordination number $\bar{n}^{\mathrm{O}}_{\mathrm{Ge}}$ obtained is in better agreement with the measurements of chapter 8. However, it is noted that the other methods (ii) and (iii) give results that are within the experimental error of the data obtained using method (i) and are thus equally valid methods of extrapolating the low-Q data.

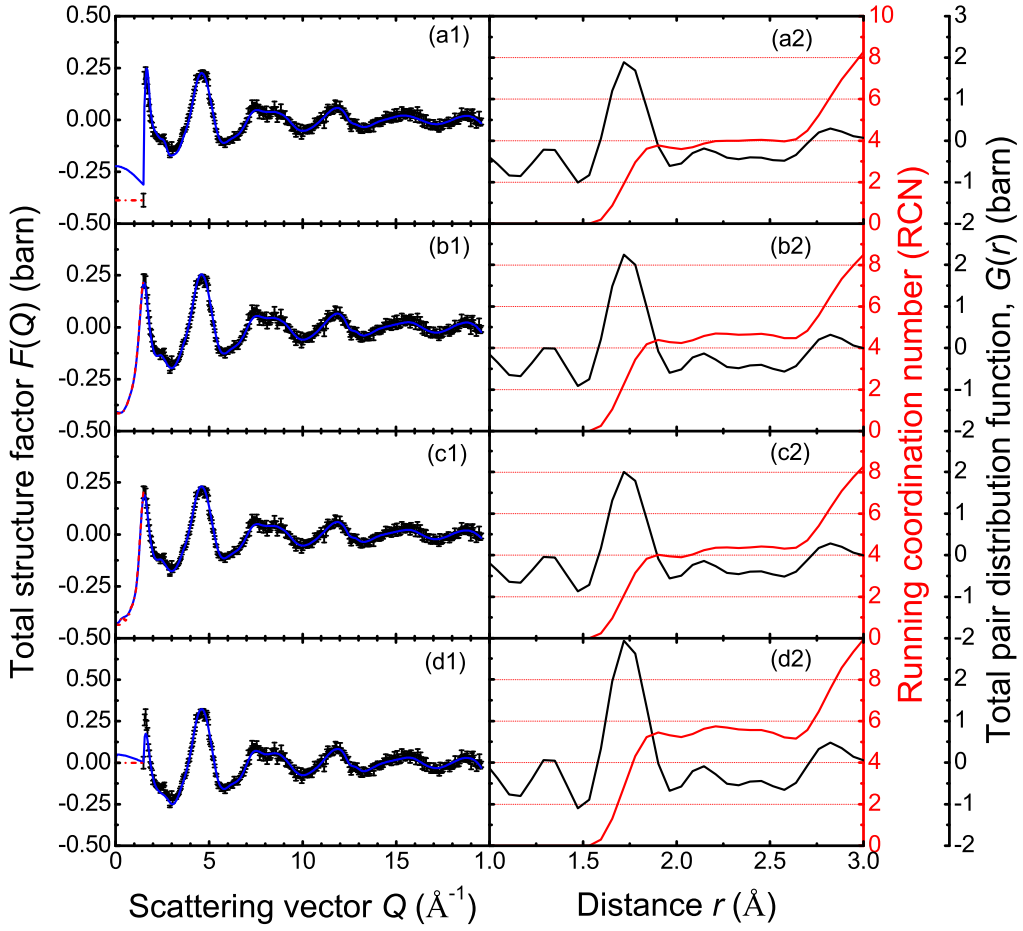

Figure 9.20: The total structure factor $F(Q)$, total pair distribution function $G(r)$ and running coordination number for GeO_2 glass at ambient pressure obtained using various methods of low-Q extrapolation. The extrapolated data at low-Q is shown by the chained (red) curve where the functions in (a1) and (a2) have been obtained using method (i), the functions in (b1) and (b2) have been obtained using method (ii), the functions in (c1) and (c2) have been obtained using method (iii) and the functions in (d1) and (d2) have been obtained using method (iv). The bars in (a1) to (d1) represent the statistical errors and the solid (blue) curves are the Fourier back-transforms of the corresponding $G(r)$ functions in (a2) to (d2) after the un-physical low-r oscillations are set to the theoretical $G(0)$ limit. The solid black curve in (a2) to (d2) shows the first peak in the $G(r)$ functions obtained by Fourier transforming the corresponding $F(Q)$ functions in (a1) to (d1) after making a Harwell spline fit [115] to the data. The solid (red) curves show the running coordination number over the region of the first peak in $G(r)$.

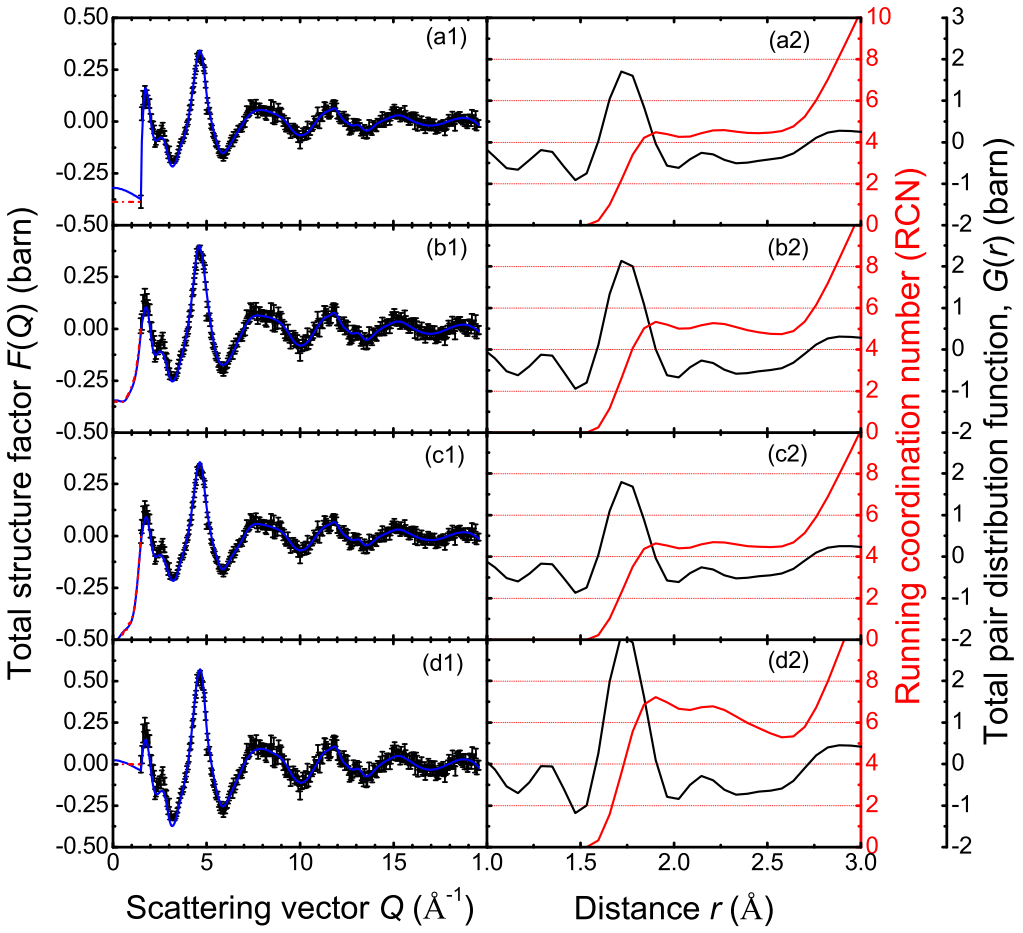

Figure 9.21: The total structure factor $F(Q)$, total pair distribution function $G(r)$ and running coordination number for GeO_2 glass at 5.0(5) GPa obtained using various methods of low-Q extrapolation. The extrapolated data at low-Q is shown by the chained (red) curve where the functions in (a1) and (a2) have been obtained using method (i), the functions in (b1) and (b2) have been obtained using method (ii), the functions in (c1) and (c2) have been obtained using method (iii) and the functions in (d1) and (d2) have been obtained using method (iv). The bars in (a1) to (d1) represent the statistical errors and the solid (blue) curves are the Fourier back-transforms of the corresponding $G(r)$ functions in (a2) to (d2) after the un-physical low-r oscillations are set to the theoretical $G(0)$ limit. The solid black curve in (a2) to (d2) shows the first peak in the $G(r)$ functions obtained by Fourier transforming the corresponding $F(Q)$ functions in (a1) to (d1) after making a Harwell spline fit [115] to the data. The solid (red) curves show the running coordination number over the region of the first peak in $G(r)$.

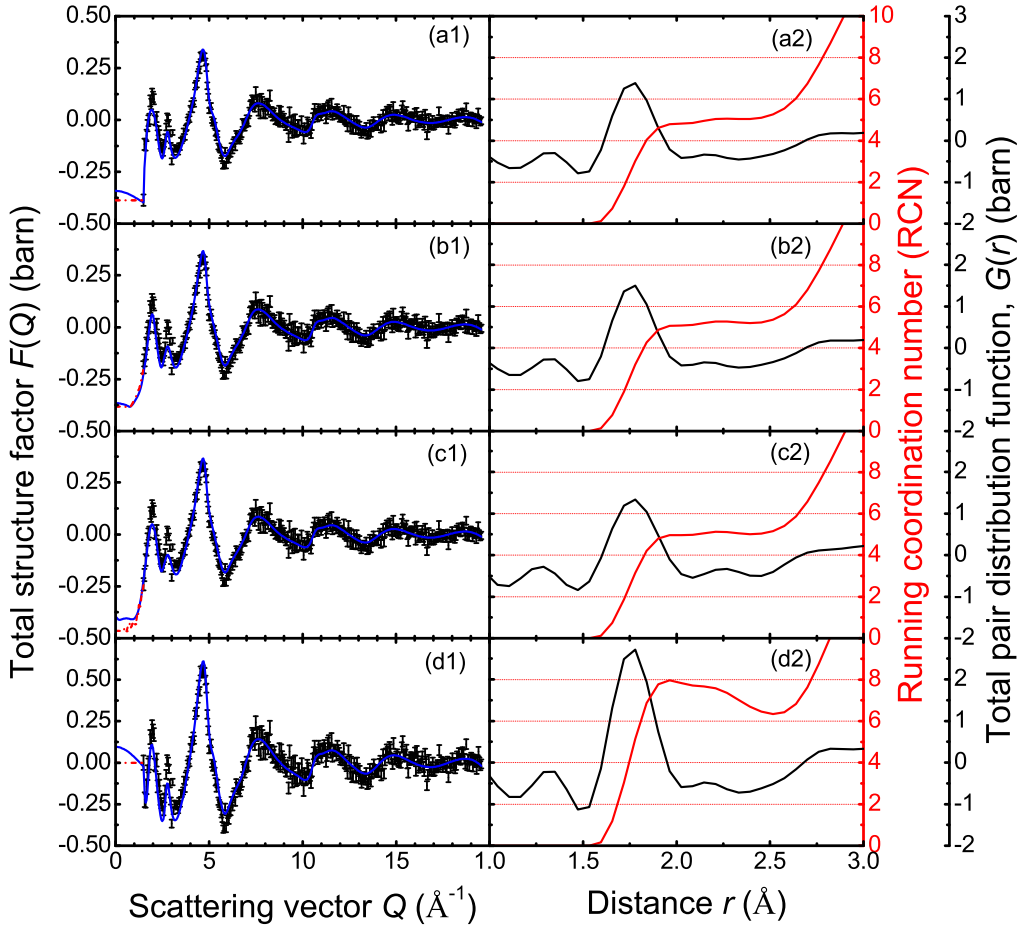

Figure 9.22: The total structure factor $F(Q)$, total pair distribution function $G(r)$ and running coordination number for GeO_2 glass at 9.0(5) GPa obtained using various methods of low-Q extrapolation. The extrapolated data at low-Q is shown by the chained (red) curve where the functions in (a1) and (a2) have been obtained using method (i), the functions in (b1) and (b2) have been obtained using method (ii), the functions in (c1) and (c2) have been obtained using method (iii) and the functions in (d1) and (d2) have been obtained using method (iv). The bars in (a1) to (d1) represent the statistical errors and the solid (blue) curves are the Fourier back-transforms of the corresponding $G(r)$ functions in (a2) to (d2) after the un-physical low-r oscillations are set to the theoretical $G(0)$ limit. The solid black curve in (a2) to (d2) shows the first peak in the $G(r)$ functions obtained by Fourier transforming the corresponding $F(Q)$ functions in (a1) to (d1) after making a Harwell spline fit [115] to the data. The solid (red) curves show the running coordination number over the region of the first peak in $G(r)$.

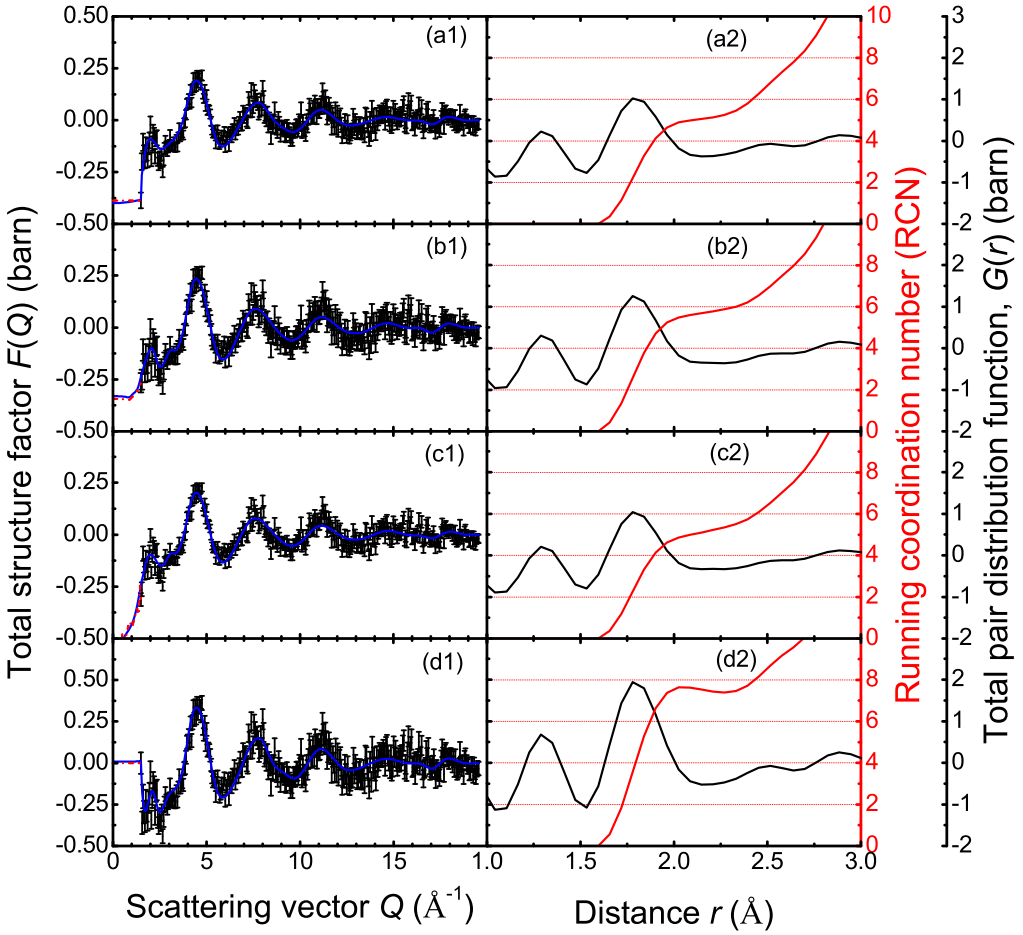

Figure 9.23: The total structure factor $F(Q)$, total pair distribution function $G(r)$ and running coordination number for GeO_2 glass at 11.5(5) GPa obtained using various methods of low-Q extrapolation. The extrapolated data at low-Q is shown by the chained (red) curve where the functions in (a1) and (a2) have been obtained using method (i), the functions in (b1) and (b2) have been obtained using method (ii), the functions in (c1) and (c2) have been obtained using method (iii) and the functions in (d1) and (d2) have been obtained using method (iv). The bars in (a1) to (d1) represent the statistical errors and the solid (blue) curves are the Fourier back-transforms of the corresponding $G(r)$ functions in (a2) to (d2) after the un-physical low-r oscillations are set to the theoretical $G(0)$ limit. The solid black curve in (a2) to (d2) shows the first peak in the $G(r)$ functions obtained by Fourier transforming the corresponding $F(Q)$ functions in (a1) to (d1) after making a Harwell spline fit [115] to the data. The solid (red) curves show the running coordination number over the region of the first peak in $G(r)$.

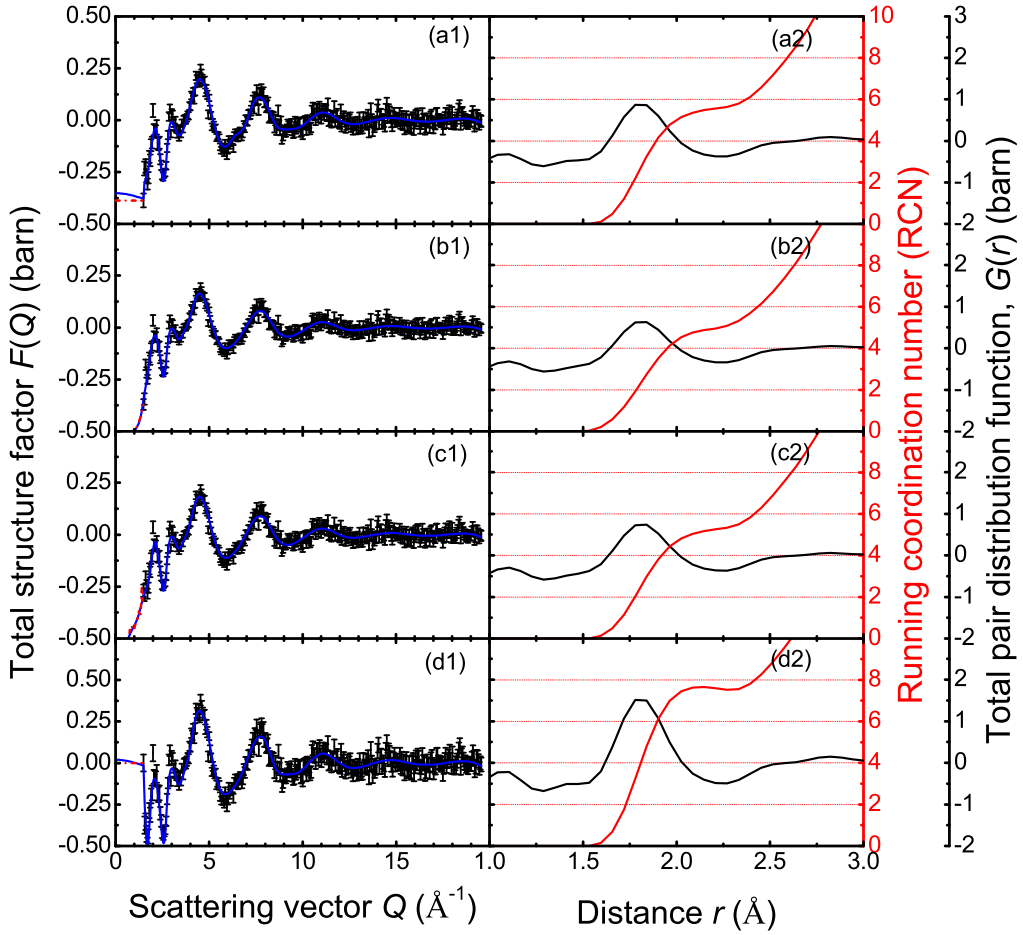

Figure 9.24: The total structure factor $F(Q)$, total pair distribution function $G(r)$ and running coordination number for GeO_2 glass at 14(1) GPa obtained using various methods of low-Q extrapolation. The extrapolated data at low-Q is shown by the chained (red) curve where the functions in (a1) and (a2) have been obtained using method (i), the functions in (b1) and (b2) have been obtained using method (ii), the functions in (c1) and (c2) have been obtained using method (iii) and the functions in (d1) and (d2) have been obtained using method (iv). The bars in (a1) to (d1) represent the statistical errors and the solid (blue) curves are the Fourier back-transforms of the corresponding $G(r)$ functions in (a2) to (d2) after the un-physical low-r oscillations are set to the theoretical $G(0)$ limit. The solid black curve in (a2) to (d2) shows the first peak in the $G(r)$ functions obtained by Fourier transforming the corresponding $F(Q)$ functions in (a1) to (d1) after making a Harwell spline fit [115] to the data. The solid (red) curves show the running coordination number over the region of the first peak in $G(r)$.

9.5 Results

Table 9.3: The leading peak positions q_1, q_2 and q_3 in the measured $F(Q)$ for GeO_2 glass at pressure P, together with the leading peak positions r_1, r_2, r_3 and coordination number $\bar{n}^{O}_{Ge}$ for the corresponding $G(r)$ functions.

	$F(Q)$				$G(r)$		
P (GPa)	q_1 (Å^{-1})	q_2 (Å^{-1})	q_3 (Å^{-1})	$\bar{n}^{O}_{Ge}$	r_1 (Å)	r_2 (Å)	r_3 (Å)
0	1.59(5)	2.58(5)	4.64(5)	3.8(1)	1.73(2)	2.83(3)	4.40(5)
5.0(5)	1.81(5)	2.64(5)	4.52(5)	4.4(1)	1.74(2)	2.90(3)	4.14(5)
9.0(5)	1.99(5)	2.77(5)	4.67(5)	4.9(1)	1.76(2)	2.89(3)	4.17(5)
11.5(5)	2.05(5)	2.80(5)	4.52(5)	4.9(1)	1.80(2)	2.94(3)	–
14.0(1)	2.10(5)	2.89(5)	4.52(5)	5.5(1)	1.81(2)	2.82(3)	4.20(5)

The final total structure factors $F(Q)$ for GeO_2 glass at the various pressures are plotted in figure 9.25. The ambient pressure $F(Q)$ function is in good overall agreement with the $F(Q)$ for glassy $^{nat}GeO_2$ measured in a conventional neutron diffraction set-up at ambient pressure [305] also plotted in figure 9.25 (a). However, the first sharp diffraction peak (FSDP) at 1.59(5) Å^{-1} is truncated at the minimum scattering vector Q_{min} = 1.55 Å^{-1} accessible in the PEARL diffraction experiments. The total pair distribution functions, $G(r)$, obtained by Fourier transforming the corresponding $F(Q)$ functions with Q_{max} = 19.55 Å^{-1} after making a Harwell spline fit [115] to the data, are plotted in figure 9.26. The positions of the leading peaks in the $F(Q)$ and $G(r)$ functions are listed in table 9.3 together with the coordination number $\bar{n}^{O}_{Ge}$.

Figure 9.27 shows a comparison of the measured $F(Q)$ functions at ambient pressure, 5.0(5) GPa and 9.0(5) GPa with the $F(Q)$ functions measured using a Paris-Edinburgh press mounted on the D4C instrument, as presented in § 8.5, at ambient pressure, 4.9(5) GPa and 8.0(5) GPa. The ambient pressure $F(Q)$ functions obtained from the two separate instruments are in good overall agreement and show the same trends with pressure in peak position and relative height. However, the partially visible FSDP at 1.59(5) Å^{-1} from the measurements obtained using PEARL is significantly higher than the FSDP in the $F(Q)$ measured on D4C. For pulsed neutron source experiments, inelasticity ef-

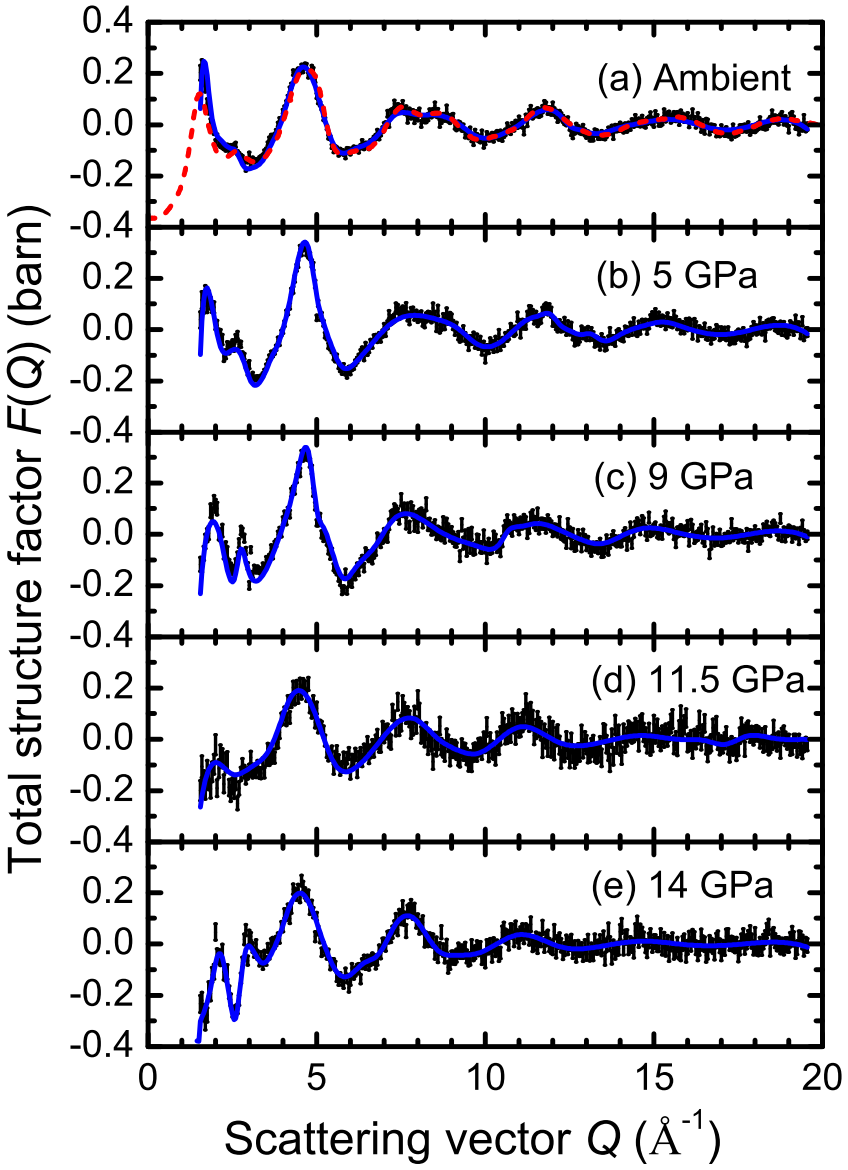

Figure 9.25: Total structure factors $F(Q)$ for GeO_2 glass at (a) ambient pressure, (b) 5.0(5) GPa, (c) 9.0(5) GPa, (d) 11.5(5) GPa, and (e) 14.0(1) GPa. The bars represent the statistical errors and the solid (blue) curves are the Fourier back-transform of the corresponding $G(r)$ functions given in figure 9.26 after the un-physical low-r oscillations are set to their theoretical $G(0)$ limit. The dashed (red) curve in (a) shows the $F(Q)$ function measured for $^{nat}GeO_2$ in a conventional neutron diffraction set-up at ambient pressure [305].

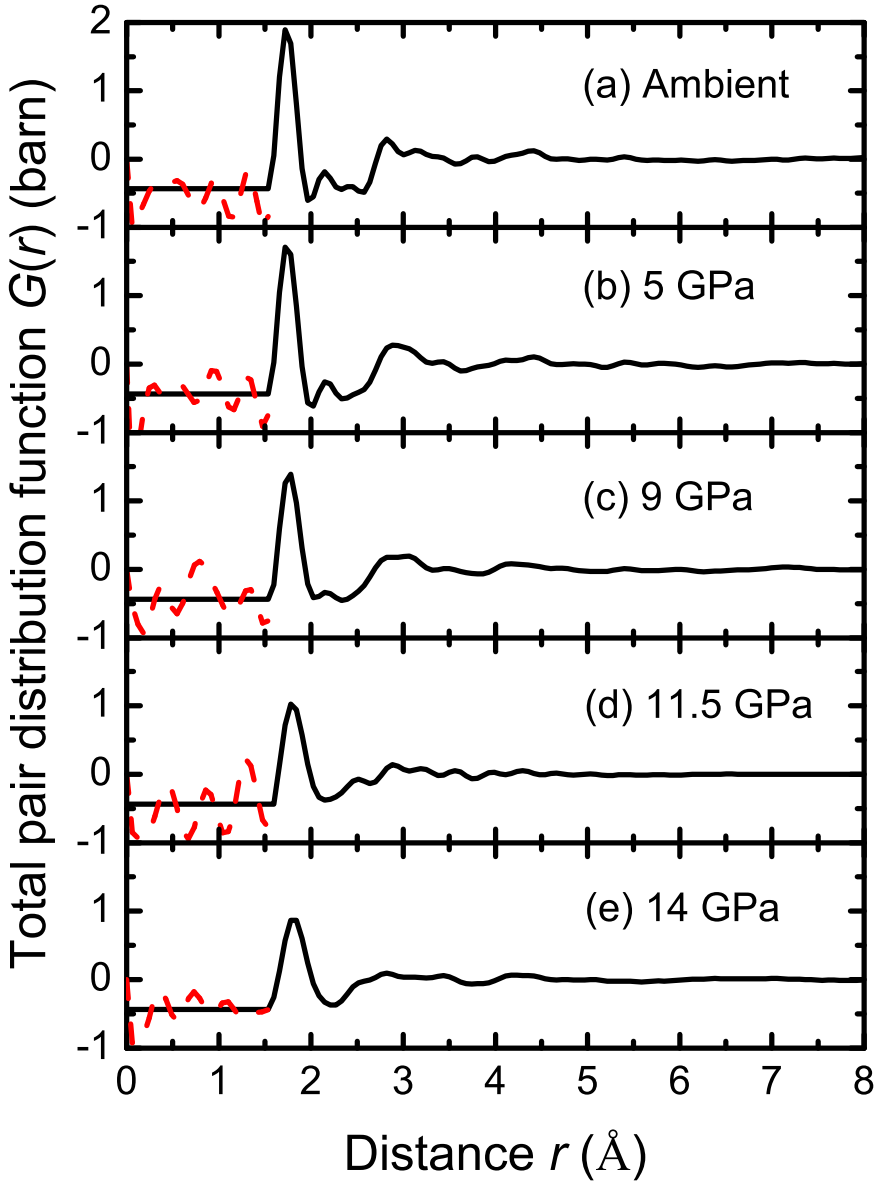

Figure 9.26: Total pair distribution functions $G(r)$ for GeO_2 glass at (a) ambient pressure, (b) 5.0(5) GPa, (c) 9.0(5) GPa, (d) 11.5(5) GPa, (e) 14.0(5) GPa as obtained by Fourier transforming the corresponding $F(Q)$ functions shown in figure 9.25 after making a Harwell spline fit [115] to the data with $Q_{\max} = 19.55$ Å^{-1}. The dashed (red) curves indicate the extent of the un-physical low-r oscillations.

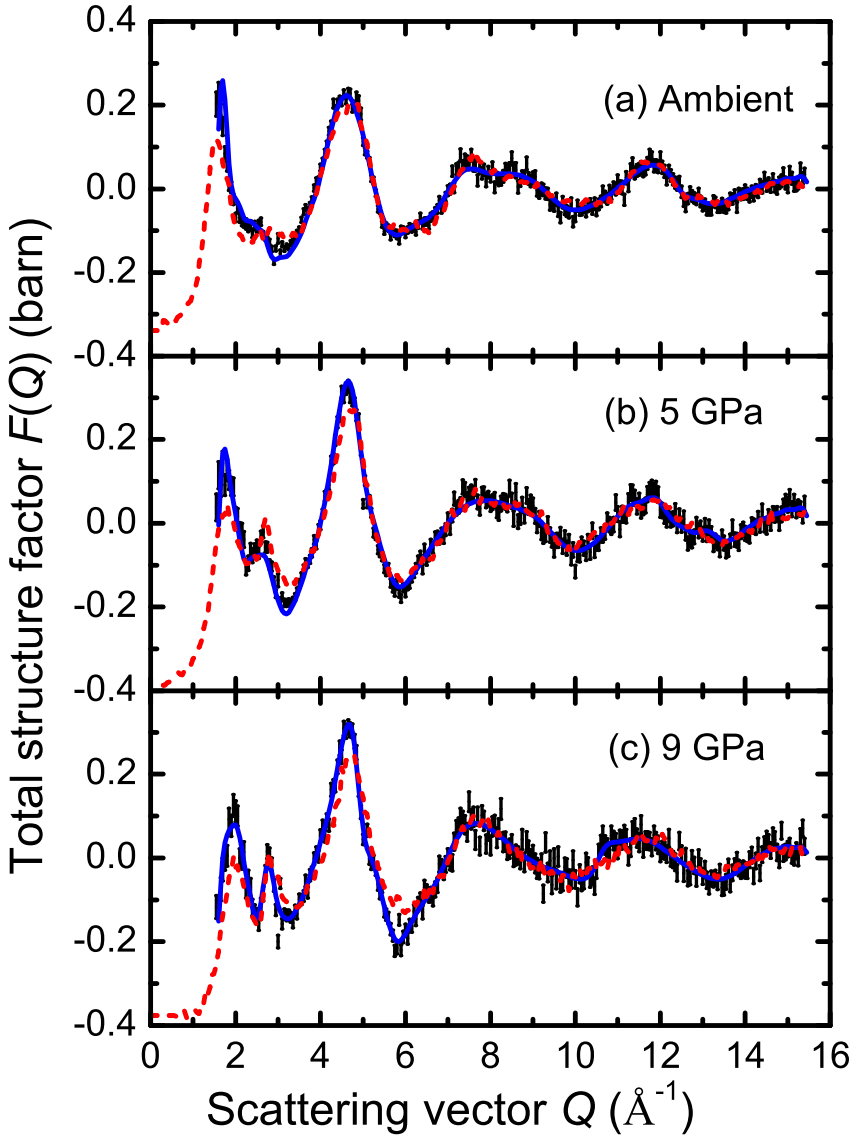

Figure 9.27: Total structure factors $F(Q)$ for GeO_2 glass at (a) ambient pressure, (b) 5.0(5) GPa and (c) 9.0(5) GPa. The bars represent the statistical errors and the solid (blue) curves are the Fourier back transforms of the corresponding $G(r)$ functions given in figure 9.31 after the un-physical low-r oscillations are set to their theoretical $G(0)$ limit. The dashed (red) curves show the $F(Q)$ functions at (a) ambient pressure, (b) 4.9(5) GPa and (c) 8.0(5) GPa as measured in a Paris-Edinburgh cell mounted on the D4C instrument and presented in § 8.5.

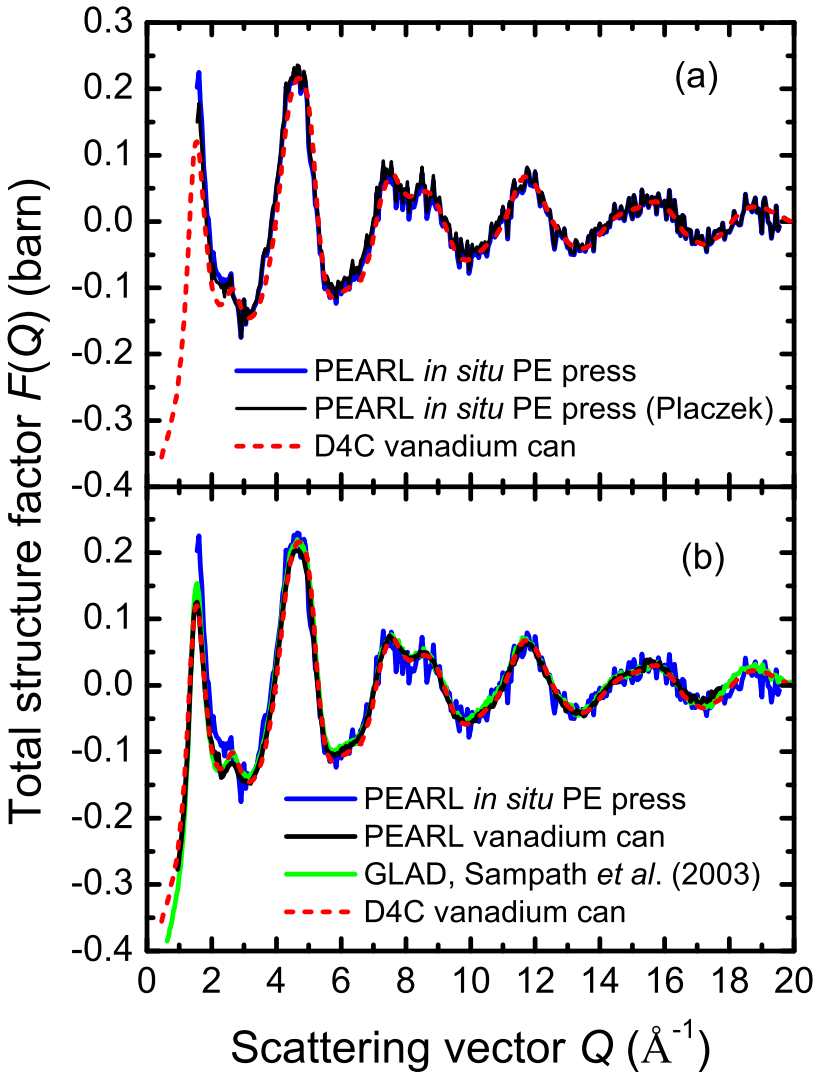

Figure 9.28: (a) The $F(Q)$ function for GeO_2 glass at ambient pressure taken *in situ* in the Paris-Edinburgh (PE) press on the PEARL instrument (solid blue curve) together with the same $F(Q)$ but with the Placzek [31] (inelasticity) correction applied (solid black curve) and the $F(Q)$ function measured on the D4C instrument [305]. (b) The total structure factor $F(Q)$ for GeO_2 glass at ambient pressure taken *in situ* in the Paris-Edinburgh (PE) press on the PEARL instrument (solid blue curve) together with the $F(Q)$ functions taken in a vanadium can at ambient pressure on the GLAD instrument [286] (green curve), on the PEARL instrument (solid black curve) and on the D4C instrument [305] (dashed red curve).

fects are most significant in the low-Q region which suggests that the increased intensity is the result of not applying the Placzek [31] (inelasticity) correction on the PEARL data sets. However, as shown in figure 9.28 (a), application of the Placzek [31] correction plotted in figure 9.11 has only a small effect on the height of the FSDP. A conventional ambient pressure diffraction pattern was therefore taken on the PEARL instrument for GeO_2 glass in a vanadium container using the lower scattering angle detector banks at $20 \leq 2\theta\ (^\circ) \leq 60$ in addition to the 90° bank used for the *in situ* measurements. The diffraction pattern was corrected for scattering from the vanadium can and normalised to the scattered intensity of a vanadium sphere but no corrections were made to account for attenuation, multiple scattering or inelasticity effects. As shown in figure 9.28 (b), the $F(Q)$ function is in good agreement with the $F(Q)$ measured using the D4C instrument. However the height of the FSDP in the $F(Q)$ for GeO_2 glass measured by Sampath *et al.* [286] on the GLAD instrument is slightly higher than for D4C. The differences can be mainly attributed to the instruments having a different resolution function, which can have a significant effect on sharp peaks at low Q values [321]. The resolution function for the 90° detector bank at PEARL has a value of $\Delta Q/Q \simeq 0.85$ %. This is significantly better than the resolution function of the D4C instrument in the vicinity of the FSDP at 1.5 Å^{-1} where $\Delta Q/Q = 3$ % for incident neutrons of wavelength 0.7 Å. The resolution function $\Delta Q/Q \simeq 1.5$ % for the lower scattering angle detector banks on PEARL, which helps to explain the agreement between the measurements obtained by the conventional diffraction experiments using both PEARL and D4C. For GLAD, the resolution function is equal to $\Delta Q/Q = 1.7$ % at $Q = 1.5$ Å^{-1} [322].

The changes in peak position and height of the FSDP are plotted in figure 9.29 together with the changes observed in the previous x-ray diffraction measurements by Guthrie *et al.* [285] and the neutron diffraction measurements presented in chapter 8. The same general trends are apparent i.e. there is a dramatic reduction in height of the FSDP with increasing pressure and a corresponding shift to higher Q values. These changes are accompanied by an

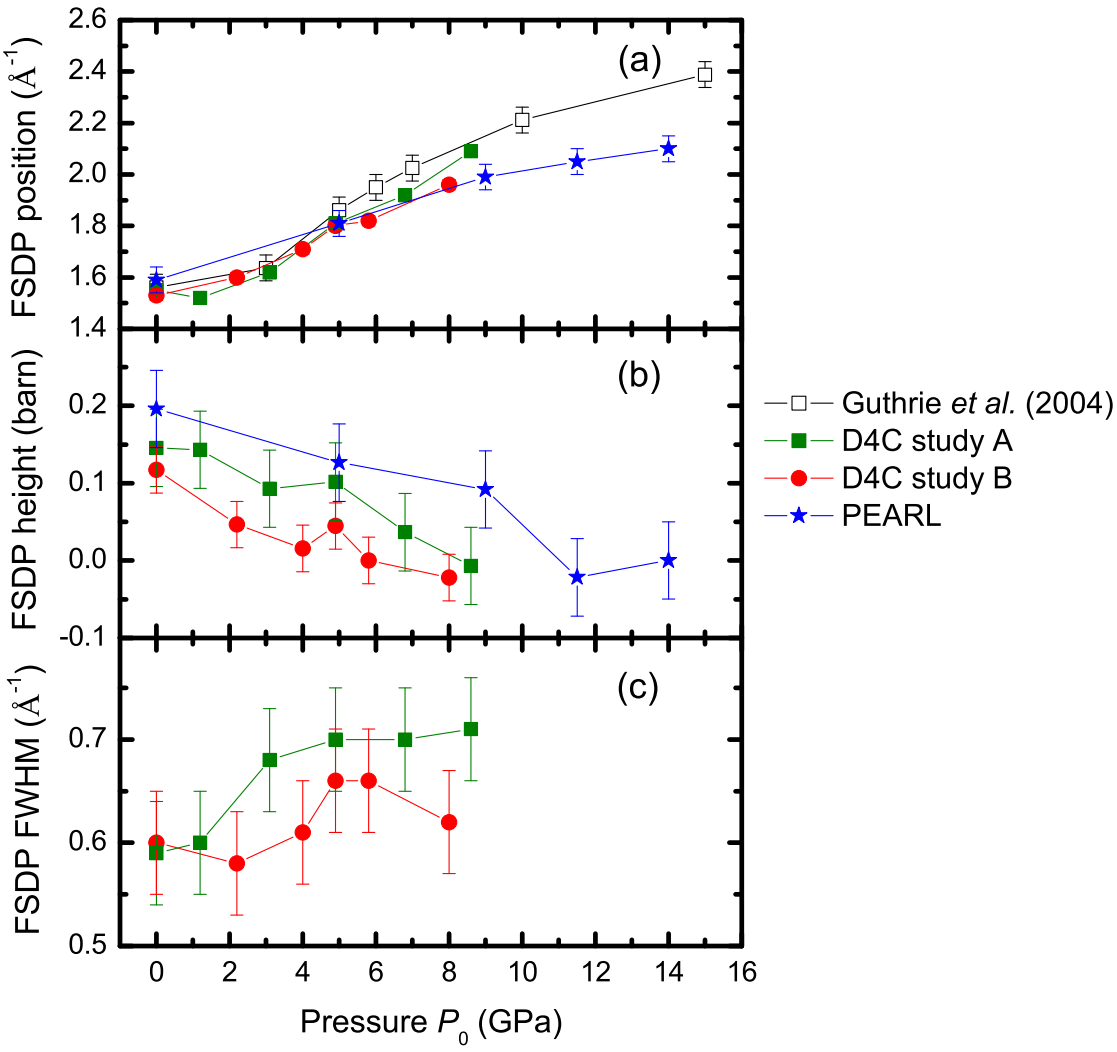

Figure 9.29: (a) Position of the First Sharp Diffraction Peak (FSDP) as a function of pressure as measured by Guthrie *et al.* [285] using x-ray diffraction (open squares), from the present study using the PEARL instrument (blue stars) and from the results presented in chapter 8 using the D4C instrument from study A (solid green squares) and study B (solid red circles). (b) Height of the FSDP, taken to be the value of $F(Q)$ at the FSDP position, from the present study using the PEARL instrument (blue stars) and from the results presented in chapter 8 using the D4C instrument from study A (solid green squares) and study B (solid red circles). (c) The full width at half maximum (FWHM) of the FSDP taken from the results presented in chapter 8 using the D4C instrument from study A (solid green squares) and study B (solid red circles).

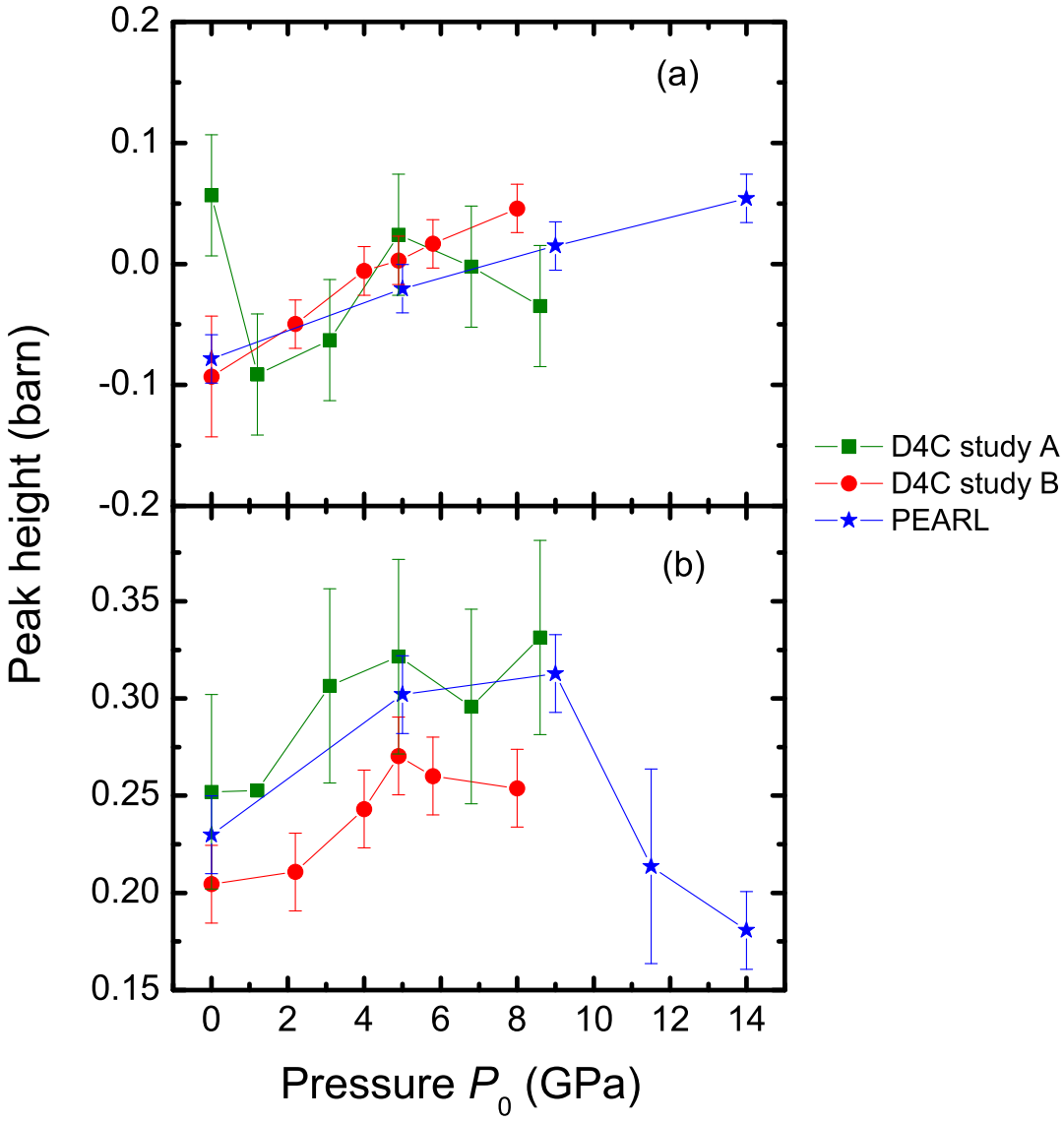

Figure 9.30: Height plotted as a function of pressure for (a) the principal peak and (b) the third peak in the reciprocal space functions, taken to be the value of $F(Q)$ at the peak position, from the present study using the PEARL instrument (blue stars) and from the results presented in chapter 8 using the D4C instrument from study A (solid green squares) and study B (solid red circles).

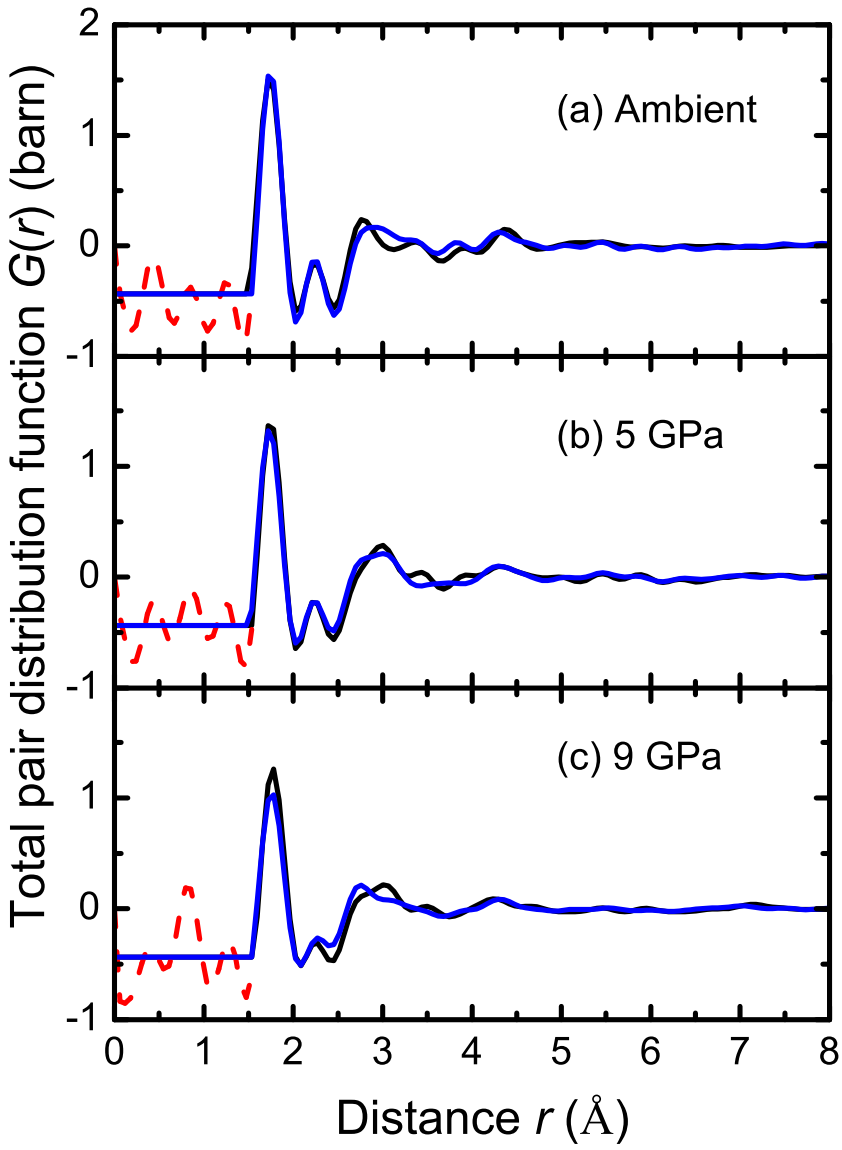

Figure 9.31: Total pair distribution functions $G(r)$ for GeO_2 glass shown by the blue curves at (a) ambient pressure, (b) 5.0(5) GPa and (c) 9.0(5) GPa as obtained by Fourier transforming the corresponding $F(Q)$ functions in figure 9.27 after making a Harwell spline fit [115] to the data and truncating at $Q_{\max} = 15.45$ Å^{-1}. The dashed (red) curve indicates the extent of the un-physical low-r oscillations. The black curves show the $G(r)$ function at (a) ambient pressure, (b) 4.9(5) GPa and (c) 8.0(5) GPa as measured in a Paris-Edinburgh cell mounted on the D4C instrument and presented in § 8.5.

increase in height of the principal and third peaks (see figure 9.30). The measurements from the PEARL instrument show that beyond 9 GPa the height of the third peak subsequently reduces such that at 14(1) GPa the height is smaller than the value at ambient pressure. The periodicity of the intermediate range ordering in real space is given by $2\pi/q_1$, where q_1 is the position of the FSDP. The coherence length, which estimates the distance in real space over which the intermediate range ordering persists, is given by $2\pi/\Delta q_1$, where Δq_1 is the full width at half maximum of the FSDP [116]. The FWHM of the FSDP could not be obtained from the PEARL measurements as the FSDP is truncated below 1.55 Å^{-1}. However, the FWHM of the FSDP obtained from the neutron diffraction measurements presented in chapter 8 are plotted in figure 9.29 (c) and suggest a general reduction in the coherence length with increasing pressure.

The $G(r)$ functions plotted in figure 9.31 were obtained by Fourier transforming the $F(Q)$ functions in figure 9.27 at ambient pressure, 5.0(5) GPa and 9.0(5) GPa, after making a Harwell spline fit [115] to the data and truncating at the same $Q_{\max} = 15.45$ Å^{-1} as the D4C results. The $G(r)$ functions obtained by PEARL are in good overall agreement with the D4C data sets presented in § 8.5 at ambient pressure, 4.9(5) GPa, and 8.0(5) GPa. However, the larger $Q_{\max} = 19.55$ Å^{-1} obtained using PEARL leads to greater resolution in real space, as evident by comparing the $G(r)$ functions plotted in figure 9.26 with the corresponding $G(r)$ functions plotted in figure 9.31 where the nearest neighbour peak is much sharper in the $G(r)$ functions obtained after truncating at the higher $Q_{\max}$. The first peak at $r_1 = 1.73(2)$ Å at ambient pressure is attributed to the nearest neighbour Ge-O correlations and yields a coordination number $\bar{n}^{\text{O}}_{\text{Ge}} = 3.8(1)$. The nearest neighbour peak position r_{GeO} and coordination number $\bar{n}^{\text{O}}_{\text{Ge}}$ obtained using the PEARL instrument are plotted as a function of pressure in figure 9.32 together with the measurements from studies A and B presented in the chapter 8, the previous x-ray diffraction measurements by Guthrie *et al.* [285], the XAS results of Itie *et al.* [282] and the recent EXAFS measurements by Vaccari *et al.* [323]. The

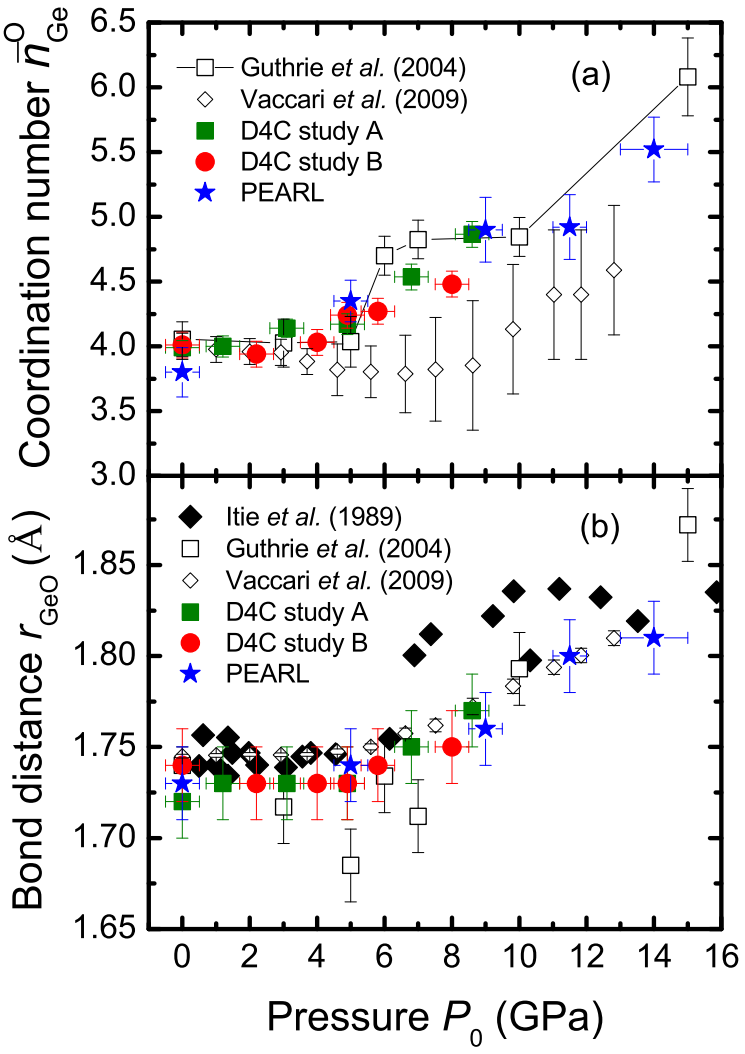

Figure 9.32: (a) Coordination number $\bar{n}^{O}_{Ge}$ as a function of pressure for GeO_2 glass taken from the present study (blue stars), study A from chapter 8 (solid green squares), study B from chapter 8 (solid red circles), previous x-ray diffraction measurements by Guthrie *et al.* [285] (open squares) and EXAFS measurements by Vaccari *et al.* [323] (open diamonds). (b) Nearest neighbour peak position r_{GeO} as a function of pressure for GeO_2 glass taken from the present study (blue stars), study A from chapter 8 (solid green squares), study B from chapter 8 (solid red circles), previous x-ray diffraction measurements by Guthrie *et al.* [285] (open squares), XAFS measurements by Itie *et al.* [282] (closed diamonds) and EXAFS measurements by Vaccari *et al.* [323] (open diamonds).

Ge-O peak position for the PEARL measurements increases to 1.81(2) Å at 14(1) GPa and there is a corresponding increase in the coordination number $\bar{n}^{\mathrm{O}}_{\mathrm{Ge}}$ to 5.5(1). The second peak at $r_2 = 2.83(3)$ Å in the ambient pressure $G(r)$ function is attributed to the nearest neighbour O-O correlations [306]. For regular tetrahedral GeO_4 units, the ratio $r_{\mathrm{OO}}/r_{\mathrm{GeO}} = \sqrt{8/3} = 1.633$. The ratio calculated from the measured partial pair distribution functions for GeO_2 glass under ambient conditions is 1.636(11) [305]. This ratio is anticipated to show a significant change with increasing pressure [324], however, the ratio calculated from the data given in table 9.3 or from the D4C results from the preceding chapter, does not display a systematic pressure dependency despite the observed increase in coordination number at elevated pressures. This may result from an increasing overlap with pressure between the nearest neighbour O-O and Ge-Ge correlations that renders unsafe the assignment of r_2 soley to O-O correlations.

9.6 Discussion

The same general trends are apparent in both the reciprocal space and real space functions obtained from *in situ* neutron diffraction measurements of GeO_2 glass at high pressure using a Paris-Edinburgh cell set up at the PEARL instrument or the D4C instrument (see chapter 8) and from the high pressure x-ray and neutron diffraction measurements made by Guthrie *et al.* [285]. That is to say, at pressures up to ≈ 5 GPa, there is a dramatic reduction in height and shift of the FSDP to higher Q with increasing pressure accompanied by an increase in the height of the principal peak. As the pressure is increased beyond 5 GPa an increase in coordination number $\bar{n}^{\mathrm{O}}_{\mathrm{Ge}}$ is observed from 4-fold to approaching 6-fold at ≈ 15 GPa (see figure 9.32) which is accompanied by an increase in the nearest neighbour Ge-O bond distance r_{GeO}. The overall results are therefore consistent with the operation of two desification mechanisms. At low pressures there is a reorganisation of the GeO_4 tetrahedra which manifests itself in the FSDP as a change in the intermediate range or-

der. Raman spectroscopy results [283, 284] in this pressure regime have been interpreted in terms of a reduction in the mean inter-tetrahedral O-Ge-O bond angle accompanied by a distortion of the GeO_4 tetrahedra which manifests itself in terms of a larger distribution of intra-tetrahedral O-Ge-O angles rather than by a change in the Ge-O bond length. At higher pressures, further reorganisation of the intermediate range order is facilitated by an increase in the local coordination number.

At ambient pressure the $F(Q)$ functions are in good overall agreement with the $F(Q)$ function measured for $^{\mathrm{nat}}GeO_2$ glass taken during an isotopic substitution experiment by Salmon *et al.* [305] using a conventional neutron diffraction set-up at ambient pressure using the D4C instrument, where the structure is based on a network of corner shared GeO_4 tetrahedra [306]. The full set of Faber-Ziman partial structure factors $S_{\alpha\beta}(Q)$ taken from Salmon *et al.* [305] are plotted in figure 9.33 where a comparison is made between the total neutron structure factor $^{\mathrm{rec}}S_N(Q)$ reconstructed from these partials and the measured ambient pressure $S_N(Q)$ from both the PEARL and D4C experiments. For comparison, the contribution of the $S_{\alpha\beta}(Q)$ to the total x-ray structure factor $S_X(Q)$ measured at ambient pressure by Sampath *et al.* [286] is shown in figure 9.34 together with the total x-ray structure factor $^{\mathrm{rec}}S_X(Q)$ reconstructed from the Faber-Ziman partial structure factors. As noted in Ref. [305], the Ge-Ge and Ge-O correlations give the largest contribution to $S_N(Q)$ in the region of the FSDP. Therefore, despite the fact that the O-O correlations have a larger weighting in $S_N(Q)$ compared with $S_X(Q)$, the changes observed with increasing pressure in the FSDP cannot be safely attributed to changes that are mostly associated with the oxygen atom correlations, as proposed by Guthrie *et al.* [285]. Instead, they are most likely to be attributed to a reduction in both the Ge-O and Ge-Ge correlations within this region. However, O-O correlations do contribute more strongly to the third peak in $S_N(Q)$ compared with $S_X(Q)$. Therefore, the initial increase in height of the third peak in $F(Q)$ with pressure increasing to ≈ 9 GPa and subsequent decrease beyond 9 GPa observed in the PEARL neutron diffraction measurements, may

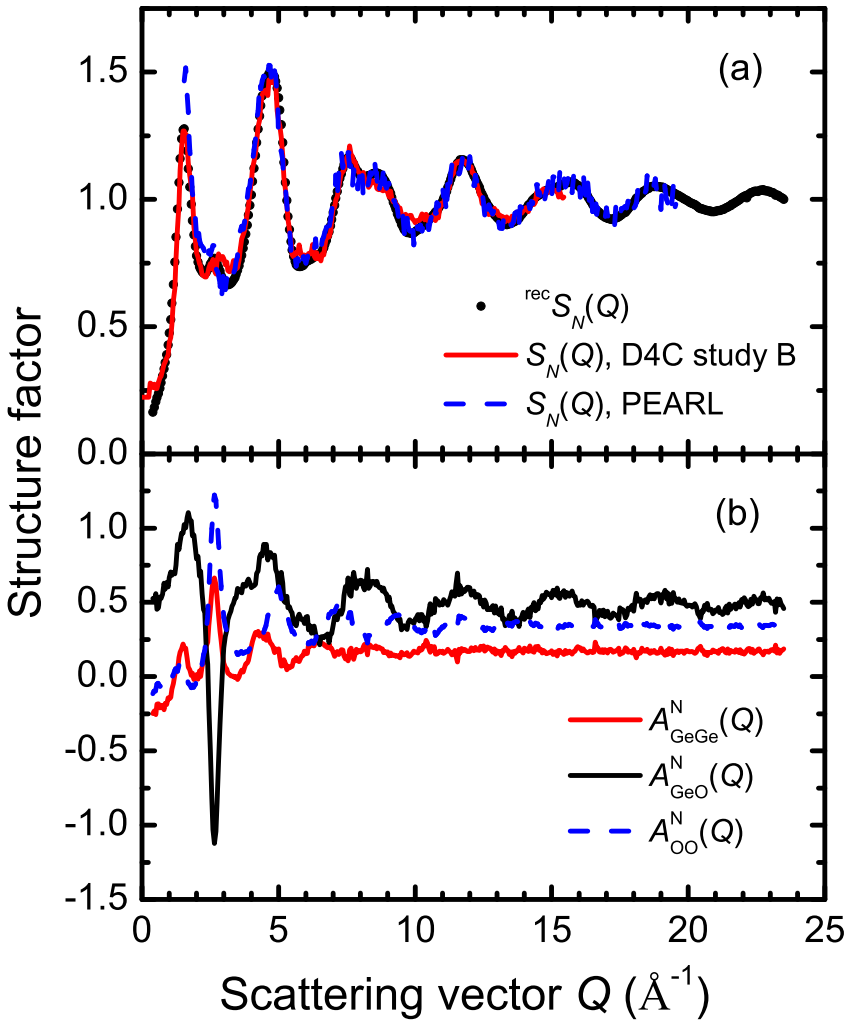

Figure 9.33: (a) A comparison between the measured $S_N(Q)$ for GeO_2 glass at ambient pressure from § 8.5 (solid red curve), the $S_N(Q)$ for GeO_2 glass at ambient pressure measured using PEARL, and the $^{\rm rec}S_N(Q)$ for GeO_2 glass (solid circles) as obtained from the neutron weighted GeO_2 Faber-Ziman partial structure factors given in (b) where $S_N(Q) = A^N_{\rm GeGe}(Q) + A^N_{\rm GeO}(Q) + A^N_{\rm OO}(Q)$. (b) The neutron weighted Faber-Ziman partial structure factors [305] are given by $A^N_{\rm GeGe}(Q) = c^2_{\rm Ge}b^2_{\rm Ge}S_{\rm GeGe}(Q)/\langle b\rangle^2$ (solid red curve), $A^N_{\rm GeO}(Q) = 2c_{\rm Ge}c_{\rm O}b_{\rm Ge}b_{\rm O}S_{\rm GeO}(Q)/\langle b\rangle^2$ (solid black curve) and $A^N_{\rm OO}(Q) = c^2_{\rm O}b^2_{\rm O}S_{\rm OO}(Q)/\langle b\rangle^2$ (dashed blue curve), where $\langle b\rangle = c_{\rm Ge}b_{\rm Ge} + c_{\rm O}b_{\rm O}$ and the neutron scattering lengths are $b_{\rm Ge} = 8.185(20)$ fm and $b_{\rm O} = 5.803(4)$ fm [30].

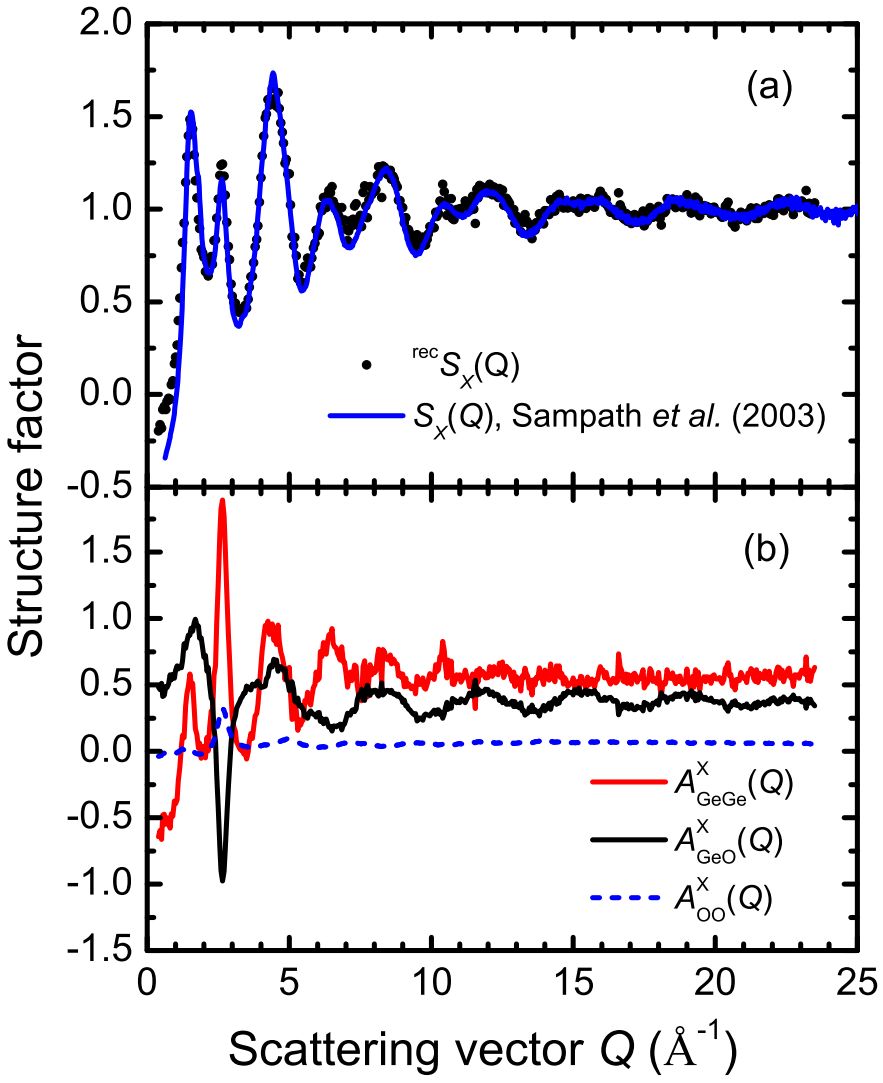

Figure 9.34: (a) A comparison between the measured $S_X(Q)$ for GeO_2 glass at ambient pressure [286] (solid blue curve) together with the $^{rec}S_X(Q)$ function for GeO_2 glass (solid circles) as obtained from the x-ray weighted GeO_2 Faber-Ziman partial structure factors given in (b) where $S_X(Q) = A^X_{GeGe}(Q) + A^X_{GeO}(Q) + A^X_{OO}(Q)$. (b) The x-ray weighted Faber-Ziman partial structure factors [305] are given by $A^X_{GeGe}(Q) = c^2_{Ge} f_{Ge}(Q)^2 S_{GeGe}(Q)/\langle f(Q)\rangle^2$ (solid red curve), $A^X_{GeO}(Q) = 2c_{Ge}c_O f_{Ge}(Q) f_O(Q) S_{GeO}(Q)/\langle f(Q)\rangle^2$ (solid black curve) and $A^X_{OO}(Q) = c^2_O f_O(Q)^2 S_{OO}(Q)/\langle f(Q)\rangle^2$ (dashed blue curve), where $\langle f(Q)\rangle = c_{Ge} f_{Ge}(Q) + c_O f_O(Q)$ and the neutral atom form factors $f_{Ge}(Q)$ and $f_O(Q)$ are taken from Ref. [201].

result mainly from changes in the O-O correlations relative to the Ge-Ge and Ge-O correlations. The small principal peak in the $S_N(Q)$ functions arises from an almost complete cancellation of the large principal peaks in the neutron weighted $S_{\alpha\beta}(Q)$. The increase in height of the principal peak of $S_N(Q)$ with increasing pressure may therefore be attributed to a change in the relative heights of the principal peaks of the Ge-Ge and O-O correlations relative to the Ge-O correlations in the neutron weighted $S_{\alpha\beta}(Q)$.

As discussed in chapter 8, the FSDP is a signature of the arrangement and packing of the structural units on an intermediate length scale where the wavelength of the associated periodicity in real space is given by $2\pi/q_1$, where q_1 is the position of the FSDP. The dramatic changes observed in the height and position of the FSDP in the measured $F(Q)$ functions for GeO_2 glass at moderate pressures therefore suggests a substantial change in the intermediate range order which can be explained by a compaction and eventual collapse of the cage-like structures that enclose open regions of the network formed by corner shared GeO_4 structural units at ambient pressure [285, 286]. As plotted in figure 9.32, the same general trends are also observed in the real space data sets obtained by high pressure diffraction methods, i.e. the coordination number $\bar{n}^{O}_{Ge}$ begins to increase from a value of four when the pressure $\gtrsim 5$ GPa. This indicates that the compression of the cage-like structures is accompanied by a transformation in the nature of the basic structural motifs as more O atoms are forced into close proximity to the Ge atoms. The increase in $\bar{n}^{O}_{Ge}$ with increasing pressure is accompanied by an increase in the position r_{GeO} of the first peak in $G(r)$, resulting from an expansion of the nearest neighbour coordination shell to accommodate the additional O atoms.

The coordination number $\bar{n}^{O}_{Ge} = 4$ at ambient pressure increases after $\approx$ 5 GPa to a value of 4.9(1) at 9.0(5) GPa. Since the $G(r)$ functions provide only an average coordination number $\bar{n}^{O}_{Ge}$, the observed increase may arise from a transformation of the structural units from GeO_4 tetrahedra to GeO_6 octahedra via GeO_5 pentahedra, a coexistence of both GeO_4 tetrahedra and GeO_6 octahedra, or even a coexistence of all three of these basic structural mo-

tifs. The nearest neighbour distance r_{GeO} increases from a value of 1.73(2) Å at ambient pressure to a value of 1.76(5) Å at 9.0(5) GPa. This distance is within the range of bond distances for GeO_5 pentahedra of $1.82 \leq r_{\mathrm{GeO}}$ (Å) ≤ 1.93 in germanate glasses [307, 308] and $1.77 \leq r_{\mathrm{GeO}}$ (Å) ≤ 1.97 in crystalline $K_2Ge_8O_{17}$ [309]. The coordination number increases to a value of 5.5(1) at 14(1) GPa with a corresponding increase in r_{GeO} to 1.81(2) Å. This distance is consistent with the EXAFS results of Vaccari *et al.* [323]. However, Guthrie *et al.* [285] report a significantly higher coordination number $\bar{n}^{\mathrm{O}}_{\mathrm{Ge}} = 6.0(3)$ and Ge-O bond distance of 1.91(2) Å at 15 GPa, which is consistent with the distance $r_{\mathrm{GeO}} = 1.87$ Å found in the crystalline rutile (octahedral) phase of GeO_2 at 16 GPa [325].

The neutron diffraction results presented in this thesis indicate that the transformation of the basic GeO_4 tetrahedral structural units to higher $\bar{n}^{\mathrm{O}}_{\mathrm{Ge}}$ is not as sharp as suggested by the high pressure x-ray diffraction measurements obtained by Guthrie *et al.* [285] or by the XAS measurements of Itie *et al.* [282]. The latter report a sharp increase in r_{GeO} at 6 GPa, however it is noted that the r_{GeO} shows significant hysteresis on decompression. The results of a recent high pressure EXAFS study on GeO_2 glass by Vaccari *et al.* [323] give values for r_{GeO} that are in much better agreement with the diffraction results. However, as shown in figure 9.32 (a), the coordination number $\bar{n}^{\mathrm{O}}_{\mathrm{Ge}}$ is not reliably determined as a function of pressure and does not reproduce the general trend observed in the diffraction results. This inconsistency is due to the inherent difficulty in extracting coordination numbers from EXAFS data due to the high correlation between the coordination number and the EXAFS Debye-Waller factor. These are both used as fitting parameters to the EXAFS oscillations, the decay of which in this specific instance could not be accurately determined due to the limited range of the data sets [323].

In order to investigate the relation between the structure of glassy GeO_2 and SiO_2, the total neutron structure factor ${}^{\mathrm{rec}}S_N(Q)$ for SiO_2 was reconstructed from the neutron weighted Faber-Ziman partials for GeO_2 glass [305]. The result is plotted in figure 9.35 (a) where a comparison is made with the

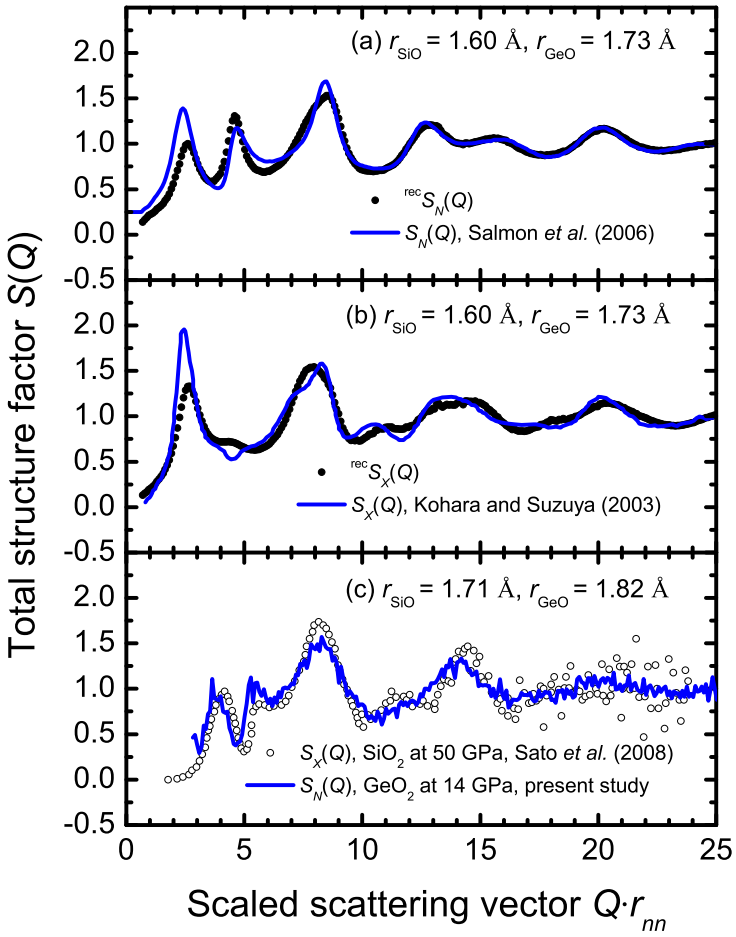

Figure 9.35: (a) The measured $S_N(Q)$ for SiO_2 glass [305] (solid blue curve) together with the $^{\rm rec}S_N(Q)$ function for SiO_2 glass (solid circles) reconstructed from the GeO_2 Faber-Ziman partial structure factors where $^{\rm rec}S_N(Q) = c_{\rm Si}^2 b_{\rm Si}^2 S_{\rm GeGe}(Q)/\langle b\rangle^2 + c_{\rm O}^2 b_{\rm O}^2 S_{\rm OO}(Q)/\langle b\rangle^2 + 2c_{\rm Si}c_{\rm O}b_{\rm Si}b_{\rm O}S_{\rm GeO}(Q)/\langle b\rangle^2$, where $\langle b\rangle = c_{\rm Si}b_{\rm Si} + c_{\rm O}b_{\rm O}$, $b_{\rm Si} = 4.1491(10)$ fm and $b_{\rm O} = 5.803(4)$ fm [30]. (b) The measured $S_X(Q)$ for SiO_2 glass [326] (solid blue curve) together with the $^{\rm rec}S_X(Q)$ function for SiO_2 glass (solid circles) reconstructed from the GeO_2 Faber-Ziman partial structure factors where $^{\rm rec}S_N(Q) = c_{\rm Si}^2 f_{\rm Si}(Q)^2 S_{\rm GeGe}(Q)/\langle f(Q)\rangle^2 + c_{\rm O}^2 f_{\rm O}(Q)^2 S_{\rm OO}(Q)/\langle f(Q)\rangle^2 + 2c_{\rm Si}c_{\rm O}f_{\rm Si}(Q)f_{\rm O}(Q)S_{\rm GeO}(Q)/\langle f(Q)\rangle^2$, where $\langle f(Q)\rangle = c_{\rm Si}f_{\rm Si}(Q) + c_{\rm O}f_{\rm O}(Q)$ and the neutral atom form factors $f_{\rm Si}(Q)$ and $f_{\rm O}(Q)$ are taken from Ref. [201]. (c) $S_N(Q)$ for GeO_2 glass at 14(1) GPa taken at PEARL (solid blue curve) by comparison to $S_X(Q)$ for SiO_2 glass at 50 GPa [276] (open circles). All of the data sets are plotted as a function of the scaled scattering vector Qr_{nn}, where r_{nn} is the nearest neighbour distance as indicated.

measured $S_N(Q)$ for SiO_2 glass [306]. Like GeO_2, the structure of SiO_2 glass at ambient pressure is based on an open network of corner shared SiO_4 tetrahedral units with a nearest neighbour Si-O bond distance $r_{SiO} = 1.60(1)$ Å [306]. However, the relative arrangement of these tetrahedra is different by comparison to GeO_2, as is evident by the higher and sharper FSDP in the measured $S_N(Q)$ for SiO_2 glass by comparison to the reconstruction ${}^{rec}S_N(Q)$ using the GeO_2 partials. The same general features nevertheless occur in the total structure factors of both glasses. The total x-ray structure factor ${}^{rec}S_X(Q)$ for SiO_2 reconstructed from the x-ray weighted Faber-Ziman partials for GeO_2 glass [305] is plotted in figure 9.35 (b) where a comparison is made with the measured $S_X(Q)$ for SiO_2 glass by Kohara and Suzuya [326]. The ${}^{rec}S_X(Q)$ function displays a less intense FSDP than the measured $S_X(Q)$. Figure 9.35 (c) shows a comparison between the $S_N(Q)$ measured for GeO_2 glass using PEARL at 14(1) GPa and the $S_X(Q)$ obtained from a recent high pressure x-ray diffraction measurement of 6-fold coordinated SiO_2 glass at 50 GPa using a diamond anvil cell [276]. Despite comparing a neutron $S_N(Q)$ with an x-ray $S_X(Q)$, which at ambient pressure display significant differences, the two data sets are in remarkable agreement. For example, both materials exhibit a prominent FSDP of comparable intensity, in contrast to the previous x-ray diffraction measurement of octahedral GeO_2 glass at 15 GPa [285] which does not show an FSDP. This is consistent with the high pressure form of glassy GeO_2 being a close structural analogue to the high pressure phase of glassy SiO_2 but with the pressure induced transformations occuring at much lower pressures, as also indicated by work on the crystalline phases of these materials [325, 327, 328]. The result is also consistent with Raman spectroscopy measurements which suggest the structure of SiO_2 at 8 GPa closely resembles that of GeO_2 at ambient pressure as the inter-tetrahedral O-Si-O bond, which is larger than O-Ge-O, tightens with negligible tetrahedral distortion [283]. With increasing pressure the Raman spectra of glassy SiO_2 follows a similar pattern to glassy GeO_2 but at much higher pressures indicating GeO_4 tetrahedra are more readily distorted than the more rigid SiO_4 tetrahedra [283].

9.7 Conclusions

Improvements were made to the incident neutron beam collimation, pressure cell shielding and experimental methods to obtain the correctly normalised total structure factor $F(Q)$ functions for amorphous GeO_2 at various high pressures using the PEARL instrument at ISIS, UK.

The results for GeO_2 glass essentially show the same trends with increasing pressure as previous x-ray diffraction measurements [285]. At moderate pressures, large changes are observed in the FSDP and principal peak of the $F(Q)$ functions suggesting a collapse of the network structure. With pressure increasing beyond 5 GPa, a gradual increase in the coordination number $\bar{n}^{\mathrm{O}}_{\mathrm{Ge}}$ is observed, reaching 4.9(1) at 9.0(5) GPa. At 14(1) GPa the coordination number reaches 5.5(1) with an associated increase in the nearest neighbour bond distance r_{GeO} to 1.81(2) Å as the nearest neighbour coordination shell expands to accept more O atoms. The FSDP is still present at this high pressure, in contrast to the previous x-ray diffraction measurement of octahedral GeO_2 glass at 15 GPa [285].

The high pressure results for GeO_2 glass will complement proposed molecular dynamics simulations on this system at high pressures. They also pave the way for applying the method of isotopic substitution in neutron diffraction to glasses at high pressures. These new experiments will be made using e.g. the D4C instrument at the ILL.

10. Overall conclusions

In this thesis the results of neutron and high energy x-ray diffraction experiments on a variety of liquid and glass systems were reported and the key results, conclusions and suggestions for further work are discussed below.

The results of neutron diffraction measurements of molten CuCl, CuI and $(\mathrm{CuCl})_x(\mathrm{CuI})_{1-x}$ $(0 \leq x \leq 1)$ mixtures were presented in chapter 4. A comparison with the information that is available on the structure of CuCl and CuI from experiment, theory and computer simulation revealed a need to improve existing models of CuCl and CuI before a realistic attempt can be made to account for the structure of their mixtures. These should take into account the presence of partially covalent Cu-Cu and Cu-I chemical bonds that have been found in CuI by the application of *ab initio* molecular dynamics methods. Further experimental measurements are required to obtain accurate partial structure factors for both molten CuI and the CuCl-CuI mixtures. This could be achieved by employing the method of isotopic substitution in neutron diffraction, to e.g. obtain the full set of partial structure factors for CuI and the Cu-Cu partial structure factor for the ternary CuCl-CuI system.

The structure and properties of the glassy $(R_2X_3)_{0.07}(\mathrm{Ga}_2X_3)_{0.33}(\mathrm{Ge}X_2)_{0.60}$ system, where R denotes a rare earth element and X denotes a chalcogenide element S or Se, were investigated in chapters 5 to 7 using a combination isomorphic substitution in neutron and x-ray diffraction, ^{71}Ga magic angle spinning (MAS) nuclear magnetic resonance (NMR) and differential scanning calorimetry (DSC) methods. The results show that the structure of these glasses is based on a network of $\mathrm{Ge}X_4$ and $\mathrm{Ga}X_4$ tetrahedra. Difference func-

tion methods were applied to the diffraction results and for the large rare earth ions provided a coordination number of $\bar{n}_R^{\mathrm{S}} = 8.1(2)$ and nearest neighbour bond distance of $r_{R\mathrm{S}} = 3.03(3)$ Å in the sulphide glass and a coordination number of $\bar{n}_R^{\mathrm{Se}} = 8.0(2)$ and bond distance of $r_{R\mathrm{Se}} = 3.05(3)$ Å in the selenide glass. For the small rare earth ions in the selenide glass a smaller distance $r_{R\mathrm{Se}} = 2.93(3)$ Å and coordination number $\bar{n}_R^{\mathrm{Se}} = 5.0(2)$ were obtained. In order to complete this study a comparison should be made with the structure of the sulphide glass containing small rare earth species. This could be achieved by using isomorphic substitution in x-ray diffraction with R = Y or Ho, or in neutron diffraction with R = Dy or Ho, for which there is a large contrast in the coherent neutron scattering lengths $b_{\mathrm{Dy}} = 16.9(2)$ fm cf. $b_{\mathrm{Ho}} = 8.01(2)$ fm [30]. Further information could be gained on the rare earth coordination environment of this glass system using ^{89}Y MAS NMR. For the selenide glass ^{77}Se MAS NMR could also be used. The rare earth correlations could be better probed by applying neutron and x-ray diffraction methods to glasses containing a greater atomic fraction of rare earth ions. It may also be possible to unambiguously identify the rare earth correlations in the total pair distribution functions measured by diffraction and to extract the $S_{RR}(Q)$ partial structure factor by using difference function methods.

In chapter 8 *in situ* high pressure neutron diffraction experiments on GeO_2 glass were reported using the Paris-Edinburgh press on the D4C diffractometer at the ILL, France. An analysis procedure was developed to account for the gasket and background scattering at each pressure point and improved neutron shielding led to the extraction of high quality total structure factors $F(Q)$ at pressures up to 8 GPa. Future improvements could be made to the D4C instrument to further reduce the contribution to the background scattering from the anvils by focussing a narrower neutron beam onto the sample position and allowing the entire press assembly to move vertically in order to maintain the sample position at the center of the incident neutron beam.

In chapter 9 *in situ* high pressure neutron diffraction experiments on GeO_2 glass were reported using the Paris-Edinburgh press on the PEARL instrument

at ISIS, UK, with sintered diamond anvils. Improvements were made to the incident neutron beam collimation, pressure cell shielding and experimental methods which enabled the extraction of correctly normalised total structure factors $F(Q)$ at pressures up to 14(1) GPa.

The results from the high pressure neutron diffraction measurements of GeO_2 glass essentially show the same trends with increasing pressure as previous x-ray diffraction measurements [285]. At moderate pressure, large changes are observed in the FSDP and principal peak of the $F(Q)$ functions suggesting a collapse of the network structure. With pressure increasing beyond 5 GPa a gradual increase in the coordination number $\bar{n}^{\mathrm{O}}_{\mathrm{Ge}}$ is observed, reaching 4.9(1) at 9.0(5) GPa. At 14(1) GPa the Ge-O coordination number reaches 5.5(1). There is an increase in the nearest neighbour Ge-O bond distance from $r_{\mathrm{GeO}} = 1.73(2)$ Å at ambient pressure to 1.81(2) Å at 14(1) GPa as the nearest neighbour coordination shell expands to accept more O atoms. The transformation in GeO_2 glass appears to be continuous, i.e. there is no evidence for a sharp transition between the ambient pressure and denser high pressure phases that would be indicative of a 1st order polyamorphic phase transition.

The total structure factor measurements obtained from the D4C instrument are of suitable calibre to enable future application of the method of isotopic substitution in neutron diffraction to measure the partial structure factors of liquid and glassy materials at pressures up to 8 GPa. Difference functions may also be obtained by combining the results of *in situ* neutron diffraction with those obtained from *in situ* x-ray diffraction. The interpretation of the results would benefit from future molecular dynamics simulations. Further neutron diffraction measurements could also be made between 9 and 15 GPa in order to fully investigate the transformation of GeO_2 glass to the octahedral form previously observed by x-ray diffraction measurements [285].

References

[1] Zallen, R. *The Physics of Amorphous Solids*. John Wiley, New York, (1983).

[2] Elliott, S. R. *Physics of Amorphous Materials*. New York: Longman Inc., 2nd edition, (1984).

[3] Cusack, N. E. *The Physics of Structurally Disordered Matter*. Bristol: IOP Publishing Ltd, (1987).

[4] Fischer, H. E., Barnes, A. C., and Salmon, P. S. *Reports on Progress in Physics* **69**, 233–299 (2006).

[5] Greaves, G. N. and Sen, S. *Advances in Physics* **56**, 1–166 (2007).

[6] Sissons, J. B. and Walker, M. J. C. *Nature* **249**, 824–825 (1974).

[7] Negash, A., Shackley, M. S., and Alene, M. *Journal of Archaeological Science* **33**, 1647–1650 (2006).

[8] Angell, C. A. *Science* **267**, 1924–2935 (1995).

[9] Jenniskens, P. and Blake, D. F. *Science* **265**, 753–756 (1994).

[10] Hansen, G. B. and McCord, T. B. *Journal of Geophysical Research: Planets* **109**, E01012 (2004).

[11] Farnan, I. *Nature* **390**, 14–15 (1997).

[12] Anderson, P. W. *Science* **267**, 1615 (1995).

[13] Poole, P. H., Grande, T., Angell, C. A., and McMillan, P. F. *Science* **275**, 322–323 (1997).

[14] McMillan, P. F. *Journal of Materials Chemistry* **14**, 1506–1512 (2004).

[15] Chamagnon, B., Martinet, C., Coussa, C., and Deschamps, T. *Journal of Non-Crystalline Solids* **353**, 4208–4211 (2007).

[16] Tulk, C. A., Benmore, C. J., Urquidi, J., Klug, D. D., Neuefeind, J., Tomberli, B., and Egelstaff, P. A. *Science* **297**, 1320–1323 (2002).

[17] Klotz, S. and Hamel, G. *Physical Review Letters* **89**, 285502 (2002).

[18] Guthrie, M., Urquidi, J., Tulk, C. A., Benmore, C. J., Klug, D. D., and Neuefeind, J. *Physical Review B* **68**, 184110 (2003).

[19] Klotz, S., Strässle, T., Nelmes, R. J., Loveday, J. S., Hamel, G., Rousse, G., Canny, B., Chervin, J. C., and Saitta, A. M. *Physical Review Letters* **94**, 25506 (2005).

[20] Sen, S., Gaudio, S., Aitken, B. G., and Lesher, C. E. *Physical Review Letters* **97**, 025504 (2006).

[21] Santoro, M., Gorelli, F. A., Bini, R., Ruocco, G., Scandolo, S., and Crichton, W. A. *Nature* **441**, 857–860 (2006).

[22] Katayama, Y., Mizutani, T., Utsumi, W., Shimomura, O., Yamakata, M., and Funakoshi, K. *Nature* **403**, 170–173 (2000).

[23] Greaves, G. N., Wilding, M. C., Fearn, S., Langstaff, D., Kargl, F., Cox, S., Vu Van, Q., Majérus, O., Benmore, C. J., Weber, R., Martin, C. M., and Hennet, L. *Science* **322**, 566–570 (2008).

[24] Squires, G. L. *Introduction to the theory of thermal neutron scattering*. Mineola, New York: Dover Publications, Inc., (1996).

[25] Bacon, G. E. *Neutron Diffraction*. Oxford: Clarendon, (1975).

[26] Lovesey, S. W. *Theory of Neutron Scattering from Condensed Matter*, volume 1 and 2 of *International Series of Monographs on Physics vol 72*. Oxford: Clarendon, (1984).

[27] Warren, B. E. *X-Ray Diffraction*. New York: Dover, (1990).

[28] Guinier, A. *X-Ray Diffraction in Crystals, Imperfect Crystals and Amorphous Bodies*. New York: Dover, (1994).

[29] James, R. W. *The Optical Principles of the Diffraction of X-Rays*. Woodbridge, CT: Oxbow, (1962).

[30] Sears, V. F. *Neutron News* **3**, 26–37 (1992).

[31] Placzek, G. *Physical Review* **86**, 377 (1952).

[32] Faber, T. E. and Ziman, J. M. *Philosphical Magazine* **11**, 153 (1965).

[33] Lorch, E. *Journal of Physics C: Solid State Physics* **2**, 229 (1969).

[34] Enderby, J. E., North, D. M., and Egelstaff, P. A. *Philosophical Magazine* **14**, 961 (1966).

[35] Balcar, E. and Lovesey, S. W. *Theory of Magnetic Neutron and Photon Scattering*. Oxford: Clarendon, (1989).

[36] Wasse, J. C. and Salmon, P. S. *Journal of Physics: Condensed Matter* **11**, 1381–1396 (1999).

[37] Bleaney, B. I. and Bleaney, B. *Electricity and Magnetism*, volume 2. Oxford: Oxford University Press, 3rd edition, (1989).

[38] Freeman, A. J. and Desclaux, J. P. *Journal of Magnetism and Magnetic Materials* **12**, 11 (1979).

[39] Fischer, H. E., Cuello, G. J., Palleau, P., Feltin, D., Barnes, A. C., and Badayal, Y. S. Simonson, J. M. *Applied Physics A* **74[Suppl.]**, S160–S162 (2002).

[40] Cicognani, G., editor. *The yellow book: Guide to neutron research facilities*. Grenoble: Institut Laue-Langevin, (2005).

[41] Benmore, C. J. and Soper, A. K. Technical Report RAL-TR-98-006, ISIS Pulsed Neutron Source, (1998).

[42] `http://www.isis.rl.ac.uk/disordered/gem/GEMdraw/GEMAnnColPic.pdf`.

[43] `http://www.pns.anl.gov/instruments/glad/`.

[44] `http://www.isis.rl.ac.uk/crystallography/hipr/`.

[45] Klotz, S. Private Communication, (2009).

[46] Jayaraman, A. *Reviews of Modern Physics* **55**, 65–108 (1983).

[47] Jayaraman, A. *Review of Scientific Instruments* **57**, 1013–1031 (1986).

[48] Brister, K. *Review of Scientific Instruments* **68**, 1629–1647 (1997).

[49] Klotz, S., Besson, J. M., Hamel, G., Nelmes, R. J., Loveday, J. S., Marshall, W. G., and Wilson, R. M. *Applied Physics Letters* **66**, 1735–1737 (1995).

[50] Besson, J. M. and Nelmes, R. J. *Physica B* **213 & 214**, 31–36 (1995).

[51] Bull, C. L., Guthrie, M., Klotz, S., Philippe, J., Strässle, T., Nelmes, R. J., Loveday, J. S., and Hamel, G. *High Pressure Research* **25**, 229–233 (2005).

[52] `http://www.aps.anl.gov/`.

[53] Rütt, A., Beno, M. A., Strempfer, J., Jennings, G., Kurtz, C., and Montano, P. A. *Nuclear Instruments and Methods in Physics Research A* **467-468**, 1026–1029 (2001).

[54] Paalman, H. H. and Pings, C. J. *Journal of Applied Physics* **33**, 2635 (1962).

[55] Soper, A. K. and Egelstaff, P. A. *Nuclear Instruments and Methods* **178**, 415 (1980).

[56] Mayers, J. *Nuclear Instruments and Methods* **221**, 609 (1984).

[57] Carlile, C. J. Technical Report RL-74-103, Rutherford Appleton Laboratory, (1974).

[58] Drewitt, J. W. E., Salmon, P. S., Takeda, S., and Kawakita, Y. *Journal of Physics: Condensed Matter* **21**, 075104 (2009).

[59] Keen, D. A. *Journal of Physics: Condensed Matter* **14**, R819–R857 (2002).

[60] Armstrong, R. D., Bulmer, R. S., and Dickinson, T. *Journal of Solid State Chemistry* **8**, 219 (1973).

[61] McGeehin, P. and Hooper, A. *Journal of Materials Science* **12**, 1 (1977).

[62] Boyce, J. B. and Huberman, B. A. *Physics Reports* **51**, 189 (1979).

[63] Hull, S. *Reports on Progress in Physics* **67**, 1233–1314 (2004).

[64] Dejus, R., Sköld, K., and Granéli, B. *Solid State Ionics* **1**, 327–336 (1980).

[65] Boyce, J. B., Hayes, T. M., and Mikkelsen, J. C. *Physical Review B* **23**, 2876–2896 (1981).

[66] Zheng-Johansson, J. X. M., Sköld, K., and Jørgensen, J. *Solid State Ionics* **70/71**, 522–527 (1994).

[67] Hull, S. and Keen, D. A. *Journal of Physics: Condensed Matter* **8**, 6191–6198 (1996).

[68] Weast, R. C., Astle, M. J., and Beyer, W. H., editors. *Handbook of Chemistry and Physics*. Boca Raton, FL: CRC Press, 67th edition, (1987).

[69] Nield, V. M., McGreevy, R. L., Keen, D. A., and Hayes, W. *Physica B* **202**, 159 (1994).

[70] Nield, V. M., Keen, D. A., Hayes, W., and McGreevy, R. L. *Solid State Ionics* **66**, 247–258 (1993).

[71] Mönkemeyer, K. *Neues Jahrbuch fur Mineralogie, Geologie und Palaontologie, Beil* **22**, 1–47 (1906).

[72] Liu, C. and Angell, C. A. *Solid State Ionics* **13**, 105–109 (1984).

[73] Bychkov, E., Bolotov, A., Grushko, Y., Vlasov, Y., and Wortmann, G. *Solid State Ionics* **90**, 289–294 (1996).

[74] Bolotov, A., Bychkov, E., Gavrilov, Y., Grushko, Y., Pradel, A., Ribes, M., Tsegelnik, V., and Vlasov, Y. *Solid State Ionics* **113-115**, 697–701 (1998).

[75] Bychkov, E. *Solid State Ionics* **136-137**, 1111–1118 (2000).

[76] Salmon, P. S. and Xin, S. *Physical Review B* **65**, 064202 (2002).

[77] Usuki, T., Nakajima, K., Furukawa, T., Onodera, Y., Nasu, T., Sakurai, M., and Kohara, S. *Solid State Ionics* **177**, 2581–2584 (2006).

[78] Page, D. I. and Mika, K. *Journal of Physics C: Solid State Physics* **4**, 3034–3044 (1971).

[79] Powles, J. G. *Journal of Physics C: Solid State Physics* **8**, 895–906 (1975).

[80] Gillan, M. J. *Journal of Physics C: Solid State Physics* **9**, 2261–2271 (1976).

[81] Bhatia, A. B. and Ratti, V. K. *Journal of Physics F: Metal Physics* **6**, 927–941 (1976).

[82] Boyce, J. B. and Mikkelsen Jr, J. C. *Journal of Physics C: Solid State Physics* **10**, L41–L43 (1977).

[83] Boyce, J. B. and Mikkelsen Jr, J. C. *Physics and Chemistry of Electrons and Ions in Condensed Matter*, volume 130 of *NATO-ASI Series C*, 273. Dordrecht: Reidel (1984).

[84] Ginoza, M., Nixon, J. H., and Silbert, M. *Journal of Physics C: Solid State Physics* **20**, 1005–1015 (1987).

[85] Stafford, A. J., Silbert, M., Trullàs, J., and Giró, A. *Journal of Physics: Condensed Matter* **2**, 6631–6641 (1990).

[86] Trullàs, J., Giró, A., and Silbert, M. *Journal of Physics: Condensed Matter* **2**, 6643–6650 (1990).

[87] Tankeshwar, K. and Tosi, M. P. *Journal of Physics: Condensed Matter* **3**, 7511–7518 (1991).

[88] Tasseven, C., Silbert, M., and Trullàs, J. *Journal of Physics: Condensed Matter* **7**, 887–8881 (1995).

[89] Koishi, T., Shirakawa, Y., and Tamaki, S. *Journal of Physics: Condensed Matter* **9**, 10101–10113 (1997).

[90] Alcaraz, O. and Trullàs, J. *Journal of Chemical Physics* **115**, 7071–7075 (2001).

[91] Trullàs, J. Private Communication, (2008).

[92] Howells, W. S. *Physica B* **241-243**, 329–331 (1998).

[93] Belashchenko, D. K. and Ostrovski, O. I. *Calphad* **26**, 523–538 (2002).

[94] Higaki, T., Tomomasa, M., Hyakawa, T., Chiba, A., and Tsuji, K. *Journal of Physics: Condensed Matter* **20**, 114106 (2008).

[95] Shirakawa, Y., Saito, M., Tamaki, S., Inui, M., and Takeda, S. *Journal of The Physical Society of Japan* **60**, 2678–2683 (1991).

[96] Shirakawa, Y., Saito, M., Maruyama, K., and Tamaki, S. *Journal of Non-Crystalline Solids* **156-158**, 767–770 (1993).

[97] Takeda, S., Shirakawa, Y., Takesawa, K., Harada, S., and Tamaki, S. *Journal of the Physical Society of Japan* **58**, 4007–4011 (1989).

[98] Trullàs, J., Giró, and Fontnet, R. *Physical Review B* **50**, 16279–16286 (1994).

[99] Waseda, Y., Kang, S., Sugiyama, K., Kimura, M., and Saito, M. *Journal of Physics: Condensed Matter* **12**, A195–A201 (2000).

[100] Trapananti, A., Di Cicco, A., and Minicucci, M. *Physical Review B* **66**, 014202 (2002).

[101] Shimojo, F., Aniya, M., and Hoshino, K. *Journal of the Physical Society of Japan* **73**, 2148–2153 (2004).

[102] Dalgic, S. S., Gurbuz, H., and Ozgec, O. *Journal of Optoelectronics and Advanced Materials* **7**, 2059–2068 (2005).

[103] Takeda, S., Fujii, H., Kawakita, Y., Kato, Y., Kohara, S., and Maruyama, K. *Physica B* **385-386**, 249–251 (2006).

[104] Kawakita, Y., Tahara, S., Fujii, H., Kohara, S., and Takeda, S. *Journal of Physics: Condensed Matter* **19**, 335201 (2007).

[105] Shimojo, F., Munejiri, S., Aniya, M., and Hoshino, K. *Journal of Non-Crystalline Solids* **353**, 3505–3509 (2007).

[106] Eisenberg, S., Jal, J. F., and Dupuy, J. *Philosophical Magazine A* **46**, 195–209 (1982).

[107] Koester, L. *Neutron Physics*. Springer Tracts in Modern Physics No. 80. Berlin. Heidelberg, New York : Springer-Verlag, (1977).

[108] Shirakawa, Y., Tamaki, S., Okazaki, H., and Azuma, M. *Journal of The Physical Society of Japan* **62**, 544–551 (1993).

[109] Inui, M., Takeda, S., and Uechi, T. *Journal of the Physical Society of Japan* **62**, 3142–3149 (1993).

[110] Shirakawa, Y., Tamaki, S., Usuki, T., Sugiyama, K., and Waseda, Y. *Journal of the Physical Society of Japan* **63**, 1814–1820 (1994).

[111] `http://www.isis.rl.ac.uk/Disordered/Manuals/gudrun/Gudrun\_manual\_2006.pdf`.

[112] Mughabghab, S. F. *Atlas of Neutron Resonances*. Amsterdam: Elsevier, 5 edition, (2006).

[113] Salmon, P. S., Xin, S., and Fischer, H. E. *Physical Review B* **58**, 6115–6123 (1998).

[114] Inui, M., Takeda, S., and Uechi, T. *Journal of the Physical Society of Japan* **60**, 3190–3191 (1991).

[115] Hopper, M. J. In *UK Atomic Energy Authority Report AERE*, R.7477. Harwell: UK Atomic Energy Authority (1973).

[116] Salmon, P. S. *Proceedings of the Royal Society: Mathematical and Physical Sciences* **445**, 351–365 (1994).

[117] McGreevy, R. L. and Pusztai, L. *Proceedings of the Royal Society: Mathematical and Physical Sciences* **430**, 241–261 (1990).

[118] Edwards, F. G., Enderby, J. E., Howe, R. A., and Page, D. I. *Journal of Physics C: Solid State Physics* **8**, 3483 (1975).

[119] Biggin, S. and Enderby, J. E. *Journal of Physics C: Solid State Physics* **15**, L305–L309 (1982).

[120] McGreevy, R. L. and Howe, M. A. *Journal of Physics: Condensed Matter* **1**, 9957 (1989).

[121] Shannon, R. D. *Acta Crystallographica A* **32**, 751 (1976).

[122] Allen, D. A. and Howe, R. A. *Journal of Physics: Condensed Matter* **4**, 6029–6038 (1992).

[123] McGreevy, R. L. and Zheng-Johansson, J. X. M. *Solid State Ionics* **95**, 215 (1997).

[124] Vashista, P. and Rahman, A. *Physical Review Letters* **40**, 1337 (1978).

[125] Parrinello, M., Rahman, A., and Vashishta, P. *Physical Review Letters* **50**, 1073 (1983).

[126] Saito, M., Park, C., Omote, K., Sugiyama, K., and Waseda, Y. *Journal of the Physical Society of Japan* **66**, 633 (1997).

[127] Pusztai, L. and McGreevy, R. L. *Journal of Physics: Condensed Matter* **10**, 525 (1998).

[128] Keen, D. A. and Hull, S. *Journal of Physics.: Condensed Matter* **7**, 5793–5804 (1995).

[129] Philips, J. C. *Reviews of Modern Physics* **42**, 317 (1970).

[130] Ihata, K. and Okazaki, H. *Journal of Physics.: Condensed Matter* **9**, 1477–1492 (1997).

[131] Chahid, A. and McGreevy, R. L. *Journal of Physics: Condensed Matter* **10**, 2597–2609 (1998).

[132] Howe, M. A., McGreevy, R. L., and Mitchell, E. W. *Zeitschrift für Physik B Condensed Matter* **62**, 15–19 (1985).

[133] Barnes, A. C., Lague, S. B., Salmon, P. S., and Fischer, H. E. *Journal of Physics: Condensed Matter* **9**, 6159–6173 (1997).

[134] Barnes, A. C., Hamilton, M. A., Beck, U., and Fischer, H. E. *Journal of Physics: Condensed Matter* **12**, 7311 (2000).

[135] Vashista, P. and Rahman, A. *Fast ion Transport in Solids*, 527. New York: North Holland (1979).

[136] Zheng-Johansson, J. X. M., Ebbsjö, I., and McGreevy, R. L. *Solid State Ionics* **82**, 115–122 (1995).

[137] Zheng-Johansson, J. X. M. and McGreevy, R. L. *Solid State Ionics* **83**, 35–48 (1996).

[138] McGreevy, R. L., Zheng-Johansson, J. X. M., and Ebbsjö, I. *Physica B* **226**, 107–112 (1996).

[139] Keen, D. A., Hull, S., Barnes, A. C., Berastegui, P., Crichton, W. A., Madden, P. A., Tucker, M. G., and Wilson, M. *Physical Review B* **68**, 014117 (2003).

[140] Shimojo, F. and Aniya, M. *Journal of the Physical Society of Japan* **72**, 2702–2705 (2003).

[141] Weber, M. J. In *Handbook on the Physics and Chemistry of Rare Earths,* Gschneider, K. A. and Eyring, L., editors, volume 14, chapter 35, 275–278. Amsterdam: North-Holland Publishing Company (1979).

[142] Kenyon, A. *Progress in Quantum Electronics* **26**, 225–284 (2002).

[143] Abe, K., Takebe, H., and Morinaga, K. *Journal of Non-Crystalline Solids* **212**, 143–150 (1997).

[144] Tver'yanovich, Y. S. and Tverjanovich, A. In *Semiconductors and Semimetals,* Willardson, R. K. and Beer, A. C., editors, volume 80, chapter 4, 169–207. Amsterdam: Elsevier (2004).

[145] Lezal, D. *Journal of Optoelectronics and Advanced Materials* **5**, 23–34 (2003).

[146] Moeller, T. *The Chemistry of the Lanthanides.* New York: Pergamon Press, (1975).

[147] Pettifor, D. G. *Journal of Physics C: Solid State Physics* **19**, 285–313 (1986).

[148] Blasse, G. In *Handbook on the Physics and Chemistry of Rare Earths,* Gschneider, K. A. and Eyring, L., editors, volume 14, chapter 34, 237–274. Amsterdam: North-Holland Publishing Company (1979).

[149] Guesic, J. E., Marcos, H. M., and Van Uitert, L. G. *Applied Physics Letters* **4**, 182–184 (1964).

[150] Greer, A. L. and Mathur, N. *Nature* **437**, 1246–1247 (2005).

[151] Zhang, X. *Laser Focus World* **3**, 73 (2002).

[152] Quimby, R. S. and Aitken, B. G. *Journal of Non-Crystalline Solids* **320** (2003).

[153] Ivanova, Z. G., Aneva, Z., Koughia, K., Tonchev, D., and Kasap, S. O. *Journal of Non-Crystalline Solids* **353**, 1330–1332 (2007).

[154] Kadono, K., Yazawa, T., Jiang, S., Porque, J., Hwang, B., and Peyghambarian, N. *Journal of Non-Crystalline Solids* **331**, 79–90 (2003).

[155] Zhao, D., Yang, G., Xu, Y., Zeng, H., Nemec, P., Frumar, M., and Chen, G. *Journal of Non-Crystalline Solids* **354**, 1294–1297 (2008).

[156] Ivanova, Z. G., Vassilev, V. S., Cernoskova, E., and Cernosek, Z. *Journal of Physics and Chemistry of Solids* **64** (2003).

[157] Aitken, B. G. and Quimby, R. S. *Journal of Non-Crystalline Solids* **213&214**, 281–287 (1997).

[158] Heo, J., Yoon, J. M., and Ryou, S. *Journal of Non-Crystalline Solids* **238**, 115–123 (1998).

[159] Man'shina, A. A., Kurochkin, A. V., Degtyarev, S. V., Grigor'ev, Y. G., Tverjanovich, A. S., and Smirnov, V. B. In *International Seminar on Novel Trends in Nonlinear Laser Spectroscopy and High-Precision Measurements in Optics,* Bagaev, S. N., Zadkov, V. N., and Arakelian, S. M., editors, volume 4429 of *Proceedings of SPIE*, 80–88, (2001).

[160] Degtyarev, S. V., Man'shina, A. A., Kurochkin, A. V., Zhuzhel'skii, D. V., Grigor'ev, Y. G., and Tver'yanovich, Y. S. *Glass Physics and Chemistry* **27**, 209–213 (2001).

[161] Barnier, S., Guittard, M., and Flahaut, J. *Materials Research Bulletin* **15**, 689–705 (1980).

[162] Loireau-Lozac'h, A. M. and Guittard, M. *Materials Research Bulletin* **12**, 887–893 (1977).

[163] Němec, P., Frumarová, B., Frumar, M., and Oswald, J. *Journal of Physics and Chemistry of Solids* **61**, 1583–1589 (2000).

[164] Kasap, S. O., Koughia, K., Munzar, M., Tonchev, D., Saitou, D., and Aoki, T. *Journal of Non-Crystalline Solids* **353**, 1364–1371 (2007).

[165] Ivanova, Z. G., Aneva, Z., Ganesan, R., Tonchev, D., Gopal, E. S. R., Rao, K. S. R. K., Allen, T. W., DeCorby, R. G., and Kasap, S. O. *Journal of Non-Crystalline Solids* **353**, 1418–1421 (2007).

[166] Koughia, K., Saitou, D., Aoki, T., Munzar, M., and Kasap, S. O. *Journal of Non-Crystalline Solids* **352**, 2420–2424 (2006).

[167] Ivanova, T. Y., Man'shina, A. A., and Povolotskiy, A. V. *Journal of Non-Crystalline Solids* **351**, 1403–1409 (2005).

[168] Borisov, E. N., Smirnov, V. B., Tverjanovich, A., and Tveryanovich, Y. S. *Journal of Non-Crystalline Solids* **326&327**, 316–319 (2003).

[169] Tverjanovich, A., Grigoriev, Y. G., Degtyarev, S. V., Kurochkin, A. V., Man'shina, A. A., Ivanova, T. Y., Povolotskiy, A., and Tveryanovich, Y. S. *Journal of Non-Crystalline Solids* **326&327**, 311–315 (2003).

[170] Ivanova, T. Y., Man'shina, A. A., Kurochkin, A. V., Tver'yanovich, Y. S., and Smirnov, V. B. *Journal of Non-Crystalline Solids* **298**, 7–14 (2002).

[171] Tverjanovich, A., Grigoriev, Y. G., Degtyarev, S. V., Kurochkin, A. V., Man'shina, A. A., and Tver'yanovich, Y. S. *Journal of Non-Crystalline Solids* **286**, 89–92 (2001).

[172] Tver'yanovich, Y., Mamedov, S., and Degtyarev, S. *Solid State Communications* **115**, 631–633 (2000).

[173] Tver'yanovich, Y. S., Degtyarev, S. V., Pivovarov, S. S., Smirnov, V. B., and Kurochkin, A. V. *Journal of Non-Crystalline Solids* **256&257**, 95–99 (1999).

[174] Park, S. H., Heo, J., and Kim, H. S. *Journal of Non-Crystalline Solids* **259**, 31–38 (1999).

[175] Heo, J., Cho, W. Y., and Chung, W. J. *Journal of Non-Crystalline Solids* **212**, 151–156 (1997).

[176] Shin, Y. B., Cho, W. Y., and Heo, J. *Journal of Non-Crystalline Solids* **208**, 29–35 (1996).

[177] Wei, K., Machewirth, D. P., Wenzel, J., Snitzer, E., and Sigel Jr, G. H. *Journal of Non-Crystalline Solids* **182**, 257–261 (1995).

[178] Wei, K., Machewirth, D. P., Wenzel, J., Snitzer, E., and Sigel Jr, G. H. *Optics Letters* **19**, 904–906 (1994).

[179] Němec, P. and Frumar, M. *Materials Letters* **62**, 2799–2801 (2008).

[180] Ivanova, T. Y., Manshina, A. A., Povolotskiy, A. V., Tver'yanovich, Y. S., Liaw, S., and Hsieh, Y. *Journal of Physics D: Applied Physics* **41**, 175110 (2008).

[181] Koughia, K., Munzar, M., Tonchev, D., Haugen, C. J., Decorby, R. G., McMullin, J. N., and Kasap, S. O. *Journal of Luminescence* **112**, 92–96 (2005).

[182] Munzar, M., Koughia, K., Tonchev, D., Kasap, S. O., Sakai, T., Maeda, K., Ikari, T., Haugen, C., Decorby, R., and McMullin, J. N. *Physics and Chemistry of Glasses* **46**, 215–219 (2005).

[183] Němec, P. and Frumar, M. *Journal of Non-Crystalline Solids* **299-302**, 1018–1022 (2002).

[184] Maeda, K., Ikuta, J., Arima, T., Sakai, T., Ikari, T., Munzar, M., Tonchev, D., and Kasap, S. O. *Physics and Chemistry of Glasses* **47**, 189–192 (2006).

[185] Munzar, M., Koughia, K., Kasap, S. O., Haugen, C., DeCorby, R., and McMullin, J. N. *Physics and Chemistry of Glasses* **47**, 220–224 (2006).

[186] Higuchi, H., Kanno, R., Kawamoto, Y., Takahashi, M., and Kadono, K. *Physics and Chemistry of Glasses* **40**, 49–53 (1999).

[187] Higuchi, H., Kanno, R., Kawamoto, Y., Takahashi, M., and Kadono, K. *Physics and Chemistry of Glasses* **40**, 122–125 (1999).

[188] Heo, J. *Journal of Non-Crystalline Solids* **353**, 1358–1363 (2007).

[189] Choi, Y. G. and Song, J. H. *Chemical Physics Letters* **467**, 323–326 (2009).

[190] Loireau-Lozac'h, A. M. and Guittard, M. *Annali di Chimica.* **2**, 101–104 (1975).

[191] Zeidler, A., Drewitt, J. W. E., Salmon, P. S., Barnes, A. C., Crichton, W. A., Klotz, S., Fischer, H. E., Benmore, C. J., Ramos, S., and Hannon, A. C. *Journal of Physics: Condensed Matter* (In Press).

[192] Petri, I. and Salmon, P. S. *Physical Review Letters* **84**, 2413–2416 (2000).

[193] Massiot, D., Vosegaard, T., Magneron, N., Trumeau, D., Montouillout, V., Berthet, P., Loiseau, T., and Bujoli, B. *Solid State Nuclear Magnetic Resonance* **15**, 159–169 (1999).

[194] Dell, L. A. and Smith, M. E. Private Communication, (2007).

[195] Duer, M. J. *Introduction to Solid-State NMR Spectroscopy.* Oxford: Blackwell Publishing Ltd, (2004).

[196] Dell, L. A., Savin, S. L. P., Chadwick, A. V., and Smith, M. E. *Applied Magnetic Resonance* **32**, 527–546 (2007).

[197] Jal, J. F., Mathieu, C., Chieux, P., and Dupuy, J. *Philosophical Magazine B* **62**, 351–372 (1990).

[198] Hannon, A. C. Private Communication, (2006).

[199] Hammersley, A. P. Internal Report ESRF98HA01T, ESRF, Grenoble, (1998).

[200] Cromer, D. T. *The Journal of Chemical Physics* **50**, 4857–4859 (1969).

[201] Maslen, E. N., Fox, A. G., and O'Keefe, M. A. *International Tables for X-ray Crystallography*, volume C. Dordrecht: Kluwer, (1995).

[202] Proffen, T. and Neder, R. B. *Journal of Applied Crystallography* **30**, 171–175 (1997).

[203] Michelet, A., Mazurier, A., Colin, G., Laruelle, P., and Flahaut, J. *Journal of Solid State Chemistry* **13**, 65–76 (1975).

[204] Julien-Pouzol, M., Jaulmes, S., and Dagron, C. *Acta Crystallographica B* **38**, 1566–1568 (1982).

[205] Dittmar, G. and Schäfer, H. *Acta Crystallographica B* **31**, 2060 (1975).

[206] Dittmar, G. and Schäfer, H. *Acta Crystallographica B* **32**, 1188 (1976).

[207] Prewitt, C. T. and Young, H. S. *Science* **149**, 535–537 (1965).

[208] Goodyear, J. and Steigmann, G. A. *Acta Crystallographica* **16**, 946–949 (1963).

[209] Tomas, A., Pardo, M. P., Guittard, M., Guymont, M., and Famery, R. *Materials Research Bulletin* **22**, 1549–1554 (1987).

[210] Jones, C. Y., Bryan, J. C., Kirschbaum, K., and Edwards, J. G. *Zeitschrift fuer Kristallographie* **216**, 327–328 (2001).

[211] Choudhury, A. and Dorhout, P. K. *Zeitschrift fuer Anorganische und Allegemeine Chemie* **634**, 649–656 (2008).

[212] Helmholdt, R. B., Goubitz, K., Sonneveld, E. J., and Schenk, H. *Acta Crystallographica E* **59**, i119–i121 (2003).

[213] Bellissent-Funel, M. C. and Chieux, P. *Physical Review A* **39**, 6310–6318 (1989).

[214] Waseda, Y. and Suzuki, K. *Physica Status Solidi B* **49**, 339 (1972).

[215] Di Cicco, A. D. and Filipponi, A. *Journal of Non-Crystalline Solids* **156-158**, 99 (1993).

[216] Wei, S., Oyanagi, H., Liu, W., Hu, T., Yin, S., and Bian, G. *Journal of Non-Crystalline Solids* **275**, 160–168 (2000).

[217] Greetham, G. M. and Ellis, A. M. *Journal of Molecular Spectroscopy* **222**, 273–275 (2003).

[218] Bermejo, F. J., Bustinduy, I., Levett, S. J., Taylor, J. W., Fernàndez-Perea, R., and Cabrillo, C. *Physical Review B* **72**, 104103 (2005).

[219] Schnering, H. G. and Nesper, R. *Acta Chemica Scandinavica* **45**, 870–872 (1991).

[220] Tampier, M. and Johrendt, D. *Journal of Solid State Chemistry* **158**, 343–348 (2001).

[221] Roques, R., Rimet, R., Declercq, J. P., and Germain, G. *Acta Crystallographica B* **35**, 555–557 (1979).

[222] Michelet, A., Mazurier, A., Collin, A., Laruelle, P., and Flahaut, J. *Bulletin de la Societe Francaise de Mineralogie et de Cristallographie* **96**, 12–17 (1973).

[223] Lychmanyuk, O. S., Gulay, L. D., and Olekseyuk, L. D. *Polish Journal of Chemistry* **81**, 353–367 (2007).

[224] Jaulmes, S. and Lauruelle, P. *Acta Crystallographica B* **29**, 352–354 (1973).

[225] Guseinov, G. G., Mamedov, F. K., Amiraslanov, I. R., and Mamedov, K. S. *Kristallografiya* **28**, 866–869 (1983).

[226] Gulay, L. D., Lychmanyuk, O. S., Stepien-Damm, J., Pietraszko, A., and Olekseyuk, I. D. *Journal of Alloys and Compounds* **414**, 113–117 (2006).

[227] Benazeth, S., Tuilier, M. H., Loireau-Lozac'h, A. M., Dexpert, H., Lagarde, P., and Flahaut, J. *Journal of Non-Crystalline Solids* **110**, 89–100 (1989).

[228] Martin, R. A., Salmon, P. S., Carroll, D. L., Smith, M. E., and Hannon, A. C. *Journal of Physics: Condensed Matter* **20**, 115204 (2008).

[229] Zeidler, A. Private Communication, (2008).

[230] Sakai, T., Maeda, K., Munzar, M., Tonchev, D., Ikari, T., and Kasap, S. O. *Physics and Chemistry of Glasses* **47**, 225–228 (2006).

[231] Giridhar, A. and Mahadevan, S. *Journal of Non-Crystalline Solids* **126**, 161–169 (1990).

[232] Worlton, T., Hammonds, J., Mikkelson, D., Mikkelson, R., Portor, R., Tao, J., and Chatterjee, A. *Physica B* **385-386**, 1340–1342 (2006).

[233] Dittmar, G. and Schaefer, H. *Acta Crystallographica B* **32**, 2726–2728 (1976).

[234] Luebbers, D. and Leute, V. *Journal of Solid State Chemistry* **43**, 339–345 (1982).

[235] Ghemard, G., Jaulmes, S., Etienne, S., and Flahaut, J. *Acta Crystallographica C* **39**, 968–971 (1983).

[236] Poduska, K. M., DiSalvo, F. J., Min, K., and Halasyamani, P. S. *Journal of Alloys and Compounds* **335**, 5–9 (2002).

[237] Wu, P. and Ibers, J. A. *Journal of Solid State Chemistry* **107**, 347–355 (1993).

[238] Gulay, L. D., Lychmanyuk, O. S., Olekseyuk, I. D., and Pietraszko, A. *Journal of Alloys and Compounds* **422**, 203–207 (2006).

[239] Choudhury, A., Polyakova, L. A., Hartenbach, I., Schleid, T., and Dorhout, P. K. *Zeitschrift fuer Anorganische und Allgemeine Chemie* **632**, 2395–2401 (2006).

[240] Chan, B. C. and Dorhout, P. K. *Zeitschrift fuer Kristallographie* **220**, 7–8 (2005).

[241] Tampier, M., Johrendt, D., Poettgen, R., Kotzyba, G., Rosenhahn, C., and Mosel, B. D. *Zeitschrift fuer Naturforschung, Teil B. Anorganische Chemie, Organische Chemie* **57**, 133–140 (2002).

[242] Rimet, R., Roques, R., Zanchetta, J. V., Declercq, J. P., and Germain, G. *Revue de Chimie Minerale* **18**, 277–285 (1981).

[243] Bhatia, A. B. and Thornton, D. E. *Physical Review B* **2**, 3004 (1970).

[244] Salmon, P. S. *Journal of Non-Crystalline Solids* **353**, 2959–2974 (2007).

[245] Benmore, C. J. and Qiang, M. Private Communication, (2006).

[246] Urquidi, J., Benmore, C. J., Neuefeind, J., and Tomerli, B. *Journal of Applied Crystallography* **36**, 368 (2003).

[247] Huang, F. Q. and Ibers, J. A. *Acta Crystallographica C* **55**, 1210–1212 (1999).

[248] Lychmanyuk, O. S., Gulay, L. D., and Olekseyuk, I. D. *Polish Journal of Chemistry* **80**, 463–469 (2006).

[249] Wasse, J. C., Salmon, P. S., and Delaplane, R. G. *Physica B* **276-278**, 433–434 (2000).

[250] Wasse, J. C. and Salmon, P. S. *Journal of Physics: Condensed Matter* **11**, 2171–2177 (1999).

[251] Drewitt, J. W. E., Salmon, P. S., Barnes, A. C., Klotz, S., Fischer, H. E., and Crichton, W. A. *Physical Review B* (Submitted: 2009).

[252] Wells, A. F. *Structural Inorganic Chemistry*. Oxford: Clarendon, (1984).

[253] Chudinovskikh, L. and Boehler, R. *Nature* **411**, 574–577 (2001).

[254] Sammis, C. G., Smith, J. C., Schubert, G., and Yuen, D. A. *Journal of Geophysical Research* **82**, 3747–3761 (1977).

[255] Anderson, D. L. *Science* **157**, 1165–1173 (1967).

[256] Poirier, J. P. *Introduction to the physics of the Earth's interior*. Cambridge University Press, 2 edition, (2000).

[257] Dziewonski, A. M. and Anderson, D. L. *Physics of the Earth and Planetary Interiors* **25**, 297–356 (1981).

[258] Anderson, D. L. *Theory of the Earth*. Boston:Blackwell Scientific Publications, (1989). `http://resolver.caltech.edu/CaltechBOOK:1989.001`.

[259] McDonough, W. F. and Sun, S. *Chemical Geology* **120**, 223–253 (1995).

[260] Boekel, R. V., Min, M., Leinert, C., Waters, L. B. F. M., Richichi, A., Chesneau, O., Dominik, C., Jaffe, W., Dutrey, A., Graser, U., Henning, T., de Jong, J., Köhler, R., de Koter, A., Lopez, B., Malbert, F., Morel, S., Paresce, F., Perrin, G., Preibisch, T., Przygodda, F., Schöller, M., and Wittkowski, M. *Nature* **432**, 479–482 (2004).

[261] Kuwayama, Y., Hirose, K., Sata, N., and Ohishi, Y. *Science* **309**, 923–925 (2005).

[262] Kirby, S. H., Durham, W. B., and Stern, L. A. *Science* **252**, 216–225 (1991).

[263] Stein, S. A. and Rubie, D. C. *Science* **286**, 909–910 (1999).

[264] Rigden, S. M., Ahrens, T. J., and Stolper, E. M. *Science* **226**, 1071–1074 (1984).

[265] Williams, Q. and Jeanloz, R. *Science* **239**, 902–905 (1988).

[266] Andrault, D., Fiquet, G., Guyot, F., and Hanfland, M. *Science* **282**, 720–724 (1998).

[267] Huang, L., Durandurdu, M., and Kieffer, J. *Nature Materials* **5**, 977–981 (2006).

[268] Rustard, J. R. and Yuen, D. A. *Physical Review B* **44**, 2108–2121.

[269] Gratz, A. J., DeLoach, L. D., Clough, T. M., and Nellis, W. J. *Science* **259**, 663–666 (1993).

[270] Wei, P. *Zeitschrift fuer Kristallographie* **92**, 355–362 (1935).

[271] Young, R. A. and Post, B. *Acta Crystallographica* **15**, 337 (1962).

[272] Smith, G. S. and Alexander, L. E. *Acta Crystallographica* **16**, 462 (1963).

[273] Stishov, S. M. and Popova, S. V. *Geokhimiya* **10**, 837 (1961).

[274] Sinclair, W. and Ringwood, A. E. *Nature* **272**, 714 (1978).

[275] Meade, C., Hemley, R. J., and Mao, H. K. *Physical Review Letters* **69**, 1387–1390 (1992).

[276] Sato, T. and Funamori, N. *Physical Review Letters* **101**, 255502 (2008).

[277] Hemley, R. J., Mao, H. K., Bell, P. M., and Mysen, B. O. *Physical Review Letters* **57**, 747–750 (1986).

[278] Champagnon, B., Martinet, C., Boudeulle, D., Vouagner, D., Coussa, C., Deschamps, T., and Grosvalet, L. *Journal of Non-Crystalline Solids* **354**, 569–573 (2008).

[279] Guissani, Y. and Guillot, B. *Journal of Chemical Physics* **104**, 7633 (1996).

[280] Horbach, J., Kob, W., and Binder, K. *Chemical Geology* **174**, 87 (2001).

[281] Micoulaut, M., Cormier, L., and Henderson, G. S. *Journal of Physics: Condensed Matter* **18**, R753–R784 (2006).

[282] Itie, J. P., Polian, A., Calas, G., Petiau, J., Fontaine, A., and Tolentino, H. *Physical Review Letters* **63**, 398–401 (1989).

[283] Durben, D. J. and Wolf, G. H. *Physical Review B* **43**, 2355–2363 (1991).

[284] Polsky, C. H., Smith, K. H., and Wolf, G. H. *Journal of Non-Crystalline Solids* **248**, 159–168 (1999).

[285] Guthrie, M., Tulk, C. A., Benmore, C. J., Xu, J., Yarger, J. L., Klug, D. D., Tse, J. S., Mao, H.-k., and Hemley, R. J. *Physical Review Letters* **93**, 115502 (2004).

[286] Sampath, S., Benmore, C. J., Lantzky, K. M., Neuefeind, J., Leinenweber, K., Price, D. L., and Yarger, J. L. **90**, 115502 (2003).

[287] Hong, X., Shen, G., Prakapenka, V. B., Newville, M., Rivers, M. L., and Sutton, S. R. *Physical Review B* **75**, 104201 (2007).

[288] Martin, R. A. Private Communication, (2007).

[289] Micoulaut, M., Guissani, Y., and Guillot, B. *Physical Review E* **73**, 031504 (2006).

[290] Klotz, S. Private Communication, (2007).

[291] Kiczenski, T. J., Ma, C., Hammarsten, E., Wilkerson, D., Affatigato, M., and Feller, S. *Journal of Non-Crystalline Solids* **272**, 57–66 (2000).

[292] Leadbetter, A. J. and Wright, A. C. *Journal of Non-Crystalline Solids* **7**, 37–52 (1972).

[293] Boolchand, P. Private Communication, (2007).

[294] Klotz, S., Padmanabhan, B., Phillippe, J., and Strässle, T. *High Pressure Research* **28**, 621–625 (2008).

[295] Smith, K. H., Shero, E., Chizmeshya, A., and Wolf, G. H. *Journal of Chemical Physics* **102**, 6851–6857 (1995).

[296] Suito, K., Miyoshi, M., Sasakura, T., and Fujisawa, H. In *High-Pressure Research: Application to Earth and Planetary Sciences,* Syono, Y. and Manghnani, M. H., editors, 219–225. Terra Scientific Publishing Company (TERRAPUB), Tokyo / American Geophysical Union, Washington, D.C., (1992).

[297] Tsiok, O. B., Brazhkin, V. V., Lyapin, A. G., and Khvostantsev, L. G. *Physical Review Letters* **80**, 999–1002 (1998).

[298] Stone, C. E., Hannon, A. C., Ishihara, T., Kitamura, N., Shirakawa, Y., Sinclair, R. N., Umesaki, N., and Wright, A. C. *Journal of Non-Crystalline Solids* **293-295**, 769–775 (2001).

[299] Vohra, Y. K. and Spencer, P. T. *Physical Review Letters* **86**, 3068–3071 (2001).

[300] Zhao, Y., Zhang, J., Pantea, C., Qian, J., Daemen, L. L., Rigg, P. A., Hixson, R. S., Gray III, G. T., Yang, Y., Wang, L., Wang, Y., and Uchida, T. *Physical Review B* **71**, 184119 (2005).

[301] Bashkin, I. O., Fedotov, V. K., Nefedova, M. V., Tissen, V. G., Ponyatovsky, E. G., Schiwek, A., and Holzapfel, W. B. *Physical Review B* **68**, 054401 (2003).

[302] Akahama, Y., Kawamura, H., and Le Bihan, T. *Journal of Physics: Condensed Matter* **14**, 10583–10588 (2002).

[303] Dmitriev, V. P., Dubrovinsky, L., Bihan, T. L., Kuznetsov, A., Weber, H. P., and Poniatovsky, E. G. *Physical Review B* **73**, 094114 (2006).

[304] Howells, W. S. Private Communication, (1989).

[305] Salmon, P., Barnes, A. C., Martin, R. A., and Cuello, G. J. *Journal of Physics: Condensed Matter* **19**, 415110 (2007).

[306] Salmon, P. S., Barnes, A. C., Martin, R. A., and Cuello, G. J. *Physical Review Letters* **96**, 235502 (2006).

[307] Hoppe, U., Kranold, R., Weber, H. J., and Hannon, A. C. *Journal of Non-Crystalline Solids* **248**, 1–10 (1999).

[308] Hannon, A. C., Martino, D., Santos, L. F., and Almeida, R. M. *Journal of Physical Chemistry B* **111**, 3342–3354 (2007).

[309] Fay, V. E., Völlenkle, H., and Wittmann, A. *Zeitschrift für Kristallographie* **138**, 439–448 (1973).

[310] Barnes, A. C. Private Communication, (2008).

[311] Henderson, G. S. *Journal of Non-Crystalline Solids* **353**, 1695–1704 (2007).

[312] *Nuclear data evaluation laboratory: Table of Nuclides.* Korea Atomic Energy Research Institute, (2000). http://atom.kaeri.re.kr/.

[313] Chadwick, M. B., Obložinský, P., Herman, M., Greene, N. M., McKnight, R. D., Smith, D. L., Young, P. G., MacFarlane, R. E., Hale, G. M., Frankle, S. C., Kahler, A. C., Kawano, T., Little, R. C., Madland, D. G., Moller, P., Mosteller, R. D., Page, P. R., Talou, P., Trellue, H., White, M. C., Wilson, W. B., Arcilla, R., Dunford, C. L., Mughabghab, S. F., Pritychenko, B., Rochman, D., Sonzogni, A. A., Lubitz, C. R., Trumbull, T. H., Weinman, J. P., Brown, D. A., Cullen, D. E., Heinrichs, D. P., McNabb, D. P., Derrien, H., Dunn, M. E., Larson, N. M., Leal, L. C., Carlson, A. D., Block, R. C., Briggs, J. B., Cheng, E. T., Huria, H. C., Zerkle, M. L., Kozier, K. S., Courcelle, A., Pronyaev, V., and van der Marck, S. C. *Nuclear Data Sheets* **107**, 2931–3118 (2006).

[314] Guthrie, M. Private Communication, (2009).

[315] Wilding, M. Private Communication, (2007).

[316] Wolanin, E., Pruzan, P., Chervin, J. C., Canny, B., Gauthier, M., Häusermann, D., and Hanfland, M. *Physical Review B* **56**, 5781–5785.

[317] Bull, C. Private Communication, (2008).

[318] Salmon, P. S. and Zeidler, A. Private Communication, (2009).

[319] Soper, A. K., Howells, W. S., and Hannon, A. C. Technical Report RAL-89-046, Rutherford Appleton Laboratory, (1989).

[320] Bolef, D. I., Smith, R. E., and Miller, J. G. *Physical Review B* **3**, 4100–4108 (1972).

[321] Salmon, P. S., Petri, I., Jong, P. H. K., Verkerk, P., Fischer, H. E., and Howells, W. S. *Journal of Physics: Condensed Matter* **16**, 195–22 (2004).

[322] Crawford, R. K., Price, D. L., Haumann, J. R., Kleb, R., Montague, D. G., Carpenter, J. M., Susman, S., and Dejus, J. Institute of Physics Conference Series Number 97, 427–450. New York: IOP Publishing Ltd., (1989).

[323] Vaccari, M., Aquilanti, G., Pascarelli, S., and Mathon, O. *Journal of Physics: Condensed Matter* **21**, 145403 (2009).

[324] Micoulaut, M. *Journal of Physics: Condensed Matter* **16**, L131–L138 (2004).

[325] Haines, J., Léger, J. M., Chateau, C., and Pereira, A. S. *Physics and Chemistry of Minerals* **27**, 575–582 (2000).

[326] Kohara, S. and Suzuya, K. *Nuclear Instruments and Methods in Physics Research B* **199**, 23–28 (2003).

[327] Haines, J., Léger, J. M., and Chateau, C. *Physical Review B* **61**, 8701–8706 (2000).

[328] Shiraki, K., Tsuchiya, T., and Ono, S. *Acta Crystallographica Section B* **59**, 701–708 (2003).